The University Of Sheffield.

Department Of Mechanical Engineering

PhD Mechanical Engineering Thesis

Zhikun **Li**

Development of Wrinkling Modelling and Testing Methods for Shear Metal Spinning

Supervisor: Professor Hui Long

Faculty of Engineering

Department of mechanical engineering

Thesis submitted to the Department of Mechanical Engineering, University of Sheffield in fulfilment of the requirements for the degree of PhD

Submission Date

August 2022

Abstract

The metal spinning process has the advantages of processing flexibility and net-shape manufacturing. Material formability of the spinning process is also improved due to the localised material deformation caused by tension, bending, shearing and cyclic loading. The high material utilisation and accuracy of product dimensions benefit small batch and customised product manufacturing in various applications, for example, automotive, military and aerospace industries. However, the design of the metal spinning process still heavily relies on empirical knowledge to avoid process failures, and wrinkling failure occurs most often. There is no established industrial standard or testing method to determine the processing parameters to prevent wrinkling failure in the spinning process. Even the wrinkling initiation on the aspect of strain is not clear. The manufacturing efficiency and product quality are compromised by repetitive trial-and-error and preliminary tests in developing the spinning process for a new product or using a new material. The trial-and-error method costs expensive human and material resources and machine time to develop a new product. The objective of this project is to develop a shear spinning finite element (FE) model and perform shear spinning experimental tests to investigate the wrinkling mechanism. Furthermore, a new wrinkling testing method is developed based on the shear spinning FE modelling and test findings.

The FE models of shear spinning are developed, and the wrinkling deformation behaviour of material AA5251-H22 is investigated. Two important processing parameters are investigated: the feed ratio and the mandrel rotational speed. Circumferential strain results are obtained from the FE modelling. The wrinkling results from circumferential strain accumulation by the cyclical loadings induced to the workpiece by the spinning roller. The wrinkling occurs when the circumferential strain starts to increase cyclically and permanently becomes positive/tensile. It has been found that different strain rates caused by different mandrel speeds do not affect wrinkling initiation. The strain rate also does not affect the circumferential strain accumulation and, thus, wrinkling propagation. The wrinkling limit as the maximum feed ratio is determined for the shear spinning process setup in this study. A higher feed ratio causes a more rapid circumferential strain accumulation.

The shear spinning experimental tests are conducted. Components such as the roller vibrate more severely when the wrinkling initiates, and the vibration is recorded as waveforms. The amplitudes of the waveforms are used to determine the wrinkling initiation time. The thickness distribution of spun workpiece is measured. The wrinkling wave amplitude of the wrinkling waves on the workpiece

flange and the thickness distribution results are measured. These measurements are used to validate the spinning FE models. The vibration waveforms prove that the dynamic effect of the different strain rates due to different mandrel speeds does not affect wrinkling initiation and propagation. It further proves that the feed ratio is the most significant factor affecting wrinkling initiation.

Six FE models of the new wrinkling testing method are developed with AA5251-H22 material. The models are developed based on the existing biaxial tension under bending and compression (BTBC) rig that can apply multiple deformation modes to the specimen. Although the wrinkling test FE modelling results do not correlate with the shear spinning FE modelling and test results, they are the first attempt to test the spinning wrinkling without the spinning process itself, and valuable findings are drawn from the modelling results. The most important feature of the specimen design to achieve wrinkling deformation is the thickness-reduced arc gauge area. The thickness reduction guarantees that the deformation only occurs on the gauge area rather than partially distributed on the arms of the specimen. The most important boundary condition is the compression applied to the arms on the two sides of the gauge area. The compression results in tensile circumferential strains on the top surface of the specimen and causes wrinkling deformation. The bending tool represents the roller in the spinning process, applying bending deformation to the specimen, which is not optimal for causing wrinkling deformation. The roller in the spinning process applies bending deformation cyclically to the workpiece, causing wrinkling due to cyclical tensile circumferential strain accumulation. It is a limitation of the BTBC rig.

The BTBC rig is modified to perform the newly developed wrinkling test. Four tests are selected from the six wrinkling test FE models and conducted on the modified BTBC test rig. The testing specimens are manufactured and etched with circular grid patterns for strain measurements. The strain results correlate with the FE modelling results but does not correlate with the spinning FE and test results. The strains of the wrinkled specimen are smaller than in the spinning process. The early-stage/minor wrinkling deformation is regarded as achieved in the BTBC wrinkling test. The loadings applied to the specimen are inadequate to cause late-stage/severe wrinkling due to the BTBC rig limitation. The constrained bending tool movement is a limitation of the BTBC rig.

The first novelty of this study is that the dynamic effect is proven to be independent of the wrinkling initiation in the spinning process. The normalised wrinkling initiation time of the spinning processes with different mandrel speeds are identical,

indicating that the wrinkling initiation is not affected by the different strain rates caused by the various mandrel speeds.

The second novelty is that the strain signature of the spinning wrinkling deformation is obtained, and the wrinkling mechanism is concluded. The strain and time history results are presented in the forming limit diagram (FLD). The wrinkling initiation and severity are affected by the roller feed ratios. The wrinkling initiates when the feed ratio exceeds the wrinkling limit feed ratio, and the circumferential strain on the wrinkling wave top surface becomes tensile and increases cyclically. Also, higher feed ratios cause more rapid strain accumulation and higher tensile circumferential strains. The circumferential strain remains compressive in a wrinkling-free shear spinning process.

The third novelty is that the wrinkling testing method is developed. Although the BTBC rig can only achieve early-stage/minor wrinkling deformation on the specimen, no previous literature reports the development of the wrinkling testing method related to the spinning process. The FE results correlate with the test results, and the test method has the potential to be greatly improved after further modification to the BTBC rig.

Acknowledgements

Foremost, I would like to express my sincere gratitude to my supervisor Professor Hui Long for my PhD study and continuous support for her patience, motivation, enthusiasm, and immense knowledge. Her guidance helped me in all the time of research and writing of this thesis. She is patient in every aspect of my study period. I could not have imagined having a better supervisor and mentor for my PhD study.

Thanks to the Faculty of Engineering, the University of Sheffield, for offering me the faculty and the opportunity to study in this prestigious university these years all the way from Bachelor to PhD.

Thank you to Jamie Booth and David Webster from the department mechanical workshop and Chris Todd from the department electronics workshop. Without your technical advice and work, the whole project will be only an imagination in my head.

Thanks to Sheng Ai, Zhaohua Li, Rui Dai, An Ping, Wenxuan Peng and Zhidong Chang, as my friends and comrades in the same group who helped me in any way all these years.

Special thanks to my girlfriend, Wanting Huang, for her love, patience, understanding and support during the final stage of my PhD study.

Last but not least, I would like to thank my parents for all the support all these years. They provide me with the opportunity to study and live in the UK for 9 years.

Contents

List of Tables

List of Figures

List of Nomenclature

$\varepsilon_{i\ (i=1,2,3)}$	The true strains
β	The strain ratio
t_0	The thickness of the workpiece before being deformed (mm)
t_1	The thickness of the workpiece after being deformed (mm)
d_0	The diameter of the circular etched pattern before being deformed (mm)
d_1	The major diameter of the circular etched pattern after being deformed (mm)
d_2	The minor diameter of the circular etched pattern after being deformed (mm)
R_0	The radius of the workpiece for the spinning process (mm)
s	The mass scaling factor
L_e	The characteristic length of the element
c_d	The stress wave speed (m/s)
E	Young's modulus (MPa)
ρ	The density of the material (m^3/kg)
ε_E	The engineering strain
ε_{EC}	The circumferential engineering strain
ε_{ER}	The radial engineering strain
ε_{TC}	The true circumferential strain
ε_{TR}	The true radial strain

List of Abbreviations and Acronyms

CNC	Computer numerical controlled
ISF	Incremental sheet forming
BTBC	Biaxial tension under bending and compression
FEM	Finite element method
DIC	Digital image correlation
FLC	Forming limit curve
FLD	Forming limit diagram
FFLD	Fracture forming limit diagram
CBT	Continuous bending under tension
TCBC	Tension under cyclic bending and compression
RPM	Revolution per mintue

Declaration

I, the author, confirm that the Thesis is my own work. I am aware of the University's Guidance on the Use of Unfair Means (www.sheffield.ac.uk/ssid/unfair-means). This work has not been previously been presented for an award at this, or any other, university.

1 Introduction

The metal spinning process is a sheet metal forming process that has recently gained considerable attention due to its unique advantages: low cost, low forming force, good surface finishing, and enhanced mechanical properties due to work hardening. It is one of the oldest methods of material forming. It has advantages over other metal forming processes because of its flexibility, simple tooling and low forming forces. The rapid emerging trend in modern industries after entering the 21st century has developed the technology into a wide range of versatile processes for producing near-net shape, lightweight and customizable components in multiple domains. Various product geometries using different spinning methods have developed, exploring the material forming limits and developing related technologies have never stopped throughout the last two decades.

This chapter presents a summary of sheet metal forming processes in Section 1.1. Metal spinning processes are further introduced in Section 1.2. Process failures in the metal spinning process, such as wrinkling and fracture failures, are briefly outlined in Section 1.3. Research aims and objectives are summarised in Section 1.4. Finally, the thesis layout is presented in Section 1.5. A planned publication of the study is listed in Section 1.6.

1.1 Sheet Metal Forming

Metal forming has been around for millennia. The earliest spinning process can be traced back to 3000 years ago as an art of potting clay using a manual-powered potter wheel by the Pharaohs in ancient Egypt. It travelled to China around 1,100 to 1,400 years ago during the Tang Dynasty. Due to the technological limitations of that era, only soft metals such as silver and tin were formable. In addition, they were only formed into axisymmetric-shaped geometrics, such as bowls and cups. Currently, sheet metal forming is a production technology widely applied for industrial applications. In the sheet metal forming process, a forming force is applied to a piece of sheet metal to modify its geometry without removing any material. The applied force generates stresses on the material and causes plastic deformation when the stresses exceed the yield strength of the material. This is expected to be done without failures, for example, fracture and wrinkling so that the metal sheet can be bent or stretched into various complex shapes.

Sheet metal spinning deforms a flat metal blank as the spinning workpiece into an axisymmetric shape of the component, as shown in Figure 1.1. The forming force is provided by a roller that directly contacts and compresses the workpiece surface.

The roller can be perpendicular to the metal sheet or at a fixed or constantly changing angle during the spinning process. The workpiece is usually centrally clamped by a backplate onto the end of a mandrel. Due to the friction force provided by the mandrel and the backplate, the workpiece rotates with the mandrel, and the roller deforms the workpiece using a specific feed rate while the workpiece rotates. In metal spinning, the mandrel can be regarded as a die to determine the finishing shape of the workpiece. In addition, the mandrel dimensions can be customised to satisfy the different demands of various component geometries. As a comparison, the traditional metal forming processes, for example, deep drawing, blanking and V-bending, produce components with simple geometries, as shown in Figure 1.2.

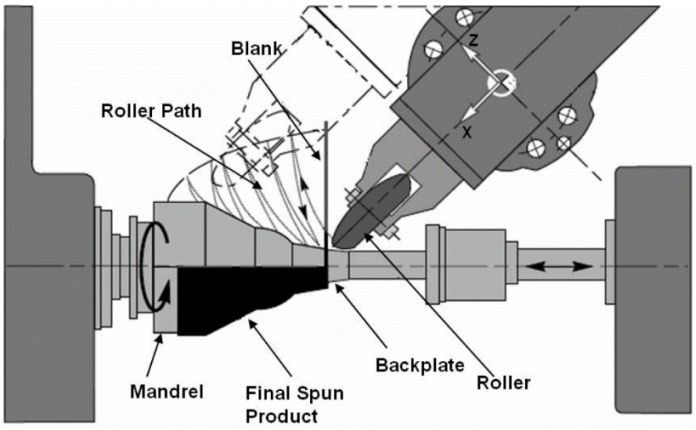

Figure 1.1 Schematic diagram of metal spinning [1].

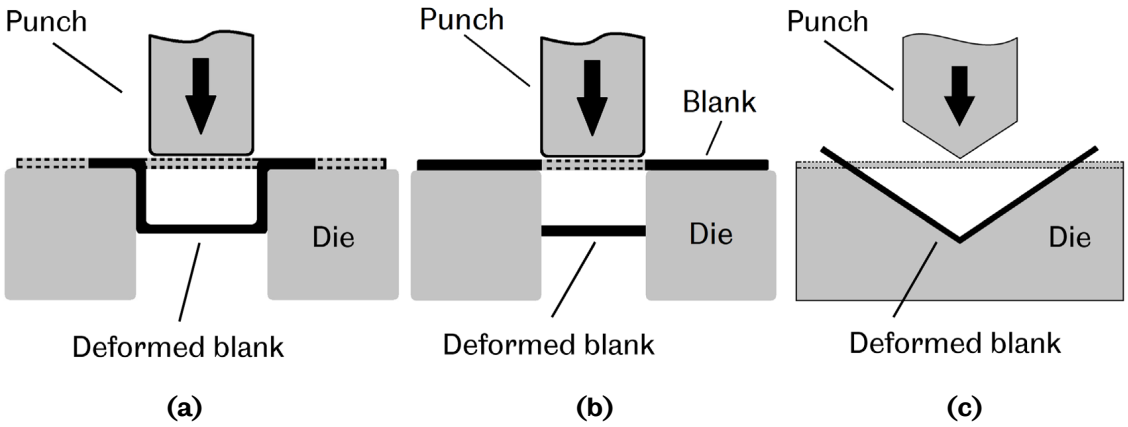

Figure 1.2 Schematic diagrams of traditional sheet metal forming processes: a) deep drawing, b) blanking, and c) V-bending [2].

The term deformation mode describes the deformation state of the workpiece. Each process has a primary deformation mode. The deformation mode of deep drawing is tension by elongating the blank around the punch. The deformation mode of blanking is shearing at both ends of the deformed blank, and the deformation mode of V-bending is bending at the centre of the deformed blank. For these traditional

sheet metal forming processes, manufacturing a specific product requires a customised punch and die with corresponding geometries. Although the cost can be reduced by mass production of the product, these traditional sheet metal forming processes remain costly for small batch production, such as manufacturing prototypes and customised products. The metal spinning process does not require specific dies or tools but a simple mandrel and a roller tool; thus, it is more flexible and customizable than traditional sheet metal forming processes.

Modern metal spinning processes are performed using a computer numerical controlled (CNC) machine. The diameter and thickness of the metal sheet used in metal spinning can be selected flexibly to fulfil various requirements of specific components within the specification of the CNC machine. Metal spinning can form components with a workpiece diameter ranging from 3 mm to 10 m and a workpiece thickness ranging from 0.4 to 25 mm [3]. For commercial and high-value production proposes, for example, Excell Metal Spinning Ltd has employed the delicate precision control technology capable of producing components with thicknesses ranging from 0.9 to 5 mm and diameters ranging from 30 to 2,000 mm [4]. Metal spinning is a flexible sheet forming process. Specialised or complex tooling for most applications is not required for spinning. A simple tool, such as a roller or a metal rod with a rounded tip, moves over the workpiece surface, producing highly localised plastic deformation that meets the manufacturing requirements. In this case, specific dies are unnecessary, and a wide range of three-dimensional shapes can be formed by moving the deforming tool along a customised tool path. In addition, metal spinning is a near-net-shape forming process, so the finished spun part is close to the required geometry of the final product and does not require additional finishing processes.

Four common roller path profiles are commonly used in metal spinning: convex path, linear path, concave path, and combined convex and concave path. Different roller path profiles are implemented according to the requirements of the finished shape of the products. The final components will be axisymmetric as circular cone shapes or circular shapes with different diameters. Examples of metal spinning products with various spun product sizes are shown in Figure 1.3.

Currently, metal spinning is a widely used manufacturing technology in civil, energy and medical and other applications for high-value products, such as aerospace and military. For example, Century Metal Spinning [5] produces metal spinning products such as cone noses for military missile systems, aerospace rockets, and satellite components, as shown in Figure 1.4. Customers of this company include Boeing, Lockheed, Northrup Grumman, Raytheon, Aerojet Rocketdyne and Honeywell. Their

product range covers radome (a protective housing for a radar antenna) parts, radar covers, rocket engines, underwater components, weapon components, weatherproof enclosures, fan shrouds for ventilation systems, radar calibration spheres and other various spun products.

Figure 1.3 Examples of metal spinning products: stainless steel housing, vacuum cleaner housing, and equipment housing with various spun product sizes [6] [7].

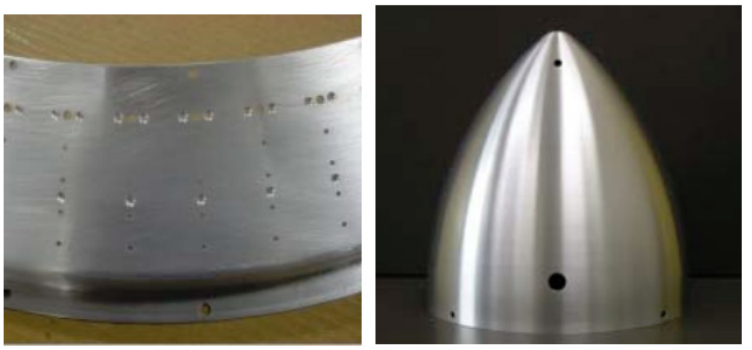

Figure 1.4 Satellite ring and nose cone for aerospace and military applications [5].

A previous limitation of the metal spinning process is that complex components with asymmetric shapes are difficult to produce. However, recent developments allow for elliptical and polygonal tool paths. As a result, the workpiece can be deformed into asymmetric and complex shapes. Examples of non-axisymmetric shape components are shown in Figure 1.5. With these relatively new spinning technologies, complex geometries can be manufactured instead of limited simple-cone and circular-tube shaped components.

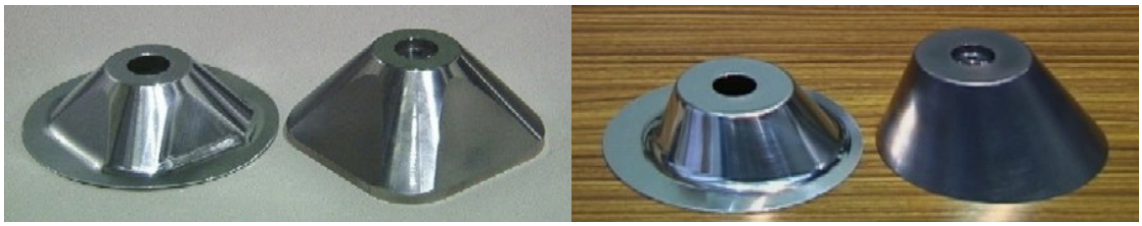

Figure 1.5 Metal spinning of non-axisymmetric products [8].

1.2 Metal Spinning

The most common three types of metal spinning processes and five types of less common novel metal spinning processes are introduced in this section. Essential features of each metal spinning process are outlined, such as the advantages and disadvantages of each process.

1.2.1 Conventional Spinning

As shown in Figure 1.6, a workpiece is formed into an axisymmetric shape in conventional spinning without a change in thickness. However, compared with the original workpiece, the diameter of the formed component is reduced. The reduction in diameter is because the roller generates internal stresses in the sheet when working on the workpiece surface.

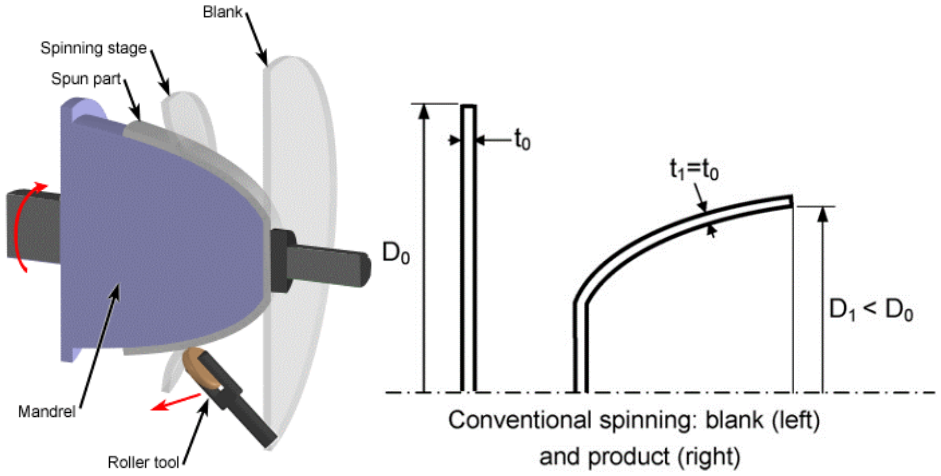

Figure 1.6 Schematic diagram of the conventional metal spinning process [9].

Roller induces internal stresses to the workpiece during the spinning process. An estimate of these stresses proposed by Lange [10] and Runge [11] is widely quoted in the literature and shown in Figure 1.7. When the roller moves towards the flange (forward pass), radial tensile stresses and tangential compressive circumferential stresses are generated, as shown in Figure 1.7 (a). The radial tensile stresses alone will cause a reduction in the thickness. However, the thickness reduction is compensated by the tangential compressive circumferential stresses, making the stress states like those in pure shear. Pure shear maintains an almost constant thickness in the spinning process. When the roller moves away from the edge towards the workpiece centre (backward pass), the material builds up in front of the roller, generating radial and tangential compressive stresses and increasing the thickness, as shown in Figure 1.7 (b). The roller also induces compression and bending to the workpiece, making the metal spinning process even more complicated than other sheet metal forming processes.

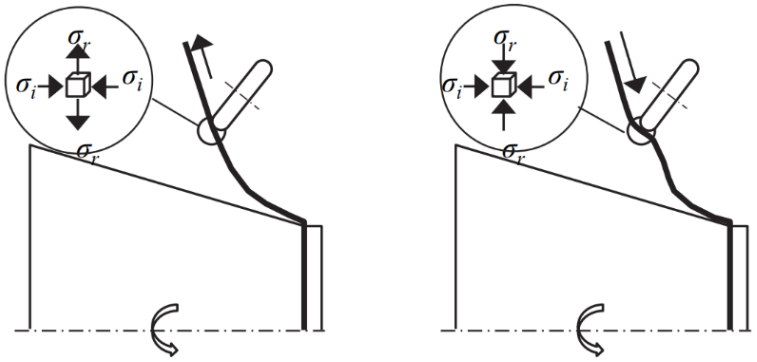

(a) (b)

Figure 1.7 Theoretical stress distributions of the forming region during spinning: (a) forward pass and (b) backward pass [12].

1.2.2 Shear Spinning

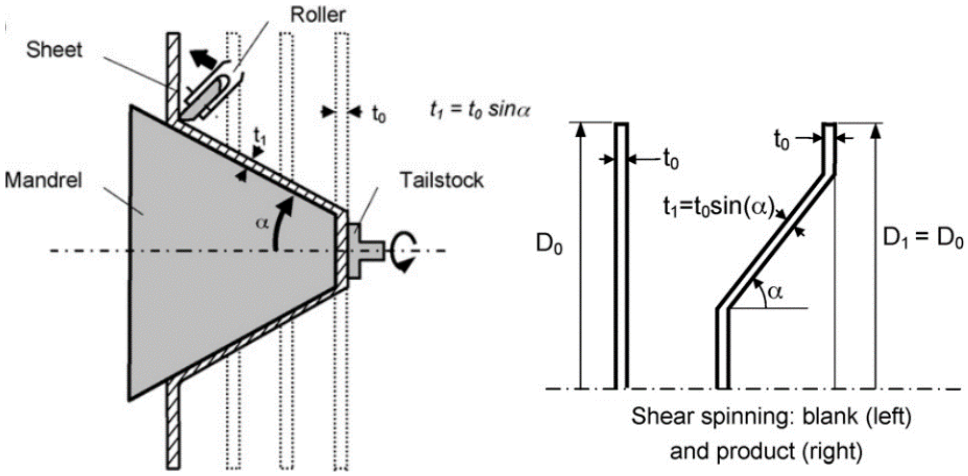

Figure 1.8 Schematic diagram of the shear spinning process [4][13].

In the shear spinning process, as shown in Figure 1.8, the thickness of the deformed section is reduced, and the diameter of the formed component remains unchanged. The thickness of the deformed area will ideally be reduced uniformly. The thickness of the deformed section is represented by the sine law, shown in Equation 1.1, described as true shear spinning.

$$t_1 = t_0 \sin(\alpha)$$

Equation 1.1

t_0 is the original thickness of the workpiece, and t_1 is the thickness of the formed component. The symbol α is the angle between the deformed section and the horizontal axis of the formed component. Shear spinning produces spun parts with different thicknesses by setting different gaps between the roller and the mandrel. Different thicknesses lead to different conditions of the formed component, as shown in Figure 1.9.

A workpiece can be spun without defects in true shear spinning, such as wrinkling on the flange. In addition, the internal stresses are confined to the area under the roller, and the flange remains virtually stress-free in true spinning [4]. Deviation from the sine law causes the stresses to extend into the flange, causing possible defects, such as wrinkling. In an under-spinning (under-reduction) condition, where $t_1 > t_0 \sin\alpha$, the material in the flange is pulled inwards. The flange is bent towards the roller, which may cause it to wrinkle. In contrast, in an over-spinning (over-reduction) condition, where $t_1 < t_0 \sin\alpha$, the material builds up in front of the roller, causing the flange to bend forward and away from the roller. Figure 1.9 illustrates the effect of thickness deviation from the sine law on the formed components.

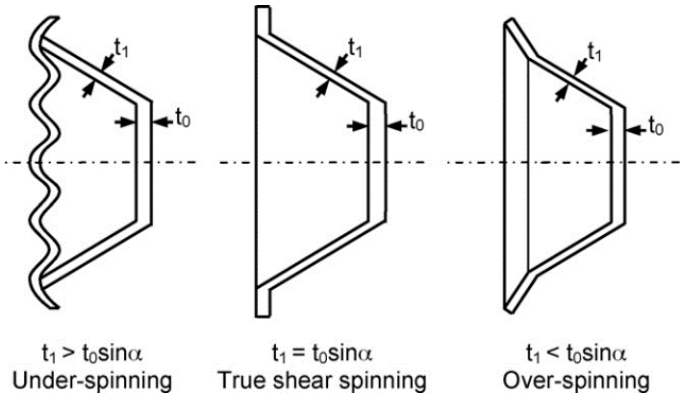

Figure 1.9 Schematic diagram of the shear spinning under different thicknesses [4].

1.2.3 Tube Spinning

Tube spinning is shown in Figure 1.10. In tube spinning, the wall thickness of the formed component is reduced from the initial workpiece thickness, and the final thickness is defined by the increase in the length of the workpiece. Thus, the length of the workpiece significantly increases after the process.

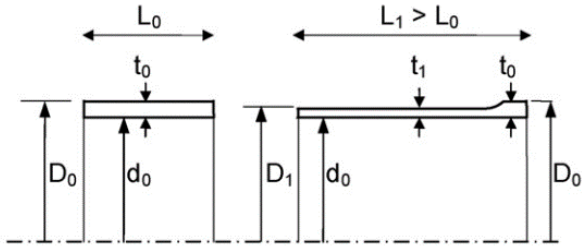

Figure 1.10 Schematic diagram of tube spinning [4].

1.2.4 Novel Spinning

In novel spinning processes reported recently, the mandrel of a complex geometry may not necessarily be required. A mandrel with a simple geometry can sufficiently support the workpiece and clamp it firmly using the back plate. In some of the novel metal spinning processes, mandrels are not necessary. Five novel processes are

shown in Figure 1.11. In Figure 1.11, processes (a), (b) and (c) are mandrel-free processes. In these flexible spinning processes, mandrels are unnecessary and are replaced by other tools, such as rollers. In process (d), a mandrel is designed in a simple shape to create conic geometries. Process (e) is similar to process (d), but the spun part will be cylindrical. In these processes, although the conventional roller is replaced with a rotating multi-roller head, a specific mandrel is still required for each product. Therefore, they are not strictly regarded as flexible spinning processes.

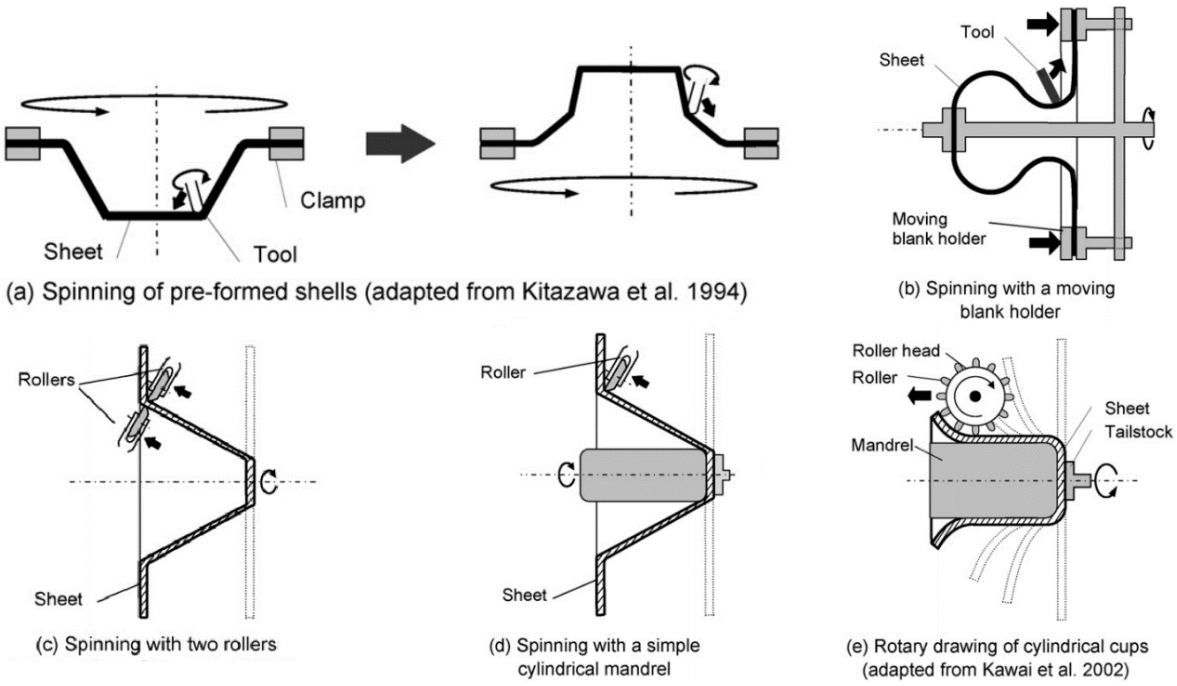

Figure 1.11 Schematic diagram of five novel spinning processes [4].

1.3 Metal Spinning Process Failures

Figure 1.12 shows three common types of failures encountered in metal spinning. Theoretically, wrinkling is regarded as buckling [13], as shown in Figure 1.12 (a), a structural instability caused by tangential compressive stresses. Fracture is another common failure in the metal spinning process. Circumferential fractures can occur on the nose or the neck of the spun part, and radial fractures can occur on the flange of the spun part. The circumferential fractures are caused by radial tensile stresses, as shown in Figure 1.12 (b), and the radial fractures are caused by tangential compressive and bending stresses, as shown in Figure 1.12 (c). These failures may be simulated by the FE simulation. The stress and strain states that cause the failures may be obtained by analysing the FE simulation results, and an in-depth understanding can be established. However, FE simulation has errors and limitations, and the accuracy of the simulation result is sometimes questionable. The FE results

need to be validated before being utilised for further analysis.

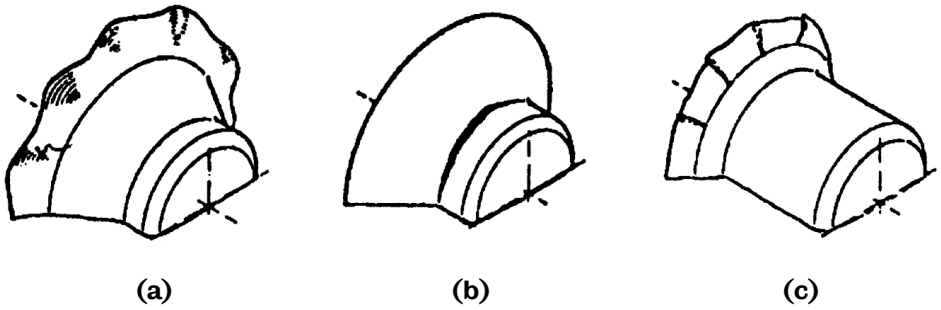

Figure 1.12 Three types of failure in metal spinning: (a) wrinkling, (b) circumferential fractures and (c) radial fractures [13].

There is a difference between conventional and shear spinning processes related to wrinkling failure. A mandrel is usually required for shear spinning as the thickness will be reduced and determined by the pre-set gap between the mandrel and the roller. Hence for early-stage non-severe wrinkling, there is a chance for the roller and mandrel to flatten the wrinkled area and ideally, no spun part quality is compromised after completing the process. However, conventional spinning is necessary to shape the workpiece to the mandrel profile without wrinkling [13]. On some occasions, there is no mandrel profile to follow, as in Figure 1.11 (d). Under this circumstance, the thickness of the workpiece tends to remain unchanged, and no thickness reduction is produced, which means the roller will not flatten the pre-formed wrinkling due to the lack of the mandrel supporting the other side of the workpiece. To summarise, non-severe wrinkling in the early stage is allowed in shear spinning, but it is intolerable in conventional spinning.

The feed ratio is a critical processing parameter in the metal spinning process. The roller usually moves towards the workpiece with a constant feed rate while the mandrel rotates at a constant rotational speed. Feed ratio (mm/revolution) is defined as the ratio of roller feed rate (mm/second) and mandrel speed (revolution/second). Wrinkling is very sensitive to feed ratio, and a relatively high feed ratio will easily cause wrinkling [14][15][16]. Finding an optimised feed ratio is critical for processing the workpiece without wrinkling failure.

1.4 Research Aims and Objectives

To date, no standard testing method for testing the spinnability of the metal spinning process has been reported. As outlined in the previous sections, metal spinning has the significant advantage of producing customised products with low material and time costs because no complex or specialised tooling is needed. However, trial-and-error is necessary for every new customised product to avoid spinning process

failures before formal production can begin. It is due to the lack of an in-depth understanding of the wrinkling mechanism and a spinnability (formability of the spinning process) testing method. These time-consuming and material-wasting test trials are also required whenever the materials and spinning process parameters are changed. In summary, there is no sufficient understanding of the spinning wrinkling failure and the material spinnability to guide the design and development of the metal spinning process. Also, there is no proposed standard testing method to test the spinnability of the metal spinning process.

To address these problems, the overall aim of this project is to establish an in-depth understanding of wrinkling failure mechanisms by analysing stress and strain results and further developing a spinnability testing method related to the wrinkling failure for the metal spinning process. Fracture failures are not investigated in this project. To achieve the aim of the project, the specific objectives are listed below:

1) To understand the wrinkling initiation and propagation by comparing the FE results such as stress and strain results between non-wrinkling and wrinkling cases with various wrinkling severity. This includes to

- Develop spinning FE models to simulate the shear spinning processes with different processing parameters, focusing on the feed ratio and mandrel speed. Quantify the wrinkling deformation and detect the wrinkling initiation to support the development of a new wrinkling testing method for the spinning process.
- Conduct shear spinning tests to obtain the results related to wrinkling deformation, focusing on the wrinkling initiation. Use the results to validate the spinning FE models to ensure the simulation accuracy and ascertain reliable conclusions drawn from the analysis of the FE results.

2) To test material formability related to wrinkling failure by developing a new wrinkling testing method. This includes to

- Develop FE models to simulate the new wrinkling testing method. Boundary conditions will be determined, including the specimen design, optimisation, and identification of key test parameters.
- Modify the existing biaxial tension under the bending and compression (BTBC) rig to perform the new wrinkling testing with testing parameters representing the parameters in the spinning process.

- Compare the new wrinkling test results with the spinning test and FE modelling results to determine whether the new method is successful and further modifications to the new wrinkling testing method.

The investigation of the material deformation in the shear spinning process would provide an in-depth understanding to support the development of the new wrinkling testing method. The spinning FE results will guide the design of the new testing method and the specimen to achieve similar deformation modes, strains and stresses as in the shear spinning process. The specimen will represent the wrinkled area in the workpiece used in the spinning process. Loadings applied to the wrinkling test specimen will be equivalent to the loadings in the spinning process. The new wrinkling testing method will be performed on the existing BTBC rig, initially developed to test the material formability in the incremental sheet forming (ISF) process. The rig will be specifically modified for the wrinkling test. In addition, the new testing method should be adaptive and universal, compatible with different testing parameters and materials as the ultimate aim is to improve the manufacturing efficiency and utilisation of the material in the spinning process. The purpose is to isolate the wrinkled area from a complete workpiece. The method will be valid only if it could achieve identical or at least similar material deformation modes to the metal spinning process. This project will utilise the finite element method (FEM) and experimental method to obtain the results from the spinning process to validate the newly developed testing method.

1.5 Structure of Thesis

This thesis consists of seven chapters.

In Chapter 1, the research background is introduced, the existing research gaps are identified, and the aim, objectives and potential outcomes of this project are outlined.

In Chapter 2, a literature review that primarily covers traditional and recent material formability testing methods is presented. It also discusses the processing failures in the spinning process and the conclusions from previous literature regarding material deformation and failure mechanisms.

In Chapter 3, the FE models of the shearing spinning process are developed based on the actual experimental setup to investigate the material deformation and wrinkling mechanism. The FE results are utilised to explain the wrinkling deformation to guide the development of the new formability testing method in Chapters 5 and 6. The complex loading conditions obtained from FE results analysis

of the spinning process are simplified and applied to the specimen in the new testing method.

In Chapter 4, the shear spinning tests are designed and conducted with AA5251–H22 aluminium alloy. These shear spinning tests are simulated by the FE modelling in Chapter 3. The test results are used to validate the spinning FE models developed in Chapter 3. Modifications are made for the further spinning tests.

In Chapter 5, FE models are developed for the new wrinkling testing method. Different designs of the testing specimen are presented, and the FE results of these tests are analysed. The strain and stress results of the wrinkled area will be compared with the results from the spinning process FE modelling and experimental tests to determine whether the new testing method is successful. The crucial features of specimen design and boundary conditions to cause wrinkling deformation are identified. Further modifications are proposed based on the findings.

In Chapter 6, the BTBC rig is modified for conducting the new testing method. The results are used to validate the wrinkling test FE models developed in Chapter 5. The loadings are identical to the boundary conditions applied to the specimen in Chapter 5, obtained from the spinning FE modelling. Test results are used to determine whether the FE models are reliable.

In Chapter 7, the key findings of the project are concluded. The research novelty is outlined. Future work to improve the shear spinning test and newly developed wrinkling method is also proposed.

1.6 Planned Publication

Zhikun Li and Hui Long, “Development of a new wrinkling test method for shear metal spinning”, to be submitted to Journal of Materials Processing Technology.

2 Literature Review

This chapter summarises previous literature related to the project. Section 2.1 discusses the stress and strain measurement methods used in the previous investigations. Section 2.2 introduces stress and strain-related investigations and reviews the material deformation modes in the spinning process. Section 2.3 reviews the failures in the metal spinning process and the existing material formability testing methods. Section 2.4 further reviews the material formability testing methods related to wrinkling failure in the metal spinning process. The current research gaps and a literature review summary are outlined in Section 2.5.

2.1 Methods of Strain and Stress Analysis

Understanding the strain and stress analysis methods to obtain results are essential before further investigating any aspects of process failures. As mentioned in the introduction chapter, fracture and wrinkling are the two significant failures in the metal spinning process. Failures are analysed by analysing the stress and strain of the workpiece. The stresses of the workpiece are complicated and constantly changing during the spinning process. However, stress is nearly impossible to measure in a test directly. The strain is the only experimentally assessable result to analyse the deformation of the workpiece. Hence, obtaining and analysing strain results became the main focus of previous studies. Due to the rapid development of the FEM, both stress and strain results could be obtained with compromise, such as results with low accuracy in some poorly modelled cases. This section reviews previous literature and investigations regarding strain measurement and stress analysis.

2.1.1 Experimental Methods of Strain Measurement

Experimental methods were widely applied in the sheet metal forming processes. They were also used in the metal spinning processes to investigate the following aspects: the mechanism of deformation and the evolution of strains, the failure mechanisms and their prediction, the forming forces, the surface quality and the process optimisation to obtain the desired product geometry [4].

Experimental methods were used to investigate the deformation mechanism and the evolution of strains in the metal spinning process. The plugged hole method was used by Avitzur and Yang [17], as shown in Figure 2.1 (a), the gridline method was used by Kalpakcioglu [18], as is shown in Figure 2.1 (b). The grid etching method was used by Quigley and Monaghan, Beni et al. [19] and Shimizu [20], as shown in Figure

2.1(c). Avitzur and Yang [13] used a metal workpiece with drilled holes following a specific pattern (e.g. radial or spiral direction) in the shear spinning process. The purpose was to investigate the strain signatures at different workpiece locations and further study the shear spinning deformation mode. After the spinning process, the workpiece was cut open to reveal the plugged holes for deformation mode analysis by measuring the elongation and compression of the holes.

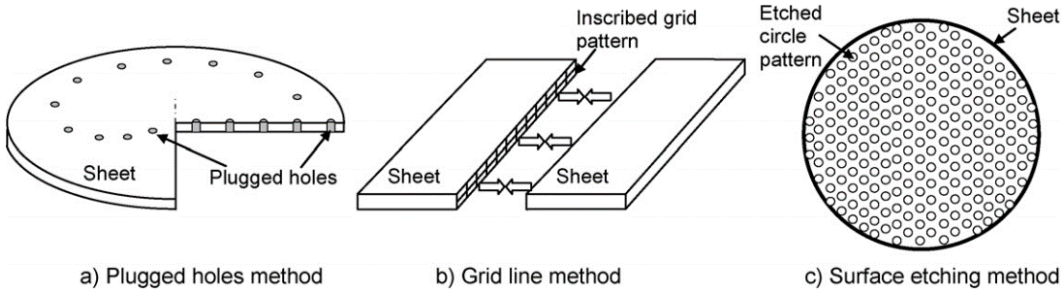

Figure 2.1 Methods for strain measurement: (a) the plugged holes method, (b) the gridline method and (c) the surface etching method [4].

Kalpakcioglu [14] proposed the gridline method on metal blanks to analyse material deformation in the shear spinning process. As is shown in Figure 2.1 (b), the metal blank was cut into two sections along the centre line of the thickness of the blank. The two blank parts were soldered together, the grid lines were engraved on the exposed surface of the blank thickness, and the spinning test was performed. After the spinning process was completed, the metal blank was separated again. The engraved grid lines were examined to study the material deformation through the thickness of the blank.

The surface etching method is widely applied in sheet metal forming processes and is also used to analyse the strain states for conventional and shear spinning processes, as shown in Figure 2.1 (c). Circles are chosen as the etching pattern because they have clear advantages over square patterns, such as no preferential orientation. They present the principal strain directions after the circles are deformed into ellipses. The deformation can also be directly quantified by measuring the elongation and shortening of a circle on the major and minor axes of the ellipses. Razavi et al. [21] also conducted experiments with this method. Before the test, a grid consisting of identical circular patterns was etched on the surface of the workpiece. After the process, the etched circular patterns were deformed into various ellipses with specific dimensions. The dimensions of these ellipses were measured by a microscope. The measurement method and the analyses of the results are similar to those used in the small punch test method, which will be reviewed in Section 2.3.

Though these methods have been utilised in metal spinning, they have drawbacks. These three methods are widely used to analyse sheet metal forming processes, but the disadvantages are obvious and undeniable. However, for the spinning process, the strain analysis is very limited. The method that provides the most comprehensive results among these three methods is the plugged hole method. The strain results on both sides of the workpiece and the strain results in the thickness direction can be obtained. The fatal flaw of this method is that the holes may reduce the strength of specific areas on the workpiece and change the material deformation behaviour locally. Furthermore, the thickness of the area around the holes has a more significant reduction than in other areas because the material around the holes will be deformed more easily. Moreover, fracture and wrinkling failures during a spinning process are more likely to occur near the holes. Therefore, it is difficult to determine whether these failures are because of the existence of the holes or resulted from the spinning process itself. A fracture may have even already formed when drilling holes on the workpiece. The result becomes unreliable under the effects of these factors. The grid line method and any other methods that change the material properties of the workpiece and cause unrealistic strain distribution will result in similar issues. The surface etching method does not have these drawbacks, and the strain result in the thickness direction equals the negative sum of the other two principal strains due to the volume conservation in the spinning process.

Using strain gauges to obtain strain results is another commonly used method in previous studies. Hayama et al. [22] attached multiple strain gauges on both sides of a workpiece and obtained the strain results along the radial and circumferential directions throughout the spinning process, as shown in Figure 2.2. The periodic variations of curvatures on the flange and the strains in the radial and circumferential directions were obtained. However, this method is not practical. Firstly, the strain gauges only cover a small area of the workpiece. In addition, due to the unpredictable location of the wrinkling occurrence, the gauges may not always capture the initiation and propagation of wrinkling waves. Secondly, metal spinning is a highly dynamic process, and the strain gauges will likely rotate with the workpiece at high speed. Therefore, setting up strain gauges wired for data transmission and measurement is challenging and requires a corresponding testing platform.

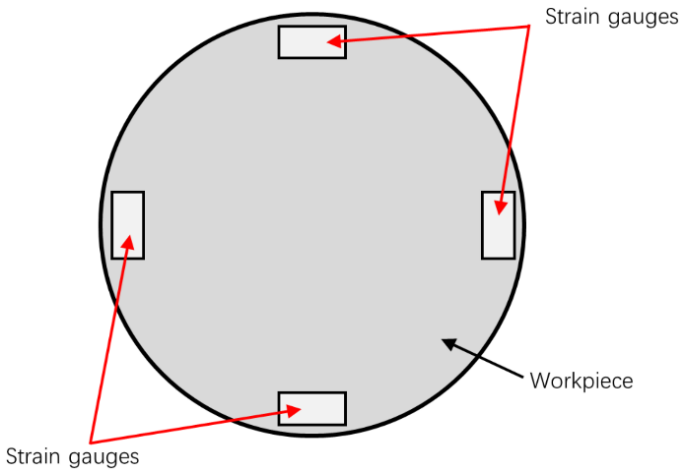

Figure 2.2 Schematic diagram of strain gauges attached to the surface [22].

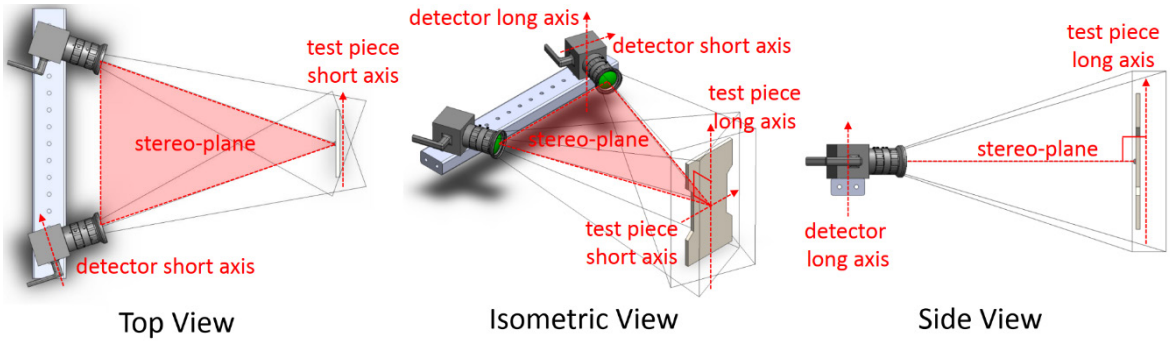

Figure 2.3 Schematics setup of DIC camera detectors [23].

Digital image correlation (DIC) is a widely used method to measure strains and analyse material deformation. The general setup is shown in Figure 2.3. A DIC device measures the deformation of the electronic speckle pattern applied to the workpiece surface. Its spectrum-style results visually and accurately show the strain distribution than a traditional measuring method like grid etching. Two-dimensional and three-dimensional DIC devices were used to measure the strain distributions for different conditions. A two-dimensional DIC device can be applied to the tests like the uniaxial tensile test as the specimen stays in a plane during the test. A three-dimensional DIC device can be applied to the out-of-plane test like the dome test reviewed in section 2.3.2. However, metal spinning is a highly dynamic process, and the workpiece will be out-of-plane during the process. Even a three-dimensional DIC device will be out of focus. Therefore, it is not feasible to apply DIC and other conventional strain measuring methods simultaneously.

2.1.2 Finite Element Method of Strain and Stress Analysis

There are two methods for solving plastic deformation problems: ABAQUS/Standard (implicit) and ABAQUS/Explicit. FE models are developed and implemented by using ABAQUS software to simulate the shear spinning process. ABAQUS/Standard and

ABAQUS/Explicit are the two solution methods in ABAQUS software to simulate plastic deformation. General differences between these two methods are listed in Table 2.1.

Table 2.1 Key differences between ABAQUS/Standard(implicit) and ABAQUS/Explicit methods [24]

Quantity	Abaqus/Standard	Abaqus/Explicit
Element library	Offers an extensive element library.	Offers an extensive library of elements well suited for explicit analyses. The elements available are a subset of those available in Abaqus/Standard.
Analysis procedures	General and linear perturbation procedures are available.	General procedures are available.
Material models	Offers a wide range of material models.	Similar to those available in Abaqus/Standard; a notable difference is that failure material models are allowed.
Contact formulation	Has a robust capability for solving contact problems.	Has a robust contact functionality that readily solves even the most complex contact simulations.
Solution technique	Uses a stiffness-based solution technique that is unconditionally stable.	Uses an explicit integration solution technique that is conditionally stable.
Disk space and memory	Due to the large numbers of iterations possible in an increment, disk space and memory usage can be large.	Disk space and memory usage are typically much smaller than Abaqus/Standard.

Abaqus/Standard uses the Hilber-Hughes-Taylor time integration with second-order accuracy. It is implicit and uses an incremental-iterative solving technique based on the Newton-Rhapson method. This implicit method solves the problem by calculating the structure stiffness in its initial state. When solving a static case, the total load is divided into smaller load increments, and when solving a dynamic case, the total time is divided into time increments. After the load is applied to the structure, the displacement is calculated using the structure stiffness at each increment. The new stiffness and the residual force, which are the differences between the external and internal forces on the nodes, are calculated. These calculations are the first iteration of the increment. Abaqus/Standard solves the problem by calculating a large number of increments and iterations, establishing equilibrium at each iteration calculation. Usually, the material of the structure with a nonlinear stress-strain response requires a large number of iterations to solve one increment within the implicit method. To guarantee the convergence of iterations, smaller time steps are used, and if the solver encounters large nonlinearities, convergence could be impossible to achieve in practical terms [25].

Abaqus/Explicit uses an explicit integration method with second-order accuracy, and the kinematic state is explicitly calculated and advanced from the previous

increment. The explicit dynamics method is initially developed for dynamic problem analysis, and the solution is calculated without using Newton-Rhapson iterations. The solver is not required to solve simultaneous equations as required by Abaqus/Standard. Hence each increment in Abaqus/Explicit is less resource-costly, which means the calculation time could be reduced. When solving a dynamic equilibrium state, the out-of-balance forces in the structure will propagate as stress waves. It is possible to capture the stress wave propagation through the structure at a high frequency if the increment size is small enough. No iteration is involved in the explicit method, and convergence problems would not be an issue.

The algorithm used in Abaqus/Standard is unconditionally stable as a robust method for both static and dynamic problems. It is especially suitable for problems with highly discontinuous, short-duration and dynamic non-linear conditions involving complex contact, material failure and sudden changes in structural stiffness. Although any size of increments can be used, the accuracy is affected by increment size when solving a dynamic problem. On the other hand, the algorithm used in Abaqus/Explicit is conditionally stable, and the time increments required are smaller than a specific value for it to be stable. The explicit method is more computationally efficient with less calculation time (CPU time). Despite the explicit method usually requiring more increments, each increment is much more computationally efficient. However, the explicit method may require too many increments for a dynamic problem that lasts a longer step time, and the overall efficiency could be compromised [26].

As previously mentioned, metal spinning is a highly dynamic process. Strain and stress results are nearly impossible to measure using methods applied in other sheet metal forming processes. Considerable effort has been devoted to developing FE models to understand material deformation in spinning. Although it is difficult to determine the exact date of the invention of the FE method, it was initially reported by Hrennikoff [27] and Courant [28] to solve complex elasticity and structural analysis problems in civil and aeronautical engineering. The method can be applied to 2D problems, the bending of plates, cylindrical shells, the general case of three-dimensional stress analysis, and a great variety of others.

Before the FE method was utilised to simulate the metal spinning process, the study of stress and strain states was limited. After the FE method was developed and implemented in the research, a large number of studies, including Quigley and Monaghan [29], Long and Wang [30], Razavi et al. [21] and many other researchers, used the FE method to simulate various metal spinning processes. Long and Wang [24] constructed FE models for conventional metal spinning processes to investigate

the process parameters related to wrinkling. The FE method obtained the results of equivalent plastic strain and von Mises equivalent stress. The compressive tangential stresses were observed at the flange area close to the local forming area at the contact area of the workpiece and the roller. However, it was observed that tangential compressive stresses on the flange area were changed to tangential tensile stresses when this area rotated away from the current roller contact area. Watson et al. [31] also reported that if the tangential compressive stresses could not transfer to tangential tensile stresses fully, wrinkling failure occurred after roller contact. Wang and Long [32] constructed FE models to investigate the wrinkling phenomenon in the metal spinning process. The wrinkling phenomenon was analysed by considering the stress and strain aspects. It was observed that the tangential compressive stresses occurred not only at the current roller contact area but also in other flange areas.

To summarise, experimental methods are more accessible to implement with accuracy than FE results. Limitations are also apparent, such as the compromise of the structural integrity of the workpiece by the plugged holes method. The direct strain observation method (e.g. DIC) is currently the most accurate method to obtain strain results. Similar to the grid etching method, the DIC measurement can only obtain the surface strains of the target area. However, the DIC device cannot capture the strains in highly dynamic processes such as the spinning process. FE method can extract almost any results, such as stress and strain in different directions at different locations on the workpiece. Currently, the FE method is wildly implemented in stress and strain analysis in modelling metal spinning processes. However, even the most comprehensive numerical models have errors and cannot represent the actual experiments completely. The FE modelling has errors and cannot be considered accurate without validation by experimental measurements.

2.2 Material Deformation Modes and Forming Limit Diagram

Different product geometry requirements can be obtained in sheet metal forming by developing different processes, resulting in different deformation modes. These deformation modes are classified by the ratio between the strains in different directions. Strain results are obtained by the experimental and the FE method. They are further processed into data points of major and minor strains plotted on the Cartesian coordinate system, forming the forming limit curve (FLC). The entire diagram is known as the forming limit diagram (FLD). The FLD was proposed and improved upon during the ongoing investigation of the deformation mechanism in sheet metal forming processes, aiming to predict the forming limit and avoid failures in actual manufacturing processes. Section 2.2 will present a detailed review of the

FLC and the FLD.

2.2.1 Deformation Mode

The term deformation mode is used to describe the deformation behaviour of a material element of the workpiece. The deformation mode is the basic concept that describes a specific deformation state of the material element. The surface grid etching method is commonly used in sheet forming processing, as reviewed in section 2.1.1. Strains in the major and minor directions could be determined by measuring the deformation of the circular patterns etched on the material surface, as shown in Figure 2.4. By convention, the direction of the greatest principal stress and, consequently, the greatest principal strain is assigned as the major principal direction. The deformation mode is further determined by the ratio between major and minor principal strains. The strain path is assumed to be linear, and the strain ratios are constant, as shown in Figure 2.5. Figure 2.6 is a schematic diagram of the corresponding deformation modes of different strain paths in Figure 2.5.

The principal strains in three directions at the end of the process are calculated as Equation 2.1.

$$\varepsilon_1 = \ln\frac{d_1}{d_0};\ \ \varepsilon_2 = \ln\frac{d_2}{d_0};\ \ \varepsilon_1 = \ln\frac{t}{t_0}$$

Equation 2.1

The strain ratio of a specific circular grid pattern is calculated as Equation 2.2.

$$\beta = \frac{\varepsilon_2}{\varepsilon_1} = \frac{\ln(d_2/d_0)}{\ln(d_1/d_0)}$$

Equation 2.2

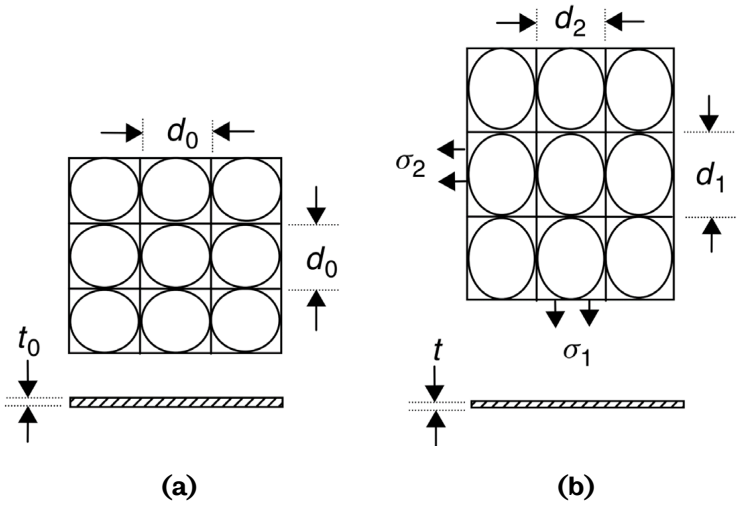

Figure 2.4 Schematic diagrams of circular girds deformation: (a) the undeformed patterns and (b) the deformed ellipses patterns with major diameter d1 and minor diameter d2 [33].

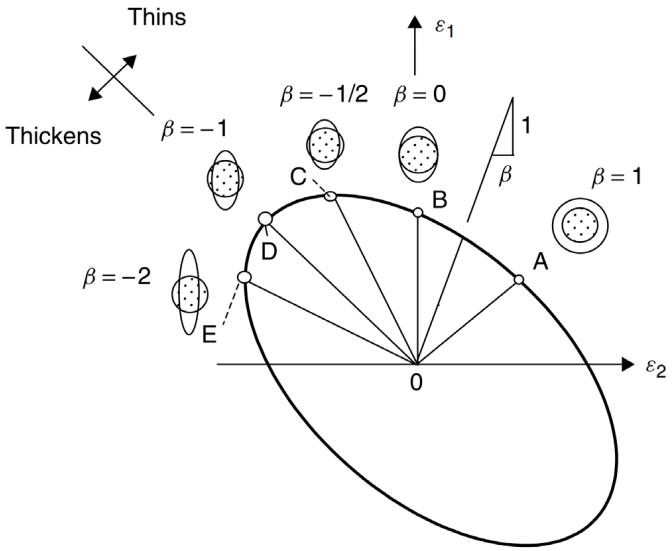

Figure 2.5 A schematic strain diagram of corresponding strain paths [33].

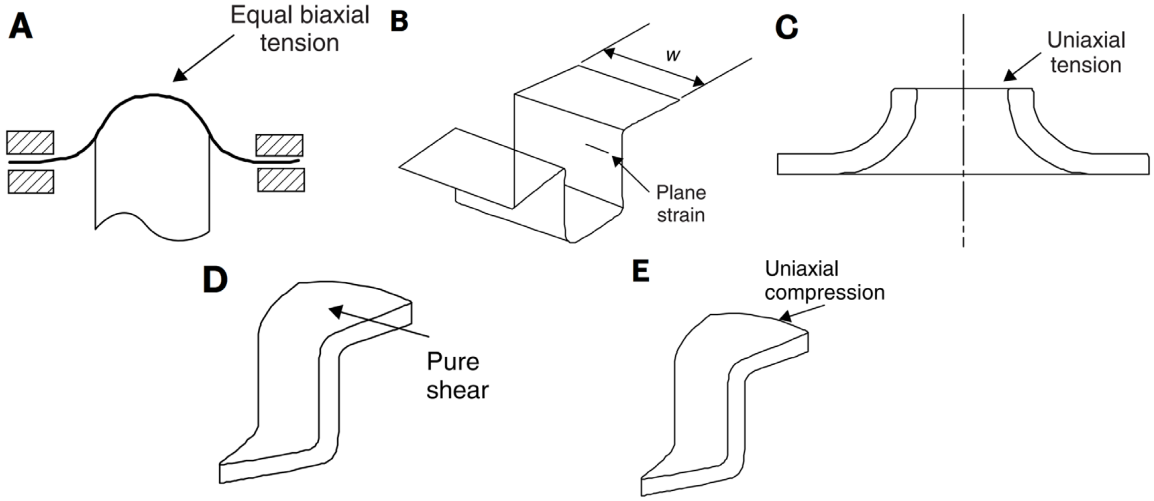

Figure 2.6 A schematic diagram of the examples of different deformation modes [33].

2.2.2 Forming Limit Diagram

Keeler [34] and Goodwin [35] first proposed a concept similar to the present FLD shown in Figure 2.7. Before the FLD, Gensamer [36] analysed the local strain and the straining limit criterion requirement. Many theoretical studies were conducted on the FLC after Keeler and Goodwin. Swift [37] proposed the diffuse necking theory, Hill [38] proposed the localised necking theory, Storen and Rice [39] investigated bifurcation, and Bressan and Williams [40] proposed failure criteria based on the maximum shear stress, among many others. Investigations regarding different metals with different forming processes were also proceeded. Marciniak et al. [41] and Marciniak and Kuczynski [42] conducted tests with different sample and punch geometries. Furthermore, different materials were tested; for example, Shinge and Dabade [43] generated an FLD for mild carbon steel by performing a small punch

test on a steel sheet.

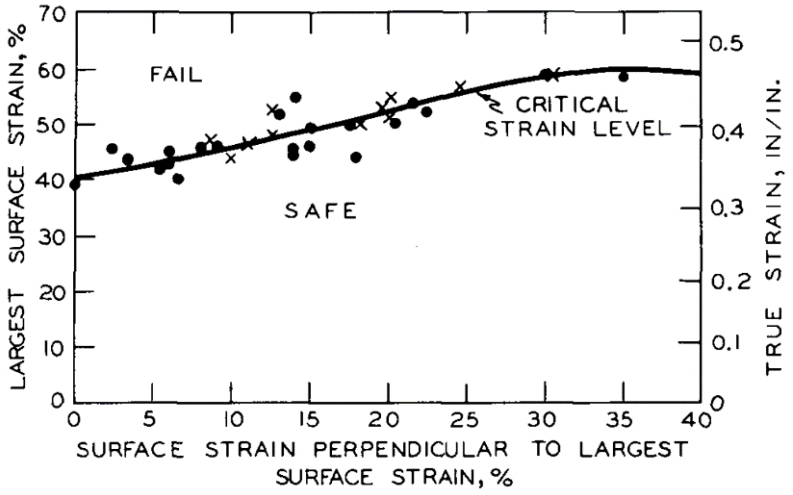

Figure 2.7 Fracture strain measurements [34].

Investigations are performed to generate FLCs through different tests. A FLC separates the region into the safe and potential failure zones in an FLD, as shown in Figure 2.8. Figure 2.9 explains the different regions in a FLD. Ideally, to generate a FLD for a specific material, the forming limits of the material under various loading paths or deformation modes must be obtained by implementing a specific testing method to test the forming limit of different deformation modes. For example, a commonly used testing method is the uniaxial tensile test, which can test the forming limit of different materials under the uniaxial tension deformation mode. In order to test the forming limit of other deformation modes, different testing methods are required. The uniaxial tension is the only deformation mode in the uniaxial tensile test. However, multiple deformation modes could be observed in other testing methods.

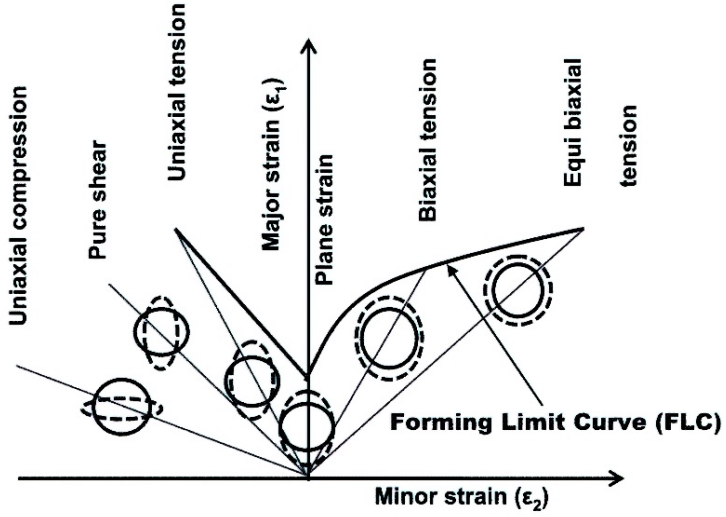

Figure 2.8 Schematic demonstration of a forming limit diagram (FLD) [44].

After Keeler proposed the concept of the FLD, FLD was widely used in various investigations of metal forming processes. The processes for different materials were conducted frequently in recent decades, and results were obtained. Typically, data points form a V-shape FLC for conventional sheet forming processes, as shown in Figure 2.8.

Later, Emmens et al. [45] claimed that a FLD was only effective in predicting the material formability when the plane stress is the primary loading condition and a linear strain path is applied. The material was more likely to fail in conventional sheet metal forming processes under simple plane stress conditions. However, the material was usually under complex loading conditions and could be observed throughout the deformed workpiece. For example, in a deep drawing process, the bottom edge of the deformed workpiece is under bending and tension deformation modes, resulting in fracture failure, and other areas are usually under two types of deformation modes.

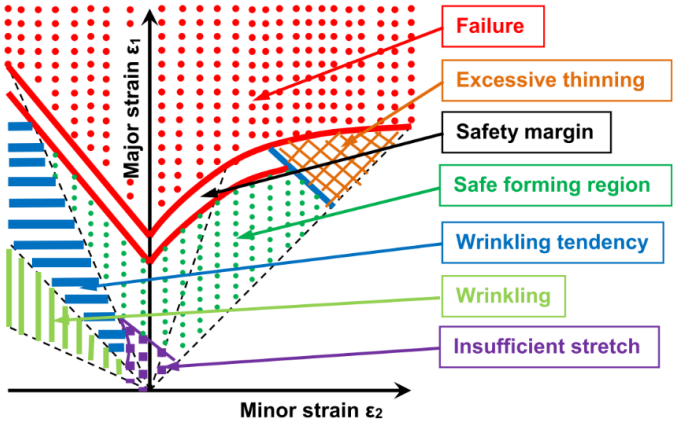

Figure 2.9 Schematic forming limit diagram (FLD) displays the safe forming region [44].

The deformation modes in the metal spinning process include compression, tension, shearing and bending, precisely like in ISF. However, unlike the metal spinning process, numerous FLD studies have been reported for ISF processes. In ISF, apart from the tension effects, the bending and shearing effects contribute heavily to material deformation. In addition, progressive toolpaths in ISF and roller toolpaths in metal spinning processes create non-linear strain paths. Benedyk et al. [74] claimed that the FLD for ISF could be influenced by processing parameters, such as vertical feed speed and different toolpaths. Therefore, the FLD method was regarded as unreliable in predicting the onset of the fracture in ISF. In general, the FLD method is not considered reliable for analysing and predicting the processing failures of the material in ISF. As ISF and the metal spinning process are similar, the FLD method is also regarded as inadequate for predicting material failures for the metal spinning process. Additionally, the FLD method is empirical and inaccurate

enough to account for fracture failure. Recent studies have focused on fundamental aspects of the unique ISF deformation characteristics and investigated their effects on predicting material processing failures. Future studies of the metal spinning process should include these aspects, and the following section presents a review of recent formability studies.

By realising these shortcomings of the previous studies, recent investigations tried to overcome the issue of the dependence of the FLD on the strain path and loading history. Kleemola and Pelkkikangas [142] and Arrieux [46] proposed a stress-based FLC, which was further optimised by Stoughton and Yoon [47][48]. Because stress-based FLD was derived from strain measurements, measuring stresses during the forming process was impractical. Stress distribution was reversely calculated from the corresponding strain results. Stress-based and strain-based FLDs are shown in Figure 2.10. The stress-based FLD indicated fewer deviations compared with the strain-based FLD. There was less difference between the data points in the strain-based FLD with more obvious continuity [48].

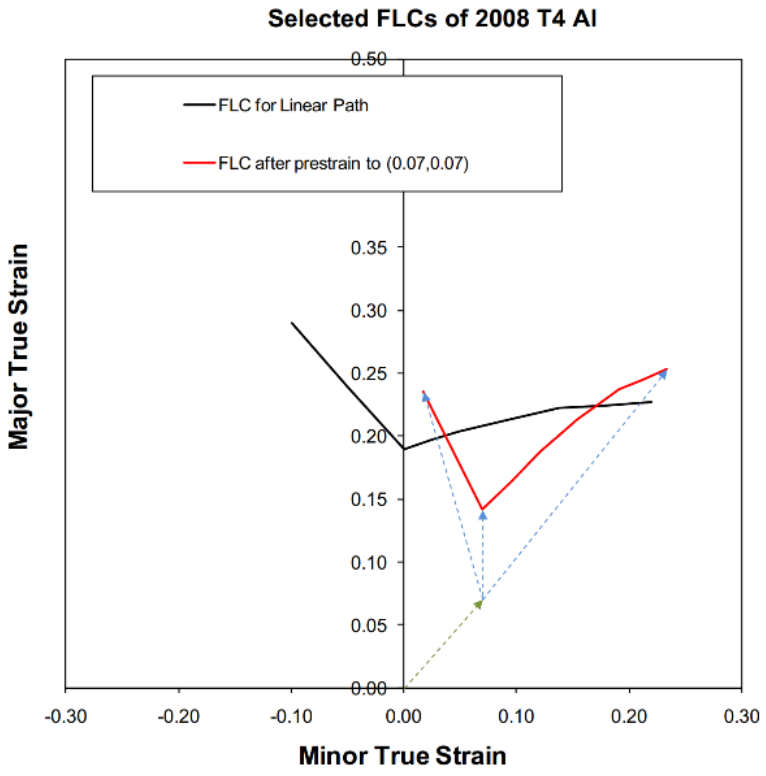

(a)

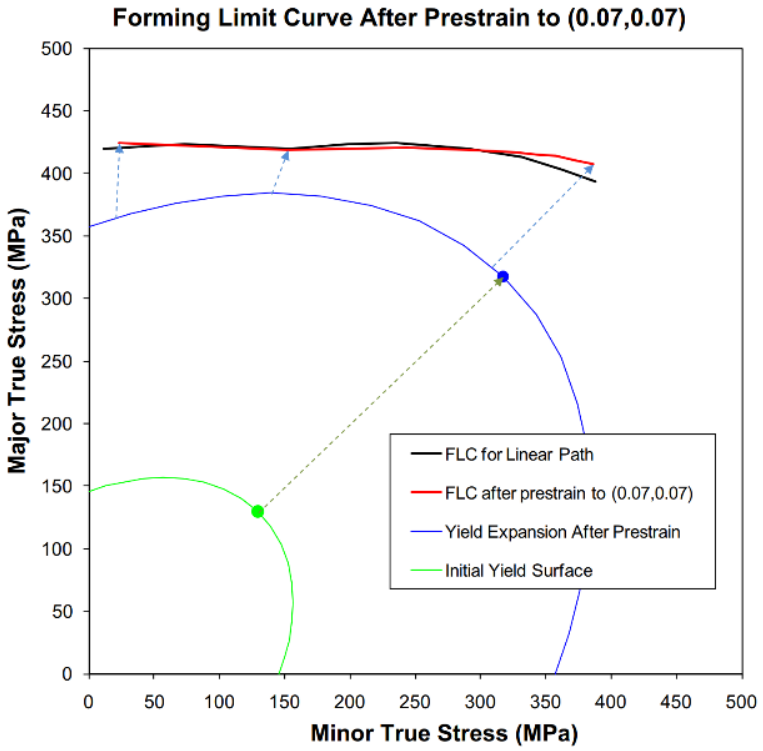

(b)

Figure 2.10 A comparison between (a) strain-based and (b) stress-based forming limit diagrams (FLDs) [48].

After the concept of the strain-based FLD was proposed, Haque and Yoon [49] further modified the stress-based FLD to predict the material formability in the single-point incremental forming process. The influence of the loading history was obtained through the reconstruction of the stress-based FLD curve, according to the reverse calculations shown in Figure 2.10 (b), even though various processing parameters were applied during the process.

Another limitation is that the FLD cannot differentiate between material rupture and fracture. Necking would not appear before the fracture in some material, so the FLD could overestimate or underestimate the forming limits, leading to the further modification of the FLD/FLC [50]. Namsu et al. [51] claimed similar results that the conventional FLD was inappropriate for predicting the fracture on advanced high-strength steel sheets. This type of steel sheet failed when a small amount of necking occurred, unlike the results obtained from other conventional steel sheets. The fracture forming limit diagram (FFLD) method was proposed as a more accurate alternative for processes based on necking. It was derived by equating the fracture strain obtained from the fracture criterion with the equivalent plastic strain corresponding to the applied yield function. The only difference between the FLD and FFLD methods is how the strain components are measured. The strain

components are measured when non-uniform deformation occurs for the FLD method. The strain components are measured when the final fracture happens for the FFLD method. Fracture is a common failure in the metal spinning process and is discussed in detail in the following Sections. Generating an FLD and an FFLD, as has been done in the studies for ISF, presents feasible methods to guide the research of material formability tests of the metal spinning process.

The FLD method is the most common and direct method for recording the material forming limit under plane stress conditions. However, the strain on thickness direction is not presented due to the 2D Cartesian coordinates used in the FLD method. For forming processes that involve large strains in three principal directions, a FLD may not be adequate to describe the forming limit of the material.

2.2.3 Deformation Modes of Spinning Process

It is essential to investigate the deformation modes in the spinning process before developing a new testing method since it would ideally apply the identical deformation modes to the testing sample. Establishing an in-depth understanding of the deformation modes in the spinning process is crucial and must be achieved before any further investigation.

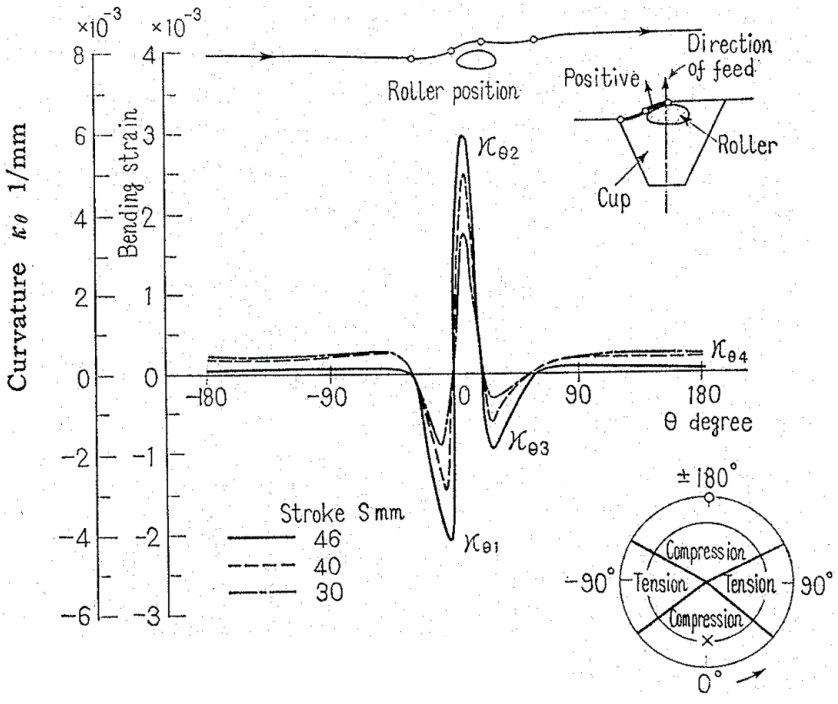

Figure 2.11 Flange curvature variation and the deformation modes related to the corresponding angle [22].

Hayama et al. [22] investigated the deformation modes in the shear spinning process related to the wrinkling of the flange of the workpiece, and the objective of the study was to know an optimum working condition or spinnability of sheet metal. The study

was focused on the outer portion of the workpiece to investigate the wrinkling failure. He attached strain gauges to the different locations on the flange to record the strain results and expressed the curvature of the flange, as shown in Figure 2.11.

The compression and tension deformation modes were cyclically changing throughout the process, depending on the location of the roller, and could be divided the workpiece into four sections, as shown in Figure 2.11. It was previously believed that roller deformed the workpiece by inducing pure shear deformation in the shear spinning. Hayama et al. [22] further confirmed the earlier conclusion by Avitzur and Yang [17] that the deformation mechanism in shear spinning was not pure shear but a combination of shear and bending as the roller induced cyclical bending and unbending near the contact zone.

However, Hayama et al. [22] investigated the deformation modes in the shear spinning process related to the wrinkling on the flange of the workpiece in 1966, only one year after Keeler [34] and Goodwin [35] proposed the early concept of FLD. The academic terms and the investigating methods related to FLD and deformation modes were not fully standardised. The deformation modes mentioned in Hayama et al. [22] did not relate to major, minor strains and strain ratios. Nevertheless, their work could still be regarded as one of the earliest studies investigating the details of the deformation modes in the shear spinning process. He measured strain results and proved that the tension, compression and bending deformation modes were cyclically changing during the process. The study also concluded that the flange wrinkling was determined by the critical values of the mean curvature amplitude and maximum compressive strain at the contacting zone between the flange and the roller. It was found that the critical condition of the flange wrinkling was influenced by the feed of roller, roller diameter and workpiece thickness as other parameters only scarcely affected the flange wrinkling. In other words, deformation modes in shear spinning are heavily affected by these three processing parameters. Moreover, the compression, tension, shear and bending are induced to the workpiece by the roller, but the value of major, minor strains and strain ratio is not investigated.

To summarise, a testing method that investigates the wrinkling failure in the metal spinning process should include compression and cyclical bending. Wrinkling curvature is observed to occur on the flange of the workpiece before the roller works on it. Hence, tension and shear may not be necessary. Moreover, a FLD for wrinkling failure in the spinning process could be obtained to describe the deformation modes of the wrinkled material accurately. Details of wrinkling failure are further reviewed in section 2.4.

2.3 Material Formability Testing Methods

Before discussing the formability testing methods, the definition of material formability should be introduced. There are multiple similar descriptions of material formability, and it commonly refers to the ability of a material to be formed without material deformation failures for industry [52]. The material formability describes the strain state and strain level that accumulate before the onset of material failures such as wrinkling, necking and fracture. The formability of a material is affected by the forming process applied to the material [53], thus different deformation modes. Furthermore, material properties, inclusion content, age hardening and prestrain (cold work) all affect the ductility of wrought aluminium products and the formability of aluminium alloys, as well as other metals. After the concept of material formability was proposed, numerous formability testing methods were developed. The main difference between different testing methods is that different deformation modes could be induced to the testing sample by the corresponding testing methods. If a test could test the material formability related to the wrinkling failure, this test can ideally generate the same deformation modes to the sample. This section introduces commonly used formability testing methods and the deformation modes they could apply to the testing samples.

2.3.1 Uniaxial Tensile Test

The uniaxial tensile test is the most common material formability testing method due to its simplicity and effectiveness for describing the material behaviour. It can test precisely one deformation mode as the uniaxial tension. Testing equipment has been industrialised, and the geometry of the specimen and the testing procedures were standardised and introduced in the ASTM-E8 standard [54].

The specimen can be strip-shaped or cylinder-shaped with a centre-narrowed gauge area. The strip-shaped specimen is commonly used for formability testing in sheet metal forming, as shown in Figure 2.12. The plastic deformation will occur somewhere on the gauge area as it is weakened by reducing the width, and the corresponding deformation mode is the uniaxial tension ($\beta = 1$) when the gauge area is being elongated, and the width is being reduced during the test. Both ends of the specimen are clamped and pulled at a constant speed until the specimen fractures. The specimen elongation, the reactive elongating force values, and the time history are recorded as data points, processed into an engineering stress-strain curve, and further processed into a true stress-strain curve, as shown in Figure 2.13.

Although the uniaxial tensile test is a commonly used material formability testing method, it can only test uniaxial tension deformation mode with $\beta = 1$ at a relatively low strain rate. According to the ASTM standard, the elongation speed of the uniaxial tensile test is 2 mm/min [54]. However, the metal spinning process is a highly dynamic process with a high-speed rotating mandrel and a fast-moving roller. In addition, material in the metal spinning process undergoes four deformation modes: tension, compression, bending and shearing. The uniaxial tensile test is not suitable for testing the material formability in the metal spinning process.

Moreover, the effect of different loading paths on material formability cannot be studied by tensile tests. For example, the material always reaches a higher equivalent strain at fracture under the biaxial tensile loading than under the uniaxial tensile loading condition. The material in the uniaxial tensile test fails much earlier than in other tests, for example, the biaxial tensile test reviewed in section 2.3.2. Therefore, a suitable testing method should create the designated deformation modes, not only uniaxial tension, to the specimen and enhance the material formability as occurred in some sheet metal forming processes.

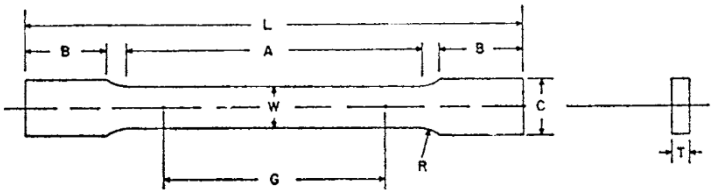

G - Gage Length T - Thickness A - Length of reduced section
W - Width R -Radius of fillet L - Overall length
B - Length of grip section C - Width of grip section

Figure 2.12 Strip-shape testing sample with geometry determining parameters [54].

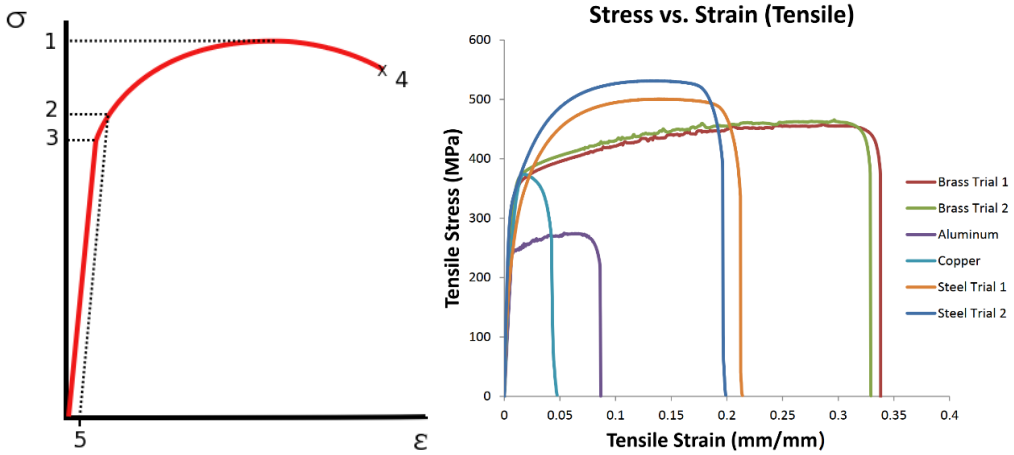

(a) **(b)**

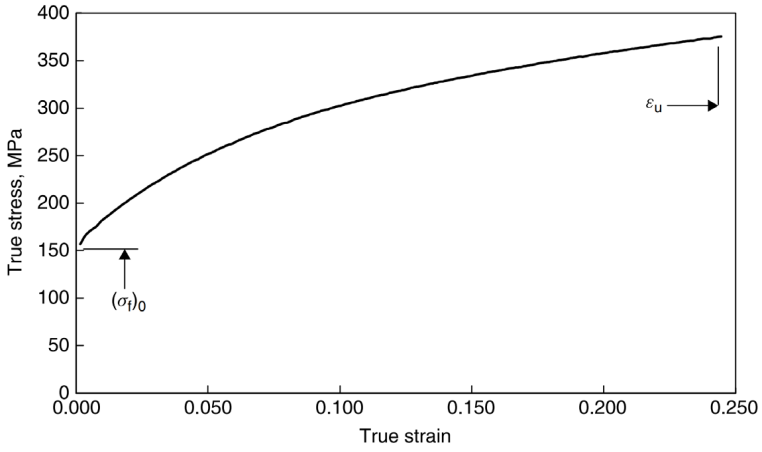

(c)

Figure 2.13 (a) A schematic diagram of a tensile test result with annotations: 1. ultimate strength; 2. yield strength; 3. proportional limit stress; 4. fracture; 5. offset strain (typically 0.2%) [55], (b) engineering stress-strain curves of different materials [56] and (c) the true stress-strain curve calculated from the engineering stress-strain curve [57].

2.3.2 Biaxial Tensile Test

The uniaxial tensile test is inadequate to describe the material behaviour since only one axis and one deformation mode are involved. Material formability testing methods are improved when the biaxial tensile test is developed. Different types of biaxial tests and specimens are designed for different loading conditions. Unlike uniaxial tensile tests with established international standards, most biaxial tensile tests are conducted using individually developed testing platforms and specimens. In general, biaxial tensile tests can be classified into two categories according to the conformity of the loading axes to the specimen: out-of-plane biaxial tensile tests and in-plane biaxial tensile tests.

Hydraulic bulge test

The test involved with a dome-shaped punch is categorised as an out-of-plane biaxial test as the gauge area of the specimen would deform out of the plane. According to the hydraulic bulge test's ISO 16808 standard [58], no solid deforming tool like a punch is involved in the bugle test. The circular sheet blank is clamped and gradually deformed by a pressurised fluid that provides identical pressure in every direction, as shown in Figure 2.14. Different strain paths are achieved by applying upper dies with hemispherical or elliptical openings [59]. The deformation modes induced onto the specimen vary between plane strain and equi-biaxial tension. The strain distribution on the centre area of the blank can be captured by a DIC device during the deformation process, and the corresponding stress distribution is calculated using the inverse method. However, the bulge test must be performed in an

enclosed environment since the pressurised liquid is involved. The leakage of high-pressure fluid is a potential hazard when the liquid is pressurised. Moreover, a new die is necessary when a different deformation mode is tested as the enclosure must be guaranteed. Compared with the bugle test, the simplicity of the Nakazima test/dome test became the most applicable test method used in the industry.

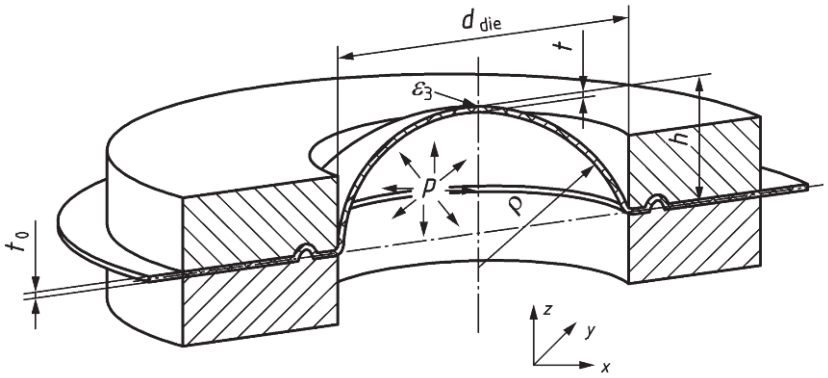

Figure 2.14 A schematic diagram of the hydraulic bulge test [58].

Nakajima test/dome test

The Nakajima test/dome test [60] is an international standard [61] which uses a hemispherical cylinder punch to apply the load to the blank instead of pressurised fluid, as shown in Figure 2.15. The main innovation of the dome test is the application of specimens with different geometries. Specimens are deformed to obtain material deformation behaviours under various deformation modes. Different types of T-shaped specimens and their corresponding deformation modes are shown in Figure 2.16. A FLD can be obtained by conducting the dome test, as shown in Figure 2.17. Lubricant is applied to reduce the friction between the punch and the specimen.

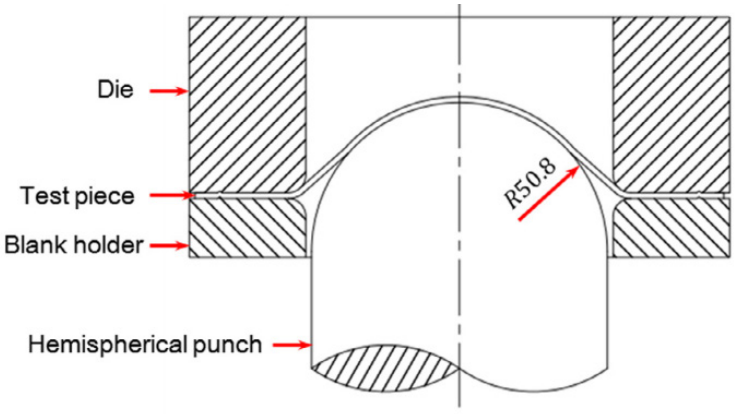

Figure 2.15 A schematic diagram of the Nakajima test/dome test [62].

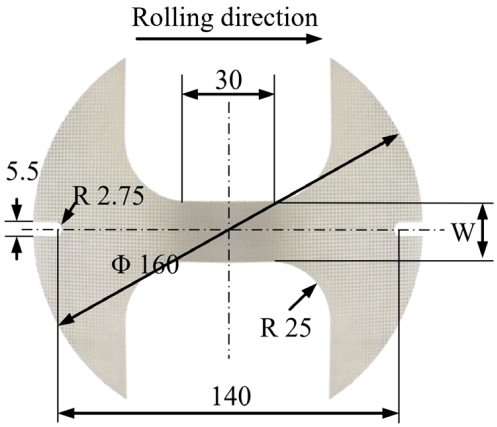

Geometry No.	W/mm	Test type
1	24	Uniaxial tension
2	64	Close to plane strain
3	80	Plane strain
4	88	Close to plane strain
5	92	Between No.4 and 6
6	160	Equi-biaxial tension

Figure 2.16 Details of different specimen geometry and corresponding test types [63].

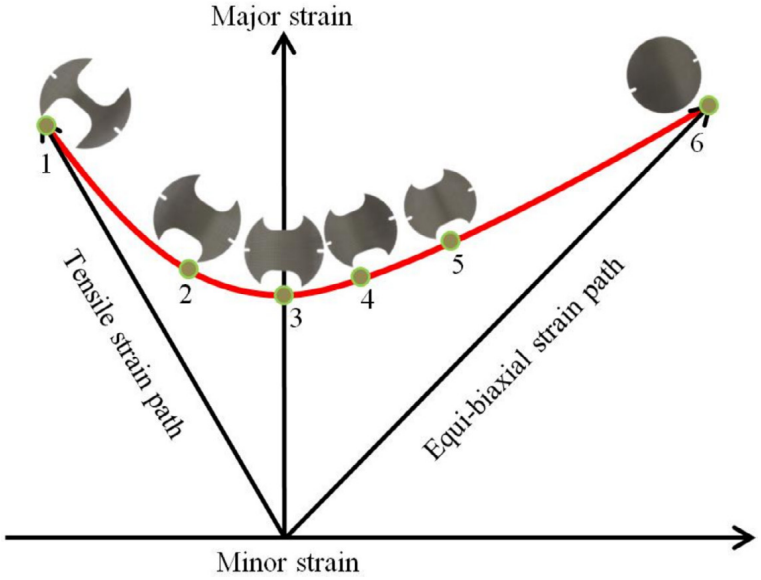

Figure 2.17 A finite element curve (FLC) obtained from different specimen geometries [63].

Groseclose et al. [64] tested several alloys using frictionless dome, bulge, and uniaxial tensile tests. Comparisons of the test results, including the results processed by the extrapolation method, are shown in Figure 2.18. Hyung et al. [65] performed tests on a platform with customised dimensions, and it was integrated with a heating system capable of heating the testing specimen to 300°C. The customised testing equipment and specimens are shown in Figure 2.19. Hyung et al. successfully integrated the dome test with other systems, obtained results and processed them into the FLDs, as shown in Figure 2.21.

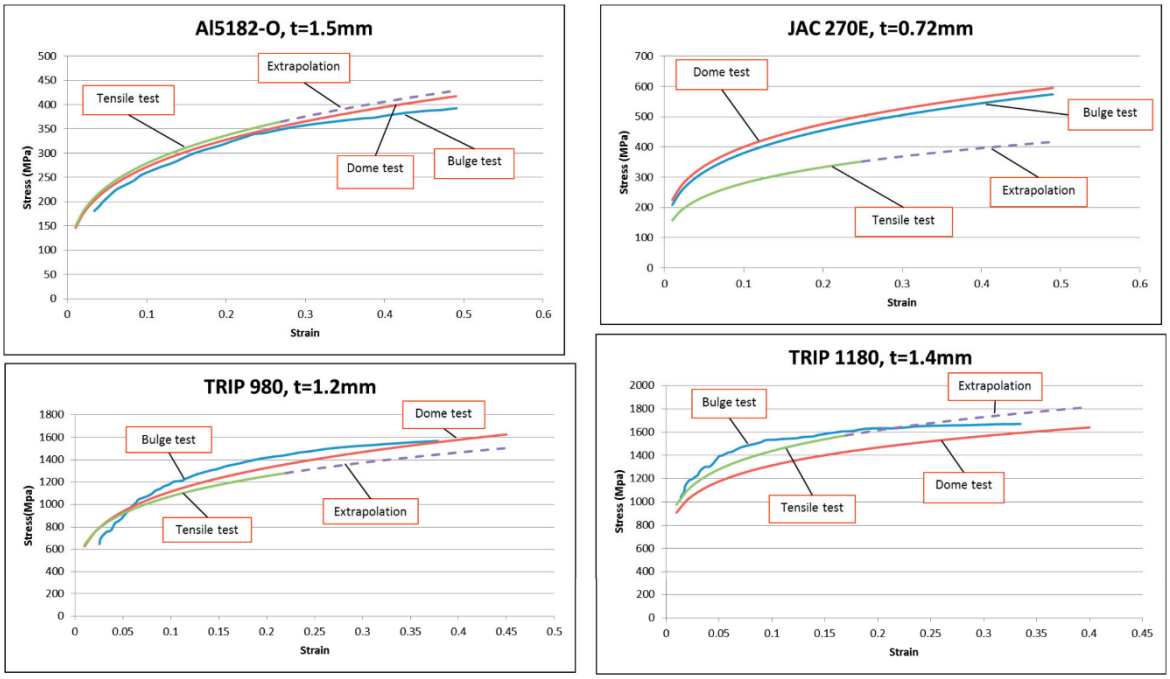

Figure 2.18 Comparison of the frictionless dome, the bulge and the uniaxial tensile tests of different materials [64].

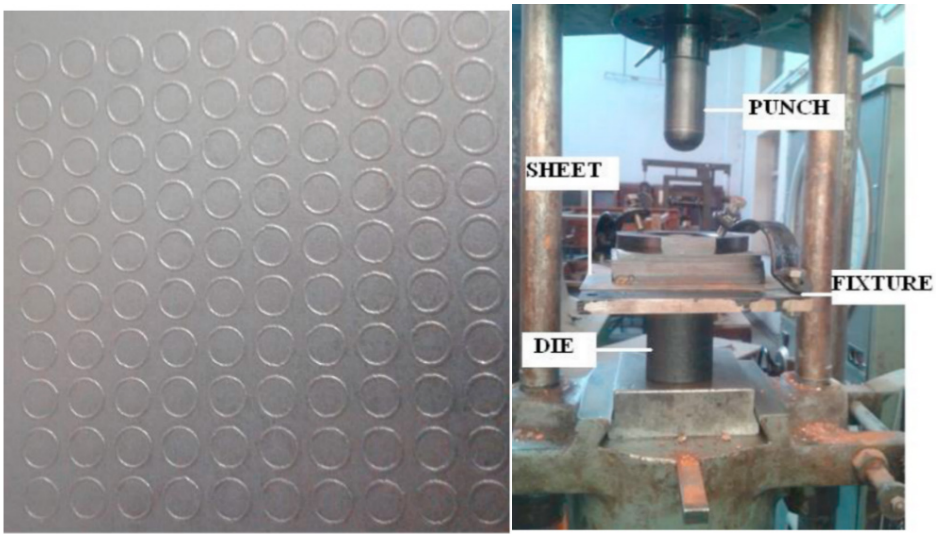

(a) **(b)**

Figure 2.19 Photos of (a) Zoom-in view of a grid-etched specimen and (b) the dome test setup [43].

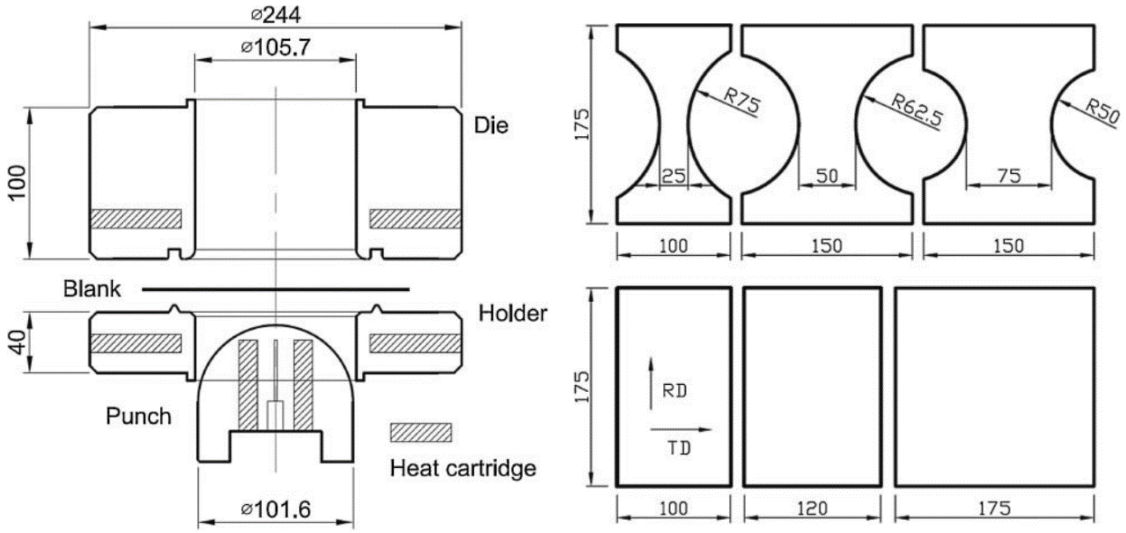

(a) **(b)**

Figure 2.20 (a) Schematic diagram of the dome test integrated with a heating system and the (b) dimensions of the forming limit diagram test specimens [65].

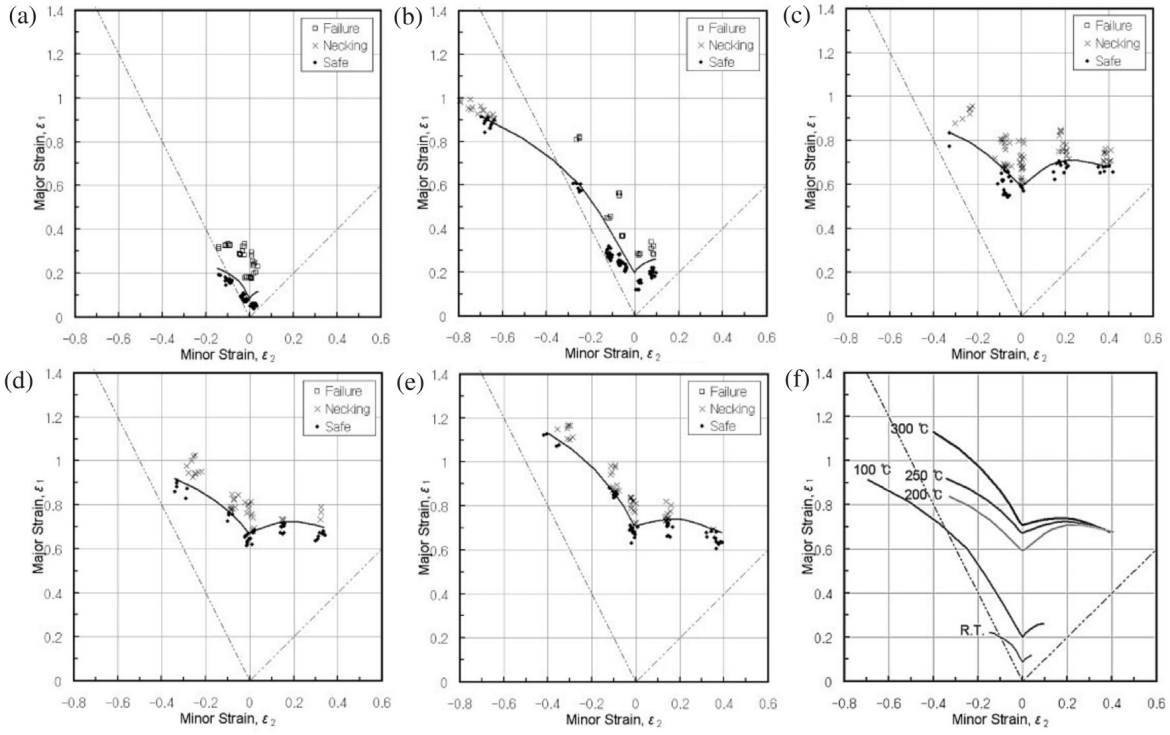

Figure 2.21 The forming limit curves at (a) 25℃, (b) 100℃, (c) 200℃, (d) 250℃, (e) 300℃ and (f) all temperatures for AZ31B magnesium alloy sheets [65].

Modifications to the dome test were made, and the quality of the results was improved. After the tests were conducted on a particular material and the FLD was obtained, the material deformation modes in sheet forming processes can be predicted to guide the development of forming processes. The advantages of the Nakazima test are apparent. It is highly customizable and adaptable to various test

conditions. Different deformation modes could be achieved by only applying corresponding specimens. The limitation of these two testing methods is that the pure uniaxial tension deformation mode is difficult to apply to the specimen due to the friction between the contact surfaces of the punch and the testing sample, even when proper lubricant is applied in the dome test [66].

Small punch test

There is a miniaturised dome test called the small punch test. It was initially developed in the United States and Japan in the 1980s. The small punch test is similar to the dome test in almost every way. The difference is that the deforming tool is smaller in diameter in the small punch test. Similar to the previously discussed tests, a displacement with constant speed is applied to the specimen by the punch. Displacement and force-time history relationships are recorded, and the result is presented as a function of time [67]. The small punch test is widely used for its further simplicity with a smaller testing platform than the dome test. Bruchhausen et al. [68] performed a small punch test, and the setup is shown in Figure 2.22. The dimensions of the main components in the test are listed in Table 2.2. Bruchhausen et al. [61] claimed that the results of the small punch test were susceptible to the geometry of the testing equipment. It was suggested that establishing an international standard for small punch tests was necessary to ensure the comparability of the test results between different investigations. In addition, unifying and standardising data formats could increase information exchange and eventually create synergies between different studies.

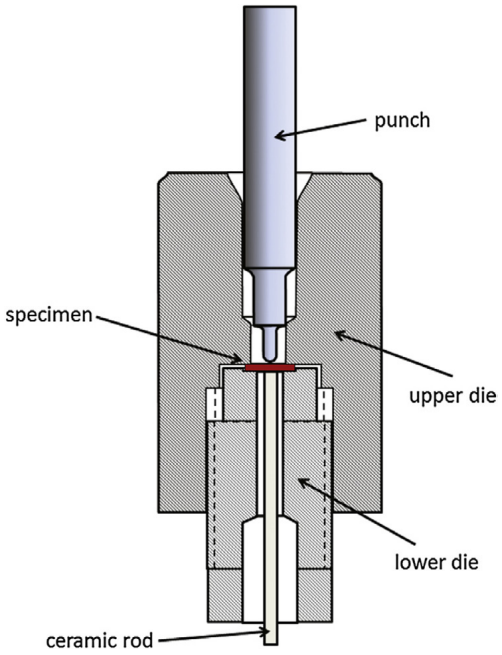

Figure 2.22 Schematic diagram of the small punch test setup [68].

Table 2.2 Principal dimensions of the small punch specimen and setup [68].

Feature	Size
Punch diameter	2.5 mm
Diameter of receiving hole (lower die)	4 mm
Chamfer length (lower die)	0.2 mm
Chamfer angle (lower die)	45°
Specimen diameter	8 mm
Specimen thickness	0.5 mm

Young and Kee [69] performed a small punch test, generated load-displacement curves and highlighted two timings of points #1 and #2, as shown in Figure 2.23. They tested the tensile strength and the anisotropy of aluminium 2024 alloy. The results were quite different from the results obtained by the uniaxial tension test. They claimed the difference was because the material manufacturing process caused anisotropic characteristics in the material before testing. They also stated that the fracture in the small punch test was caused by shear deformation, different from the uniaxial tensile test.

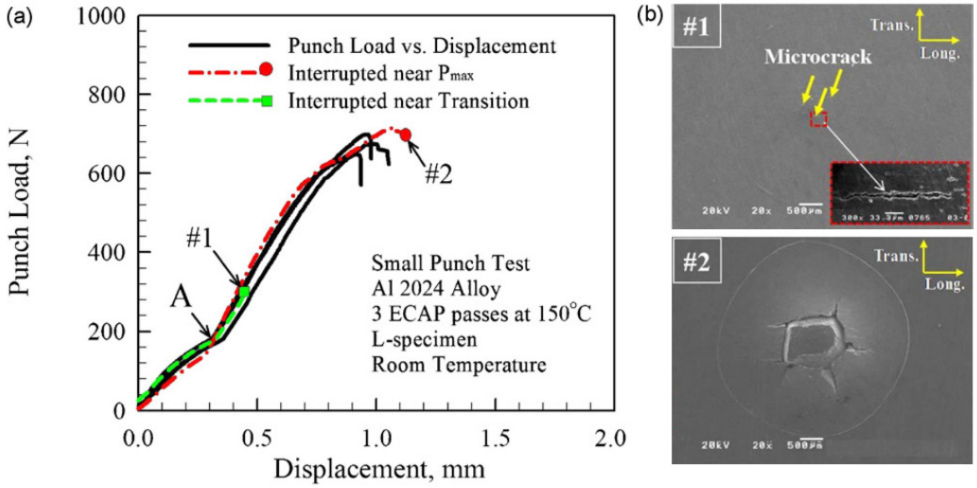

Figure 2.23 Results of the small punch test of Al 2024 alloy: (a) punch load-displacement curve and the (b) bottom surface of the small punch specimen at timing #1 and #2 [69].

In general, the small punch test and other out-of-plane biaxial tensile tests have advantages over the uniaxial tensile test. They can predict the material deformation behaviour by extracting stress-strain relationships from load-displacement curves through miniature specimens [69]. In the uniaxial tensile test, necking and fracture will occur at a random location on the gauge area because the material is not perfectly uniform with pre-formed grains and micro-structure imperfection. In the small punch test, failure would always occur at the stress-concentrated location under the tip of the small punch. As the failure location can be anticipated, specific data from the designated area can be collected.

The thickness of the specimens in the out-of-plane biaxial tensile tests tends to remain unchanged after the tests. However, in metal spinning processes, especially in the shear spinning process, deformation in the thickness direction is significant and could not be neglected. The thickness reduction of the workpiece is controlled and ideally follows the sine law. Unlike in the shear spinning process, the thickness reduction in the out-of-plane biaxial tensile tests is uncontrollable as the tests increase in the surface area of the testing specimen, thus reducing thickness. In addition, the thickness reduction in the conventional spinning process is not as significant as it is in the shear spinning process, and it is difficult to keep the thickness to follow the sine law as the ideal condition.

The FLDs of out-of-plane biaxial tensile tests have the advantage of monitoring the displacements in the major and minor strain directions rather than in only one direction like the uniaxial tensile test. The FLDs of out-of-plane biaxial tensile tests describe the material formability in 2D as a plane stress state. Nevertheless, out-of-plane biaxial tensile tests are worth introducing to the spinning process as they are the most common methods utilised by the industry to identify the necking and fracture failures in sheet metal forming processes [60].

Marciniak Test

A deforming tool (such as a punch) with hemispherical geometry will unavoidably directly contact and apply bending to the testing specimen. Therefore, a pure tensile loading condition is difficult to achieve. In-plane biaxial tensile tests solved this problem. The Marciniak test is a commonly used in-plane biaxial tensile test [42]. The purpose of this test is to investigate the loss of stability in sheet metal forming processes when the material is under equal-biaxial tension. A punch with a flat area that contacts the specimen is used to apply the loading, as shown in Figure 2.24. The geometry of the contact area can be circular, elliptical or rectangular, depending on the desired strain path. To avoid friction between the punch and the test specimen and to further avoid early-stage necking and fracture at the sharp corner of the punch, a ring-shaped metal blank as the carrier blank is applied between the punch and the test specimen. The ring-shaped metal blank deforms with the test specimen. The test specimens have similar geometry to the dome test, as shown in Figure 2.16. Marciniak initially obtained limited results, such as thickness variations and strains near the fracture and necking areas, as shown in Figure 2.25. After Marciniak developed the testing method, other researchers perfected the test and obtained more comprehensive results, such as major and minor strains to plot FLD [70].

Marciniak tested the material formability under specific loading conditions and successfully obtained the strain results. However, the test only used one specimen

design, so only one group of strain results was obtained. To achieve different strain paths, the geometry of the deforming tool and the testing specimen must be specifically designed and optimised for every strain path. The strain state of the specimen gauge area is a consequence of the combined effect of the geometric constraints of the deforming tool and the specimen. The major and minor strain limits in the Marciniak test could achieve a linear strain path without the friction between the punch and the specimen. However, the requirement of a carrier blank made the test more complicated than the Nakajima testing and less popular [71].

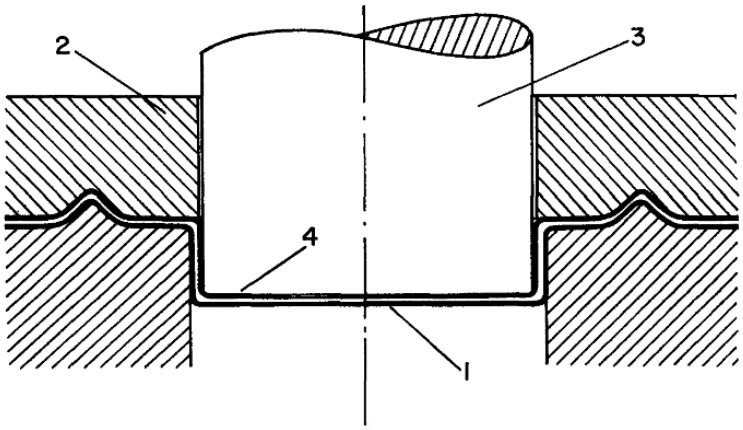

Figure 2.24 A schematic diagram of the Marciniak test: 1. testing specimen, 2. annular blank holder, 3. punch and 4. sheet metal ring [42].

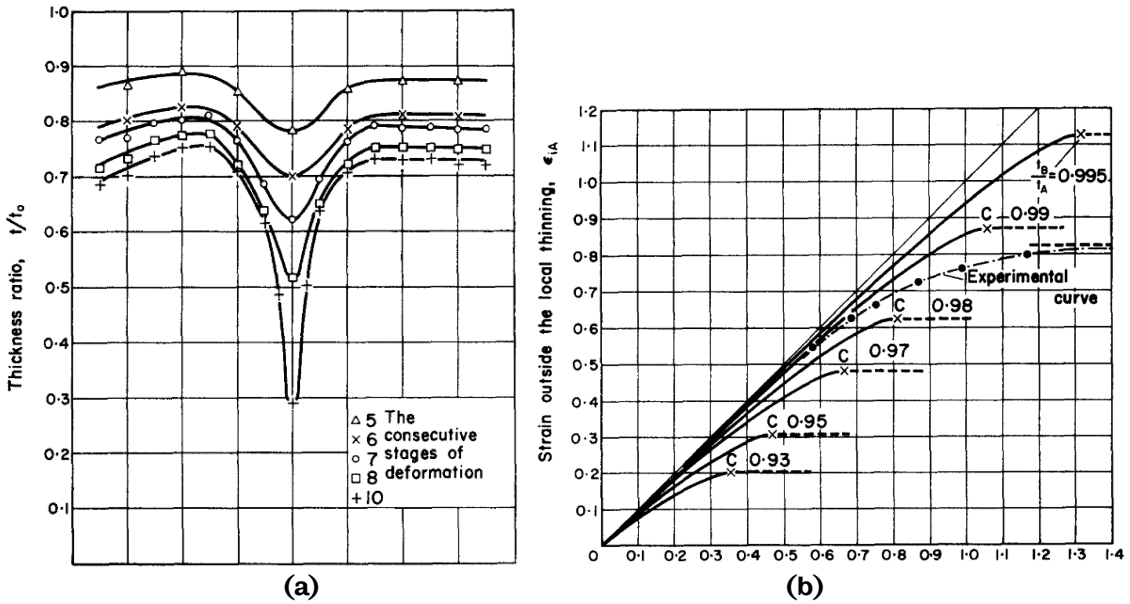

Figure 2.25 Testing results of (a) thickness variation of the specimen in the plane perpendicular to the forming groove and the (b) strain concentration [42].

In general, the international standard for the uniaxial tensile test was established, and the dimensions of the specimens, as well as the testing parameters, are clearly defined for different purposes and different types of materials such as metal [54],

metallic foil [72] and plastic [73] materials. Therefore, the experimental procedures of different studies follow the same standards, making the published results comparable. However, international standards are not yet established for every in-plane biaxial tensile test. As a result, individually designed specimens have been reported in various investigations, resulting in difficulties in extracting meaningful results from these studies. In addition, it is very difficult to reproduce a test setup reported in various studies since the specimens and the testing equipment are specifically designed for different purposes and materials. While the geometries of the testing specimens are relatively easy to redesign and manufacture, the changes to the testing equipment are costly and time-consuming.

To reduce the complexity of the out-of-plane biaxial tensile tests, the planar biaxial tensile test was recently proposed in the ISO 16842 standard [74] and was currently being developed. The new design of the cruciform specimen and the constraints were developed in this standard. Bending and contact effects from deforming tools were eliminated in this test as a cruciform specimen was stretched in both directions with four arms fixed on tensile equipment. The specimen was modified from the geometry developed by Kuwabara et al. [75] and Hanabusa et al. [76], as shown in Figure 2.26. Four arms of the specimen were fixed on the testing equipment and transferred the tension to the central gauge area. Slots cut on the arms distributed the load to the gauge section more evenly and reduced the load sharing between the arms. However, the stress and strain distribution were susceptible to the number of slots, the slots' dimensions, and the slots' location [77]. Moreover, the strain results obtained from the central gauge area were comparatively small. Necking and fracture occurred on the arms first rather than on the central gauge area due to the width reduction that was resulted from cutting slots on the arms.

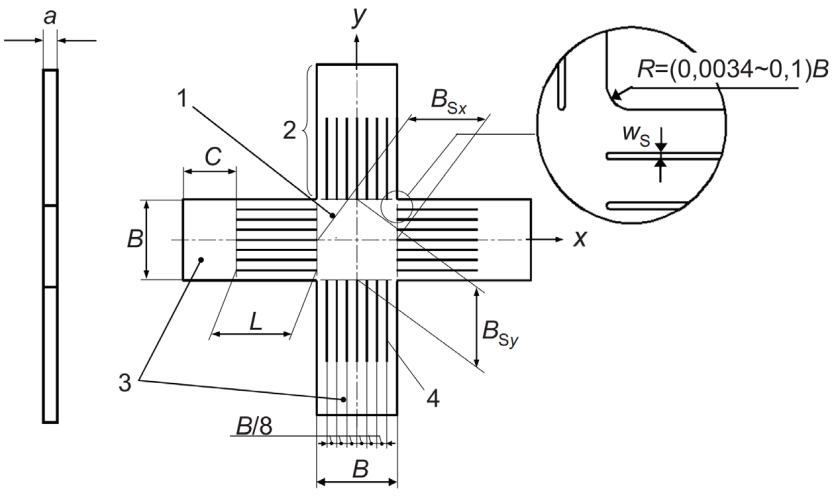

(a)

1 gauge area
2 arm
3 grip
4 slit
a thickness of a test piece
B arm width
B_{Sx} distance between opposing slit ends in the x direction
B_{Sy} distance between opposing slit ends in the y direction
C grip length
L slit length
R corner radius at the junctions of arms to the gauge area
w_S slit width

(b)

Figure 2.26 (a) the testing specimen proposed by ISO 16842 standard and (b) the annotations [74].

After the ISO 16842 standard was proposed, the specimen modification achieved more significant deformation on the central gauge area. At the very least, deformation was distributed more uniformly throughout the cruciform specimen. For the specimen design, Hannon and Tiernan [78] summarised that the plastic deformation was required to be concentrated and distributed evenly on the central gauge area of the specimen, and the gauge area should stay still during the test.

The FE method was applied for geometry optimization of the cruciform specimen. Yu et al. [79] and Song [80] used the FE method and proved that the deformation requirements proposed by Hannon and Tiernan [71] were achievable. Approaches were developed to ensure that the plastic deformation occurred and was evenly distributed on the central gauge area. Fillets with specific radii were introduced to the sharp corners between the adjacent arms to reduce the stress concentration. The thickness of the gauge area was reduced on one or both sides of the specimen. The gauge area was machined to be a circular or rectangular concave shape.

As mentioned in section 2.2.3, cyclical bending and compression are necessary for wrinkling in the spinning process. Although the testing methods reviewed in sections 2.3.1 and 2.3.2 could test material under different deformation modes and test fracture failure, they still cannot apply cyclical bending and compression, and thus they cannot test wrinkling failure.

2.3.3 Continuous Bending Under Tension Test

Although the biaxial tensile test has overwhelming advantages over the uniaxial tensile test, not every aspect of the material deformation can be investigated. For

example, the spinning process includes compression, bending and cyclic loading, which biaxial tensile tests could not achieve. Hence the deformation modes in the spinning process could not be applied to the biaxial testing samples. Moreover, the complex contact conditions induced by the deforming tool on the workpiece in sheet metal forming processes to investigate the effect of individual deformation modes on the material formability is inadequate. In metal spinning processes, especially in shear spinning, the thickness of the workpiece is reduced according to the sine law. Therefore, a better testing method should involve the deformation in the thickness direction. The continuous bending under tension (CBT) test was developed based on the uniaxial tensile test, involving the deformation in the thickness direction. The purpose of the CBT test is to obtain the material behaviour until the specimen fractures, identical to the uniaxial and the biaxial tensile tests. The CBT test is regarded as a modified tensile test with a set of three rollers continuously rolling forwards and backwards, applying bending and tension simultaneously to the specimen. Benedyk et al. [71] developed the earliest CBT test to evaluate the material formability of a wide range of sheet metals, as shown in Figure 2.27. The schematic diagram of the rollers moving on the strip specimen and the photo of the roller set mounted on a strip specimen is shown in Figure 2.27 (a) and Figure 2.27 (b).

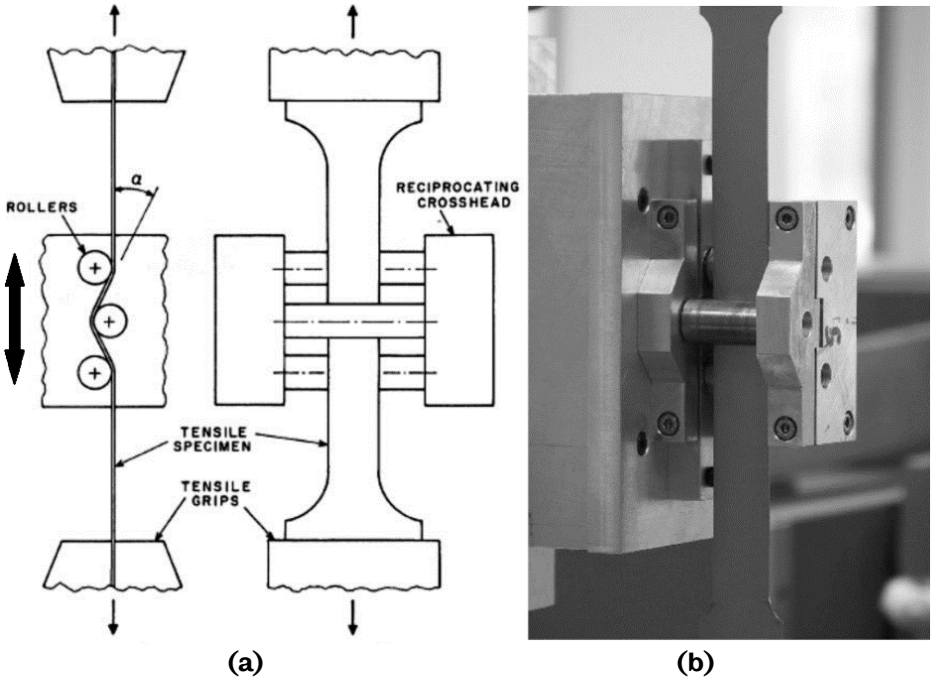

Figure 2.27 (a) A schematic diagram of the continuous bending under tension (CBT) test [82], and (b) the CBT rolling unit mounted on a strip specimen [81].

Emmens and Boogaard [81] conducted the CBT test on different materials with different roller set moving speeds. A comparison of specimens tested by the uniaxial tensile test and the CBT test is shown in Figure 2.27. The maximum elongation

recorded in the CBT test significantly exceeded the results obtained in uniaxial tensile testing, and the CBT results matched better with the results obtained from some sheet metal forming processes. The pulling force and elongation history of DC04 steel obtained from the uniaxial tensile test and the CBT test are shown in Figure 2.29 (a) and Figure 2.29 (b).

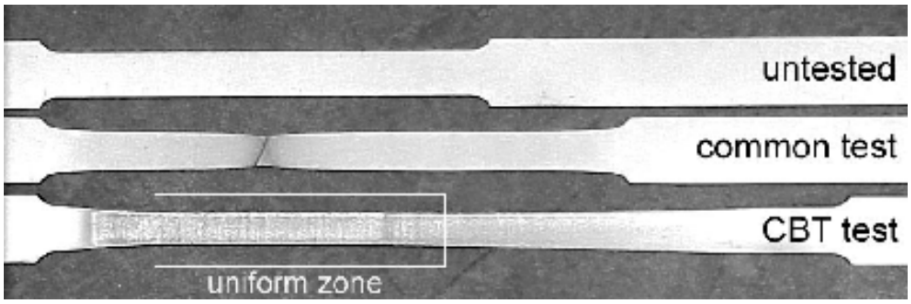

Figure 2.28 Untested, the uniaxial tensile tested and the continuous bending under tension (CBT) tested specimens [81].

Emmens and Boogaard [83] concluded that the CBT test was suitable for studying the bending-under-tension mechanism in ISF. Benedyk et al. [82] further improved the CBT testing platform and tested aluminium AA6022-T4. Similar results were obtained with enhanced material formability. These tests obtained results where the strain was doubled before failure. Based on the results, Benedyk et al. [75] concluded that the CBT test could be further exploited and beneficial to automotive manufacturing. Barrett et al. [84] also obtained similar results indicating that the elongation forces required to deform the specimen plastically in the CBT test were lower than that required in the uniaxial tensile test. Barrett et al. [84] concluded that this phenomenon was due to the synergy between the tension and the bending applied to the specimen. The results suggested that the maximum elongation increased with the rolling speed and decreased with the bending depth. However, these trends were not always valid due to variations in the fracture limit of different testing parameters and different materials. Zecevic et al. [85] discovered that the material anisotropy in the CBT test significantly affected the results in tests conducted on specimens cut along the rolling and transverse directions. The results are shown in Figure 2.30. The force-displacement results obtained from the uniaxial tensile tests were slightly affected by the material anisotropy. However, the maximum elongation force and elongation showed noticeable differences.

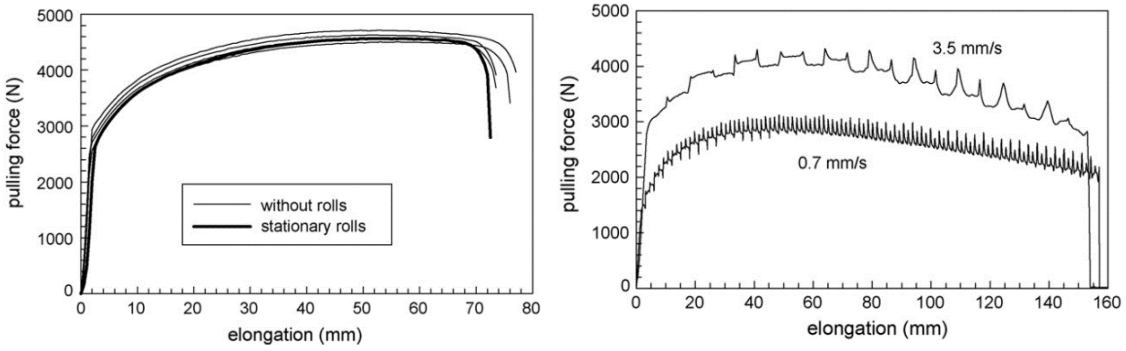

Figure 2.29 Force-displacement results obtained from the (a) uniaxial tensile test and the (b) continuous bending under tension (CBT) test [81].

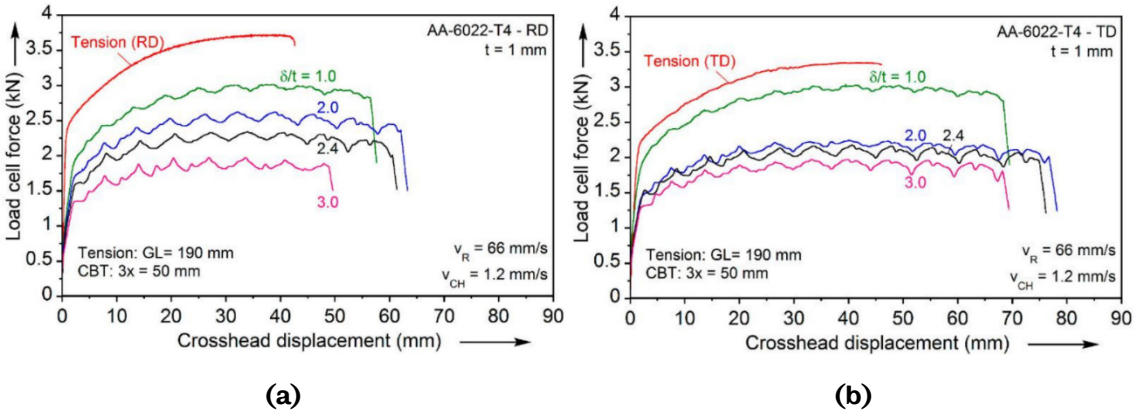

Figure 2.30 Force-displacement curves obtained from (a) specimen cut along the rolling direction and (b) specimen cut along the transverse direction [85].

In general, applying bending and tension simultaneously to the specimen suppressed the deformation instability, leading to localised deformation and fracture [84]. The CBT test achieved elongation that significantly exceeded the results obtained from the uniaxial tensile test. The CBT test results correlated better with some sheet metal forming processes as the strains in these processes were significantly greater than the strains in the uniaxial tensile test [82]. The testing parameters, such as pulling speed and bending depth, significantly affected the maximum elongation. Optimal testing parameters existed for a specimen with a specific geometry to obtain the maximum elongation. For example, the optimised pulling speed was usually below a specific value to prevent the loss of localised deformation and the initiation of failure by overloading. At relatively low pulling speeds, the material formability was enhanced as the number of processing cycles was simultaneously increased [81].

2.3.4 Tension Under Cyclic Bending and Compression

After developing the CBT test, the tension under cyclic bending and compression (TCBC) test was developed at the University of Sheffield [86]. Compared with the

CBT test, one more roller was installed to the roller set in the TCBC test to provide a compressive force to the specimen. Therefore, three deformation modes, tension, bending and compression, were applied to the specimen by the TCBC test platform. A schematic diagram of the test is shown in Figure 2.31.

The comparison of the specimens tested under different deformation modes is shown in Figure 2.32. Although the TCBC test improved upon the CBT test, the test platform is incompatible with direct strain measuring methods (e.g. a DIC device). In the TCBC test, both sides of the contact area of the specimen are covered by the loading device, as shown in Figure 2.33.

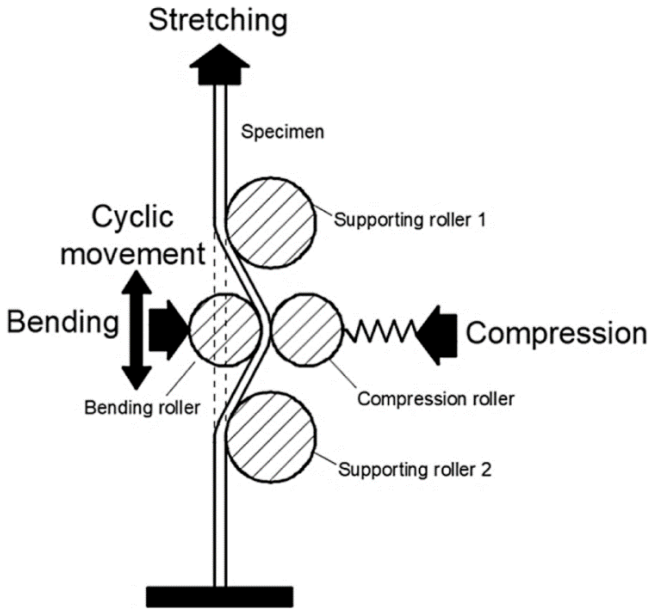

Figure 2.31 The schematic diagram of the TCBC test [86].

Figure 2.32 The comparison of the untested, uniaxial tested and tension under cyclic bending and compression (TCBC) tested specimens [87].

Due to the limitation of the testing platform, FE simulation was used to obtain the strain results. Localised deformations were found throughout the specimen, and several weak zones existed before the fracture. The fracture only happened when the rollers were in contact with the damaged zone, leading to crack propagation [88]. It was concluded that if the compression force was adequately large, the contact area would be yielded by compression, and a weak zone was created after a short period of cyclic loading. The theoretical analysis also indicated that the pulling speed adversely affected the maximum elongation of the specimen. If the

pulling speed is zero, the TCBC test will become a pure cyclic rolling process, and the deformation can be excessively large without fracture.

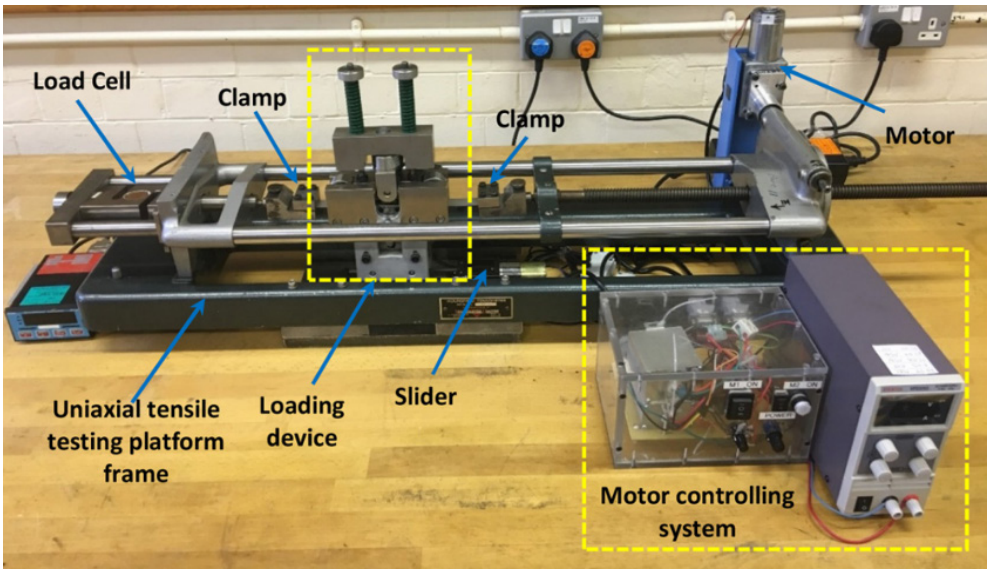

Figure 2.33 Key components of the tension under cyclic bending and compression (TCBC) testing machine [86].

TCBC test considerably improved to incorporate one more deformation mode into the test, leading to the active deformation in the thickness direction. However, the limitation of the TCBC test is apparent. The current TCBC testing machine can only apply bending and compression cycles on a fixed specimen length. The elongated section is only pulled without cyclical bending and compression. Therefore, the small cracks are only found on the left side of the gauge area, as shown in Figure 2.32. So far, the TCBC test is the most suitable testing method to test the fracture limit of the metal spinning process as it involves three deformation modes and cyclic loading to simulate the roller movement of processing the workpiece in repeated revolutions. However, in the shear spinning process, the thickness reduction of the workpiece follows the sine law and the gap between the roller and the mandrel are usually fixed. Hence, after the workpiece is processed by the roller, the thickness throughout the workpiece will be uniform. In the TCBC test, the compression force is provided by winding two nuts to compress the springs on the loading device. Due to the design drawback that the loading device can only move cyclically on the path with a fixed length, the thickness reduction of the specimen is not uniform throughout the specimen. In general, the targeted thickness reduction can only be guaranteed on one path with a fixed length. If the testing rig could be improved and this drawback could be eliminated, the material formability could be further enhanced as more material of the specimen could be cyclically deformed and elongated.

2.3.5 Biaxial Tension Under Bending and Compression

After developing the TCBC test, Ai [89] developed the biaxial tension under bending and compression (BTBC) test rig at the University of Sheffield. The original purpose of the BTBC test was to test the material formability in ISF. The computer-aided design (CAD) drawing is shown in Figure 2.34, and the critical components of the BTBC testing machine are shown in Figure 2.35.

The BTBC test was developed as a novel formability testing method for ISF, applying bending and compression while pulling the specimen biaxially. The geometry of the specimen was developed, as shown in Figure 2.36. The strain results were obtained by the grid etching method, and the grid was etched on the other side of the thickness-reduced gauge area, as shown in Figure 2.37.

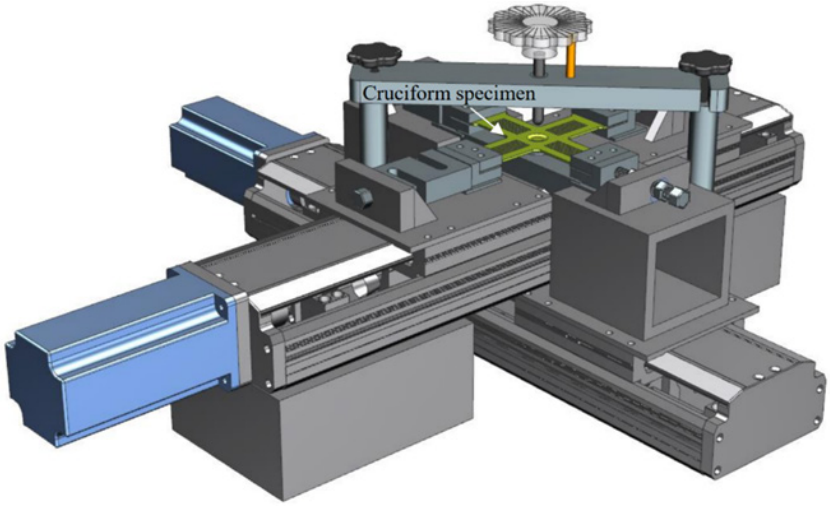

Figure 2.34 Computer-aided drawing (CAD) of the biaxial tension under bending and compression (BTBC) testing machine [89].

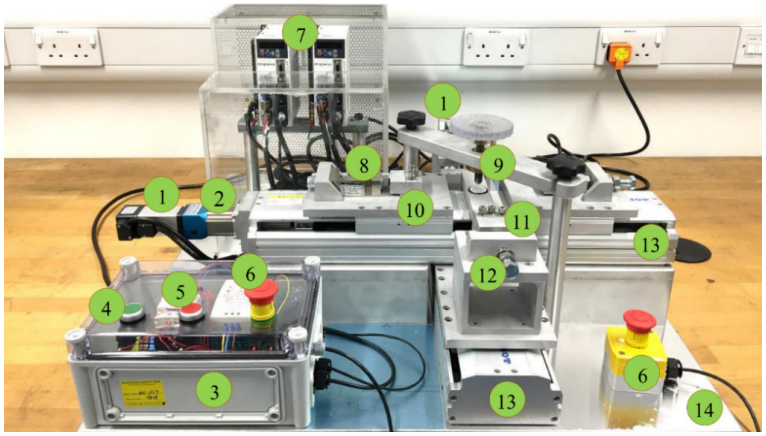

Figure 2.35 Critical components of the BTBC machine: 1. motor; 2. gearbox; 3. power control box; 4. power-on button; 5. power-off button; 6. emergency stop button; 7. motor speed control units; 8. load cell; 9. bending tool; 10. spring; 11. clamp; 12. clamp location adjusting screw; 13. bi-directional linear screw (inside) and 14. base plate [89].

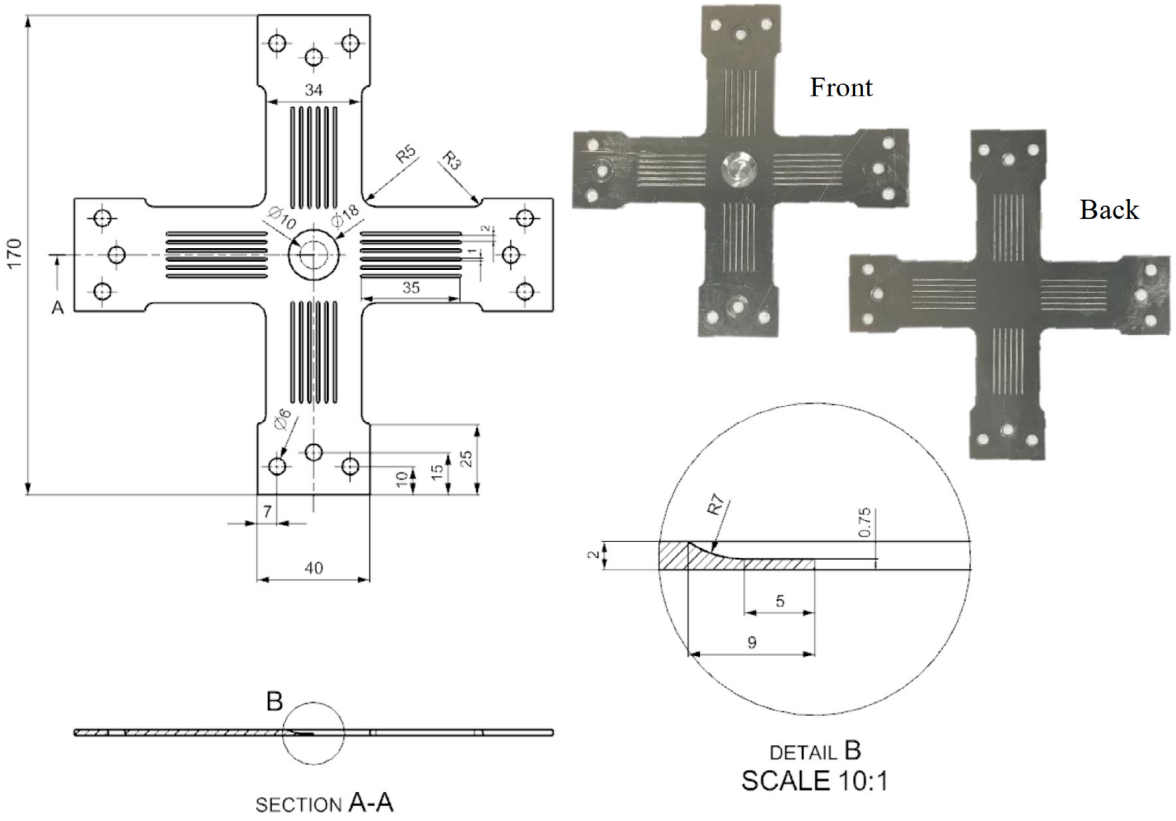

Figure 2.36 The geometry of the specimen for the biaxial tension under bending and compression (BTBC) test from Sheng [89].

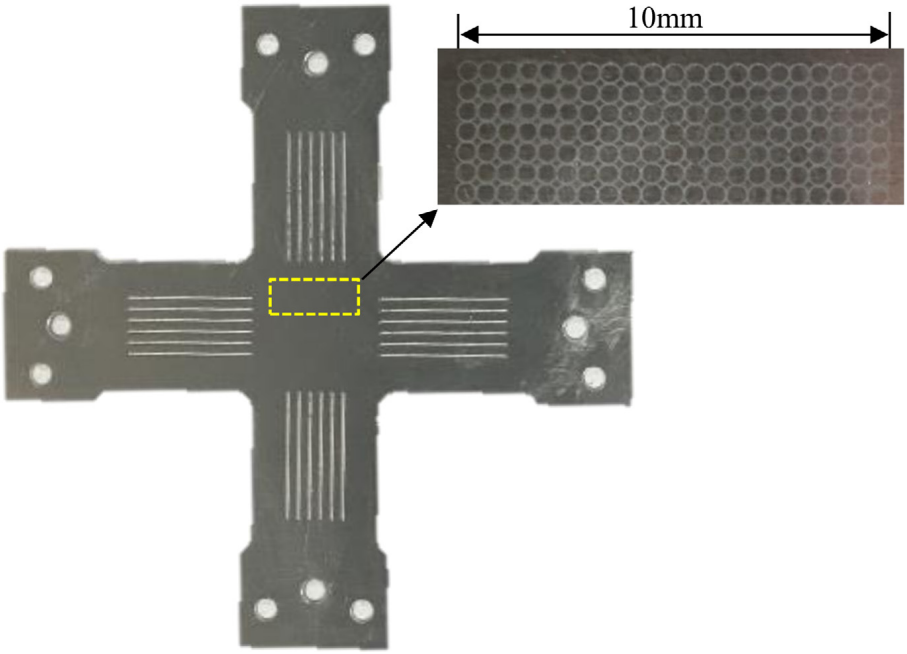

Figure 2.37 The grid etching method applied to the biaxial tension under bending and compression (BTBC) specimen by Sheng [89].

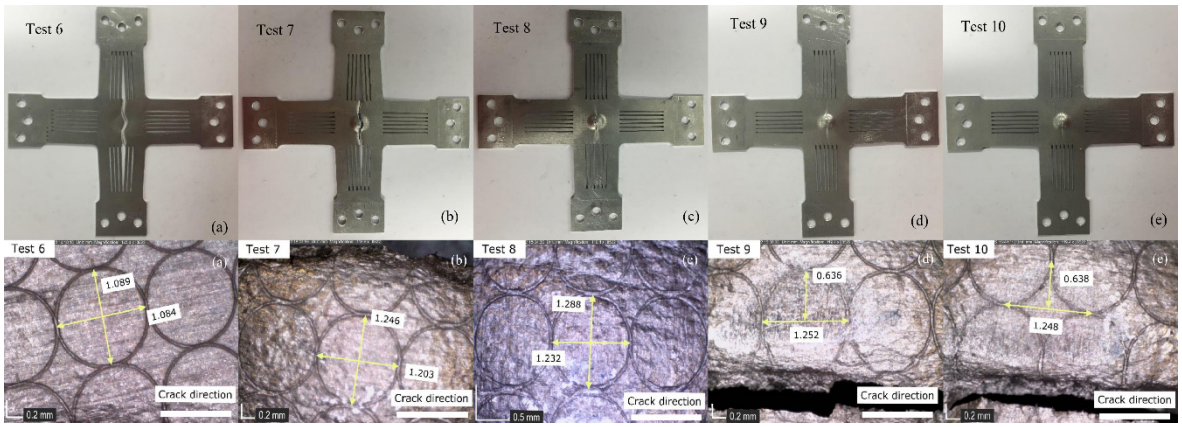

Figure 2.38 Deformed circular patterns of the gauge area tested under (a) pure tension, (b) tension and bending, (c) tension, bending and cyclic loading, (d) tension, bending and compression and (e) tension, bending, compression and cyclic loading [89].

The forming limit of 5251-H22 aluminium was successfully obtained to investigate ISF, as shown in Figure 2.38. The strain was measured from the deformed circular grids on the back of the gauge area. It was claimed that the BTBC test could represent the material deformation in the double-sided incremental sheet forming process. The BTBC testing machine can elongate and compress the specimen at different speeds, similar to the Zwick/Roell commercialised biaxial testing machine. An extra compressing tool was installed above the BTBC rig specimen. However, any device installed above the gauge area will affect the installation of other direct strain measurements, such as the DIC device. The thickness reduction is concentrated on the tip of the compressing tool in the BTBC test.

In general, the purpose of material testing is to accurately describe or predict material deformation behaviour in sheet metal forming processes. Materials behave differently under different loading conditions and thus resulting in different deformation modes. Therefore, the appropriate testing method should be selected for the specific forming process. Selecting the most suitable testing method for a sheet material forming process requires understanding the material deformation modes and potential processing failures that occur in the process. None of the existing testing methods is perfectly suitable for testing the wrinkling failure in the metal spinning process. The spinning process is highly dynamic, and the processing time is usually only a few seconds, thus a relatively high strain rate. However, the testing methods reviewed in this section are static and take much longer to complete. For example, the elongation speed of the uniaxial tensile test is 2 mm/min. It takes several minutes for the specimen to fracture, much longer than the spinning processing time. Therefore, for testing the material formability, an understanding should be established from the failures in the material spinning process specifically.

The test could be simplified by isolating the failure and testing it with a smaller and specifically designed specimen to represent it rather than performing the entire spinning process using a complete metal blank. If strain rate could be proved to have no effect on the wrinkling failure, a slow-speed testing method will be sufficient with less difficulty and cost by modifying the existing low-speed tests. As mentioned in section 2.2.3, the test for wrinkling in the spinning process must include the deformation modes in the spinning process, which are compression and cyclical bending. Tension and shear may also exit in the spinning process. TCBC testing platform could apply cyclical bending, but it only tests one direction. BTBC could test two directions and apply the desired deformation modes to the specimen except cyclical bending. If the problem could be solved, the BTBC testing platform ideally could test the wrinkling failure in the spinning process.

2.4 Failures in Spinning Process and Testing Methods

As mentioned in Introduction Chapter, there are three common failures in the spinning process: circumferential fracture, radial fracture and wrinkling, and investigating wrinkling failure is the main focus of this study. The shear spinning cases were studied in the published literature. It was found that fracture failure only occurred when the thickness of the workpiece was excessively reduced. Previous studies related to wrinkling failure and the existing testing methods for wrinkling failure are reviewed in this section.

Many studies on the material formability of sheet metal forming processes have been reported, for example, deep drawing and incremental sheet forming. However, only a handful of studies investigated the material formability of metal spinning processes. For the spinning process, another term to describe the material formability in the metal spinning process is spinnability, defined as the ability to undergo deformations without the fracture of any material [90]. Specifically, spinnability is the maximum thickness reduction of the material before fracture under the applied process parameters, including the roller toolpath, feed rate, and mandrel speed. Only a handful of studies has investigated the formability related to fracture failure, and no research has investigated the formability due to wrinkling failure in the metal spinning process.

It is easier to determine tube spinning material formability than conventional and shear spinning. For tube spinning, Chang et al. [91] investigated the material formability in tube spinning with two approaches. The first approach reduced the wall thickness stepwise to the final thickness without the failure of the workpiece. The second approach applied a one-pass roller toolpath to reduce wall thickness

without failure. These two approaches to determine the maximum reduction are straightforward for application to any material. In tube spinning, the typical failure is fracture as the thickness reduction ratios in tube spinning are much higher than in shear spinning. Moreover, deformation modes and processing parameters in shear spinning are much more complex, and the approaches for tube spinning could not apply to shear spinning to determine the wrinkling forming limit.

Ruffle, unevenness, folding, ripple, crack, and adhesion are some examples of surface defects. Bugling, localised bugling, springback, wrinkling and fracture are severe defects regarded as processing failures [92]. Some are significantly more severe than others. Severe defects could potentially interrupt the process and prevent the successful manufacturing of a spun part. The following section focuses on reviewing the fracture and wrinkling failures that seriously affect the quality of the spun part.

2.4.1 Fracture Failure

It is commonly understood that there are two types of fracture failures in the metal spinning process: radial and circumferential fracture, as shown in Figure 2.39.

In the early years of research, fracture failure was used to define the spinnability of the material in the spinning process [90]. Music et al. [4] reviewed that the radial fracture was caused by localised tensile stress concentrations beneath the roller contact with the workpiece, and the circumferential fracture was caused by cyclical tensile stresses induced by the roller during every pass. The fracture failure in the spinning process is similar to the other sheet metal forming processes. Necking would occur before fracture, caused by excessive stresses induced to the workpiece by the roller [33], and these stresses could be regarded as the upper-stress limit [3]. The maximum strain prior to the onset of necking would govern the maximum thickness reduction ratio and indicate the spinnability of a specific material in the spinning process.

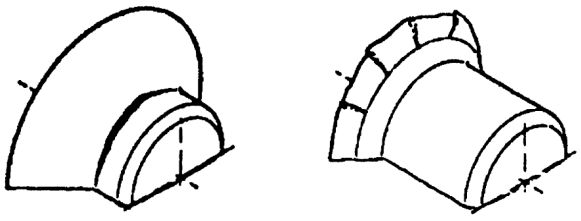

(a) (b)

Figure 2.39 Fracture failures in the spinning process: (a) circumferential fracture due to radial tensile stresses and (b) radial fracture due to tangential compressive stresses and bending stresses [13].

2.4.2 Testing Methods for Fracture Failure

Kegg [90] was among the first group of researchers who attempted to predict the failure in the spinning process. The test was conducted to test the spinnability in a primitive way by designing mandrels with different nose shapes, as is shown in Figure 2.40. A trend line was obtained, similar to the strain signature proposed later as the results. Fracture failure was studied by observing the cross-sectionally cut workpiece, as shown in Figure 2.41. In the experiments, the mandrel with the ellipsoidal nose caused a gradual change in the material cross-sectional area. Kegg [83] also claimed that sudden changes in the material section weakened the material structures as a well-acknowledged design principle was also applicable in the spinning process. It was concluded that the mandrel with the ellipsoidal nose could test the material formability. Compared with true shear spinning, Kegg [90] revealed that the under-spinning condition ($t_1 > t_0 \sin\alpha$) enhanced the spinnability, and the over-spinning condition ($t_1 < t_0 \sin\alpha$) reduced spinnability ($t_1 > t_0 \sin\alpha$).

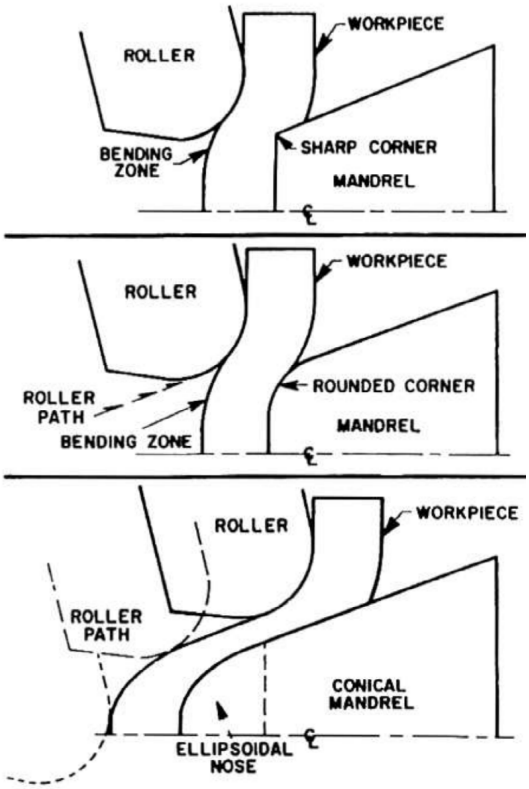

Figure 2.40 - Geometries of three types of mandrel noses [90].

Kegg [90] further developed a testing method and tested different materials on the mandrel with the ellipsoidal nose. The angle of the mandrel wall varied from 0° to 90°, and the thickness reduction of the workpiece ranged from 0% to 100%. It proposed an empirical relationship to determine the spinnability of a given material based on the testing results of this method. This empirical relationship correlated

with the maximum spinning reduction of the area at fracture in a tensile test, as shown in Figure 2.42.

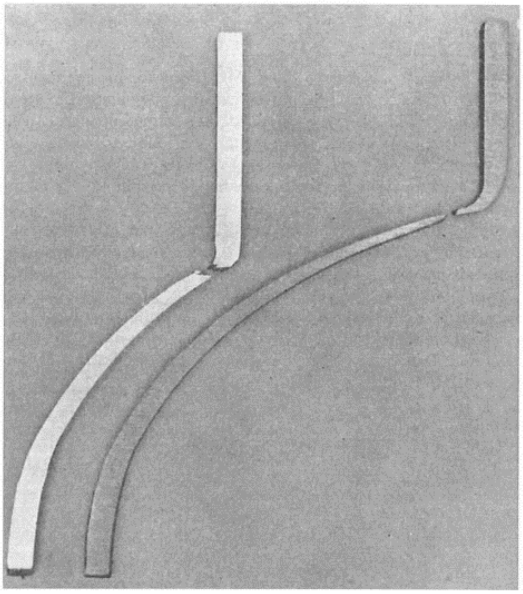

Figure 2.41 Fracture failure in the metal spinning process [90].

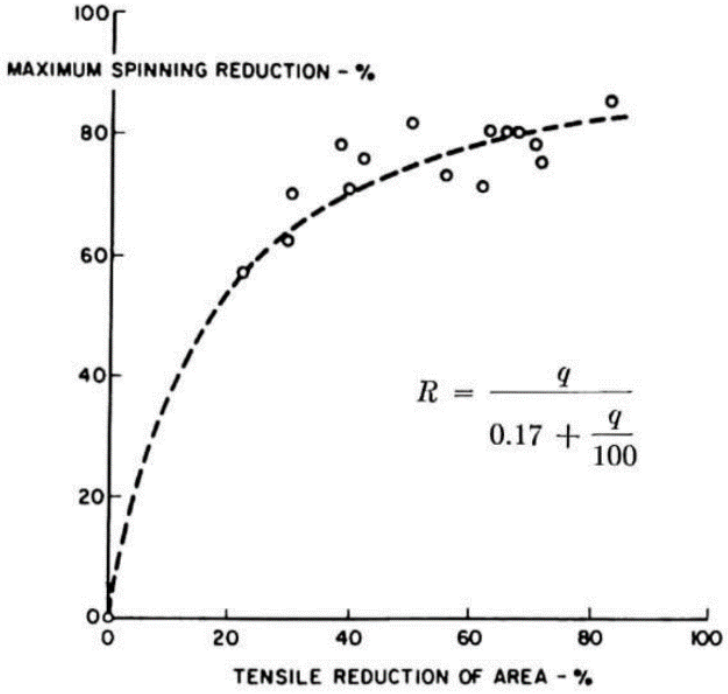

Figure 2.42 Spinnability versus tensile reduction of the area at fracture in a tensile test [90].

This method was further extended by Hayama and Tago [93], who argued that results for the ellipsoidal mandrel were not valid for cone shapes because the forming forces were not taken into account. The definition of the term spinnability was expanded to include failure by wrinkling and failure by wall fracture, as proposed by Kegg. Hayama and Kodo [94]. It related the spinnability to the strain hardening

exponent and claimed that the flange wrinkling was determined by the strain hardening exponent, and the wall fracture was determined by the reduction of the potential fracture area.

Later, Kawai [95] proposed establishing a database for the metal spinning process. The database consisted of many industrial cases searchable by dimensions, geometries and materials for workpieces and spun products. Kawai [96] expanded the database and knowledge by relating it to the failures. Product quality characteristics were added, such as surface finishing in the metal spinning process. Multiple process parameters could affect the spinnability of the material in the spinning process [97]. Generally, the idea was to try every setting and processing parameter combination to the workpiece with different geometries. However, the metal spinning process is a highly customizable sheet metal forming process, so the database cannot cover all the product geometries and combinations of processing parameters. The idea is straightforward but inefficient, making it difficult for the collected data to be comprehensive. The synergy between different studies is challenging, and developing a unified format for sharing data is also burdensome.

Wang [32] also summarised previous literature and claimed that the Bauschinger effect should not be neglected in investigating the spinning process due to the cyclic tensile stress and compressive stress induced by the roller. However, no studies included the Bauschinger effect when analysing the stress and strain states due to the lack of test data on specific material. Only a handful of studies investigated the fracture mechanics, and no testing methods were developed to test the fracture failure in the metal spinning process. The existing methods explored the maximum thickness reduction ratio by applying different thickness reduction ratios to the workpiece. Also, the spinning process enhanced material formability, and the maximum thickness reduction strain achieved were excessively high, much higher than the sine law value in the true shear spinning process. Hence, wrinkling would be the only possible failure when investigating the true spinning process, and the effect of fracture on the spinning process failure is less critical than the wrinkling failure.

2.4.3 Wrinkling Failure

Wrinkling is commonly seen in the metal spinning process, and the onset and propagation of wrinkling are shown in Figure 2.43. Wrinkling usually occurs in the un-spun flange of the workpiece during the process, and it becomes more severe while the deforming tool (the roller) continues to deform the workpiece [4]. In wrinkling, the material becomes unstable with wave tops and bottoms of the flange in the circumferential direction. Wrinkling is a significant failure mode in both shear

and conventional spinning processes because it potentially reduces production efficiency and increases material wastage. The trial-and-error and empirical methods are still commonly used in the industry to avoid wrinkling failure during product manufacturing. No method is available to obtain the wrinkling forming limit.

As reviewed in section 2.2.3, Hayama et al. [22] claimed that the deformation modes of wrinkling failure involve tension, compression, shear and cyclical bending. However, wrinkling occurred on the flange before being directly worked over by a roller in some cases, as shown in Figure 2.44 (a).

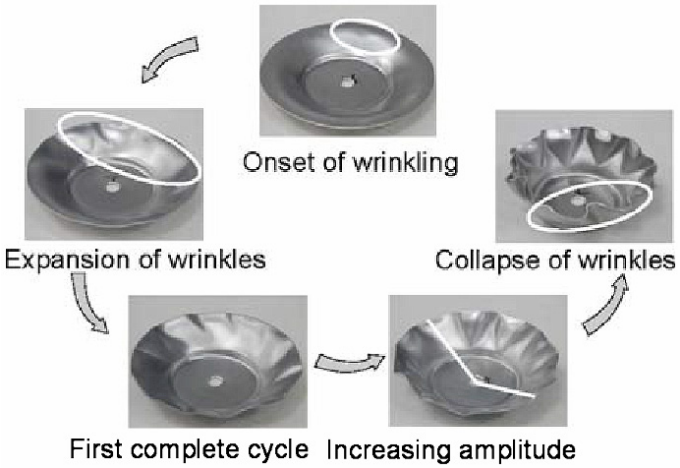

Figure 2.43 Onset and propagation of wrinkling in the metal spinning process [98].

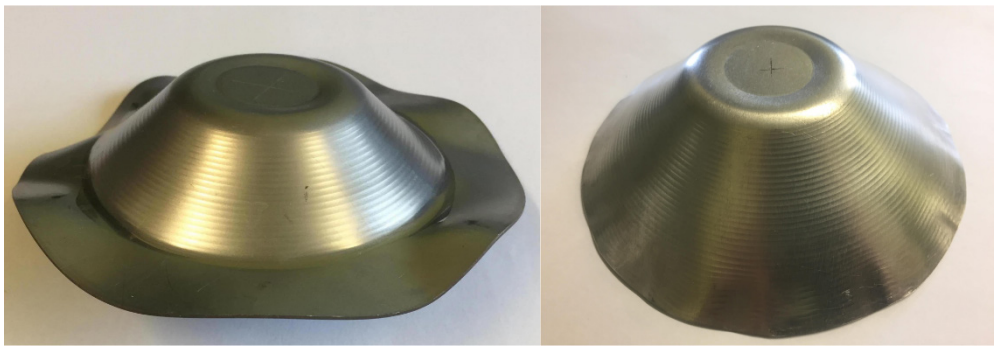

(a) **(b)**

Figure 2.44 Two examples of the shear spinning workpieces: (a) DC01 workpiece wrinkled before being worked by the roller and (b) AA5251 workpiece flattened after wrinkled [15].

The process was aborted when the wrinkling occurred on the flange as the roller had not induced shearing deformation to the flange yet. Also, the roller could flatten the wrinkled area after the wrinkling occurred and finish the process, as shown in Figure 2.44 (b). The spun part survived the process when the wrinkling occurred and flattened, but the surface finishing was coarse. Hayama et al. [99] and Wang et al. [100] concluded that wrinkling could be flattened in subsequent roller passes in the conventional spinning processes. In general, wrinkling tended to occur when the

roller feed ratio and workpiece diameter were increased and the workpiece thickness was decreased. The subsequent passes could eliminate the non-severe wrinkling waves even if wrinkling occurred. However, the surface finishing of the spun part was coasre when the wrinkling occurred and flattened as shown in Figure 2.44 (b). Hence, the forming limit of the shear spinning process should be determined by wrinkling initiation as in the conventional spinning process, rather than whether the process could be finished without excessive distortion caused by severe wrinkling.

Flange wrinkling can be observed in both shear and conventional spinning. According to the first study on flange wrinkling in conventional spinning performed by Kobayashi [101], it is caused by buckling due to compressive tangential stresses in the flange, . An analytical model was developed by modifying the theory of instability in deep drawing. Later, Hayama et al. [102] reported that the wrinkling in shear spinning was different from deep drawing. They concluded that the circumferential stress was uniform around the flange in deep drawing, and it was non-uniform in spinning because of the indentation formed by roller movement.

Kleiner et al. [98] concluded that wrinkling occurred in the sheet metal spinning process when the tangential compressive stress exceeded the buckling stability limit in the flange. It was also claimed that wrinkling was caused by static buckling and was triggered by the dynamic effects of the roller movement and the mandrel rotation. Moreover, Watson and Long [12] developed a FE model and further investigated the effect of cyclical loading. A significant bending residual stress remained in the un-spun flange of the workpiece and formed a plastic hinge between the roller and the workpiece. The plastic hinge was worked over by the roller on every rotating revolution of the mandrel, and if the load applied to the plastic hinge was beyond its limit, wrinkling formed on the flange of the workpiece.

The FE method was applied to obtain the strains and stresses previously that could not be obtained. Watson et al. [95] applied FEM to investigate the wrinkling failure mechanism in a conventional spinning process and concluded that wrinkling occurred due to circumferential compressive stress in the flange.

Kleiner et al. [98] introduced an experimental design into the spinning process to determine the influence of the process parameters on wrinkling in the conventional spinning process. It was concluded that the diameter and thickness were the most significant factors of wrinkling failure, followed by the feed rate, the mandrel speed, the roller path and the workpiece material. Hayama et al. [22] obtained similar results indicating that the feed ratio, workpiece thickness and diameter were critical for affecting wrinkling failure. Since then, many studies have focused more on the

effects of process parameters because the stress and strain results were quite difficult to obtain as the metal spinning process was highly dynamic. Multiple studies proved that wrinkling failure caused high roller feed ratios, resulting in higher stresses in the workpiece. For example, Wang et al. [100] investigated the effects of the roller feed ratio on wrinkling failure in the conventional spinning process. Childerhouse and Long [15] investigated the effects of feed ratio, spindle speed, initial workpiece thickness, and thickness reduction on wrinkling in the shear spinning process. Additionally, it was confirmed that thinner workpieces with lower yield strength were more susceptible to wrinkling [103]. Satoh and Yanagimoto [104] claimed that wrinkling occurred due to elastic buckling and that wrinkling resistance could be enhanced if a material with a higher yield strength was used.

To summarise, studies have been conducted on the wrinkling failure in the conventional metal spinning process. Further investigation on the shear spinning process is required. The strain evolution history of the wrinkled area is essential to predict wrinkling failure.

2.4.4 Testing Methods for Wrinkling Failure

There is no testing method for the wrinkling failure in the metal spinning process, only a handful of studies investigated the wrinkling initiation and growth. Yoshida [105] developed the Yoshida buckling test to investigate the wrinkling forming tendency of sheet metals, creating wrinkling by applying uniaxial tension on the two ends of the specimen. Due to the technology limitation at the time, the results were not comprehensive. The original test was modified, and the FE method and DIC device were used to obtain further results, for example, strain evolution history, in later studies, which Yoshida could not achieve.

The geometry of the original Yoshida test was fixed, and thus, it could not be representative of other deformation cases, as the stress ratio was also fixed. Kim et al. [106] conducted a modified Yoshida buckling test to investigate the effects of geometry and stress ratios on wrinkling initiation and growth. The test was conducted by employing the same method as the Yoshida test, by applying tension on the two ends of the specimen with different widths and griping distances. The specimen design is shown in Figure 2.45. The deformed samples are shown in Figure 2.46 and Figure 2.47. The buckling height and displacement results for tests with different specimen widths and gripping distances are shown in Figure 2.48.

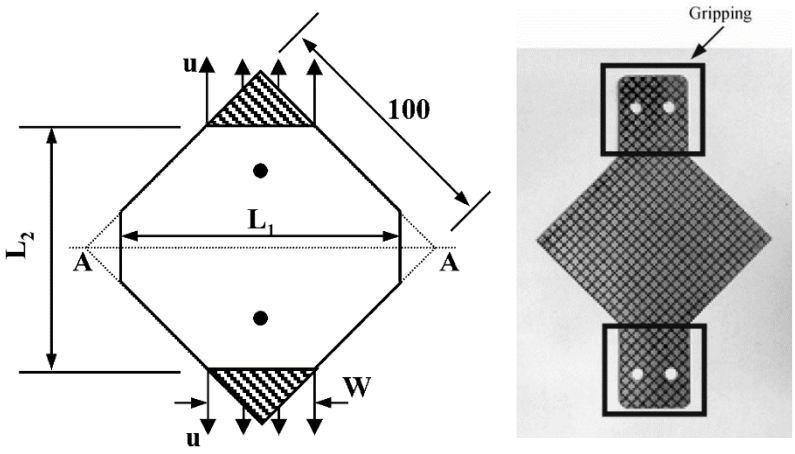

Figure 2.45 Specimen design for the Yoshida test with customizable width L1 and grip distance L2 [106].

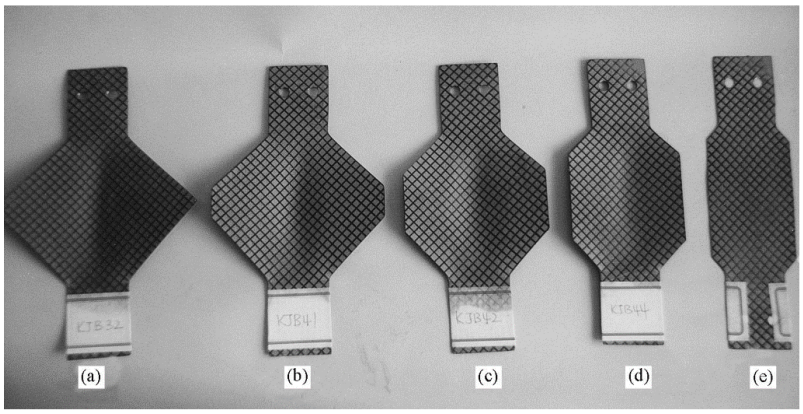

Figure 2.46 Deformed specimens with different widths: (a)140 mm; (b) 120 mm; (c) 100 mm; (d) 80 mm; and (e) 60 mm [106].

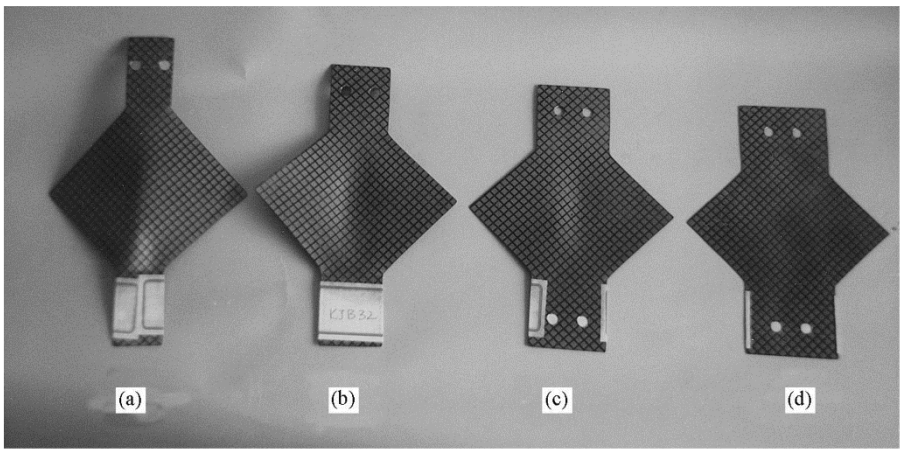

Figure 2.47 Deformed specimens with different grip distances: (a) 110 mm; (b) 100 mm; (c) 90 mm; and (d) 80 mm [106].

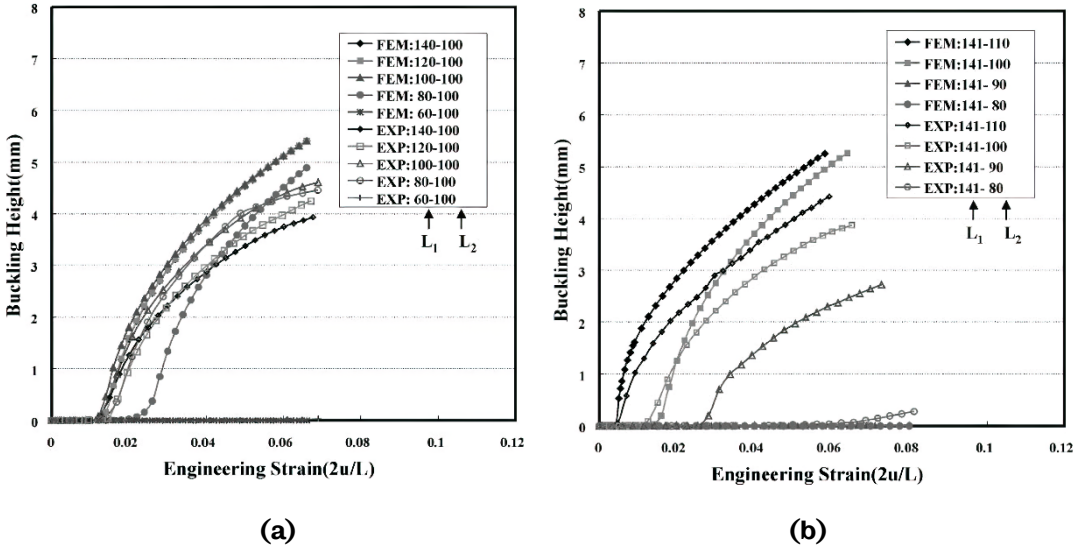

Figure 2.48 Curves of buckling height and displacement for tests (a) specimen with different widths and (b) specimen with different gripping distances [106].

Kim et al. [106] obtained the strain results by the gird etching method and quantified wrinkling by directly measuring the buckling height. It was claimed that the modified Yoshida test could be applied to analyse the wrinkling in sheet metal forming processes as different buckling behaviours were achieved under various specimen widths and gripping distances. However, the study focused on using the test results to validate the FE models. The analysis of stress and strain was not comprehensive, and it needs further investigation to describe the wrinkling initiation and evolution.

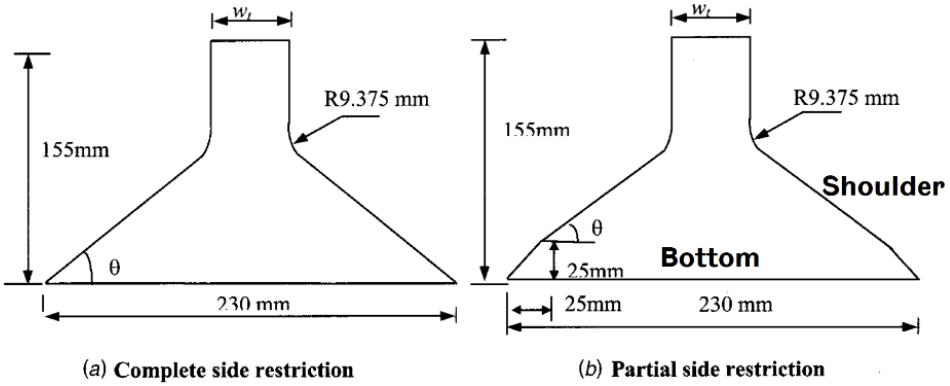

Figure 2.49 Geometries of the specimens used under different boundary conditions [107].

Cao et al. [107] developed a novel wedge strip test by simply using a regular uniaxial tensile machine to apply different boundary conditions to constrain the specimens and investigated the wrinkling behaviour of sheet metal. The geometry of the specimen is shown in Figure 2.49, and the experimental setup to measure the buckling height is shown in Figure 2.50. An example of the result is shown in Figure 2.51. The boundary conditions were applied by simply adjusting the constraints to the bottom and two shoulders. Tests were conducted under various conditions:

including the bottom was free, and the two shoulders were entirely constrained; the bottom and two shoulders were entirely constrained, the bottom was entirely constrained, and the two shoulders were partially constrained.

The advantage of the wedge strip test was that different boundary conditions could be applied to the specimen. In other words, more stress ratios could be applied to the specimen. With different combinations of processing parameters and boundary conditions, the onset of the buckling was investigated. Cao et al. [107] concluded that the strain needed to trigger the buckling was relatively small. The buckling was very sensitive to the compression caused by the shoulders and the bottom constraint. Also, the stress states could be reproduced easily by performing the test on a uniaxial tensile testing machine.

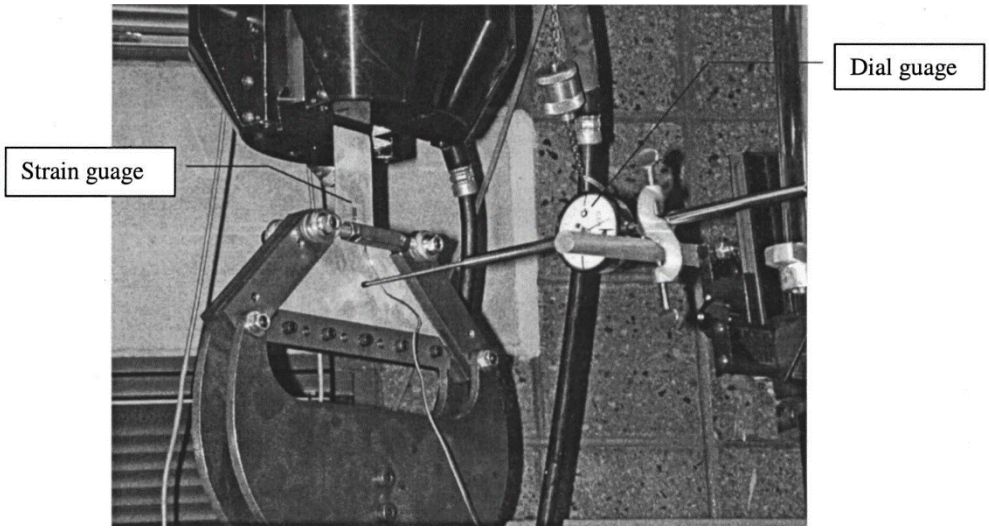

Figure 2.50 Experimental setup for measuring the buckling height [107].

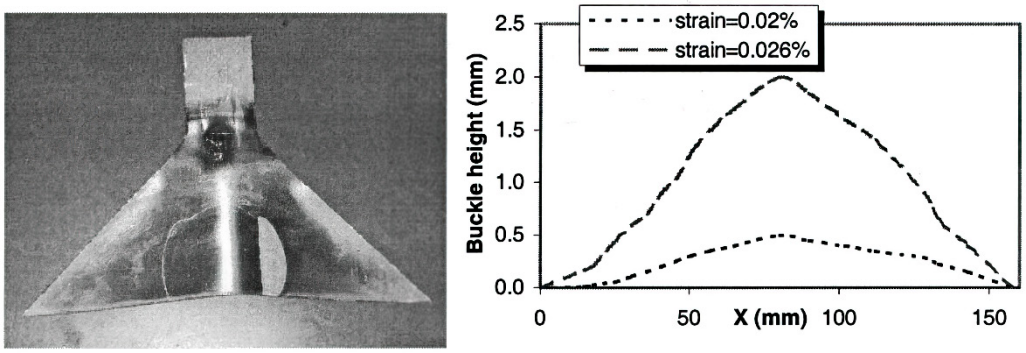

Figure 2.51 Deformed specimen and strain result [107].

To summarise, the specimen design for achieving the desired deformation modes is crucial. Kim et al. [106] proved that different specimens under identical loading conditions would result in different deformation modes. Moreover, both tests reviewed in this section were performed on the uniaxial tensile machine, which

could only apply the uniaxial tension deformation mode to the uniaxial tensile test specimen, as reviewed in section 2.3.1. However, Yoshida managed to achieve buckling by designing the specimen differently. Although the buckling/wrinkling in the Yoshida test is different from the spinning process, the wrinkling on the workpiece flange in the spinning process is similar to the partially constrained specimen in the wedge strip test. The material on the wrinkled area in the spinning process is also constrained by the nearby material as the specimen in the Yoshida test. Also, these two tests measured buckling height to quantify the buckling other than measuring strains. It is the most straightforward method to quantify the buckling, and this method could be applied to further investigation when quantifying the wrinkling in the spinning process.

2.4.5 Other Types of Failures

It is more suitable to describe the following failures as defects in the metal spinning process. Unlike the three most common failures mentioned in Sections 2.4.1 and 2.4.3, these defects are mild and have a relatively small impact on the successful completion of the spinning process. Most of these defects would not cause failures but result in a coarse surface finish affecting the quality of a spun part.

Ruffle

A ruffle is shown in Figure 2.52. It usually occurs when the material accumulates near the roller. Material accumulation could cause an excessive thickness reduction with over-increased stresses induced by the roller. Furthermore, the material could fracture due to excessive stress. A ruffle occurred under different thickness reduction ratios for different materials. It was also affected by the material strength, the roller feed ratio and the roller processing angle.

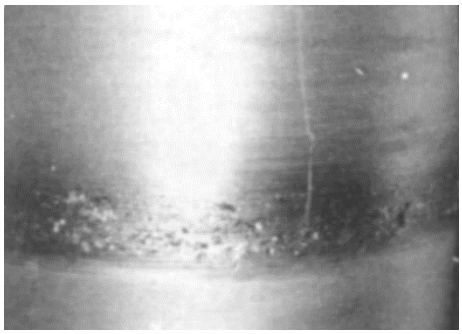

Figure 2.52 Ruffle on the surface of the spun part in tube spinning [92].

Ripple

Ripple could happen in both conventional and shear spinning processes. It was confirmed that a ripple was not the indentation caused by the roller movement on

the workpiece surface. It was caused by thermal expansion and contraction due to improper lubrication and cooling that constantly changed the temperature. In addition, a ripple could occur due to the vibration of the roller and the mandrel during the process if the processing precision was not set up to the standard. Properly applied lubricant and coolant could ease the condition.

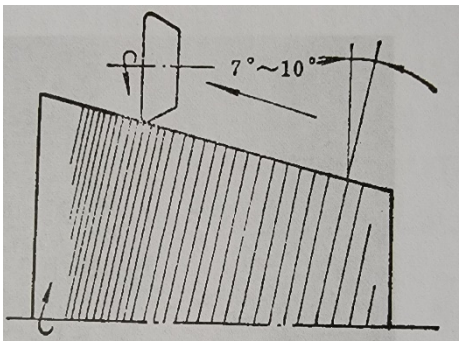

Figure 2.53 A schematic diagram of a ripple in the metal spinning process [108].

Adhesion

Adhesion rarely occurred. Adhesion occurred when the roller was welded with the workpiece due to an excessive temperature caused by friction when the roller was working over the surface of the workpiece. Adhesion could be eliminated by adequately applying lubricant and coolant.

Bulging and Localised Bulging

Localised or general bulging occurred when applying excessive thickness reduction to the workpiece, as shown in Figure 2.54. Bulging occurred on the weak area when the area had stresses that caused the material to deform backwards. Ideally, an optimised combination of roller feed ratio, thickness reduction and temperature could eliminate bulging.

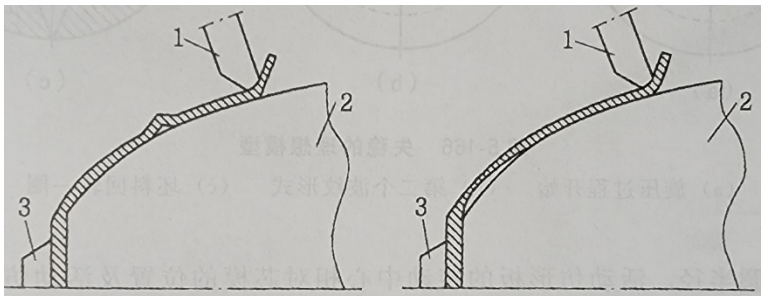

(a) **(b)**

Figure 2.54 A schematic diagram of (a) localised bulging and (b) bulging in the metal spinning process with 1 - roller, 2 - mandrel and 3 - backplate [108].

In summary, there are multiple types of failures other than the three common failures mentioned in the Introduction Chapter. Wrinkling, radial fractures and

circumferential fractures are severe defects regarded as processing failures in spinning. If any of these failures occur on the workpiece, it may damage the deforming tool and interrupt the process. Other defects are either mild or highly localised. These defects can be eliminated by employing a more advanced process platform with a better-lubricated condition and precision control under optimised processing parameters [92]. The literature review shows that only a few studies investigated failure mechanisms in the metal spinning process. These failure mechanisms still need further investigation, and an in-depth understanding is worth establishing.

2.5 Summary of Research Gaps

To date, there is a massive amount of literature related to material formability tests in sheet forming processes, but only a handful for metal spinning processes. Although different deformation modes in sheet metal forming processes were studied, the common features of these deformation modes in spinning processes have not been thoroughly studied. In addition, the spinning process involves multiple processing parameters, all of which significantly impact the final quality of the workpiece and processing failures such as wrinkling and fracture. Most of these parameters were systematically investigated. However, detailed results, for example, different stresses and strains of the wrinkled material, still need further investigation. Three research gaps have been identified:

- The common features of different deformation modes in the spinning process related to the wrinkling failure and forming limit have not been thoroughly studied. Also, the spinning process is complex, combined with different material deformation modes. The previous study has considerable limitations due to the technology limitation at that time.
- FEM has been used widely to simulate various spinning processes. The stress and strain results were studied. However, previous studies focused on analysing the spinning process, such as forming force, rather than the deformation modes and failures. It is necessary to develop FE models further to investigate the initiation and propagation of wrinkling failure. Investigating the wrinkling initiation and propagation is the first aim of the current study.
- No testing method is suitable to test the material formability related to the wrinkling failure in the metal spinning process. Studies related to wrinkling failure in the spinning process are very limited. Establishing universal standards and developing formability testing methods for wrinkling is the second aim of the current study.

3 FE Modelling of Wrinkling in Shear Spinning Process

In this chapter, FE models of the shear spinning process are developed to obtain the strain and stress results for analysing the wrinkling failures and establishing an in-depth understanding. The primary focus of this chapter is to investigate the cause of the wrinkling occurrence and to analyse the initiation and propagation of the wrinkling in the shear spinning process. The FE strain results can guide further investigation and development of the wrinkling test in Chapters 5 and 6.

Section 3.1 introduces FE model development, including spinning tools and workpiece geometry, meshing, and defining the flow stress of the workpiece material. Section 3.1 also defines the boundary conditions and process parameters applied to the FE models. Section 3.2 validates the modelling results and further introduces mesh refinement and model optimization. Section 3.3 presents an analysis and discussion of the FE results. Section 3.4 is a summary of the key findings of this chapter.

3.1 FE Model Development

3.1.1 Abaqus/Standard and Abaqus/Explicit Methods

There are two methods for solving plastic deformation problems: ABAQUS/Standard (implicit) and ABAQUS/Explicit. Details of these two methods are mentioned in Chapter 2. The general description of ABAQUS/Standard and ABAQUS/Explicit methods and the reason for choosing the ABAQUS/Explicit to solve the metal spinning is introduced in Section 3.1. The current section also introduces the FE model construction and presents the geometry, the boundary conditions and the material properties used in the shear spinning model.

Explicit and implicit methods are used in numerical analysis to obtain numerical approximations of ordinary time-dependent and partial differential equations required to simulate physical processes. In general, the explicit method calculates the future state of the system according to the state at the current time, while the implicit method searches for the solution by solving equations involving both the current and the future states of the system.

The metal spinning process is a highly dynamic problem with a rotating mandrel, and the rotational speed is commonly over 1000 revolutions per min (RPM). However, the total spinning processing time (step time in ABAQUS) is relatively short, usually

within 30 seconds. The contact condition is complex between the roller and the workpiece. Material nonlinearity is expected in the metal spinning process. The material properties and the boundary conditions are likely to change after the load induced by the roller is applied, resulting in the material plastic deformation leading to the change of the workpiece geometry. Dividing the solution time into smaller increments allows the solution path to be followed progressively step by step rather than the entire computation continuing to follow the initial state. Hence the Abaqus Explicit is selected to solve the metal spinning process for balanced modelling accuracy and calculation efficiency.

3.1.2 Element Selection

Several techniques can be implemented in developing the FE modelling of spinning processes to improve computational efficiency without compromising the accuracy of the simulation results. The mandrel, backplate, and roller are made of steel, and they are more rigid than the workpiece due to the workpiece geometry and different constraint conditions. Compared with the deformation of the workpiece, the deformation of the forming tools during the process is much small and considered to be elastic. Hence, these three forming tools are defined as rigid bodies with no deformation modelled. Hence, there are no stress and strain on these three tools, and CPU time can be reduced.

In ABAQUS, more than ten element types could be assigned to the workpiece. These elements have different characters and should be selected considering the boundary conditions, deformation modes, model complexity, and many other aspects. For the workpiece in the spinning process, the continuum shell element is selected instead of a solid element for common plastic deformation problems. The solid element, such as C3D8, a general element type with eight-node fully integrated characteristics, is suitable for modelling the plastic deformation of all deformation modes. Due to its fully integrated characteristics, the solutions are much more computationally expensive than the continuum shell element, but with minor accuracy improvement. The continuum shell element in ABAQUS is the SC8R element, with eight nodes and quadrilateral, using first-order interpolation to calculate stresses and displacements with reduced integration [109]. Compared with conventional shell elements, the SC8R element can model problems with complex contact conditions and, most critically, consider transverse shear deformation. As Long et al. [110] reported, the SC8R elements could be used to model metal spinning processes, and the accuracy of the results was not compromised after comparing them with experimental results. Also, Wang et al. [100] reported that using SC8R element type in FE spinning process simulations

could capture wrinkling failure. Although the C3D8 element can model material failures for better accuracy in some cases, wrinkling is the sole failure considered in the current study of the shear spinning process. Other material failures which may need the C3D8 element to model are not considered in this study. In the shear spinning process, bending deformation mode is also heavily involved. The accuracy of the results could be improved by increasing the number of interpolation points of the SC8R elements in the workpiece thickness direction with acceptable compromisation of CPU calculating efficiency. In this study, the SC8R element is selected to model the workpiece instead of the C3D8 element for the above reasons.

The workpiece is deformed by the roller, and its deformation is different when applying different spinning processing parameters. Through the thickness direction of the workpiece, nine integration points are used to model bending deformation accurately. It is compensation for using the SC8R element to solve the metal spinning problems. More integration points will improve the accuracy of the stress and strain distributions along the thickness direction [111]. When using the SC8R element to model the spinning processes, the hourglass effect is likely to happen due to the reduced stiffness of the SC8R elements introduced by using reduced integration. When the hourglass issue happens, the elements deform abnormally in the FE simulation. Using more integration points, more refined mesh and enhanced hourglass control settings could reduce the occurrence of the hourglass issue. As observed from the FE results later in this chapter, it has been found that the hourglass issue is the most influencing effect, and the most effective solution is to refine the mesh if the hourglass issue is observed.

3.1.3 Material Properties

The workpiece material is AA5251-H22 aluminium alloy. It is considered isotropic and homogenous, and the imperfection and anisotropy induced by the manufacturing process, like rolling, are neglected. Three material properties of AA5251-H22 aluminium alloy are presented in Table 3.1. The plastic deformation behaviour of the materials is obtained from the uniaxial tensile test. The workpiece is deformed at room temperature; hence any temperature-related aspects are neglected.

Table 3.1 Mechanical properties of AA5251-H22 aluminium alloy

Density (kg/m^3)	Young's modulus (GPa)	Poisson's ratio
2690	69	0.3

Uniaxial tensile tests are performed to obtain the flow curve of AA5251 aluminium. The test is conducted at room temperature, and an elongation speed of 1.0 mm/min is applied during the test. Test specimens are manufactured in the direction parallel

to the rolling direction of the workpiece. The specimen dimensions are determined according to the Standard Test Methods for Tension Testing of Metallic Materials (ASTM) [73]. The true stress-strain curve of AA5251-H22 aluminium alloy is calculated from recorded force and displacement history data, shown in Figure 3.1.

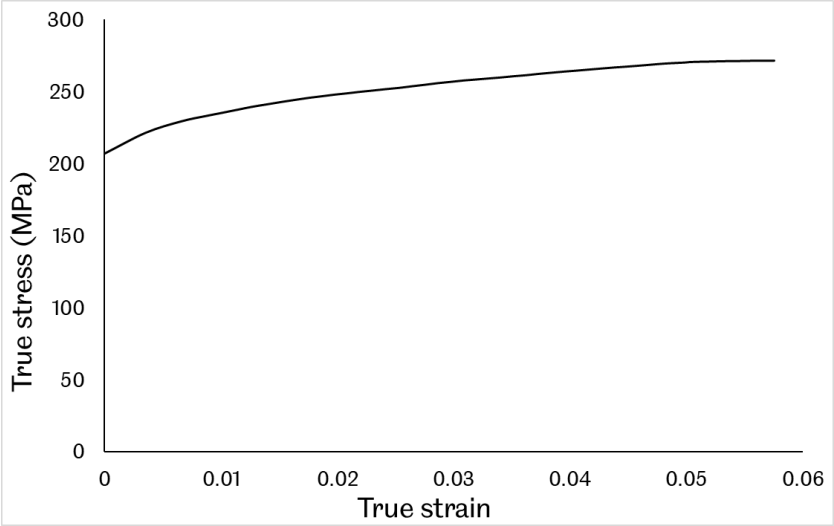

Figure 3.1 The true stress and true plastic strain curve of AA5251-H22 aluminium.

The schematic diagram of the spinning process setup is shown in Figure 3.5. The geometries of the workpiece and the spinning tools are identical to the actual experimental setup reported in Chapter 4. The global coordinate system is assigned to the backplate, workpiece and mandrel, as the only motion is rotation along its rotational axis at a constant speed. A local coordinate system is established on the roller tool, shown by the yellow dashed line in Figure 3.5 (a), to define the roller toolpath conveniently. The angle between the roller and mandrel axes is 45°, also identical to the experimental setup on the CNC lathe in Chapter 4. The roller is moving according to the input coordinates in the modelling step. Multiple combinations of processing parameters will be studied, and the details are presented in Section 3.3.1.

The material anisotropy is not included in the modelling. The spinning process is highly dynamic as the workpiece is circular and rotates at high speed of 1000 RPM. The anisotropy is usually induced by rolling when manufacturing the metal sheets. It will cause differences, for example, when testing the material properties like the uniaxial tensile test since the loading has a fixed angle with the rolling direction. The workpiece is cut from the metal sheet with apparent rolling grains on the workpiece surface. The roller constantly moves on the workpiece surface while the workpiece is rotating. The angle between the loadings of the roller and the rolling grain is constantly changing. It is unnecessarily complicated to construct a model to include these features. Hence the anisotropy is not included in the FE model construction.

Also, the shear spinning process in this project is considered temperature-independent. The process is conducted at room temperature, around 20 degree Celsius. The temperature fluctuation of the roller, mandrel and workpiece in the cold spinning process (spinning process conducted under room temperature) due to the friction is also neglectable since the material properties are not affected [112].

3.1.4 Mass Scaling

The mass scaling method is applied in the spinning FE models, and different mass scaling factors, s are tested. The factor is set to zero by default when the method is not applied. As mentioned in Section 3.1.1, the stable time step is usually very small to maintain numerical stability when the explicit method is used. However, small time step increments due to small element sizes would result in excessively long CPU time. In extreme cases, for example, the workpiece meshed by strategy F in Table 3.4 has 88750 elements, resulting in excessively small element sizes. The stable time step size in the explicit analysis is related to the material density, calculated by Equation 3.1:

$$\Delta t = \frac{L_e}{c_d}$$

Equation 3.1

L_e is the characteristic length of the element, which is determined by the element geometry and formulation. Different formulations are appointed to corresponding elements like first-order and second-order elements. c_d is the stress wave speed.

$$c_d = \sqrt{\frac{E}{\rho}}$$

Equation 3.2

Equation 3.2 calculates the stress wave speed in the model, where E is Young's modulus and ρ is the density of the material. The mass scale method works by multiplying the material density by factor s and s^2 in the simulation. Artificially increasing the material density increases the mass of the material and reduces the stress wave speed, resulting in a greater stable time step size by a factor of s [113].

The mass scaling method increases the time step size in each calculation increment and reduces the CPU calculation time. However, excessively increasing the mass scaling factor would cause severe penetration problems and significantly increase the dynamic effect as the inertia increases with the mass of the material because the material density increases along with the mass scaling factor. It is necessary to ensure that the FE model is reliable, stable and efficient; thus, applying the mass

scaling method should not significantly affect the simulation results. Unreasonable deformation, for example, the elements distorted due to excessive inertia must be prevented, and thus the kinetic energy must be monitored. Two essential criteria must be satisfied to ensure reliable FE simulation results. The first criterion is that the ratio of the kinetic energy to the internal energy must not exceed 0.1 during the majority (usually 2/3) of the simulation process [114]. The second criterion is that the ratio of the artificial strain energy to the internal energy must be less than 0.05 [113]. Furthermore, satisfying these two criteria ensures that the elements are not excessively stiff under bending loads, thus ensuring simulation accuracy [115].

3.1.5 Hourglass Problem

In the shear spinning process, workpiece thickness is reduced due to the shear deformation induced by the roller. The roller works over the surface of the workpiece, reducing the thickness and inducing bending deformation and even wrinkling to the workpiece. However, when a linear element with reduced integration is subjected to bending moment M, as shown in Figure 3.2, the length of dashed lines does not change after deforming. The angles between the dashed lines are also unchanged, resulting in the stress of the single integration point of this element being zero. Hence, the current bending deformation becomes a zero-energy deformation with no strain energy generated by distortion. The problem may occur when the elements, such as reduced integration elements like the SC8R element type, are assigned to the workpiece. The element cannot resist bending since it has no stiffness under this circumstance. Mesh strategy to solve the hourglass problem is developed and introduced in section 3.1.6.

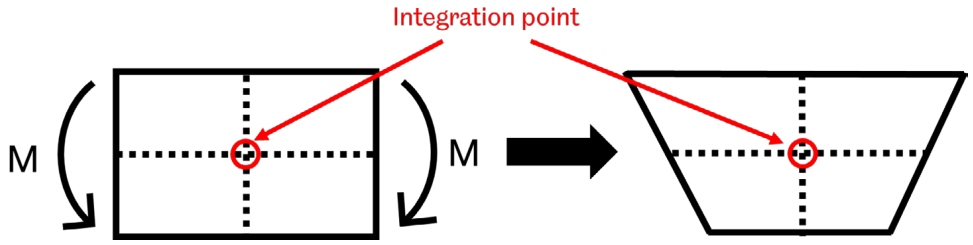

Figure 3.2 Deformation of a linear element with reduced integration subjected to bending moment M.

If the model is coarsely meshed, this zero-energy condition propagates through the meshed elements, generating meaningless stress and strain results, defined as the hourglass effect. For cases with relatively small feed ratios, the hourglass problem would occur when the process is near completion, as shown in Figure 3.3. In cases with relatively large feed ratios, severe wrinkling occurs. The simulation terminates earlier due to the excessive distortion of elements, as shown in Figure 3.4.

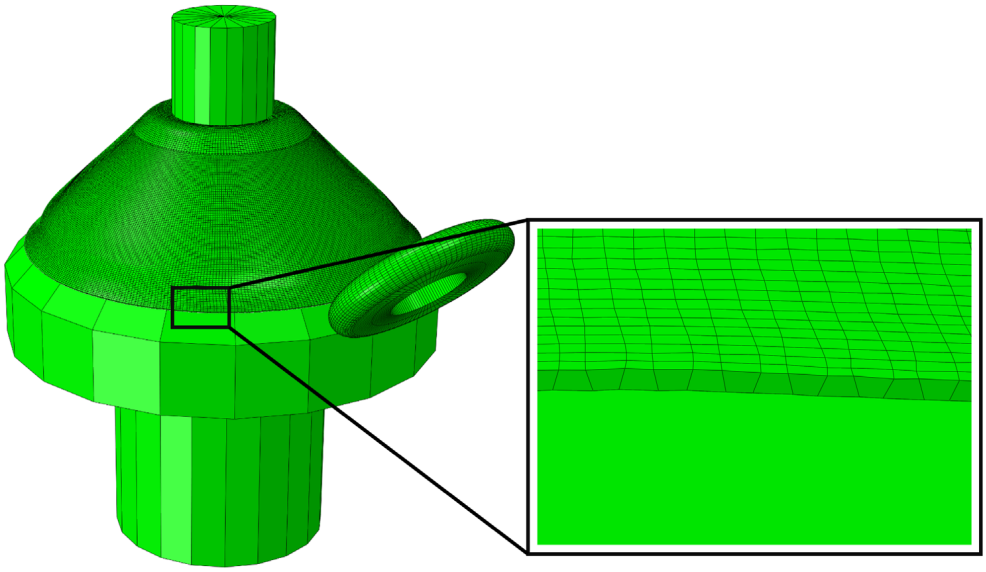

Figure 3.3 Hourglass problem in shear spinning FE simulation without excessive distortion at the late stage of the process.

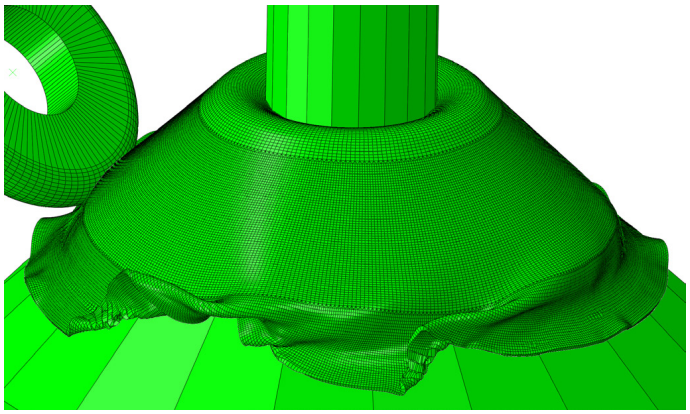

Figure 3.4 Excessive distortion of the spinning process using a larger feed ratio.

3.1.6 FE Model Construction

A typical forming process set up for a shear metal spinning includes a workpiece, a backplate, a mandrel and a roller. The backplate and the mandrel clamp the workpiece, rotating with the mandrel speed between 3000 RPM and 8000 RPM in industrial production. The most important processing parameters are the mandrel rotational speed, the roller feed rate and the feed ratio, determine by the mandrel rotational speed and the roller feed rate, to deform the workpiece incrementally. The mandrel speeds used in this study are much lower than those used in industrial production. Lower mandrel speeds result in a slower deformation of the workpiece and, thus, lower strain rates, reducing the experimental requirements. The CNC lathe in the university workshop has limitations and cannot achieve higher mandrel speeds as in industrial production. Also, the wrinkling failure is not affected by the mandrel speeds if the feed ratio remains the same, as mentioned in Chapter 2.

The spinning FE simulation is divided into four steps. The boundary conditions applied to the model of each step are shown in Figure 3.6. Step 1 is clamping: a 20 kN axial force as load boundary condition 1 is applied on the backplate to clamp the workpiece between the backplate and the mandrel. The movement of the mandrel is constrained by the velocity boundary conditions to represent the state of being fixed on the CNC lathe. Step 2 is rotation: an angular velocity boundary condition is applied to the mandrel and the backplate as boundary conditions 2. These two tools start to rotate in this step. Friction forces are produced on the workpiece bottom and top surfaces due to the contact with the mandrel and the backplate. The workpiece starts to rotate with the same angular velocity as the mandrel and the backplate. Step 3 is roller feeding in: the roller starts to move towards the workpiece, and the toolpath is defined by the displacement boundary condition 3. Step 4 is roller moving out: after the spinning process is finished, the roller moves away from the workpiece as the displacement boundary condition 4.

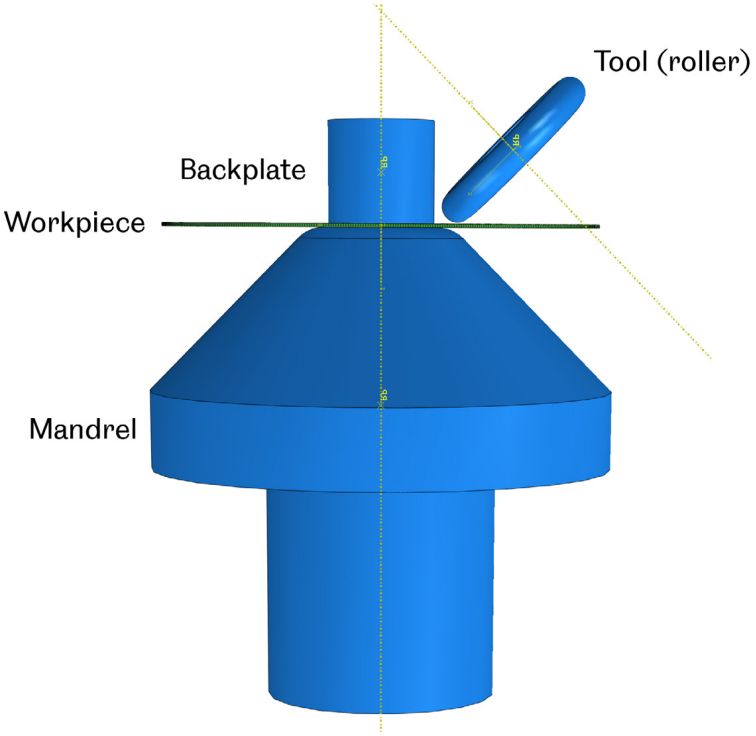

(a)

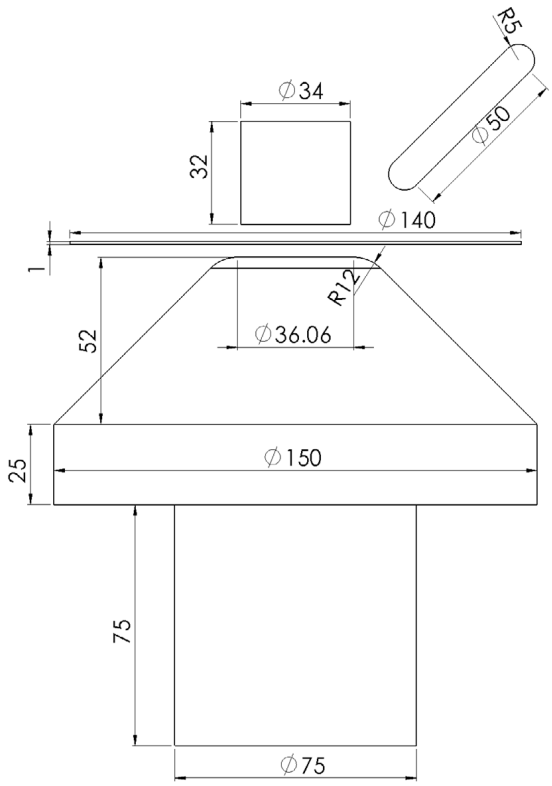

(b)

Figure 3.5 (a) assembly of the spinning FE model and (b) dimensions of the workpiece and spinning tools.

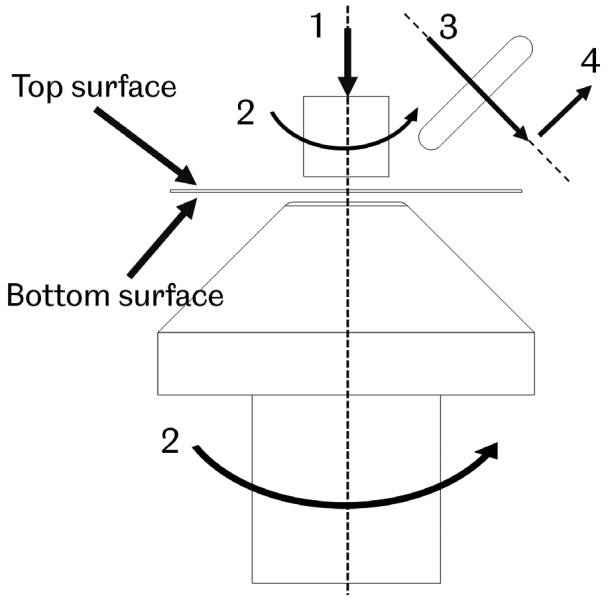

Figure 3.6 Schematic diagram of boundary conditions on the model: 1. 20kN clamping force applied to clamp the workpiece; 2. rotational speed (rad/s) applied to the mandrel and the backplate; 3. roller feeding defined by the displacement and the amplitude table, and 4. roller moving away from the workpiece.

There are three contact interactions: the backplate with the top surface of the workpiece, the roller with the top surface of the workpiece, and the mandrel with the bottom surface of the workpiece. The top and bottom surfaces of the workpiece are shown in Figure 3.6. The contact condition is defined by the penalty contact algorithm and Coulomb's friction law. The friction coefficients between different contact surfaces are listed in Table 3.2. Three frictional coefficients are assigned to the contact interactions between the spinning tools and the workpiece. The frictional coefficient between the roller and workpiece is much smaller than other surfaces (static friction) due to the rotational motion of the roller over the top surface of the workpiece (kinetic friction).

Table 3.2 Coulomb frictional coefficients of contact surfaces [116]

Backplate - Workpiece	Mandrel - Workpiece	Roller - Workpiece
0.5	0.5	0.02

The mass scaling method is applied to the FE simulation to speed up computations without compromising the accuracy of the results [117]. Also, a double-precision mode is used to prevent truncation errors after many incremental time steps to model the spinning process.

The rotational speed of the mandrel and the backplate is defined as 1000 RPM. The toolpath of the roller is a single pass and follows the 45-degree slope of the mandrel, as shown in Figure 3.7. The clearance is the gap distance between the roller toolpath and the mandrel and is also defined by the sine law. Ideally, after the roller works over the workpiece, the thickness of the workpiece would reduce to 0.71 mm from an initial thickness of 1 mm (1.0mm×sin45°). Therefore, the clearance between the roller toolpath and the mandrel is set to 0.71 mm.

Six stages of the spinning process with 1000 RPM mandrel rotational speed and 1.5 mm/rev feed ratio are shown in Figure 3.8. The roller moves along the slope of the mandrel to deform the workpiece incrementally with a constant speed of 1.5 mm/rev and a 0.71 mm clearance. The deformed workpiece is deformed into 0.71 mm thickness and in touch with the mandrel surface, the same as the clearance. The time for the roller to move from the initial to the final location is 2.16 seconds, defined as the processing time. As mentioned in Chapter 1, the feed ratio equals the feed rate divided by the mandrel rotational speed, Equation 3.3. The spinning time is calculated by Equation 3.4. All the spinning cases in this study are simulated with the same mandrel. Hence, the roller moving distance in the axial direction for all the cases is 52 mm, and the roller feeding distance along the 45-degree slope is 73.5mm (52/cos45°), as shown in Figure 3.7.

Table 3.3 Processing parameters of the case used in for validating the FE model

Processing Parameters	Value
Mandrel and backplate rotational speed (RPM)	1000
Workpiece radius R_0 (mm)	70
Workpiece thickness t_0 (mm)	1
Feed ratio f (mm/rev)	1.5
Thickness reduction (mm)	0.29
Clearance (mm)	0.71
Roller processing vertical distance (mm)	52
Processing time (s)	2.16

$$\text{feed ratio } f \text{ (mm/rev)} = \frac{\text{feed rate (mm/s)}}{\text{mandrel speed (rev/s)}}$$

Equation 3.3

$$\text{processing time (s)} = \frac{\text{roller processing distance (mm)}}{\text{feed rate (mm/s)}}$$

Equation 3.4

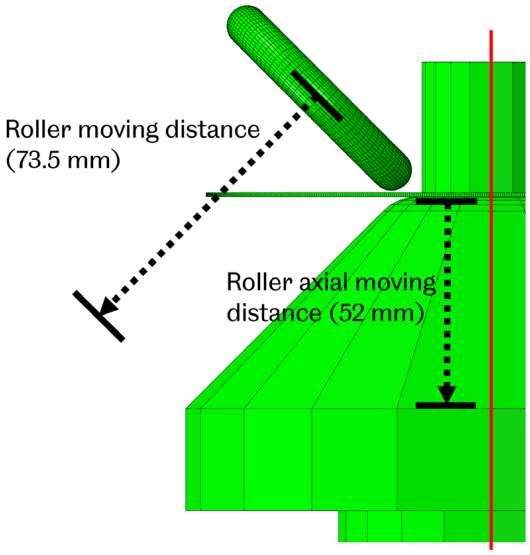

Figure 3.7 Roller moving distance and axial moving distance.

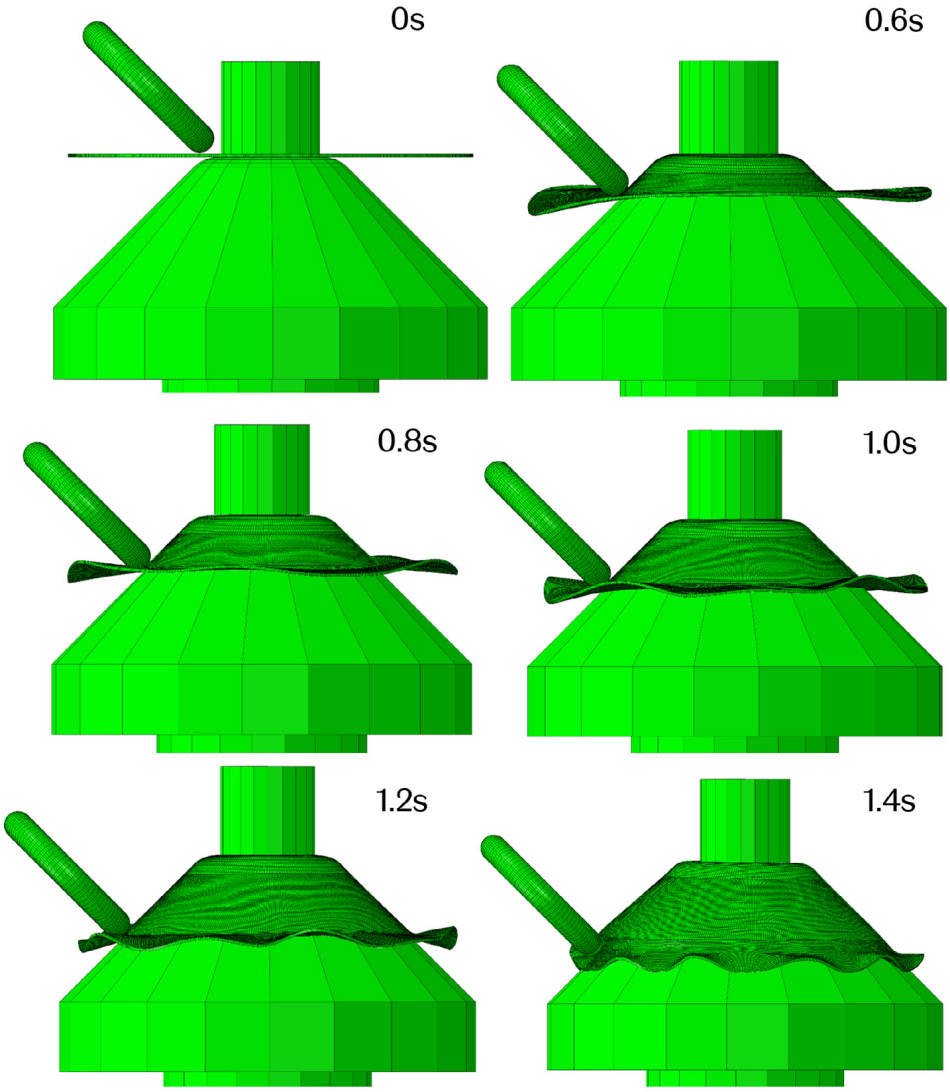

Figure 3.8 Diagrams related to the time history of the spinning process.

3.2 Verification of FE Model

The mesh convergence and mass scaling methods are evaluated in this section. Different results, including wall thickness distribution and the maximum von Mises stress, are selected to validate the spinning FE model.

3.2.1 Development of Meshing Strategy to Prevent Hourglass Issue

A mesh convergence study is conducted, and various meshing strategies are developed to prevent the hourglass problem of using the SC8R element type to model the workpiece. The hourglass affects the accuracy of the modelling results, and the most effective way to solve the problem is to refine the mesh by increasing the mesh density. Three mesh strategies for different zones are shown in Figure 3.10. The detailed parameters of these strategies, the occurrence of the hourglass problem and the CPU time to simulate each case are listed in Table 3.4. The enlarged

view of the connection elements between mesh regions of the workpiece is shown in Figure 3.11.

The sweep meshing strategy is used to mesh the workpiece, as shown in Figure 3.9. The neglected area in the centre of the workpiece is smaller than the clamped area between the backplate and the mandrel. The compression on this central area of the workpiece resulting from the clamping between the backplate and the mandrel only induces a minor deformation to the workpiece in the thickness and other directions. The deformation is neglectable at the centre of the workpiece. Hence, an area with a 10 mm radius is removed and smaller than the diameter of the clamped area of 17 mm; thus, it reduces the number of elements resulting in a shorter CPU time. The technique of neglecting a specific area at the centre of the workpiece was investigated by Sebastiani et al. [118], who concluded that the practical benefits outweighed the negative effects on the numerical results.

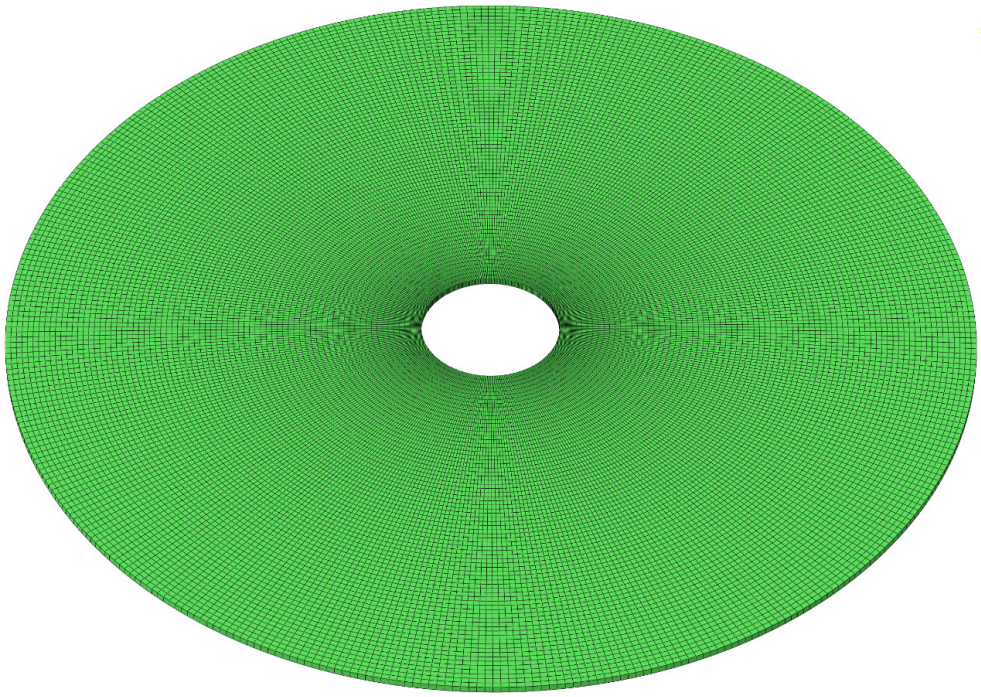

Figure 3.9 Meshed workpiece using sweep meshing strategy.

Increasing the number of circumferential elements as strategies A, B, and C is initially considered to solve the hourglass problem. However, strategy C with 480 circumferential elements still does not have enough elements to overcome the hourglass problem. The CPU time is increased with the number of elements, as shown in Table 3.4. Since the hourglass problem always occurs near the flange of the workpiece, the strategy of meshing the workpiece with different regions is developed. When the number of elements increases using strategy E, the hourglass problem is avoided for both large and small feed ratios applied. When simulating a

spinning model with a relatively low feed ratio, increasing the element number for an even finer mesh using strategy F results in a CPU time longer than 14 days. The computer could not finish such calculations because too many errors accumulated in the random-access memory of the computer, and the simulation was terminated; thus, no results could be obtained.

The hourglass problem has occurred in meshes using strategies A and B regardless of the feed ratios applied. The hourglass problem occurs when low feed ratios are applied in meshed models C and D. Hence, results from meshing strategies D and E are compared when a large feed ratio of 1.5 mm/rev is applied.

Table 3.4 The occurrence of hourglass problem in models meshed by different strategies (large feed ratio: ≥1.0 mm/rev; small feed ratio: <1.0 mm/rev)

Strategy	A	B	C	D	E	F
Number of elements	24000	43200	67200	43600	56800	88750
Region 1 radial elements	100	120	140	35	35	45
Region 1 circumferential elements	240	360	480	200	200	250
Region 2 radial elements	-	-	-	90	60	75
Region 1 circumferential elements	-	-	-	400	400	500
Region 3 radial elements	-	-	-	-	30	40
Region 3 circumferential elements	-	-	-	-	800	1000
Occurrence of hourglass problem on large/small feed ratios	Yes/Yes	Yes/Yes	No/Yes	No/Yes	No/No	N/A
CPU Time (h:m:s)	68:07:03	148:07:22	317:42:36	172:37:22	256:07:22	could not complete

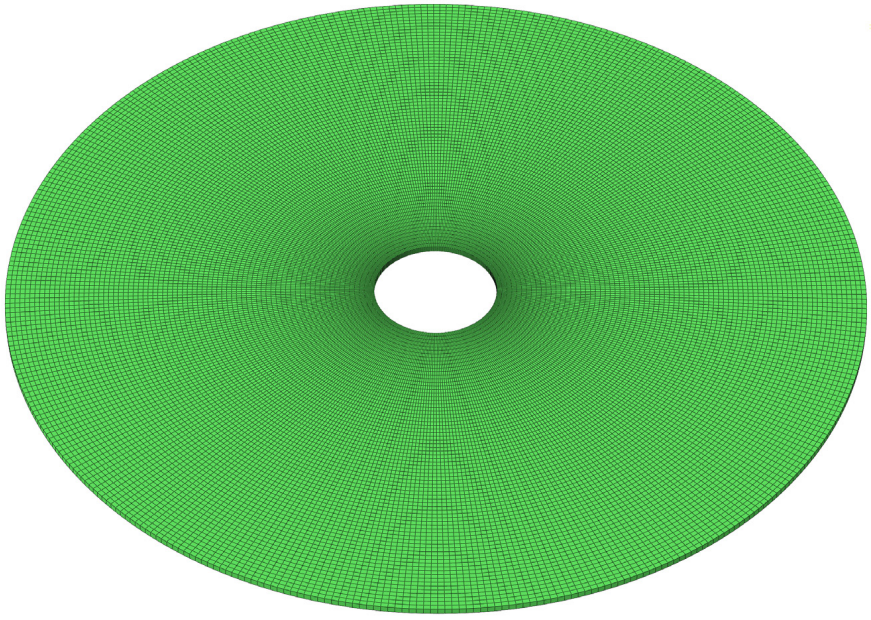

(a)

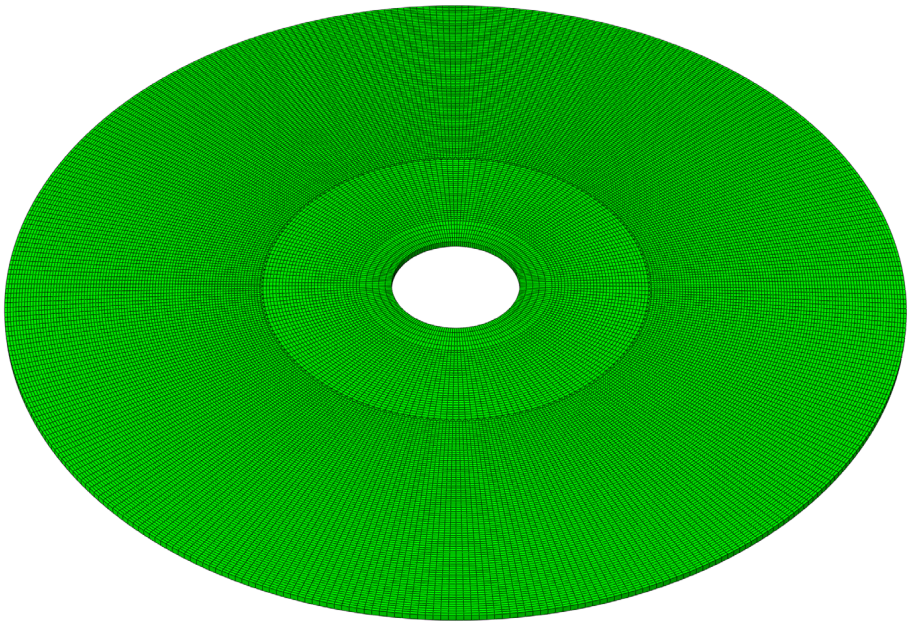

(b)

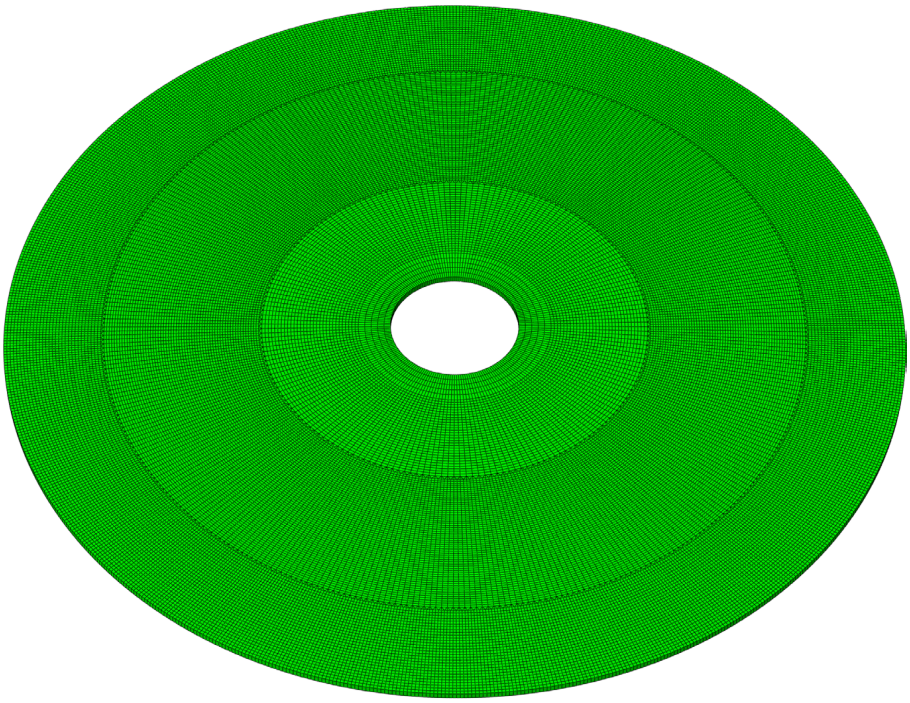

(c)

Figure 3.10 Workpieces meshed by strategy (a) A; (b) D; and (c) E.

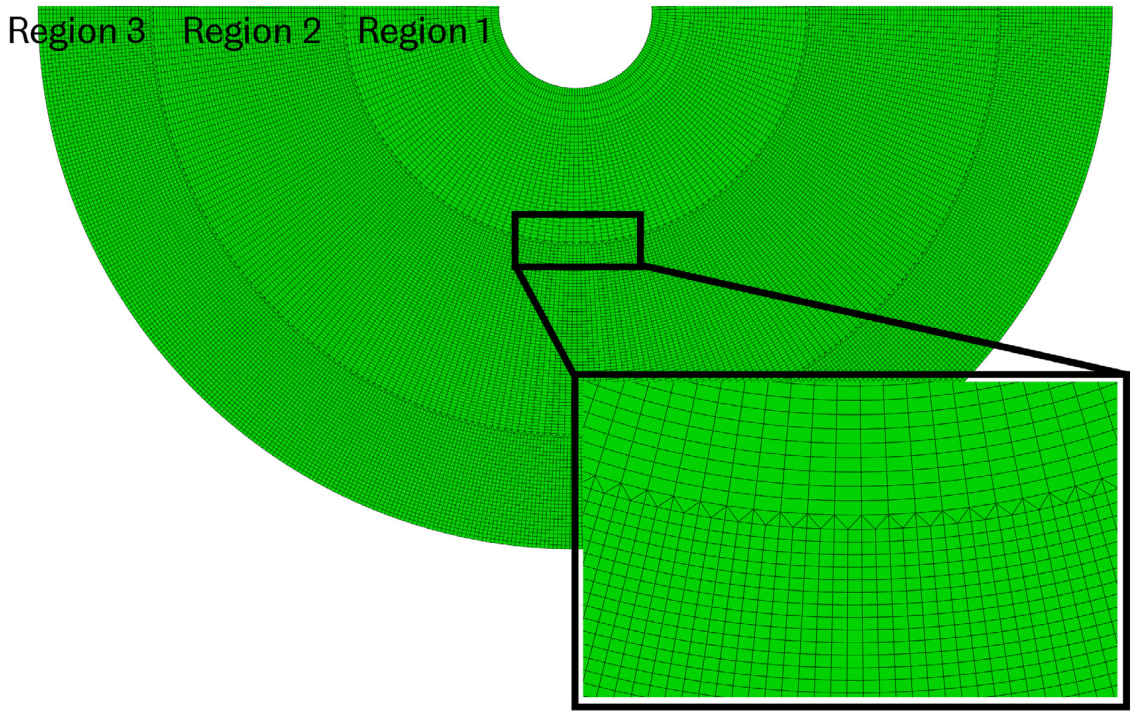

Figure 3.11 Details of meshed elements and connecting elements between different regions.

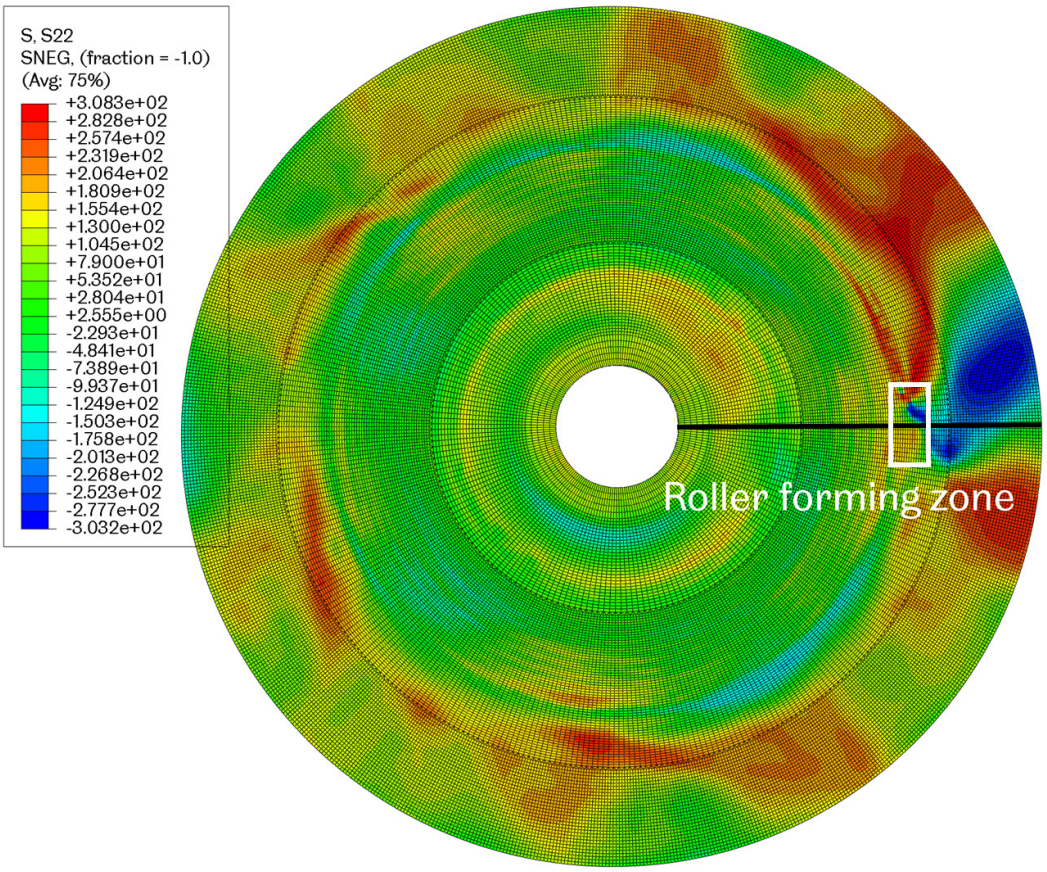

(a)

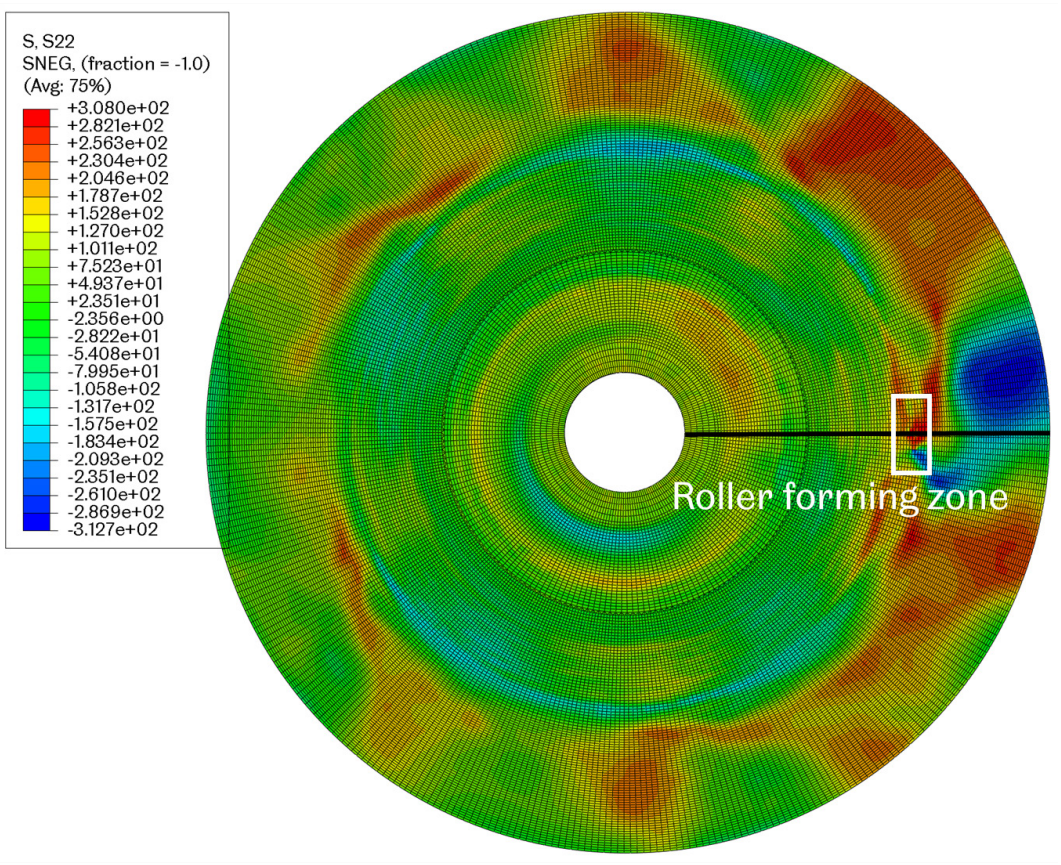

(b)

Figure 3.12 Comparison of the circumferential stress distribution on the workpiece meshed by (a) strategy D and (b) strategy E.

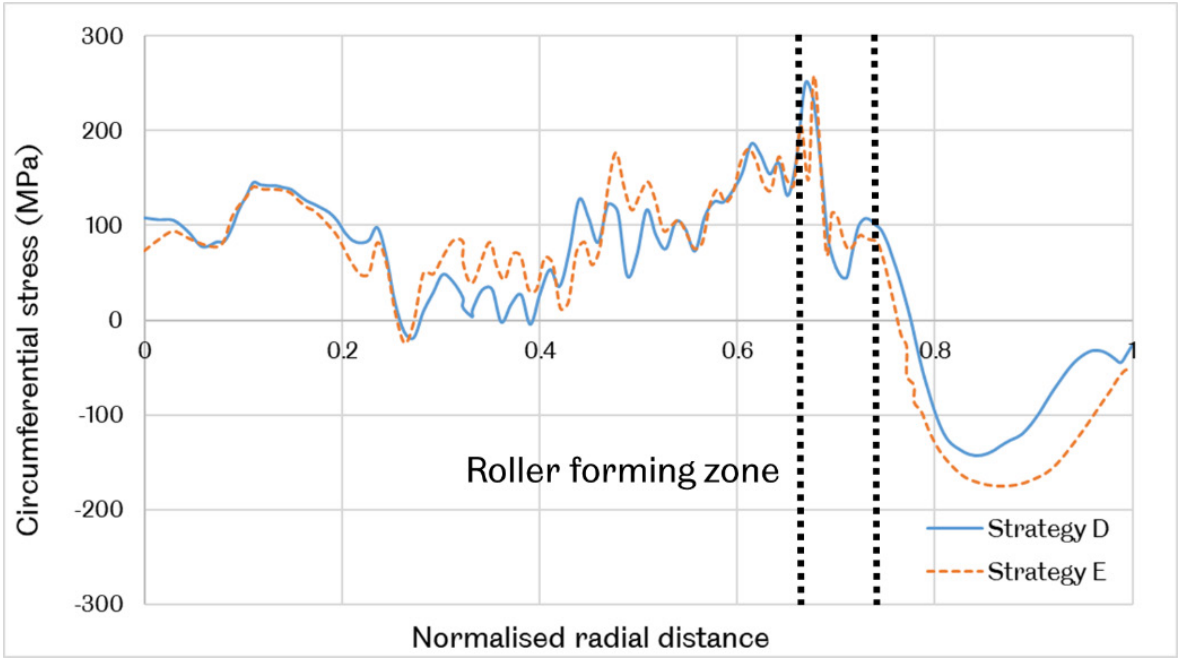

Figure 3.13 Comparison of the circumferential stress on the normalised radius of the workpiece.

Similar circumferential stress distribution results are observed in the radial direction, as shown in Figure 3.12. The stress results obtained from the nodes in the radial direction are marked by the black lines in Figure 3.12 (a) and Figure 3.12 (b), further converted to the normalised radius, as shown in Figure 3.13. The stress fluctuations are very similar, with the corresponding minimum and maximum stress results from meshing strategies D and E being –142.94 and –174.98 MPa; 250.055 and 257.609 MPa, respectively. As plotted in Figure 3.13, the stress results of two different meshes show very good agreement in the roller forming zone, where the maximum difference is around 10%.

Good agreement is also obtained for the thickness distribution results in the radial direction of the workpiece between meshing strategies D and E, with the maximum difference being 4.1% only, as shown in Figure 3.14. Two thickness distribution curves from meshing strategies D and E almost coincide with each other. The corresponding minimum and maximum thickness results are 0.742mm and 0.741mm; 1.00885mm and 1.00758mm, respectively, almost identical.

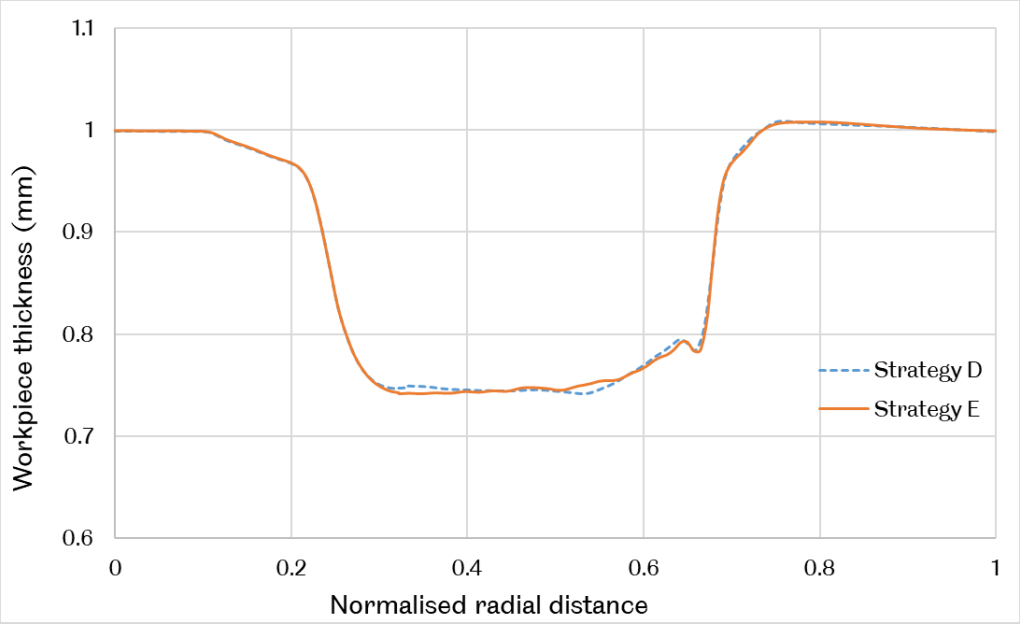

Figure 3.14 Thickness distribution comparison on normalised workpiece radial direction.

Comparing the circumferential stress and the thickness distribution results of the nodes in the radial direction shows that sufficient mesh convergence is achieved by both meshing strategies D and E. However, the hourglass problem still occurs on a few elements meshed by strategy D under relatively small feed ratios. Although strategy D is suitable for modelling spinning processes using large feed ratios, strategy E is selected for all the FE models due to the need to apply low feed ratios in this study, resulting in a longer CPU time to complete FE spinning process modelling but achieving better simulation accuracy.

3.2.2 Assessment of Mass Scaling Effect

The FE model used to validate the mass scaling factor in shear spinning applies 1000 RPM mandrel speed and 1.5 mm/rev feed ratio. This model is chosen because severe wrinkling failure occurs, and the workpiece is excessively distorted as a complicated case representing all types of conditions requiring consideration. A model without applying the mass scaling method (mass scaling factor equals zero) is first established as a benchmark for reference. Then mass scaling factors of 9, 16, 36, 49, and 64 are applied to the FE models to test which mass scaling factor could satisfy two criteria. The energy ratios using time history data under different mass scaling factors are shown in Figure 3.15. The black line marks the 0.1 upper limit of the energy ratio curves. This model, with 1000 RPM mandrel speed and 1.5 mm/rev feed ratio, failed at 1.5 seconds because of excessive distortion. Hence for the energy ratio lines, at least two-thirds (1.0 seconds) of the processing time (step time) should be below the 0.1 upper limit. Among all the models, the model using mass scaling factor 64 exceeds the upper limit, and the model with factor 49 barely meets the criteria, as shown in Figure 3.15. In contrast, the artificial strain and internal energy ratios using all other mass scaling factors are below 0.05 throughout the entire processing time, as shown in Figure 3.16. Hence, a mass scaling factor of 36 is proven to be sufficiently accurate and thus is applied to all the spinning FE simulation models.

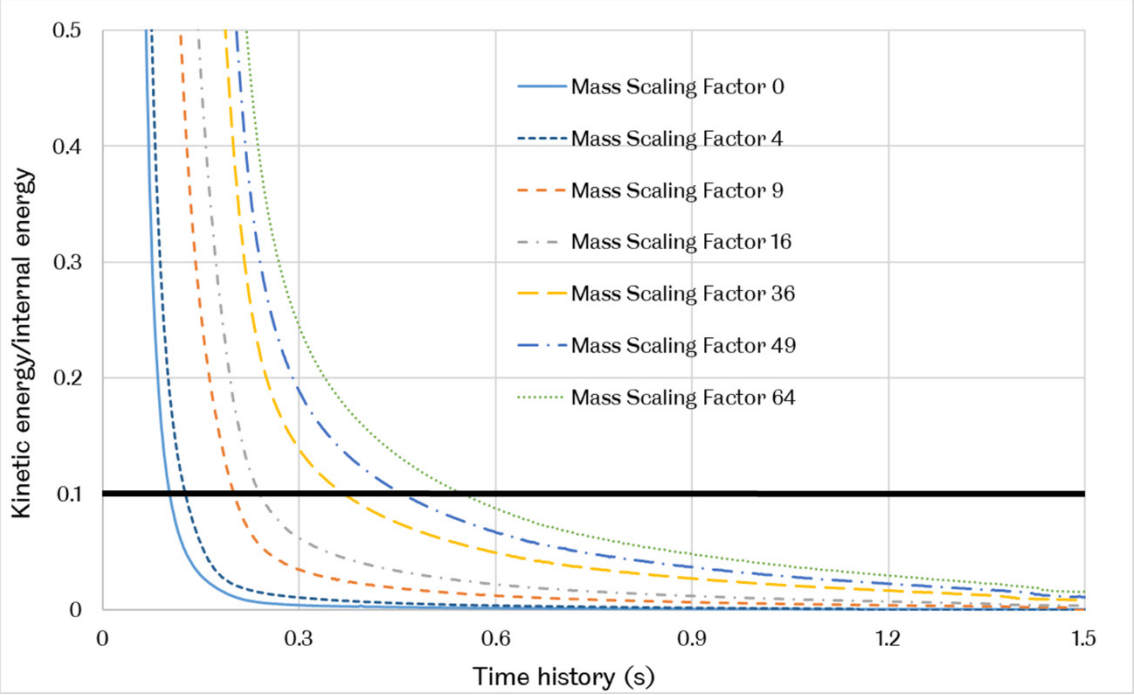

Figure 3.15 The kinetic/internal energy ratio using time history data under different scaling factors.

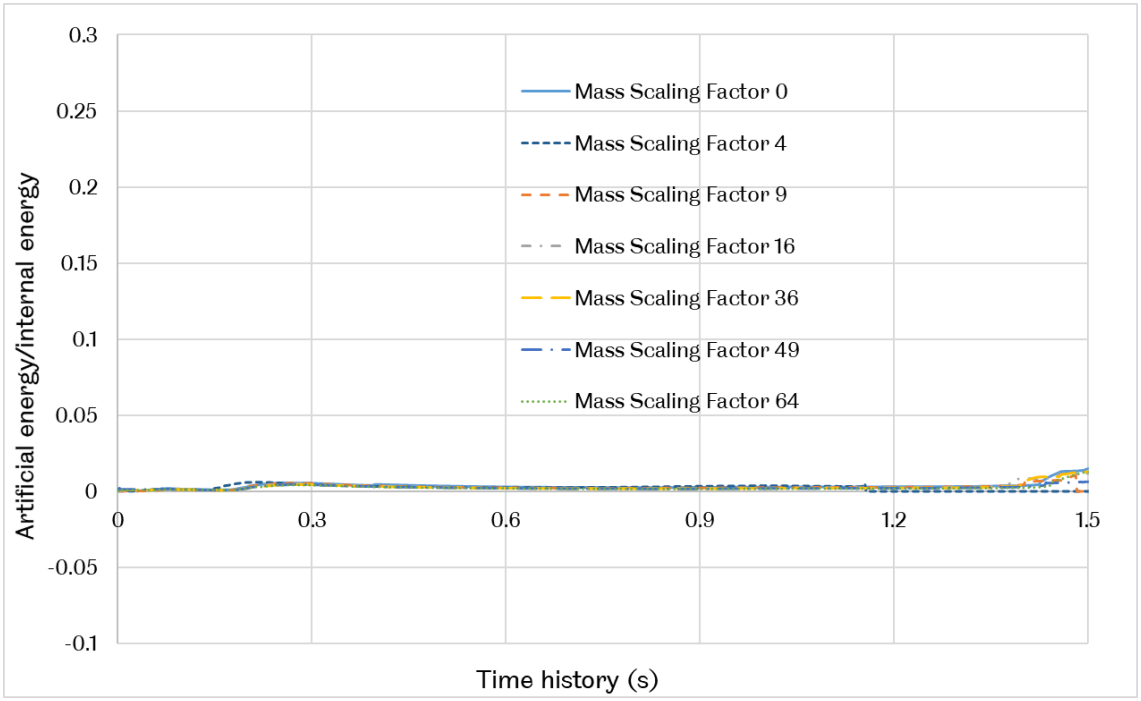

Figure 3.16 The artificial/internal energy ratio using time history data under different scaling factors.

3.3 FE Modelling Results and Discussion

This section presents FE results analysis and discussion to develop an in-depth understanding of material deformation mechanics related to wrinkling in the spinning process. A unique variable, the height of a displaced node of the workpiece surface in the Y-axis, is defined. The Y-axis is the vertical direction of the mandrel, as shown in Figure 3.17. The height is defined as the Y-coordinate in mm, measured from the bottom of the mandrel where Y = 0 mm and the initial height of the top surface of the workpiece is Y = 154 mm. Since there is no standard to determine the severity of the wrinkling nor method to quantify the wrinkling, the Y-coordinate (height) of the nodes on the wrinkled area is used to describe the wrinkling.

Limited literature analysed the shear spinning process in detail, not as detailed as investigated in this study. In this investigation, the stress and strain results of various deformation areas of the workpiece at different spinning stages are extracted from FE simulations and are compared to evaluate the thickness distribution of the workpiece. These results will be used to direct the development of the wrinkling testing method in Chapters 5 and 6. The local coordinate system is established according to the local orientation of the material deformation of every element and node of the workpiece for evaluating results locally; instead of analysing results obtained from the global coordinate system.

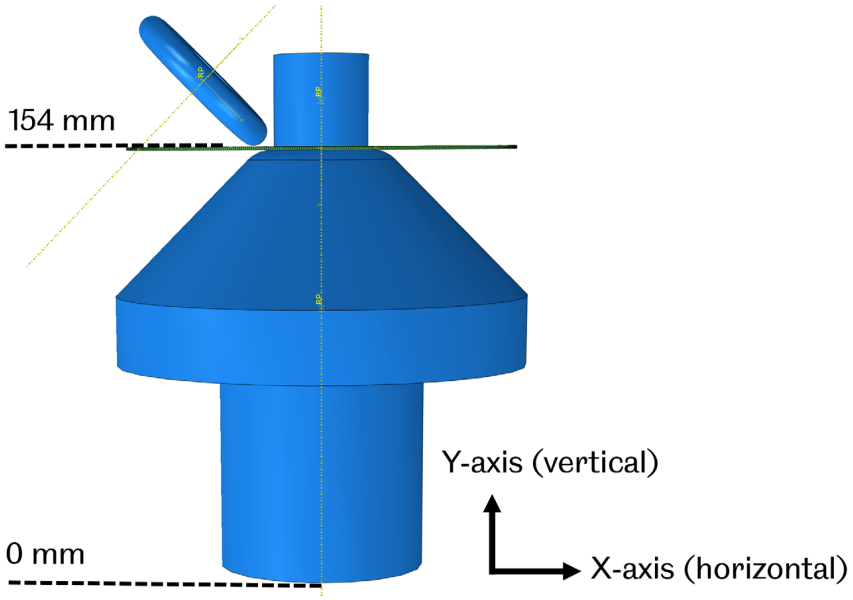

Figure 3.17 The Y-axis (vertical) and the X-axis (horizontal) directions.

3.3.1 Strain Rate Effect

Although the mandrel rotational speed is usually considered to have no significant impact on the wrinkling severity and thus the FE results [15], it is essential to confirm this assumption before analysing detailed stress and strain results. FE models using different mandrel rotational speeds are compared to prove that the mandrel rotational speed does not significantly affect the onset of wrinkling if the feed ratio remains constant. The mandrel speeds and feed ratios applied in the spinning simulation of the AA5251 aluminium are listed in Table 3.5. The wrinkling occurrence and whether the modelling process is completed without excessive mesh distortion caused by wrinkling failure are also recorded.

As listed in Table 3.5, different feed ratios and mandrel rotational speeds are used in different spinning process models. Similar to the findings of the previous studies [15][14][16], it has been found in this study that the feed ratio affects the wrinkling onset timing and the severity in the subsequent process. The roller feed rates must be changed accordingly by applying identical feed ratios but using different mandrel rotational speeds in the spinning simulations. Therefore the material deformation rate (strain rate) may be investigated. For example, Model No. 10 uses a feed ratio of 1.5 mm/rev and a mandrel rotational speed of 1000 RPM. The spinning processing time is 2.16 seconds, but it is 10.8 seconds for Model No. 1 with a 1.5 mm/rev feed ratio and 200 RPM mandrel rotational speed. The FE results relevant to wrinkling, for example, the time of wrinkling occurrence, the strains of the wrinkled area of the workpiece and whether the modelling could be completed without excessive mesh distortion, should be similar if different mandrel rotational speeds do not affect the

onset and the severity of the wrinkles. FE models No. 1 and No. 10 have the same feed ratio but different mandrel rotational speeds. The roller feed rates and the spinning times are linearly related, determined by Equation 3.3 and Equation 3.4, respectively. The roller feed rate of the 200 RPM in FE model No. 1 is 1/5 of that of the 1000 RPM in FE model No. 10. Thus, the spinning time of Model No. 1 is five times longer. In other words, if the strain rate does not affect wrinkling in spinning, all relevant FE results at the corresponding spinning time of these two models would be similar. For example, the workpiece is excessively distorted at 7.17s in the 200 RPM model and 1.43s in the 1000 RPM model, shown in Figure 3.18. The corresponding spinning time is almost exactly five times. Also, the workpiece thickness is constrained to 1 mm to eliminate the thickness-related factors. Including multiple thicknesses will excessively increase the workload of spinning FE simulation and test. The strain result related to the wrinkling deformation on the workpiece with 1 mm thickness is investigated thoroughly as a novelty of this project, which is not reported in the previous literature. The spinning process with multiple workpiece thicknesses and various geometries can be investigated in future work.

Table 3.5 Processing parameters of shear spinning simulation using AA5251 aluminium.

No.	Mandrel rotational speed (RPM)	Roller feed ratio (mm/rev)	Sheet thickness (mm)	Wrinkling (Y/N)	Modelling completion (Y/N)	Spinning time (s)
1	200	1.5	1	Y	Y	10.8
2	1000	0.3	1	N	Y	10.8
3	1000	0.4	1	N	Y	8.1
4	1000	0.5	1	Y	Y	6.48
5	1000	0.75	1	Y	Y	4.32
6	1000	1.0	1	Y	Y	3.24
7	1000	1.25	1	Y	Y	2.592
8	1000	1.3	1	Y	N	2.492
9	1000	1.4	1	Y	N	2.016
10	1000	1.5	1	Y	N	2.16

In addition to comparing the time of the wrinkling failure occurrence in the spinning process, the nodes on the workpiece edge along the circumferential direction are selected to extract the node height using the Y-coordinate to prove the strain rate does not affect the results related to wrinkling. The nodes on the top surface of the workpiece are selected, and a detailed view is shown in Figure 3.19.

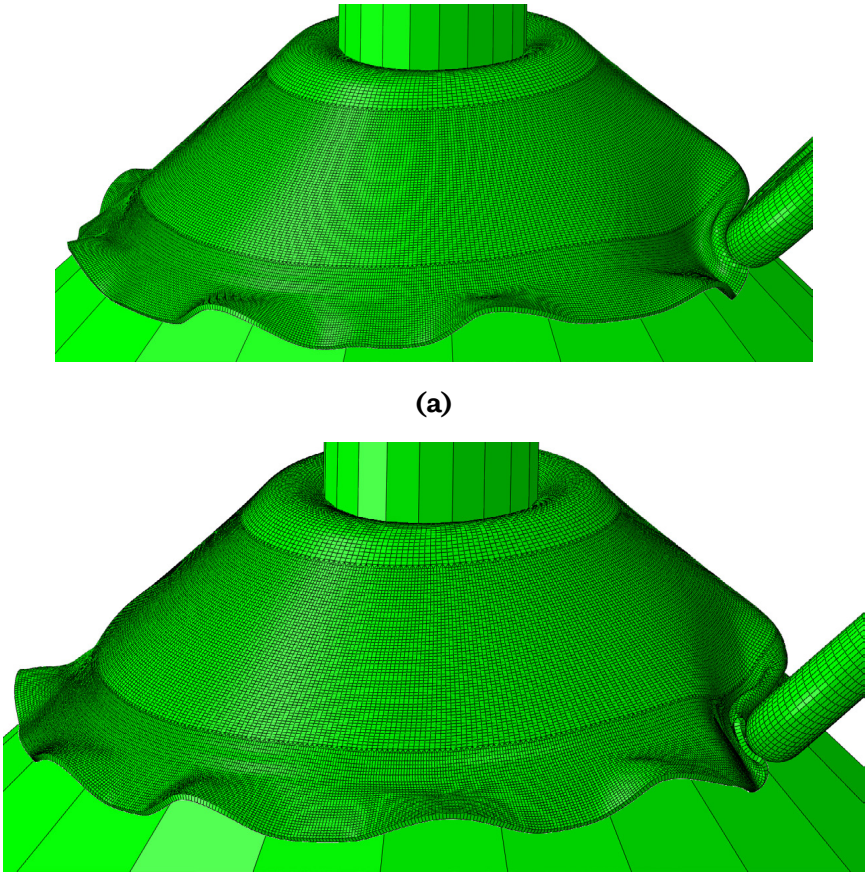

Figure 3.18 Excessive distortion caused by roller working over severe wrinkling waves at the spinning time (a) 7.17s for FE model No. 1 of mandrel speed of 200 RPM and (b) 1.43s for FE model No. 10 of mandrel speed of 1000 RPM.

In the spinning process, the wrinkling always occurs around the circumference of the workpiece flange as a form of wrinkling waves with tops and bottoms, as shown in Figure 3.20. The wrinkling top is the node with the greatest height on the Y-axis, as defined in Figure 3.17, and the wrinkling bottom is the node with the lowest height near the wrinkling top. Y-coordinates of the nodes at different spinning times are compared, as shown in Figure 3.21, between Model No. 10 (1000 RPM mandrel rotational speed) and Model No. 1 (200 RPM mandrel rotational speed) with the same feed ratio of 1.5 mm/rev). The two curves of the Y-coordinates are plotted to describe the wrinkling tops and bottoms formed in the wrinkled zone on the edge of the workpiece.

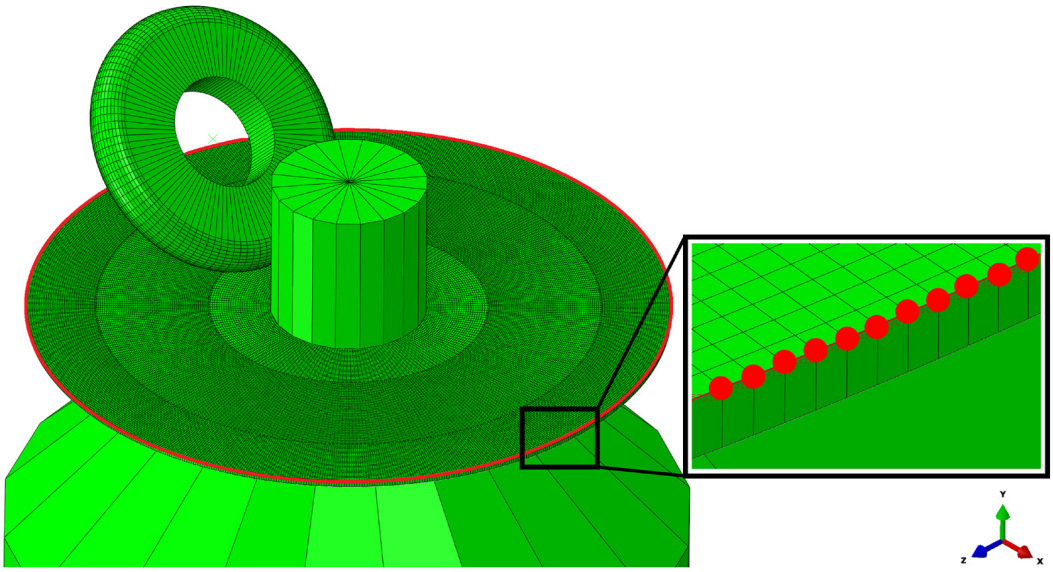

Figure 3.19 A detailed view of node selection along the circumference edge of the workpiece.

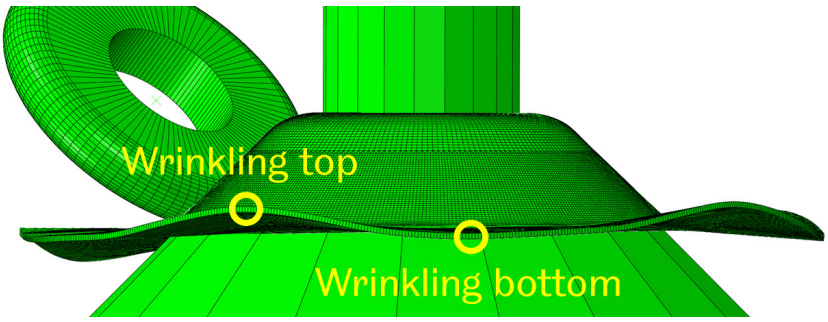

(a)

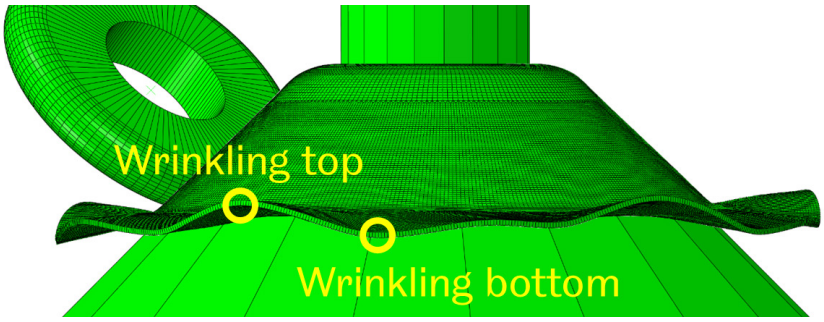

(b)

Figure 3.20 Wrinkling wave top and bottom in (a) the early stage and (b) the late stage of the spinning process.

The timing 5.0s for Model No. 1 and 1.0s for Model No. 10 in Figure 3.21 (a) is at the early stage of the spinning process, shortly after the wrinkling occurs. The maximum and minimum Y-coordinates, the height of the relevant nodes, indicate the wrinkling top and bottom of a wrinkling wave, as marked on the curve in Figure 3.21 (a). In general, the lowest point of the Y-coordinate curve indicates the current roller

location, as marked in Figure 3.20 (a), due to the roller constantly working over the workpiece and inducing bending to the flange material of the workpiece. However, the height of the nodes near the current roller location is smaller because the material is overly bent around the roller. The elastic deformation in the local zone affected by the roller will recover after the roller moves away. The height of the overly bent nodes increases and return to normal, matching the height of nearby nodes on the other wrinkling waves. The height of the wrinkling tops and bottoms, ranging from 125 to 135 mm, indicates the severity of the corresponding wrinkling wave. The greater difference in height between the tops and bottoms, the more severe the wrinkling waves are. The number of wrinkling tops on the curve is regarded as the number of wrinkling waves.

The number of wrinkling waves of the two models is different from the early spinning stage at 5.0s and 1.0s. There are eight wrinkling tops (waves) for the 200 RPM model (FE model No. 1) and seven for the 1000 RPM model (FE model No. 10). As the spinning process proceeds, the number of wrinkling waves in both FE models becomes the same at time 6.0s/1.2s, as shown in Figure 3.21 (b); they are also reasonably close at time 7.0s/1.4s, as shown in Figure 3.21 (c). The maximum and minimum heights are even closer, and the curves almost coincide at 7.0s/1.4s, as shown in Figure 3.21 (c). Two models correlate well as the deviations between the maximum, and the minimal heights are within 2 mm in the late spinning stage.

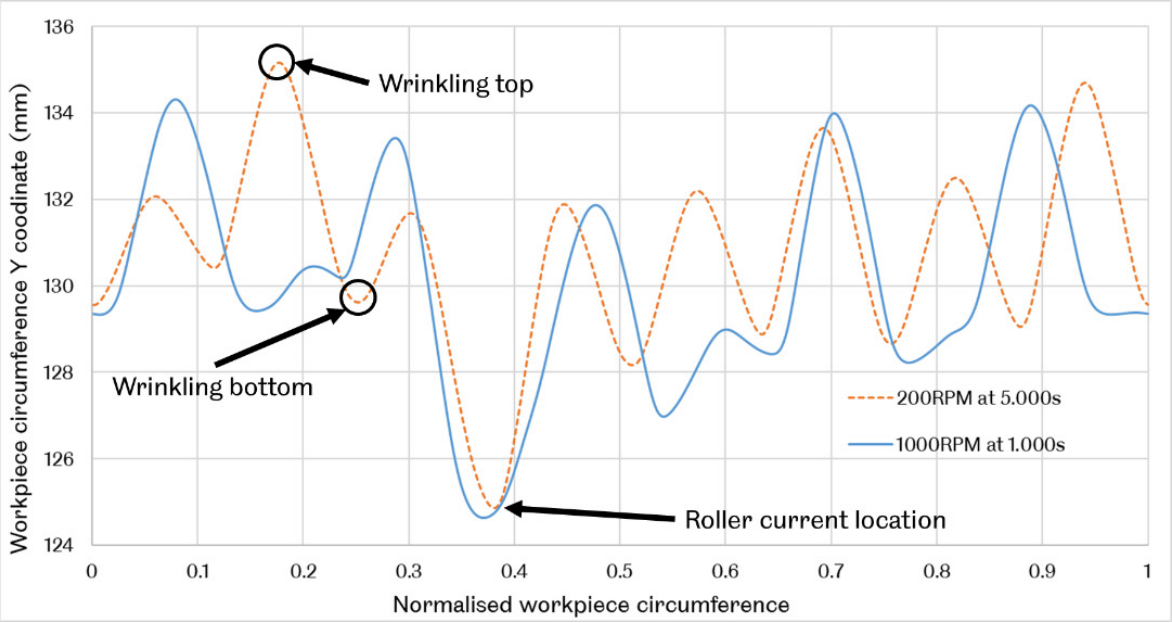

(a)

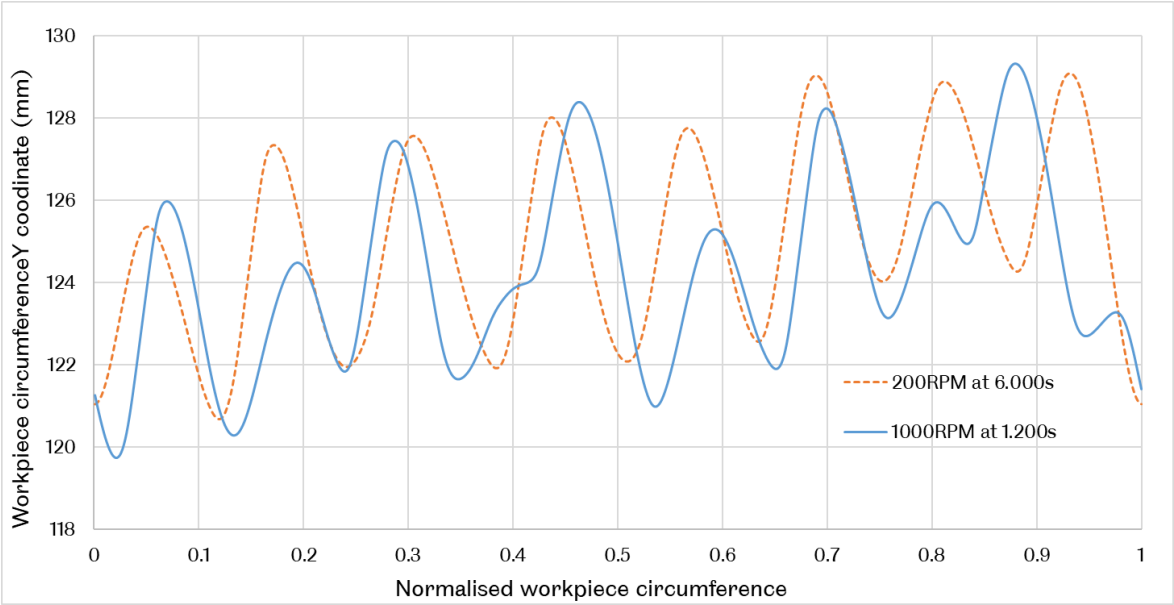

(b)

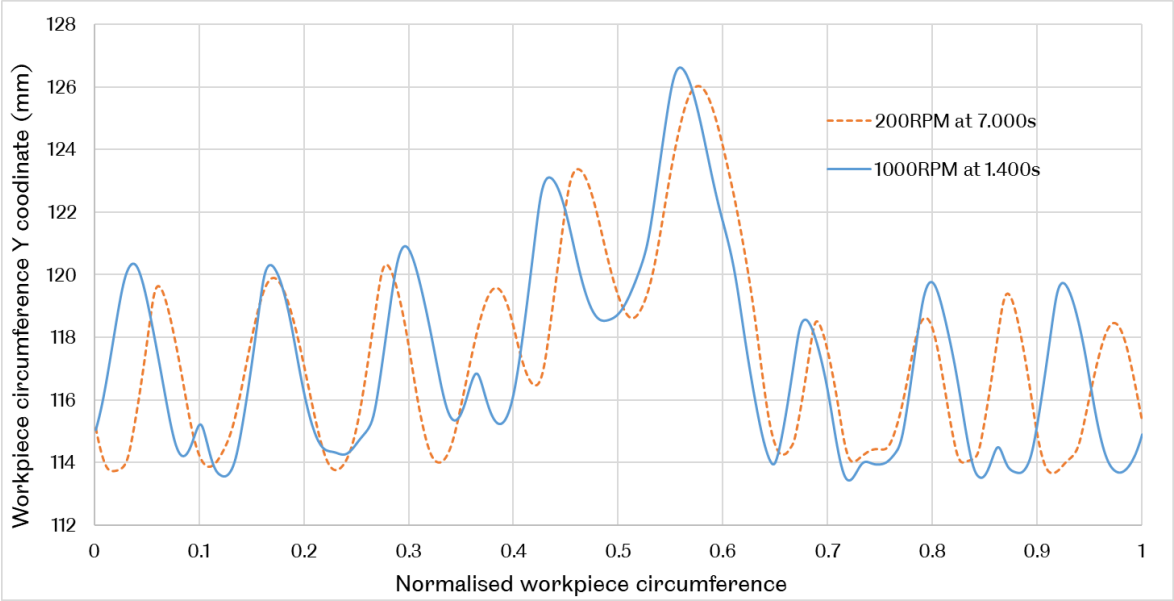

(c)

Figure 3.21 Heights of the workpiece circumference edge at different times: (a) at 5.0s/1.0s; (b) at 6.0s/1.2s, and (c) at 7.0/1.4s of FE model No.1 of mandrel speed of 200 RPM and FE model No.10 of mandrel speed of 1000 RPM.

Based on the results of wrinkling wave tops and bottoms, it may be concluded that the strain rate does not affect the wrinkling occurrence in spinning, and the early assumption can be considered valid. In the subsequent investigation related to the wrinkling mechanism, extracted results from FE models with the same mandrel rotational speed, for example, models with 1000 RPM, can be considered valid and representative of other FE models of different mandrel rotational speeds, as long as the feed ratio remains the same between these models.

3.3.2 Wrinkling Wave Amplitude Analysis

To obtain comprehensive results, FE model No.10 using 1000 RPM mandrel rotational speed and a 1.5 mm/rev feed ratio with 1 mm workpiece thickness is selected for detailed analysis because it involves both wrinkling and excessive mesh distortion.

There is no existing standard to decide whether the wrinkling is initiated in the spinning process. Initially, the idea is to determine the wrinkling occurrence time to distinguish it from the wrinkling-free state. However, by observing the FE results, it is difficult to identify the time and whether the workpiece has been wrinkled already. For example, the wrinkling waves in the early stage are difficult to be identified, as shown in Figure 3.22. Hence, a reverse tracing method is used to determine the wrinkling time in order to output the FE results for analysis. The results analysis starts when the workpiece is wrinkled most severely, and the analysing procedure is to gradually trace back from the most severely wrinkled time to the wrinkling initiation time.

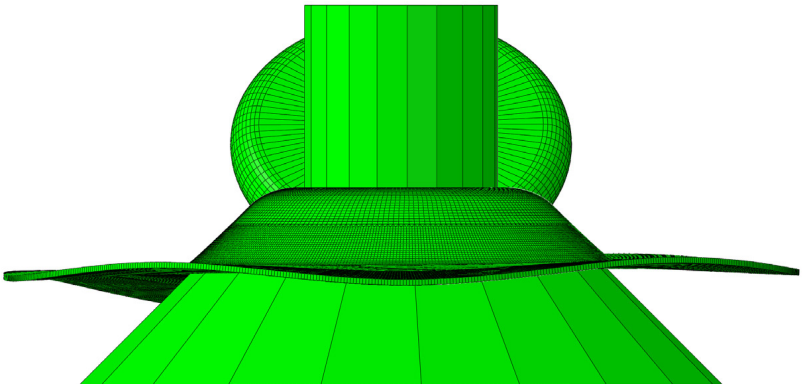

Figure 3.22 Wrinkling waves in the early stage of the spinning process.

In FE model No. 10 (mandrel speed 1000 RPM and feed ratio 1.5 mm/rev), the mesh of the workpiece is excessively distorted at 1.425s. Before the excessive distortion occurs, the wrinkling wave amplitude reaches the maximum value at 1.373s, which is the time of the 23rd revolution of the workpiece, as shown in Figure 3.23. For FE result analysis, two node sets on wrinkling top and bottom lines are selected.

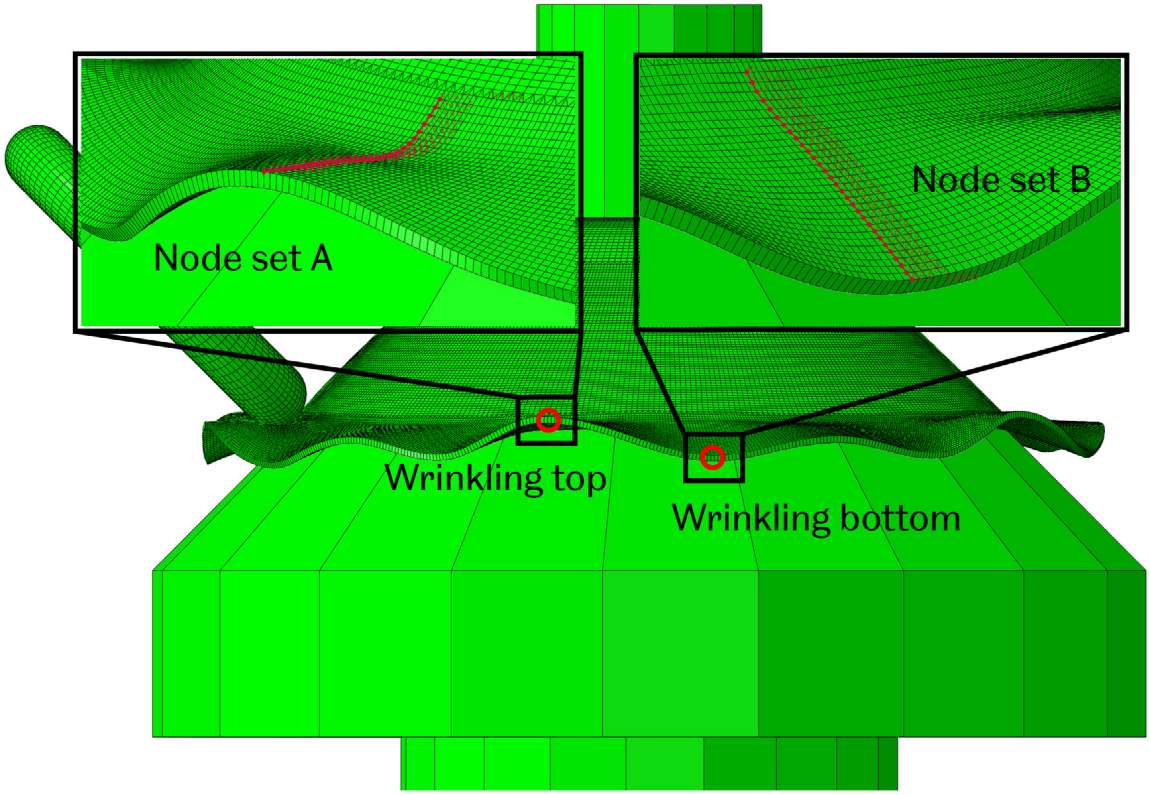

Figure 3.23 Selected nodes along the wrinkling top and bottom lines.

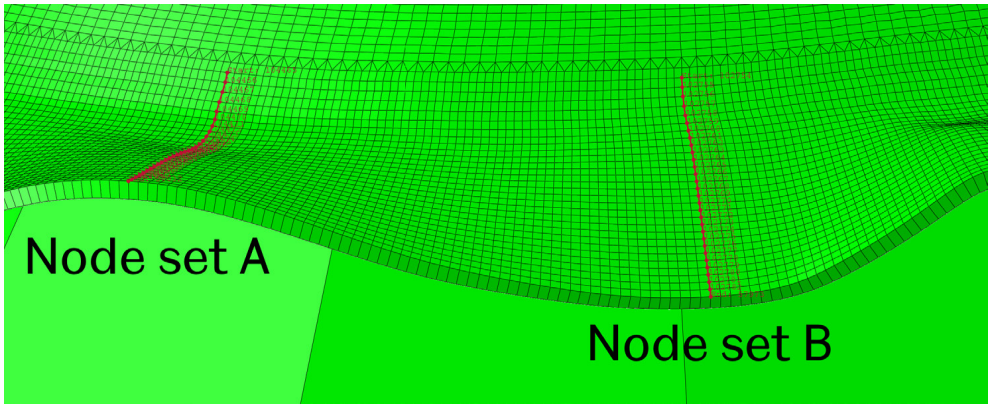

(a)

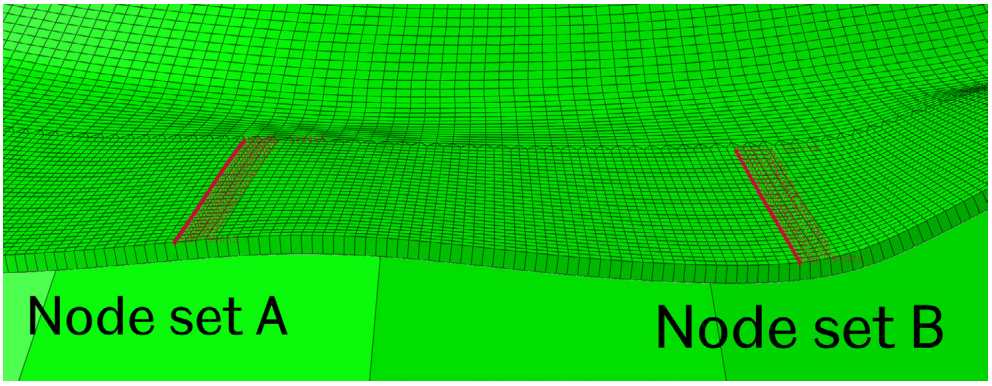

(b)

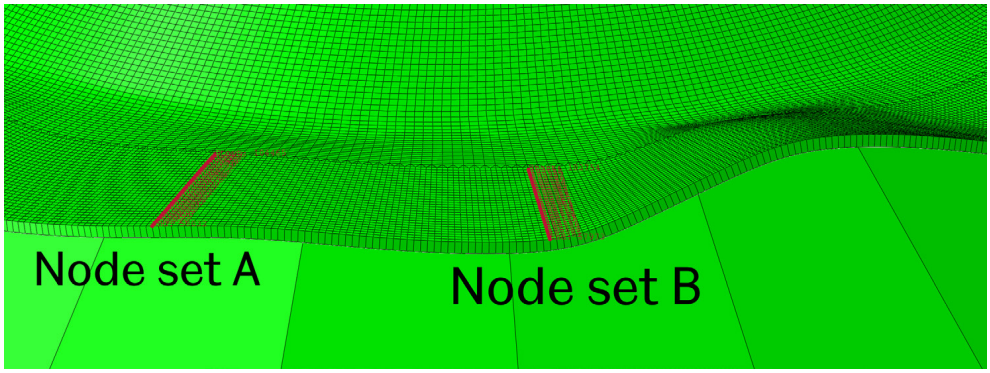

(c)

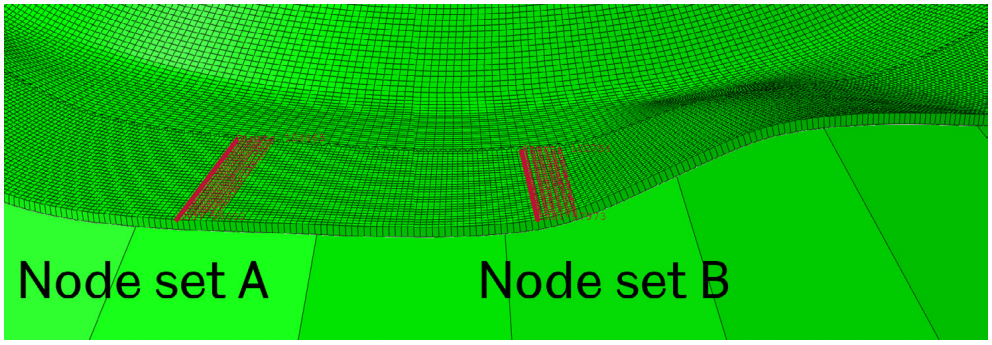

(d)

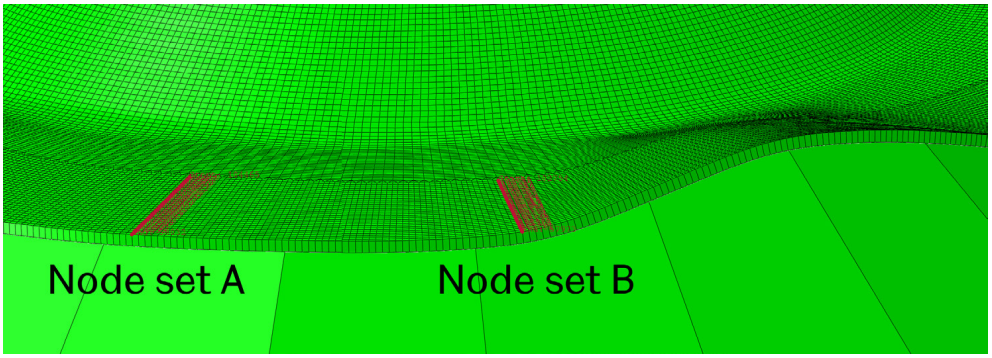

(e)

Figure 3.24 Deformation of the node sets A and B at (a) 1.373s (23th revolution), (b) 1.073s (18th revolution), (c) 1.103s (17th revolution), (d) 0.9525s (16th revolution) and (e) 0.8925 (15th revolution) in FE model No.10 with 1000 RPM mandrel speed and 1.5 mm/rev feed ratio.

A noticeable feature is that the node sets A and B, as shown in Figure 3.23, do not always coincide with the wrinkling top and bottom lines at different times during the spinning process, as shown by zoom-in views in Figure 3.24. The deformation of the wrinkling top and bottom lines is constantly changing as the spinning process proceeds. Node sets A and B only coincide with the wrinkling top and bottom line at 1.373s, as shown in Figure 3.24 (a). For a model with 1000 RPM, each roller revolution takes 1/16.667s, which is 0.06s. Hence the roller enters the 23rd revolution at 1.373s

after completing the 22nd revolution. Node sets A and B do not coincide with any wrinkling top and bottom lines before the process proceeds to 1.373s. The node set A is not located on the wrinkling top line at 1.073s on the 18th revolution, five revolutions prior, as shown in Figure 3.24 (b). The material wrinkling around the node set A is also less severe before 1.373s, as shown in Figure 3.24 (b) and Figure 3.24 (c). The wrinkling wave is barely noticeable at 1.013s (17th revolution) in Figure 3.24 (d), and node set A is completely flat at 0.8925s in Figure 3.24 (e).

Although a wrinkling wave already formed at the right-hand side of the node sets A and B at the early spinning stage, as shown in Figure 3.24 (e), the wrinkling wave is still formed on node sets A and B later in the process. The observation indicates that the wrinkling waves form in a sequence at different times; the wrinkling waves do not form simultaneously. Furthermore, the wrinkling top line on an already formed wrinkling wave is constantly changing when the spinning process proceeds, as shown in Figure 3.25. The node set C coincides with the wrinkling top line at 0.8925s and moves in the anti-clockwise direction. At 1.373s, as shown in Figure 3.25(d), it can be noticed that node set C is moving away from the current wrinkling top line node set A. The movement of the wrinkling wave tops of the workpiece follows the opposite direction to the relative roller rotating direction, as shown in Figure 3.26. The workpiece rotates with the clamp and mandrel in the anti-clockwise direction; hence the relative roller rotating direction is clockwise and moves towards the left-hand side.

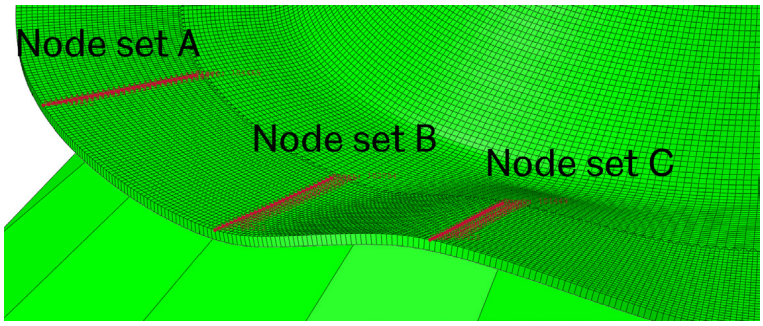

(a)

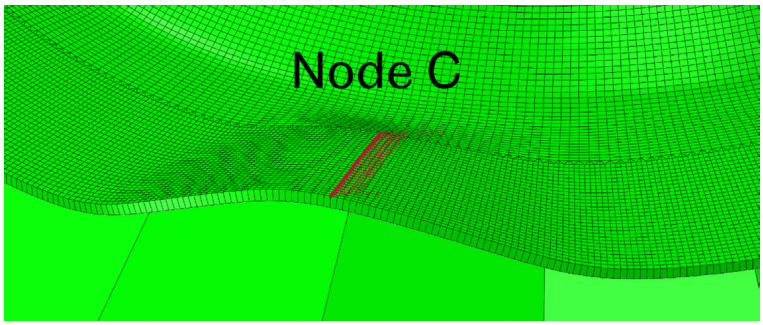

(b)

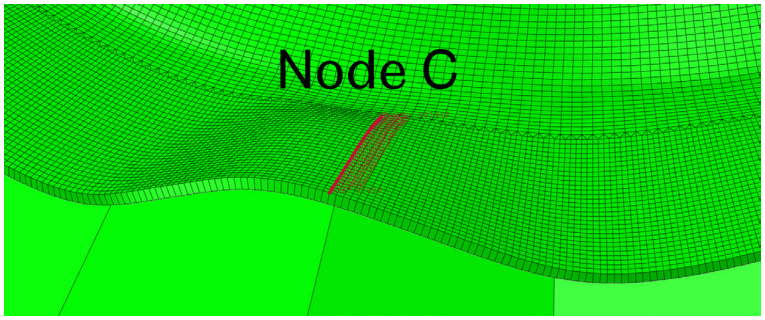

(c)

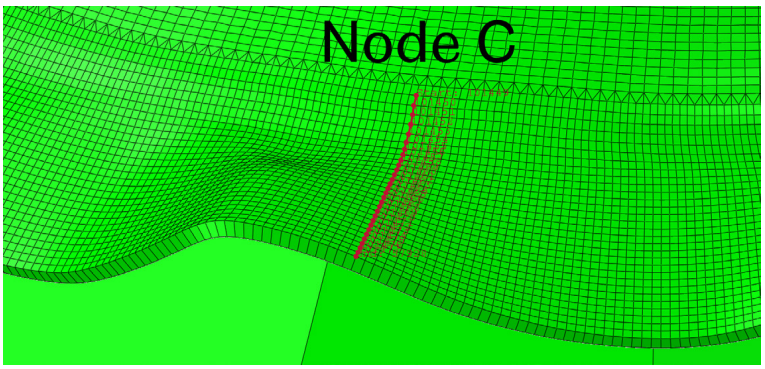

(d)

Figure 3.25 Deformation of the node set C on a different wrinkling top near node sets A and B (a) at 0.8925s (15th revolution); (b) at 1.013s (17th revolution); (c) at 1.133s (19th revolution) and (d) at 1.373s (23rd revolution) in FE model No. 10 with mandrel speed 1000 RPM and feed ratio 1.5 mm/rev.

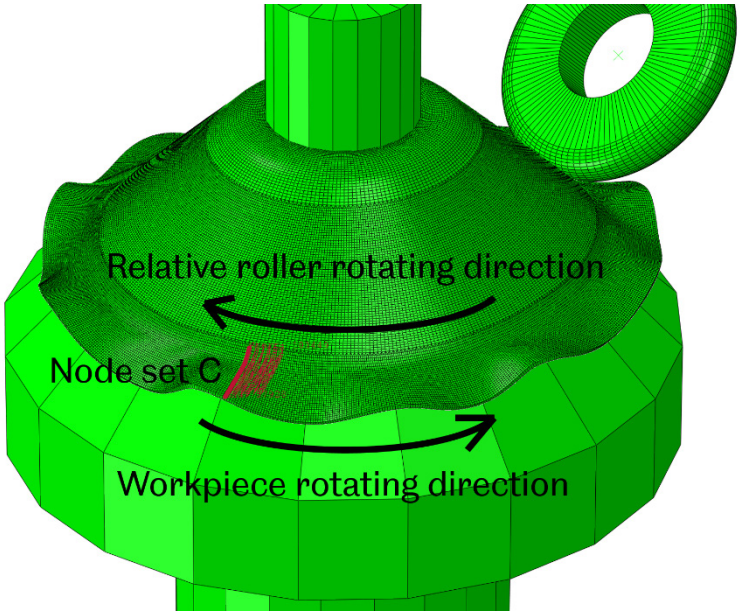

Figure 3.26 Workpiece rotating direction and relative roller rotating direction at 1.373s.

After the wrinkling happens, a series of wrinkling waves are formed on the edge of the workpiece. However, there is no standard method to determine what level of deformation is categorised as wrinkling occurrence or quantify its severity. Only a

handful of studies developed wrinkling tests, such as the Yoshida wrinkling test. In the Yoshida wrinkling test [107], the wrinkling height was used to quantify the wrinkling. The displacement sensor was placed above the specimen and detected the displacement of the specimen. The displacement was regarded as the wrinkling height since the material buckled upwards when wrinkling happened. Therefore, this definition of wrinkling height is inherited in the current study and further extended to the wrinkling wave amplitude in the spinning process. The wrinkling wave amplitude of a node is the difference between the height of the node and the reference height, as shown in Figure 3.27. The yellow dashed line in Figure 3.27 is the reference height line marking the ideal location of the workpiece circumference edge if wrinkling does not happen. If there are no wrinkling tops and bottoms in a wrinkling-free spinning, the wrinkling wave amplitude would be zero. The maximum wrinkling wave amplitude is obtained when the workpiece is under the most severely wrinkled state by normalising the vertical nodal coordinates (Y-coordinates) of the wrinkling tops and bottoms.

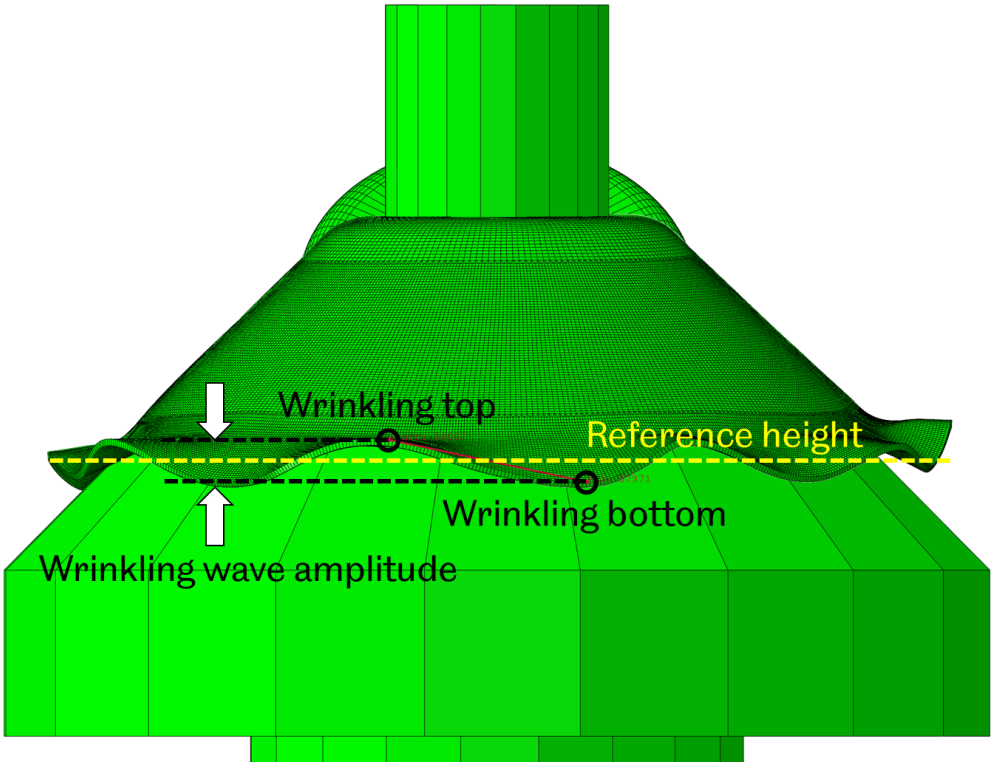

Figure 3.27 Definition of wrinkling top, bottom and wrinkling wave amplitude.

The wrinkling wave amplitude curves shown in Figure 3.28 highlight the locations of the wrinkling wave bottoms at a specific time of 1.2s of Model No. 10. The wrinkling tops and bottoms can be traced to the highest and lowest nodes on the edge of the workpiece. For example, the wrinkling bottoms on the workpiece circumference edge at 1.200s are traced to the corresponding locations on the wrinkling wave

amplitude curve marked by red circles. For easy comparison, the circumference is also normalised to a range from 0 to 1.

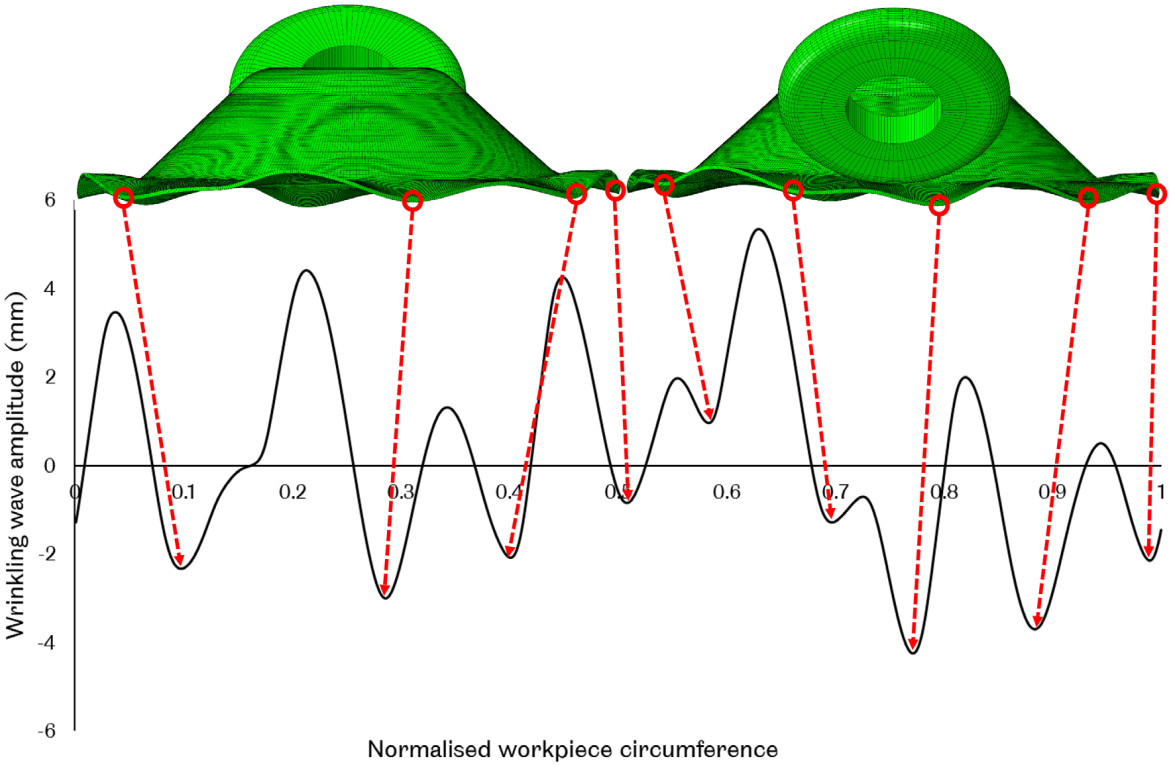

Figure 3.28 Corresponding wrinkling bottoms on the wrinkling wave amplitude curve at 1.200s in FE model No. 10 with mandrel speed 1000 RPM and feed ratio 1.5 mm/rev.

The wrinkling wave amplitude results in Figure 3.29 are obtained from Model No. 10 with 1000rpm mandrel rotational speed and a 1.5 mm/rev feed ratio at 2.16s process time. The excessive distortion that causes the spinning process to fail happens at 1.420s (24th revolution); hence, five sets of the results at different times are traced back from the processing time of 1.373s (23rd revolution). The curves in Figure 3.29 (a) for different process times have an obvious pattern: the wrinkling wave amplitude increases over time, reaching a maximum at 1.373s (23rd revolution). There is another pattern in the zoom-in view of the normalised workpiece circumference from 0.53s to 0.63s, as shown in Figure 3.29 (b). This wrinkling wave does not form until the process passes 0.8925s (15th revolution). Also, the location changes of the wrinkling top could be observed as the wrinkling top gradually moves to the left-hand side, in the same direction as the roller moving direction. The number of wrinkling waves increases to ten at 1.373s (23rd revolution) from five at 0.8925s (15th revolution), as shown in Figure 3.29 (c). The variation of wrinkling wave amplitudes with the process time shows that the wrinkling waves do not form simultaneously. The roller movement over the workpiece circumference edge will form new wrinkling waves while simultaneously intensifying the previously formed

ones. However, the roller will not increase the amplitude of the previously formed waves without a limit. Eventually, the amplitude of every wrinkling wave reaches a relatively same level at 1.373s (23rd revolution), as shown in Figure 3.29(c).

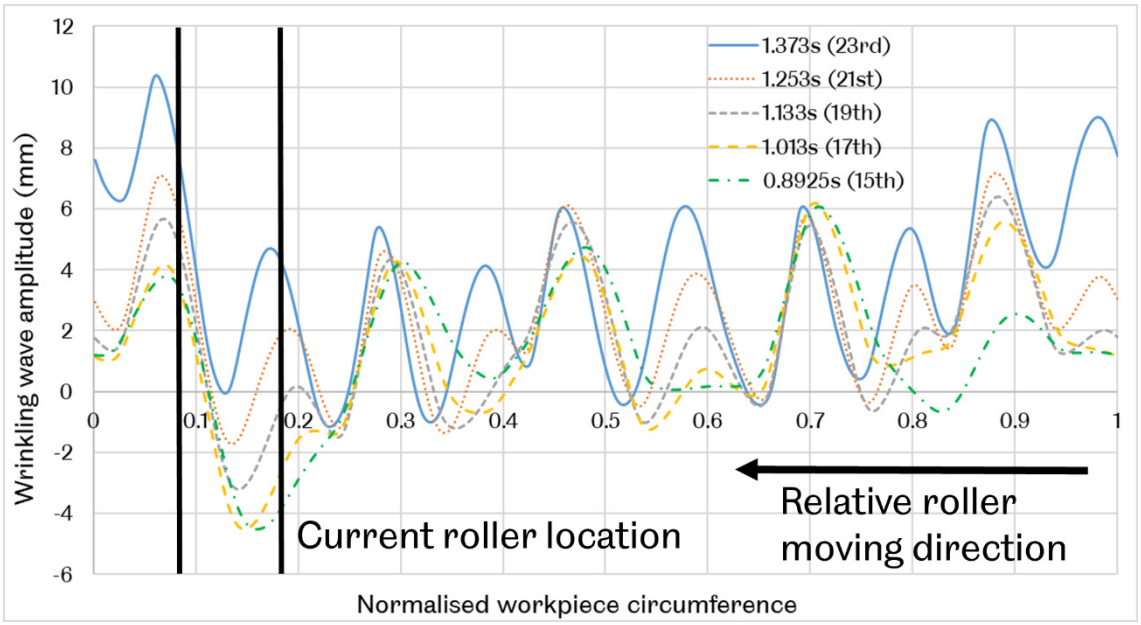

(a)

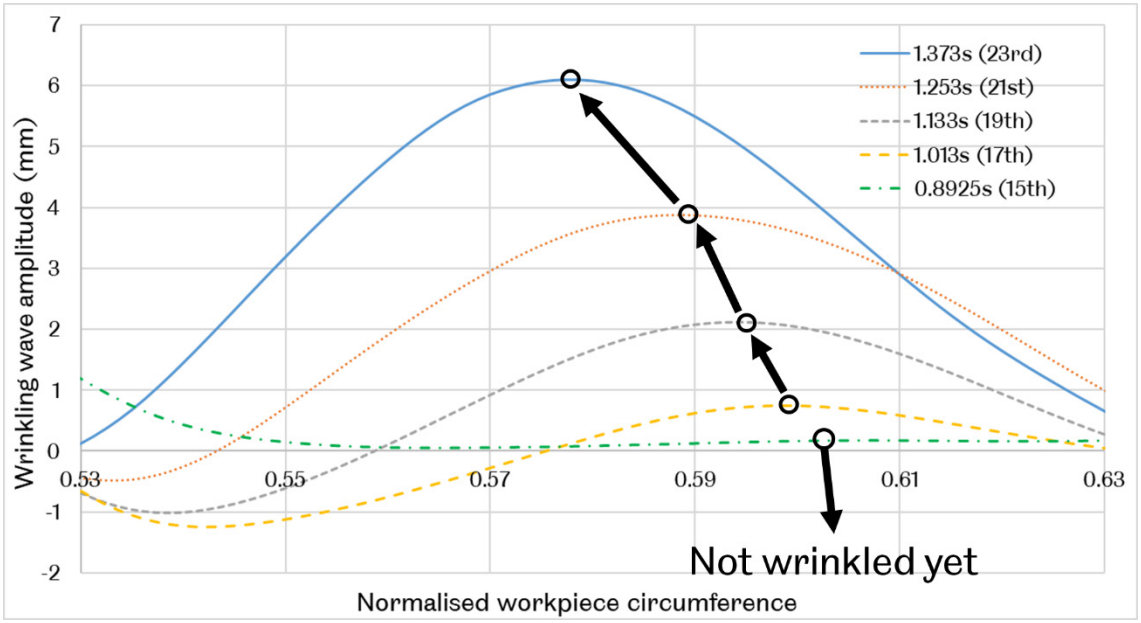

(b)

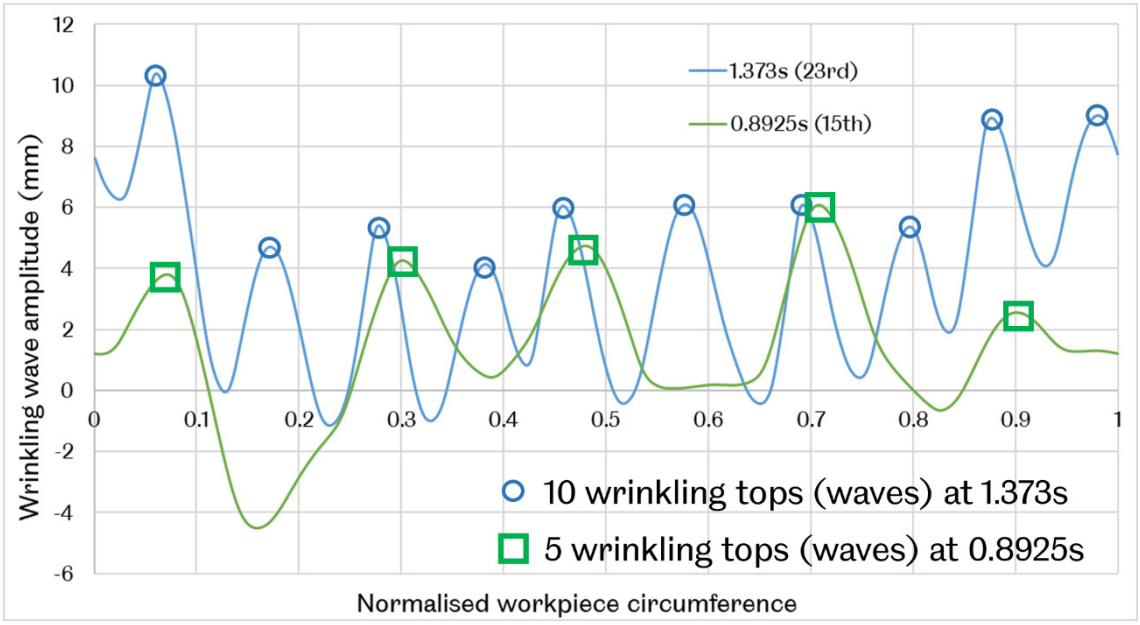

(c)

Figure 3.29 Wrinkling wave amplitude on (a) the entire normalised workpiece circumference; (b) zoom-in view of 0.53 to 0.63 normalised circumference, and (c) the number of wrinkling waves at 0.8925s and 1.373s in FE model No.10 with mandrel speed 1000 RPM and feed ratio 1.5 mm/rev.

Another wrinkling feature that affects the node selection for output results is that only the wrinkling top is formed in the early stage of the spinning process but without the wrinkling bottom, i.e. wave amplitude is zero, as shown in Figure 3.30. The workpiece circumference edge always buckles upwards, as shown in Figure 3.30 (a), and the majority of the wrinkling wave amplitudes are above the X-axis (greater than 0), as shown in Figure 3.30 (b), meaning there are no wrinkling bottoms formed in the early stage of the spinning process. Therefore, strain results at the early stage of the spinning process could only be extracted from the wrinkling tops.

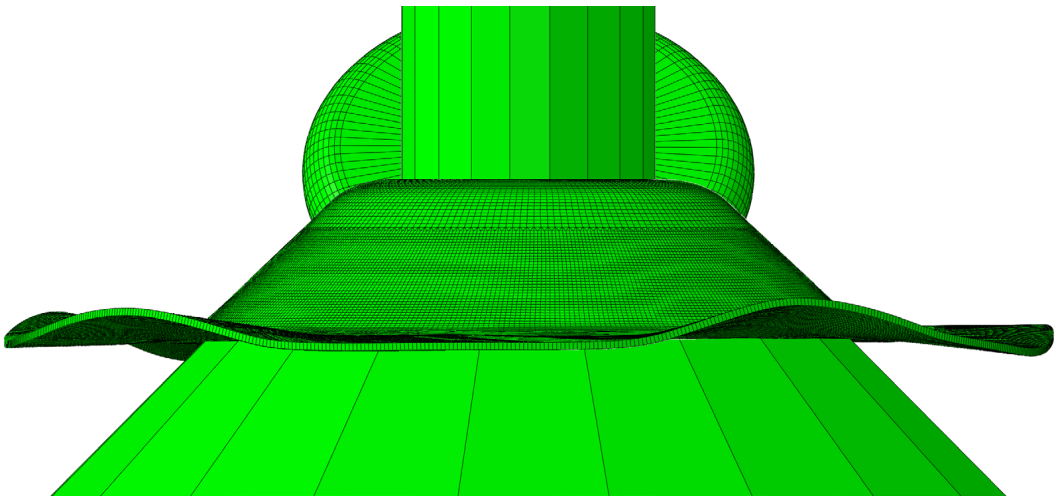

(a)

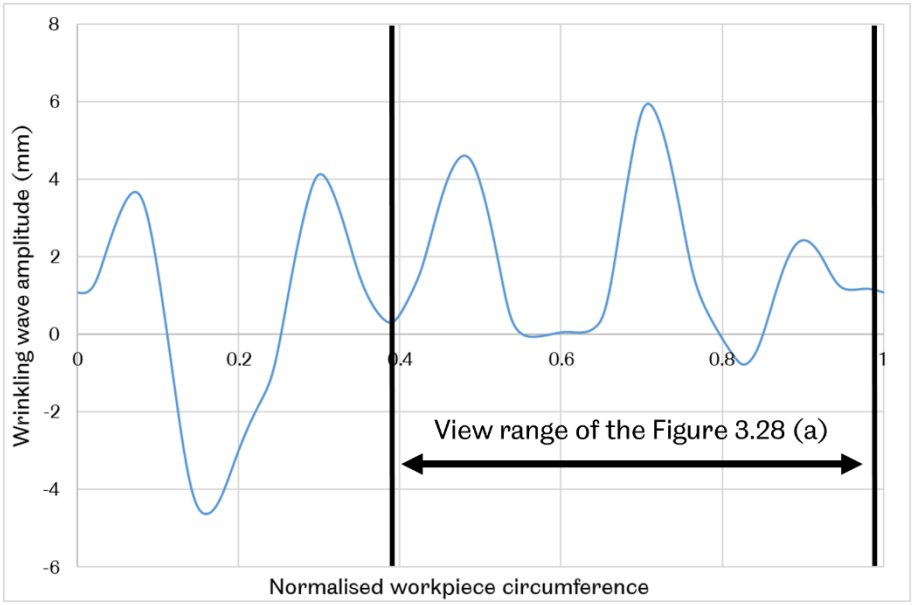

(b)

Figure 3.30 (a) Wrinkling status of the workpiece at 0.8925s and (b) wrinkling wave amplitude at 0.8925s in FE model No.10 with mandrel speed 1000 RPM and feed ratio 1.5 mm/rev.

In summary, the locations of the wrinkling tops and bottoms are constantly moving during the spinning process, and their moving direction is the same as the relative moving direction of the roller to the workpiece. This unique feature directs the following detailed analysis of stress and strain results, which will be extracted from different node sets at different times rather than focusing on the same node set selected at the same time.

3.3.3 Definition of Wrinkling Limit

There are three possible outcomes related to wrinkling in the shear spinning process:

Outcome 1: severe wrinkling. The workpiece suffers excessive distortion due to severe wrinkling when the feed ratio is excessively large. The quality of the spun part is completely compromised after the roller collides with the wrinkling waves and excessively distorts the workpiece material.

Outcome 2: minor wrinkling. If the feed ratio applied is slightly smaller than in Outcome 1, the workpiece wrinkles but does not suffers excessive distortion. Less severe wrinkling occurs at the early stage, and the roller flats the wrinkled material in the late stage of the spinning process. The spun part meets the geometrical requirement. However, the quality of the workpiece may be compromised due to poor surface finishing and uneven thickness distribution.

Outcome 3: wrinkling-free. If the feed ratio is small enough, the workpiece does not have any distortion after completing the spinning process. The wrinkling does not occur, and the deformation of the flange of the workpiece is stable throughout the entire spinning process. The quality of the workpiece would meet the manufacturing requirements.

If the wrinkling wave amplitude is excessively large, the roller will collide with the wrinkling waves and fold the material towards the relative roller moving direction. This outcome is regarded as a failed spinning process, and an example of an excessively distorted workpiece is shown in Figure 3.18, which occurred in FE model No.10. The roller cyclically works on the workpiece material as the mandrel rotates constantly. The roller working cycles are the same as the revolutions that the mandrel rotates under 1000 RPM, ranging from 36 (Model No. 10 with 1.5 mm/rev feed ratio) to 120 (Model No. 3 with 0.3 mm/rev feed ratio) cycles. The wrinkling occurs earlier in the spinning processes with relatively higher feed ratios but later in the spinning processes with lower feed ratios. However, the wrinkling does not occur at a specific time that distinguishes the wrinkling and wrinkling-free statues of the workpiece. Wrinkling is a consequence mainly because the circumferential plastic strain gradually accumulates during the spinning process.

For the spun parts obtained from Outcome 2, where no excessive distortion occurs, FE thickness results are analysed to evaluate thickness uniformity. Figure 3.31 (a) shows that the thickness of the workpiece is evenly distributed after completion of the spinning process without wrinkling (wrinkling-free, Outcome 3) of Model No. 2 with a feed ratio of 0.3 mm/rev. The thickness of the majority of the workpiece ranges from 0.7169 to 0.7642 mm, with only a maximum 8% deviation, compared with the sine law thickness of 0.707 mm. The maximum thickness is 0.805 mm, close to the edge of the workpiece, as shown in Figure 3.31(a). Although without severe wrinkles from Outcome No.2 of Model No. 6 with a feed ratio of 1.0 mm/rev, unlike in Outcome 1, in which the roller could not flatten the severely wrinkled workpiece, the thickness distribution may still not be acceptable. The toothed thickness contour patterns, shown in Figure 3.31(b), indicate an uneven thickness distribution of the workpiece flange. These toothed patterns indicate the locations of eight wrinkling waves, and the roller imperfectly flattens these wrinkling waves, resulting in the thickness unevenness of the workpiece. The thickness is supposed to follow the sine law. However, the average thickness of the majority of the circular area close to the edge of the workpiece is 0.860 mm, 21.6% greater than the thickness predicted by the sine law thickness of 0.707 mm as a result of minor wrinkling that occurred in the early stage of spinning.

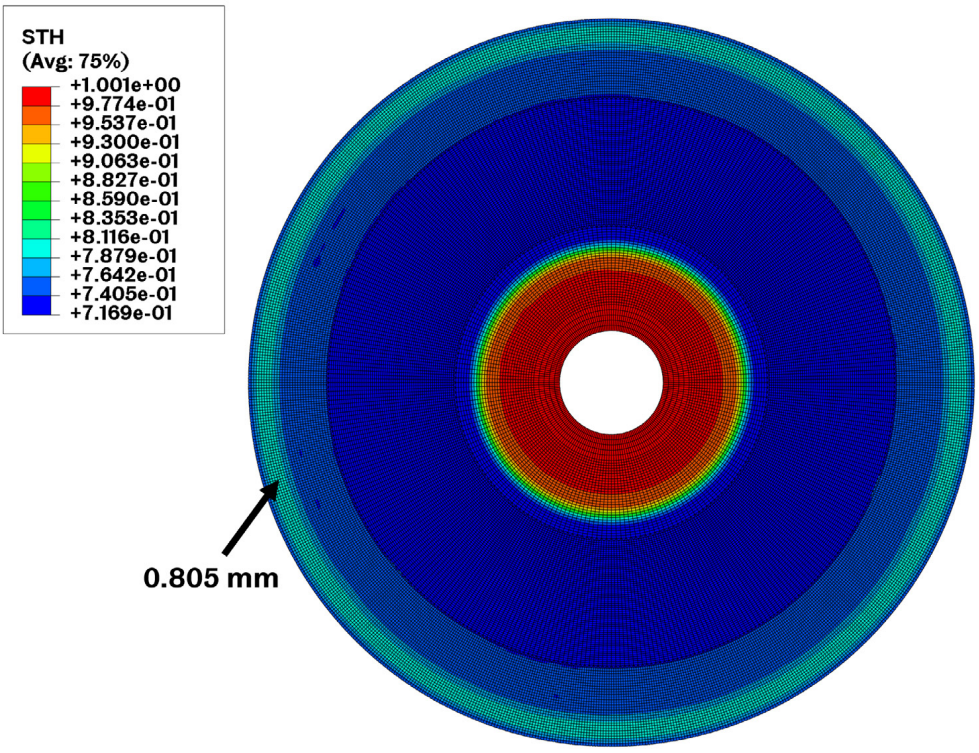

(a)

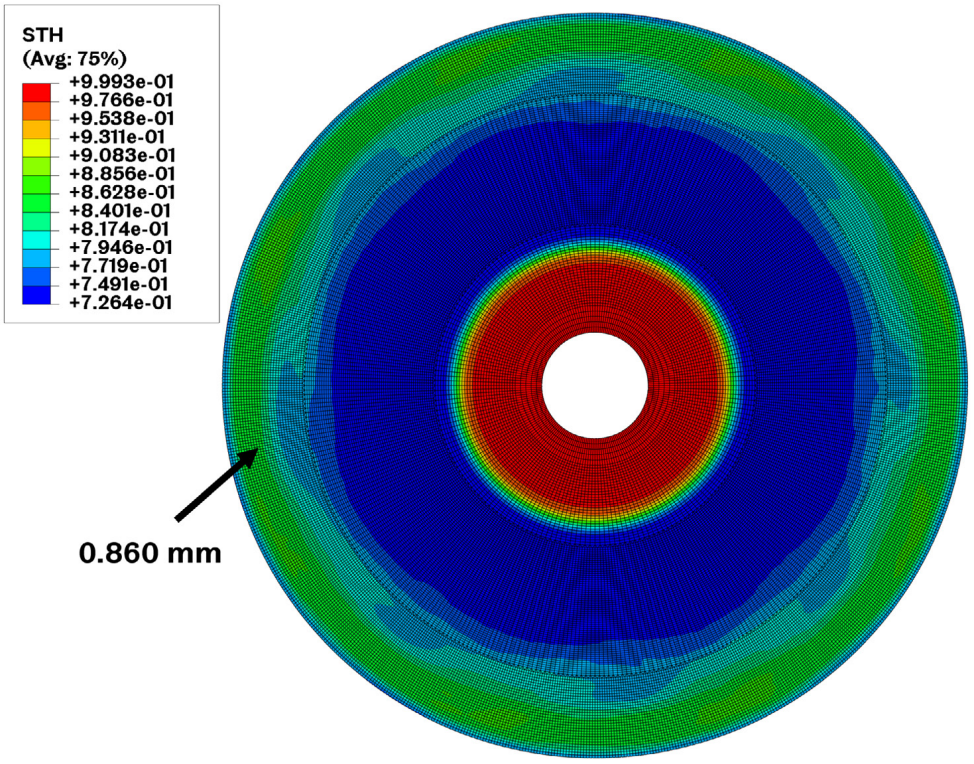

(b)

Figure 3.31 Workpiece thickness contour of (a) wrinkle-free (Outcome 3) FE model No.2 with 0.3 mm/rev feed ratio and (b) minor wrinkling (Outcome 2) FE model No.6 with 1.0 mm/rev feed ratio.

In summary, FE simulation could be used to determine the uniformity of the thickness distribution. The wrinkling limit cannot be determined by whether a spinning process is completed without excessive distortion. For spinning processes completed with minor wrinkles, the quality of the workpiece may still not be acceptable because of the thickness and unevenness of the workpiece resulting from the roller working over the wrinkled material. Hence, the wrinkling limit, presented as a feed ratio, should be found to determine whether the spinning process is wrinkling-free, eliminating uneven thickness distributions.

3.3.4 Strain Analysis of Wrinkling Initiation

Analysing the strain results of the deformed workpiece in sheet metal forming is commonly used to investigate plastic material deformation. As concluded in the previous studies, wrinkling occurs in sheet metal forming due to excessive compressive circumferential stresses that buckle the flange of the workpiece [3]. Forming Limit Diagram (FLD) is commonly involved when analysing the strain results of sheet metal forming processes. FLD consists of the major and minor strains, and an example of FLD is shown in Figure 3.32.

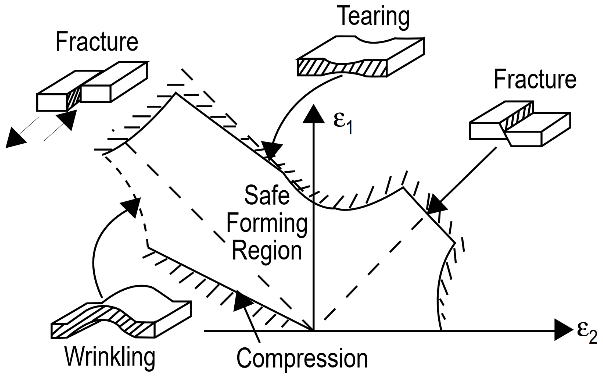

Figure 3.32 A schematic diagram of different types of failure in the deep drawing process and the processing window under different strain paths [3].

By convention, the major strain, ε_1, is defined as being in the direction with the greatest deformation and the most positive principal strain. It is assigned to the vertical axis in FLD. The minor strain, ε_2, is defined as being in the direction with less deformation and assigned to the horizontal axis. The ratio of minor strain to major strain, $\varepsilon_2/\varepsilon_1$, in the wrinkling region, is smaller than –1 or close to the compression forming limit line on the lower left section in the FLD, as shown in Figure 3.32. In a spun workpiece, it means that wrinkling occurs if the absolute value of the circumferential compressive stress is greater than the radial tensile stress. However, Figure 3.32 was obtained from a deep drawing process, and the results related to the wrinkled material were unclear. In this section, to investigate the

wrinkling initiation, critical locations of the workpiece in the spinning process will be identified first before detailed strain results will be presented.

As concluded in Section 3.3.2, FE simulation results should be extracted from different node sets since the location of the most severely wrinkled region of the workpiece is constantly changing. The material on the wrinkling top line with the greatest wrinkling amplitude is initially considered the most severely wrinkled location. However, it has been noticed that the wrinkling top line does not coincide with the maximum circumferential strain, shown as the red triangular area in the strain contour plot at 0.8925s in Figure 3.33. This observation shows that the material on the wrinkling top line does not have the highest circumferential strain of the most severely wrinkled location. Hence, a new node set is selected on the contour centre line where the maximum circumferential strain is located to output the results for analysis rather than using the node set on the wrinkling top line. Fourteen nodes from 1 to 14 are selected at 1.373s of Model No.10 as an example, as shown in Figure 3.34.

In the earlier stage in the spinning process, for example, for FE model No. 10, after the 12th mandrel revolution, the circumferential strain is very small, and there is barely any wrinkling wave noticeable, as shown in Figure 3.35. Hence the strain results after the 12th mandrel revolution are included in the following analysis of the strain results.

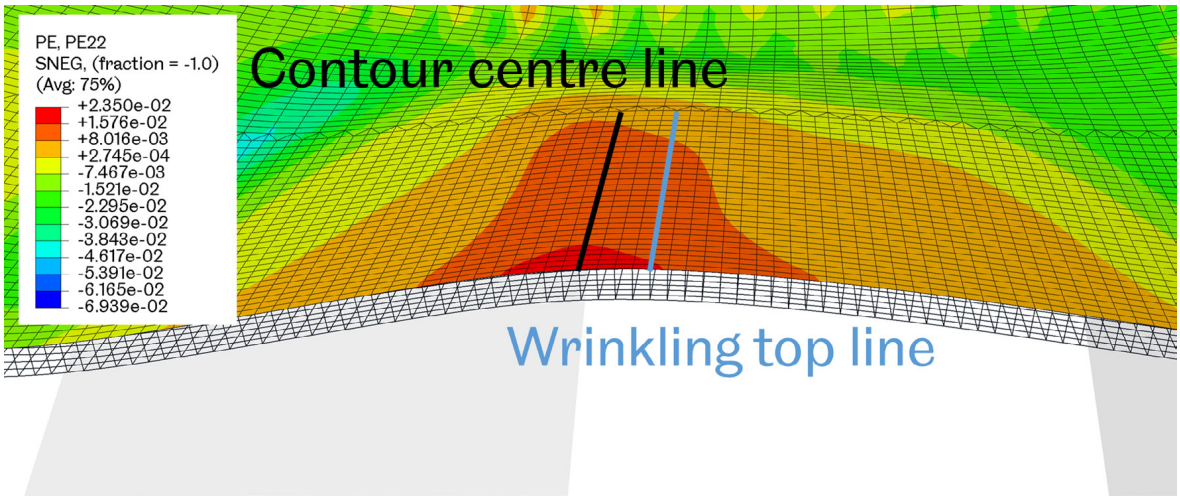

Figure 3.33 Wrinkling top line and contour of the circumferential strain at 0.8925s of FE model No. 10.

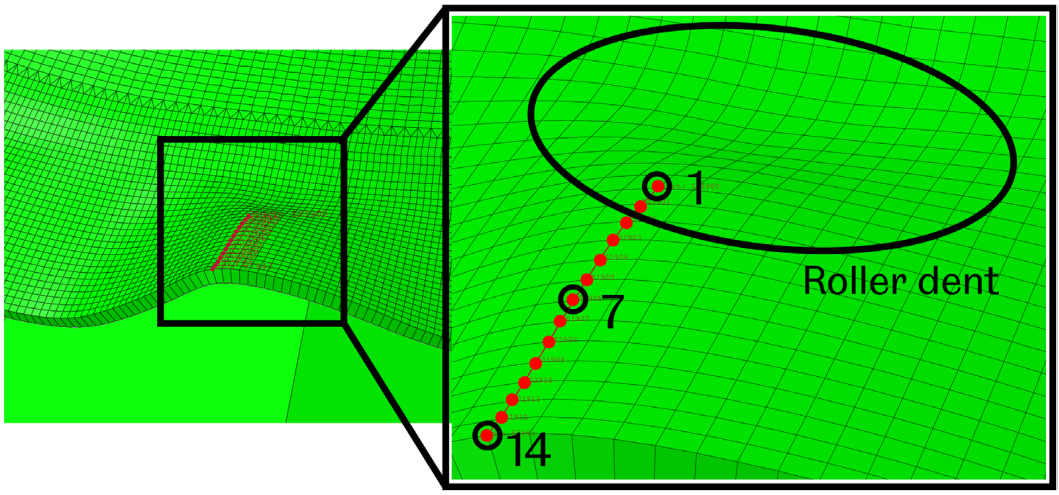

Figure 3.34 An example of nodes selection for strain analysis at 1.373s of FE model No.10.

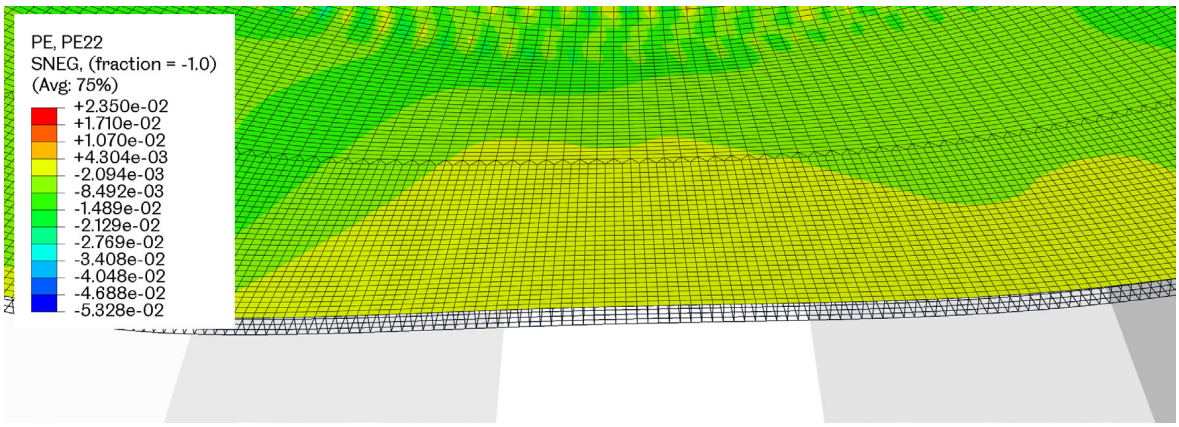

Figure 3.35 Circumferential strain contour at 0.7125s (12th revolution) of FE model No.10.

As described at the beginning of section 3.3.4, the vertical and horizontal axes represent the major and minor strains in FLD. The circumferential strain is the most positive strain as the major strain, and the radial strain is the minor strain most of the time in the shear spinning process. However, the radial strain is occasionally greater than the circumferential strain, resulting in a sudden turn of the strain signature in FLD, as shown in Figure 3.36. To ensure the strain signature has a better continuity, the circumferential strains are only displayed on the major (vertical) strain axis, and the radial strains are only displayed on the minor strain (horizontal) axis, replacing the major and minor strains.

The circumferential and radial strains of the 14 selected nodes, at different times during the spinning process, from 0.7725s (13th revolution) to 1.373s (23rd revolution) of FE model No.10 with 1000 RPM mandrel speed and 1.5 mm/rev feed ratio, are shown in Figure 3.37. The results from 4.0s (13th revolution) to 7.0s (23rd revolution) of FE model No.1 with 200 RPM mandrel speed and 1.5 mm/rev feed ratio are shown in Figure 3.38. Three straight dashed lines indicate the strain ratios of –1,

–0.5 and 1, representing pure shear, uniaxial tension and equal biaxial tension strain paths.

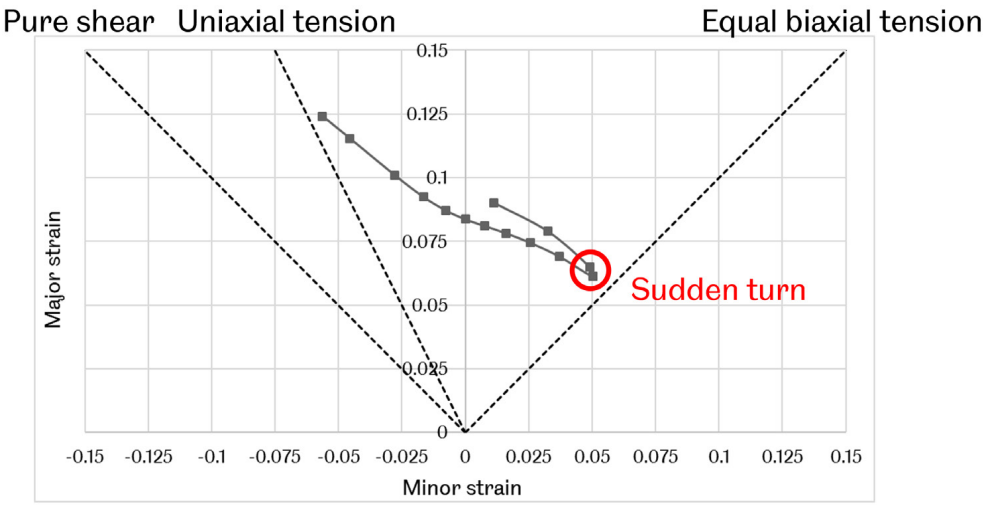

Figure 3.36 Example of the sudden turn of the strain signature.

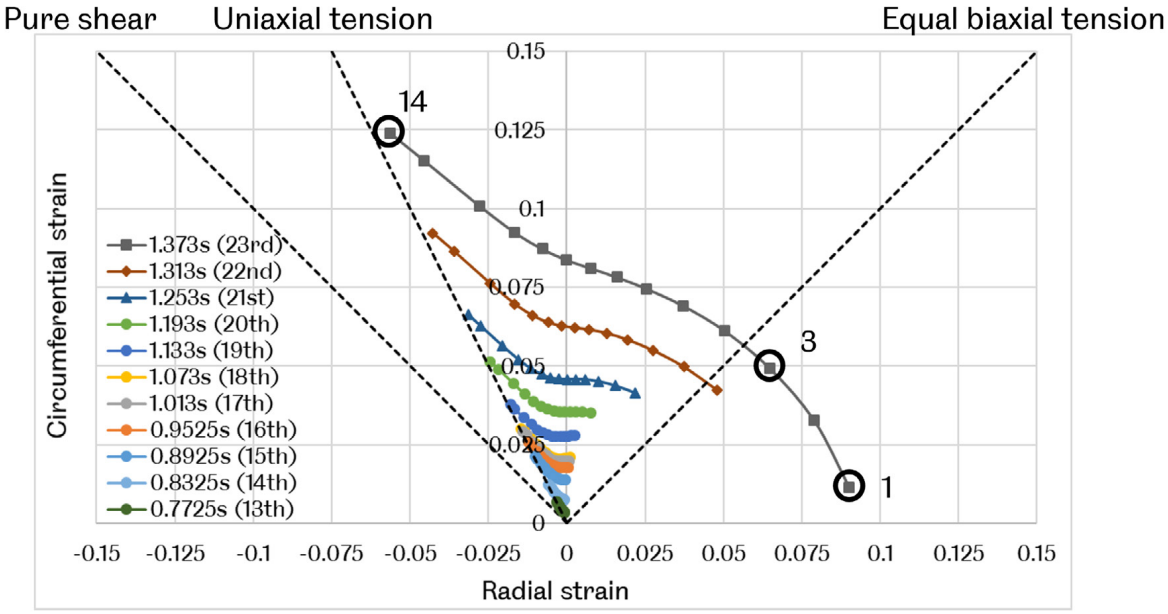

Figure 3.37 Circumferential and radial strains at different times of FE model No.10.

The circumferential and the radial strains are compressive at the early spinning stage, propagating to a wider space on the strain diagram when severe wrinkling occurs in the late spinning stage. As shown in Figure 3.37, nodes No. 1 to 3 become too close to the roller contact location when the severe wrinkling occurs at 1.373s and these nodes locate beyond the equal biaxial tension line.

There is an obvious tendency that the strain signatures gradually expand after each mandrel revolution because the material has been worked by the roller. The roller induces greater strains after each revolution. The strain ratios of the nodes are

mostly between –1/2 to 0. For these selected nodes, the closer to the edge, the greater the circumferential strain. The closest node to the edge, node No.14, has the greatest circumferential strain, as shown in Figure 3.37.

As shown in Figure 3.38, the circumferential and radial strains of FE model No.1 have a very similar pattern to FE model No.10 in Figure 3.37. The strain signatures gradually expand, and strains of some nodes close to the roller expand beyond the equal biaxial tension line in the late stage of the spinning process.

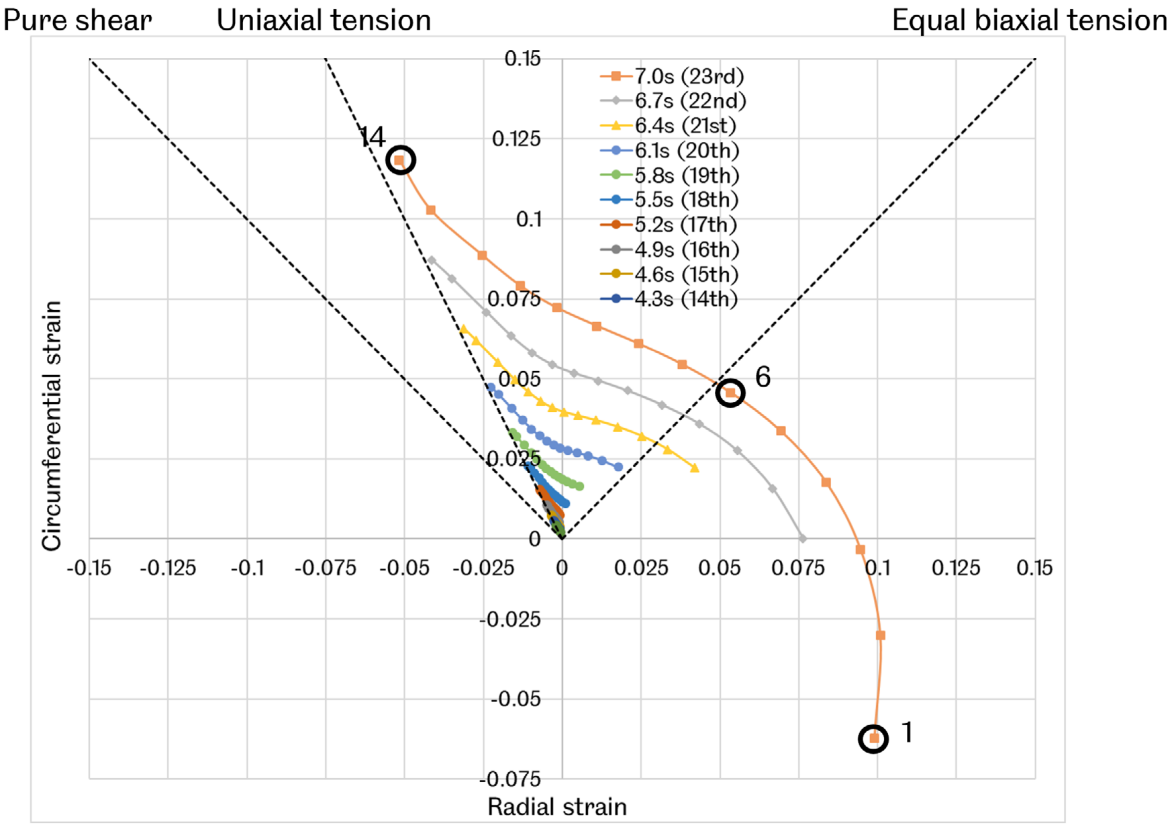

Figure 3.38 Circumferential and radial strains at different times of FE model No.1.

At the 23rd revolution, six nodes in FE model No.1 expand beyond the equal biaxial tension line. Only three nodes in FE model No.10. The rest of the nodes show similar results to that in FE model No.10. The maximum strains of FE Models No.1 and No.10 are 0.118 to 0.124 (circumferential strains) and –0.056 to –0.052 (radial strains) respectively. Two FE models with the same feed ratio but different mandrel rotational speeds result in slightly different roller feed rates and workpiece deformation speeds, thus, different strain rates. The dynamic effect caused by different strain rates seems to have minor effects on the strain results. The maximum circumferential and radial strains before excessive distortion at the 23rd revolution reach almost the same values. The strain accumulated during every roller working revolution is the most important aspect that causes two FE models with

different strain rates but has the same maximum strains. For strain accumulation, the feed ratio determines the amount of material deformed and thus determines the amount of strain accumulated in each revolution.

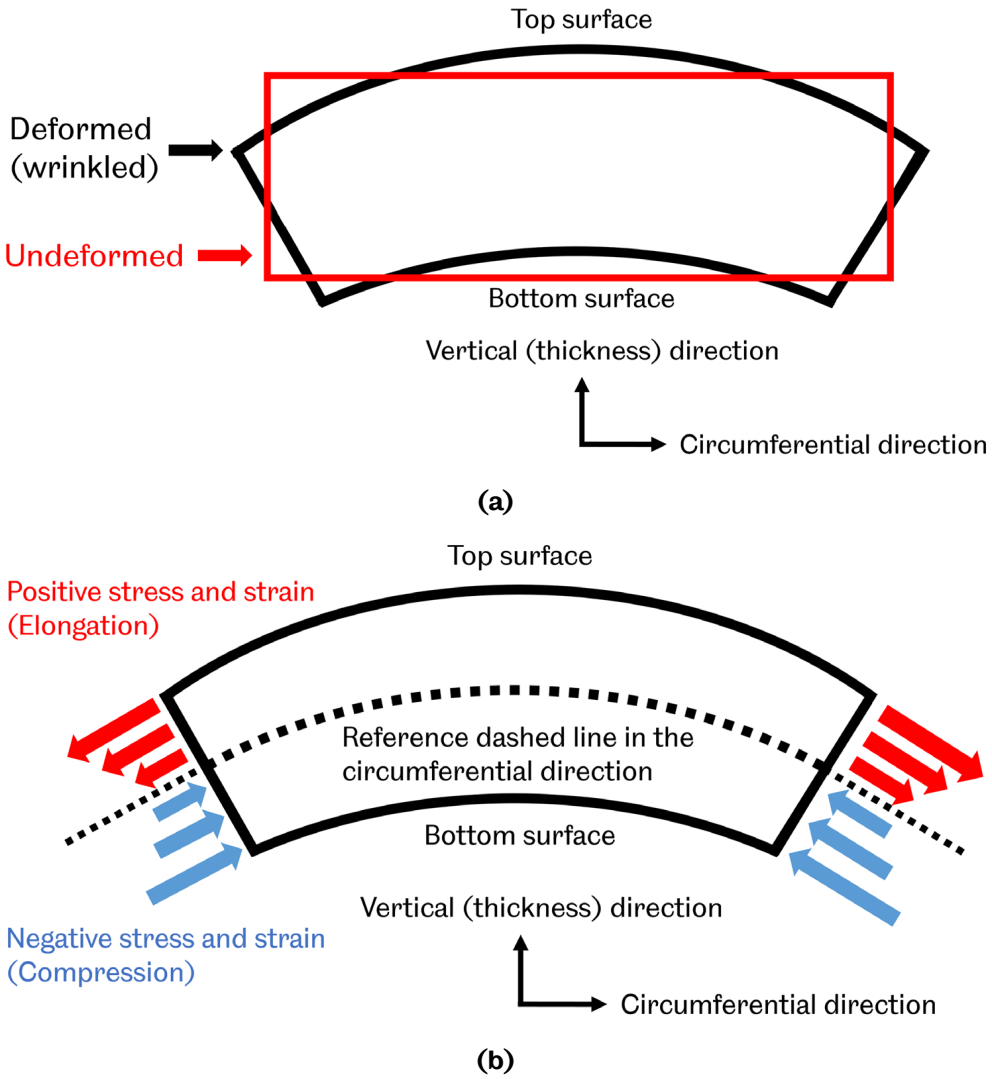

Figure 3.39 Schematic diagram of (a) undeformed and deformed (wrinkled) element and (b) stress and strain on the deformed (wrinkled) element.

Two schematic diagrams of an undeformed and then wrinkled element of the workpiece circumference flange in the thickness direction and their stress and strain patterns in the circumferential direction are shown in Figure 3.39 (a) and Figure 3.39 (b), respectively. The dashed reference line in Figure 3.39 (b) indicates the neutral plane of the thickness with zero stress and strain. The top surface buckles upwards in the thickness direction with tensile stresses and strains. Due to wrinkling, the length of the top surface is elongated to produce tensile circumferential strains. The bottom surface is compressed to produce compressive circumferential stresses and strains, thus in compression. Since the tensile circumferential stress and strain on the top surface gradually become compressive

through the thickness of this element, there will be a neutral plane where the length of the element remains unchanged with zero strain and stress.

Although nine integration points are assigned in the thickness direction to each element, ABAQUS could only output the results from the nodes on the top and bottom surfaces, the first and the ninth points. The results on other integration points could not be extracted. The most elongated and compressed nodes on the wrinkling wave at 1.373s (23rd revolution) are selected, as shown in Figure 3.40 (a), to evaluate the strain results from the top and bottom surface of the wrinkled workpiece flange with the change of time in the spinning process in FE model No. 10, as shown in Figure 3.40 (b). The strain ratios of radial and circumferential strains are shown in the major and minor strain diagram in Figure 3.40 (c). Since the workpiece is excessively distorted after 1.373s (23rd revolution), the results after 1.373s are not included in the diagram.

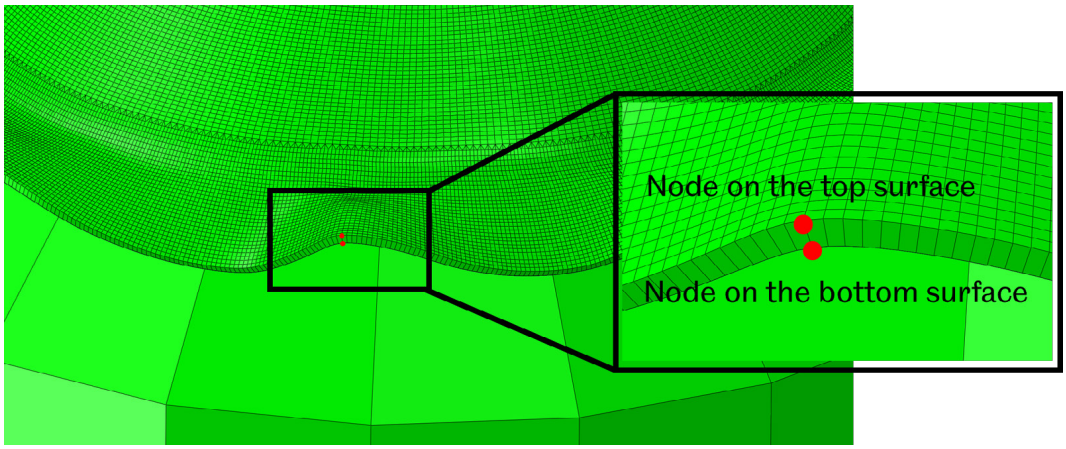

(a)

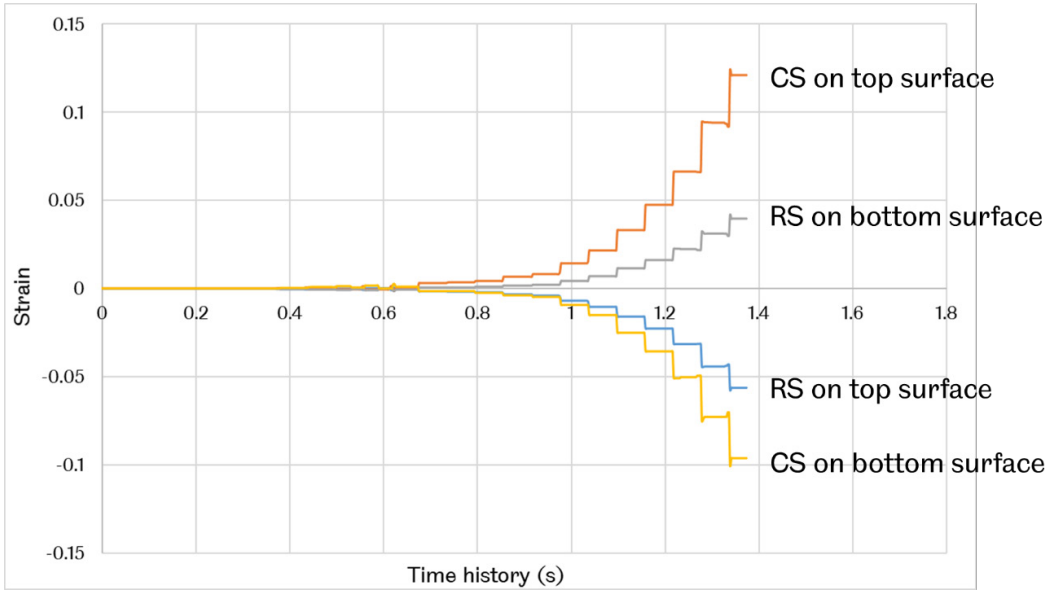

(b)

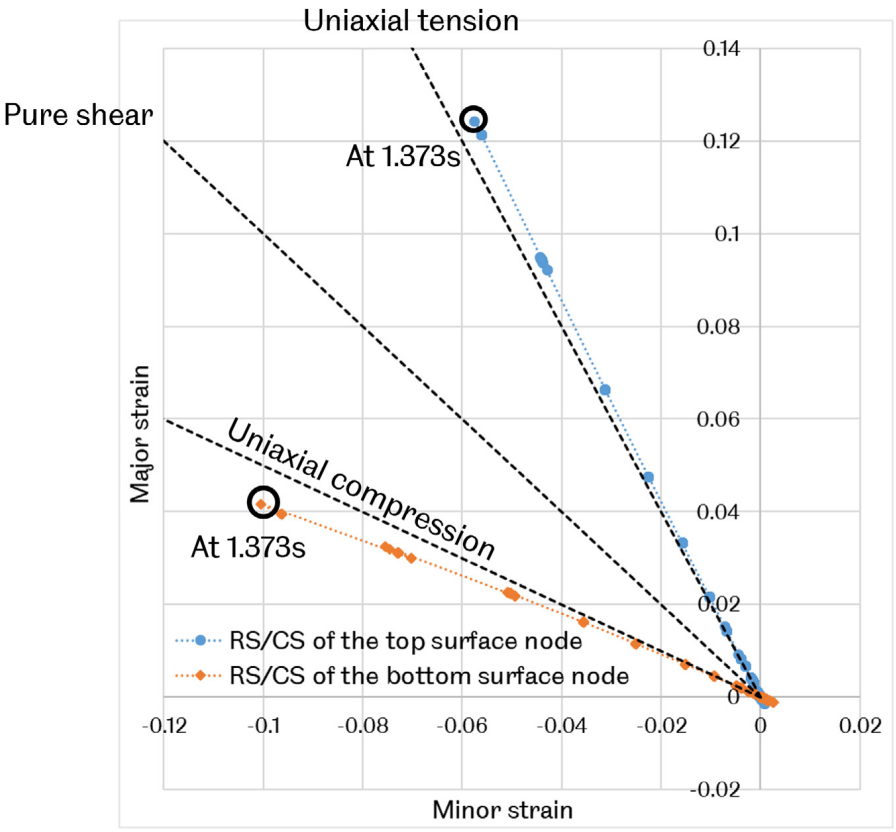

(c)

Figure 3.40 (a) Top and bottom nodes of wrinkling wave with maximum circumferential strains; (b) time history of the circumferential strain (CS) and radial strain (RS), and (c) strain ratio of RS/CS of FE model No.10.

There is an obvious pattern that the strains increase continuously as the spinning proceeds when the roller deforms the workpiece material gradually. There is a small strain increase after each deformation cycle. Moreover, the deformation is highly localised. After the roller moves away from the current contact area, the strain remains unchanged until the roller moves back to the same area in the next revolution to deform the material again, as shown in Figure 3.40 (b). Using strains of the nodes on the bottom surface to calculate the strain ratio, it has been found that the strain ratio, shown in Figure 3.40, is located in the wrinkling limit zone, as illustrated in Figure 3.32. The data points on the major and minor strain diagram do not deviate, form a perfectly straight line and reach the greatest strain values at 1.373s, as the orange line shown in Figure 3.40(c).

The roller finishes working over the most severely wrinkled wave within 0.003s, as shown in Figure 3.41. The elliptic contact contour consists of green, yellow, and red colours, indicating the workpiece area is currently being contacted by the roller. The roller works over this already formed wrinkling wave, from right to the left-hand side, within 0.003s.

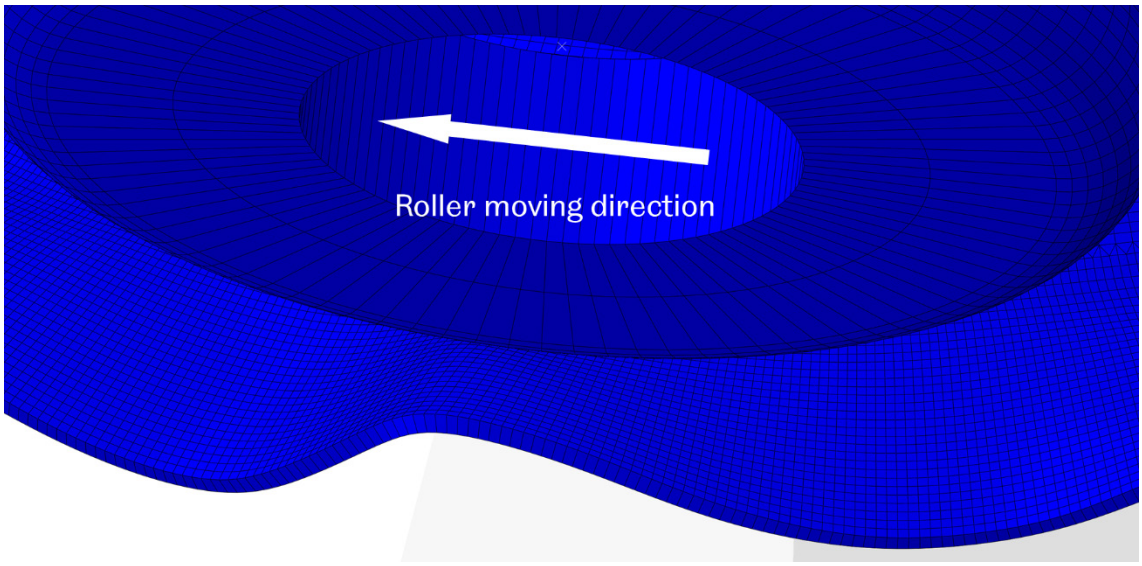

(a)

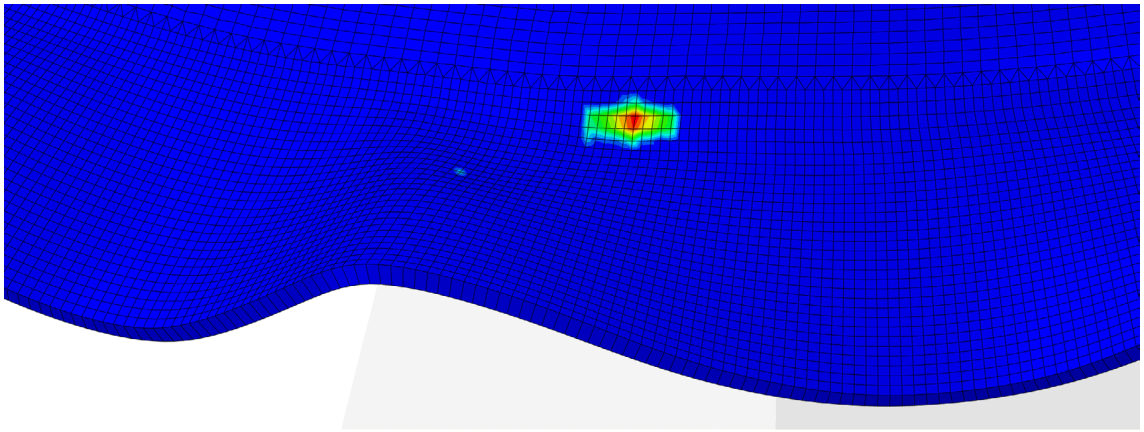

(b)

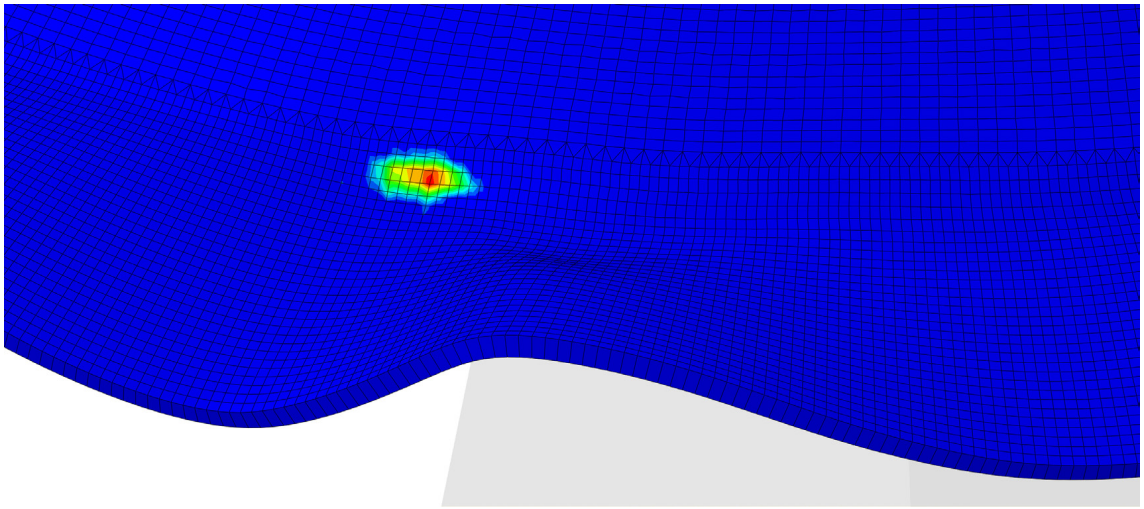

(c)

Figure 3.41 Contact between roller and workpiece (a) location of the roller at 1.315s and its moving direction; contact contour at (a) 1.315s and (c) 1.318s of FE model No.10.

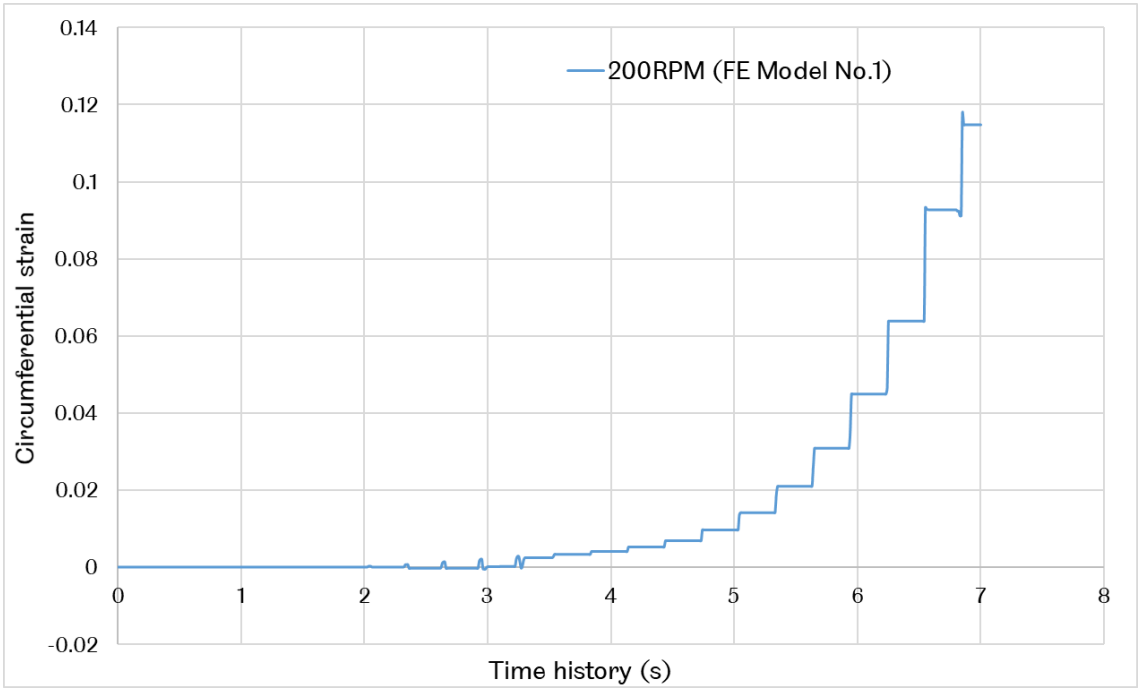
200RPM (FE Model No.1)
Circumferential strain
Time history (s)
0.14
0.12
0.1
0.08
0.06
0.04
0.02
0
-0.02
0
1
2
3
4
5
6
7
8

(a)

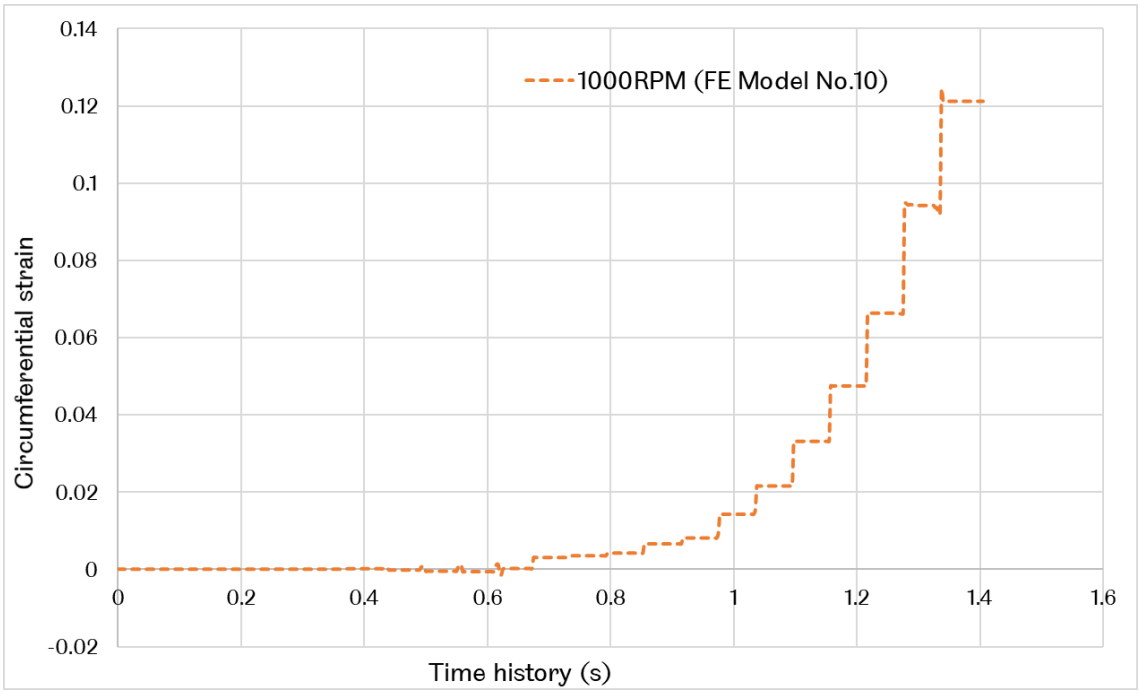
1000RPM (FE Model No.10)
Circumferential strain
Time history (s)
0.14
0.12
0.1
0.08
0.06
0.04
0.02
0
-0.02
0
0.2
0.4
0.6
0.8
1
1.2
1.4
1.6

(b)

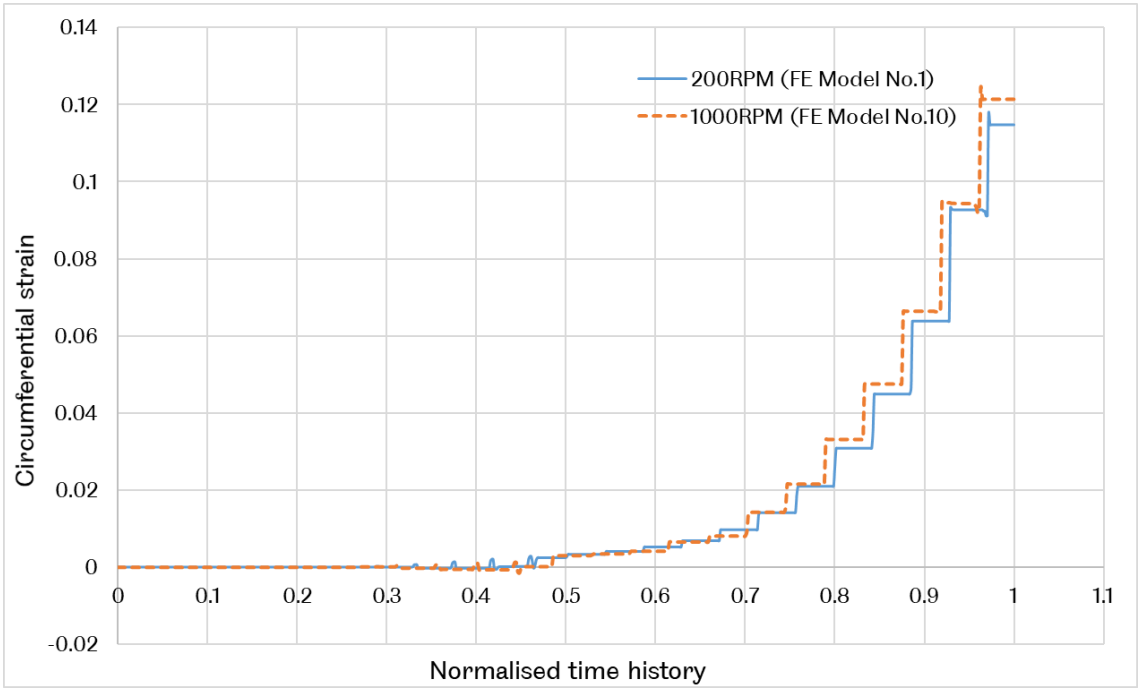

(c)

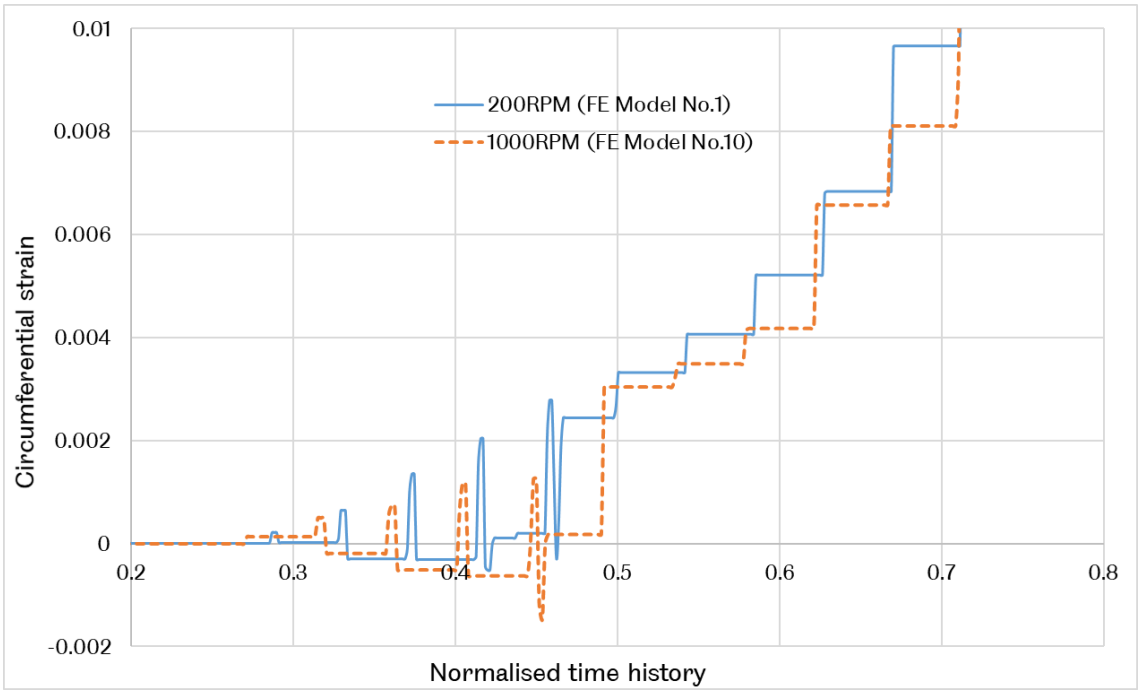

(d)

Figure 3.42 Circumferential strains (a) 200 RPM (Model No.1); (b) 1000 RPM (FE model No.10); (c) strains of FE models No.1 and No.10 with normalised time history, and (d) strains of FE models No.1 and No.10 between 0.2 to 0.8 of the normalised time history.

Figure 3.42 (a) and Figure 3.42 (b) present the circumferential strains of the top surface of FE Models No.1 and No.10. The spinning times of FE model No.1 and No.10 are around 7.170s and 1.430s when excessive distortion occurs. Hence, results from

0 to 7.0s (FE model No.1) and 0 to 1.4s (FE model No.10) are selected and displayed for better illustration and further comparison. Figure 3.42 (c) shows the strain results with normalised time history. Normalising the spinning times of these two FE models provides a direct comparsion between two models with different spinning times and, most importantly, comparing the strain results of FE models with different strain rates.

The strain results between FE Models No.1 and No.10 have very similar patterns, as shown in Figure 3.42 (c). Figure 3.42 (c) shows that the two curves progress very similarly. Although they are slightly different, for example, the strains of FE model No.10 increase before that in FE model No.1, the maximum strain when excessive distortion occurs is almost identical. The patterns of strain increase are also very similar. The detailed strain results at 0.2 to 0.8 of the normalised time are shown in Figure 3.42 (d). In the early stage of the spinning process, the circumferential strain remains unchanged from 0 to 0.2 (1st to 7th revolution). From the 7th revolution (near 0.3 of the normalised time) to the 12th revolution (near 0.5 of the normalised time), the strain keeps a slightly increasing trend to very small positive values, indicating that the top surface is slightly elongated after the roller works over the nearby material. The strain reduces immediately after the roller moves away from the area. The strain reduces to a negative value but is very close to zero, indicating that the top surface is slightly compressed; between the 7th and the 12th revolution, the material recovered from the deformation induced by the roller. After the 12th revolution, the strains induced by the roller became greater and greater after each revolution. The strains accumulate and cyclically increase because the strains are excessively greater for the material to recover.

The compression from the roller at each revolution causes tensive strain accumulation. In the early stage of the spinning process, the roller travels a shorter distance on the specimen surface to complete one revolution. The distance for the roller to complete one revolution gradually increases as the roller deforms material progressively and moves outward from the workpiece centre. As the roller deforms and induces compression to more material during the same period of time than in the early stage, wrinkling occurs when the tensive strain accumulation exceeds strain recovery.

For FE model No.10 with 1000 RPM mandrel speed, the strain increases with the spinning process within 0.003s while the roller works over an already formed wrinkling wave, judged by the contact locations of the roller working over the nearby area of the wrinkling wave, as shown in Figure 3.42. As previously explained, the roller feed rates of FE Models No.1 and No.10 are linearly related. Thus the time for the

roller to work over an already formed wrinkling wave in FE model No.1 is 0.015s. Under the same 1.5 mm/rev feed ratio, the strain rate of FE model No.10 is five times that of FE model No.1 since the roller deforms the workpiece five times faster in FE model No.10. However, almost every aspect related to the strain results of FE model No.1 is similar to that of FE model No.1. The detailed analysis of the strain results further prove that even with a five-time difference in strain rates, the feed ratio is the most critical factor that affects the wrinkling initiation and strain accumulation in the spinning process, not the dynamic effect.

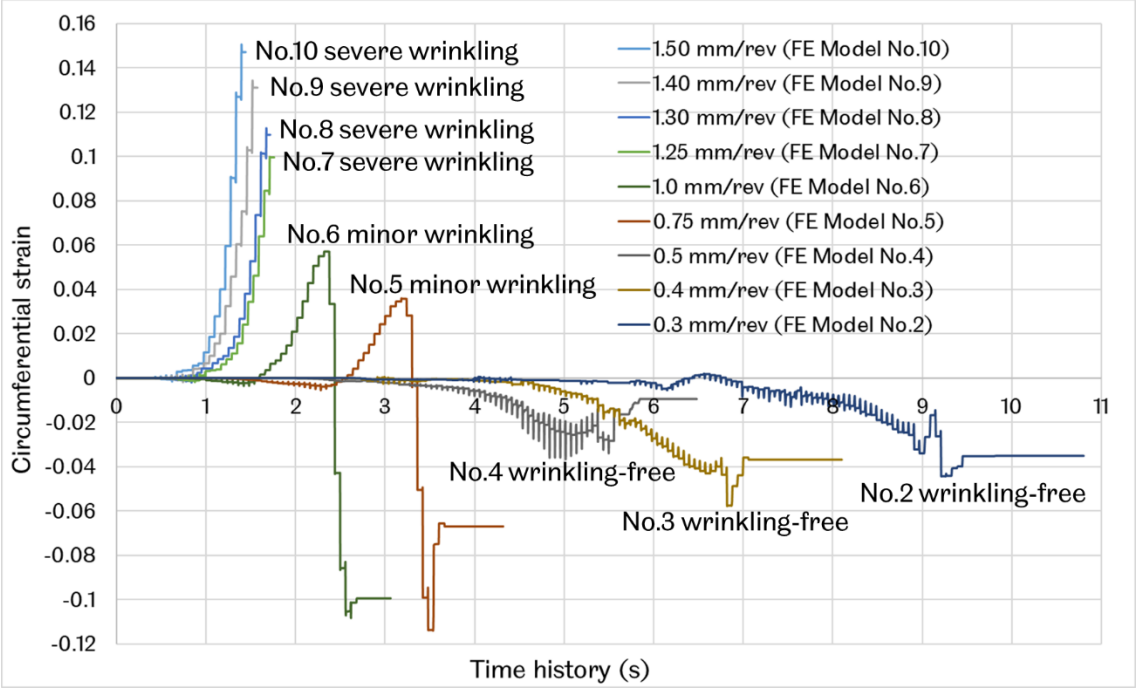

Figure 3.43 Circumferential strains of the nodes on the top surface with different feed ratios of FE models No.10 to No.2.

In this study, the circumferential strain is used to describe the severity of the wrinkling. Generally, for a same period of time, greater strain accumulation in the FE models with higher feed ratios than in the models with lower feed ratios. Circumferential strains from FE spinning simulation models employing different feed ratios are evaluated, as shown in Figure 3.43. FE model No.7 to No.10 fail due to severe wrinkling, thus experiencing excessive mesh distortions. Hence the results after excessive distortion are not included in the analysis. FE models No.5 to No.6 are completed, and minor wrinkling waves are flattened by the roller directly working on the wrinkling waves in the late stage of the spinning process. The strains become compressive as the workpiece conforms to the surface of the mandrel. FE model No.2 to FE model No.4 are completed as wrinkling-free with no wrinkling waves formed in the spinning process, and FE model No.4, as an example, is shown

in Figure 3.44. The strains cyclically change but remain compressive almost all the time throughout the entire process.

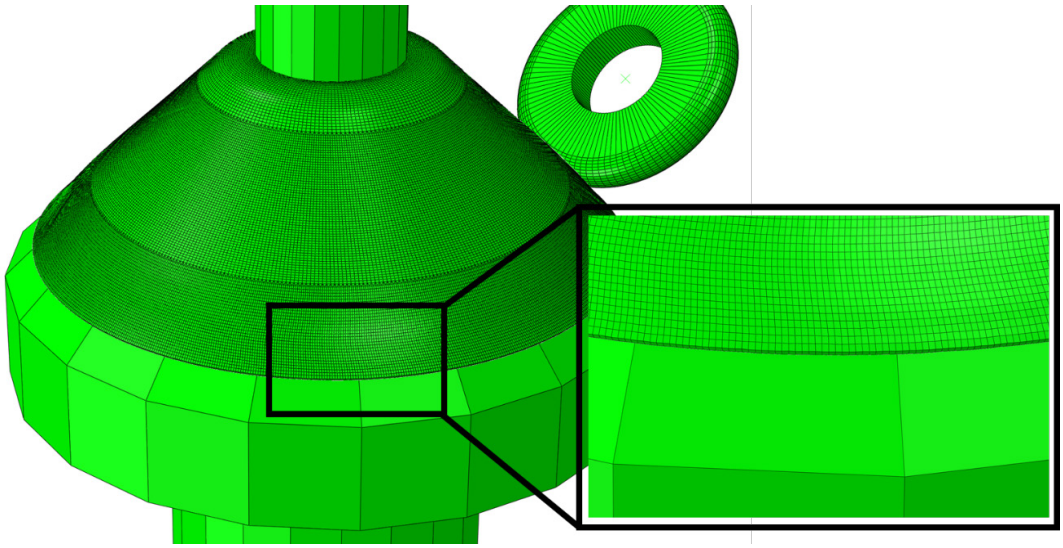

Figure 3.44 Schematic diagram of flattened wrinkling waves and zoom-in view of workpiece clings to the mandrel surface FE model No.4 with feed ratio of 0.5 mm/rev.

The obvious pattern is that the greater the feed ratio, the greater the circumferential strain. For spinning processes severely wrinkled, after the circumferential strain increases to around 0.1, the spinning process fails by wrinkling shortly. But for spinning processes with lower feed ratios, the workpiece material would not be excessively distorted, and the circumferential strain increases slowly with much lower values than that produced by the spinning processes employing higher feed ratios. The feed ratio determines when the strains start to increase and accumulate. The smaller the feed ratio is, the later the circumferential strain starts to increase, and the later the wrinkling occurs or may be avoided. Although the strains of FE model No.4 (0.5 mm/rev feed ratio) remain compressive in the process, minor wrinkling can be observed through wrinkling wave amplitude results at 4.0s (the spinning completion time is 6.48s), as shown in Figure 3.45. The fluctuations on the curves reveal some very minor wrinkling waves along the workpiece circumference. However, most amplitude fluctuations are less than 0.5 mm, only half of the workpiece thickness of 1 mm. The front and back view of FE model No.4 at 4.0s is shown in Figure 3.46. As shown in Figure 3.43, FE models with feed ratios higher than 0.5 mm/rev cause the circumferential strain to accumulate at certain times. The circumferential strains gradually increase to positive values, become tensile and severe wrinkling waves start to form. Hence, the feed ratio of 0.5 mm/rev applied in FE model No.4 is considered the wrinkling limit without tensile strain accumulation or severe wrinkling wave amplitude fluctuations in the spinning process.

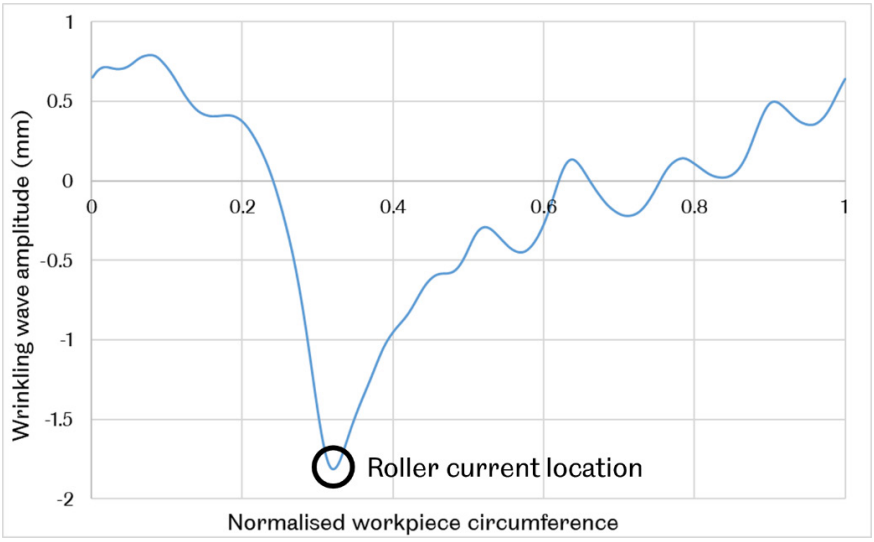

Figure 3.45 Wrinkling wave amplitude with normalised workpiece circumference at 4.0s FE model No.4 with feed ratio of 0.5 mm/rev.

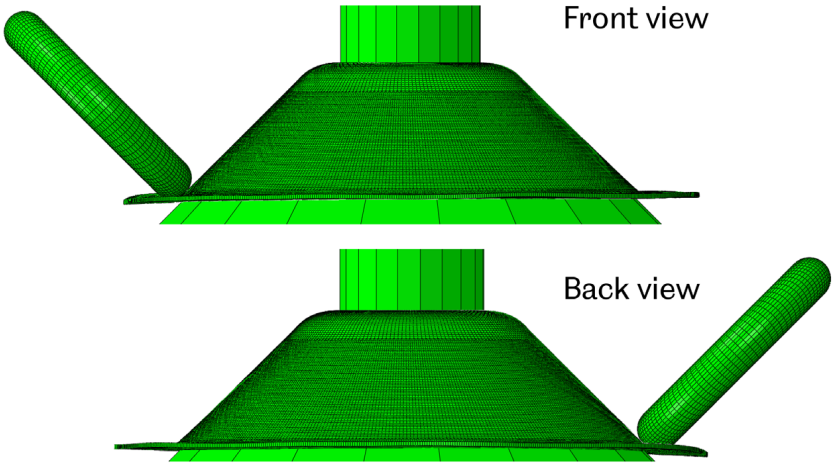

Figure 3.46 The front and back views of FE model No.4 at 4.0s.

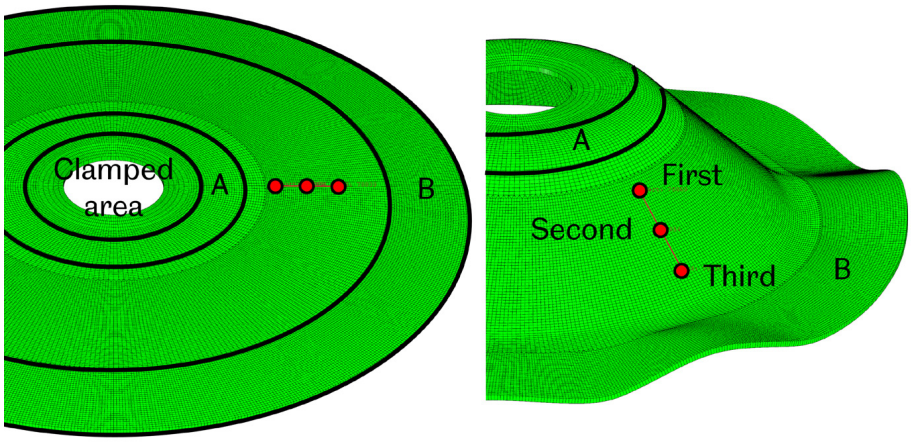

Figure 3.47 Three selected nodes on the well-deformed area of the spinning workpiece.

The reason to select model No.2, mode No.6 and Model No.10 to output the circumferential strain results is that these three models involve three outcomes of

the spinning process, and the results are comprehensive. Since the spinning time for these three models to finish the process are different, the spinning time is normalised to make the results comparable across the three models. In general, three nodes are being worked over by the roller one after another. These nodes start to be deformed very early at the beginning of the process at approximately 0.07 to 0.1 normalised time. When the roller is working on the nearby area, the circumferential strains of these nodes are cyclically changing and eventually become permanent compressive at around 0.2 to 0.4 normalised time. The deformation on these nodes finishes much earlier than the wrinkling initiation at 0.5 normalised time and propagates after, as shown in Figure 3.42. The wrinkling initiation and propagation in area B are not affected by the priorly well-deformed material. The wrinkling is localised and occurs in the late stage of the spinning process. Thus the wrinkling deformation can be treated independently when developing the wrinkling test method.

The strain results of the well-deformed area are also analysed to demonstrate the localised deformation in the shear spinning process. The first, second and third nodes are selected to output the circumferential strain results, as shown in Figure 3.47. Three nodes are selected between area A and area B. Area A is close to the workpiece clamped area and bent downwards onto the mandrel slope. Area B is the potentially wrinkled area when the feed ratio is relatively high. The strain results of FE model No.2 (wrinkling-free), model No.6 (minor wrinkling) and No.10 (severe wrinkling) are shown in Figure 3.48.

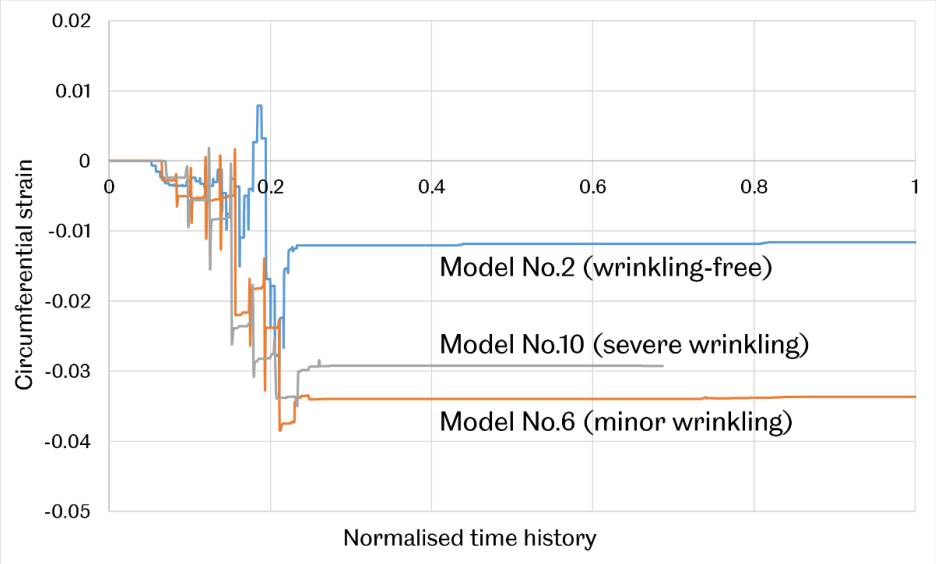

(a)

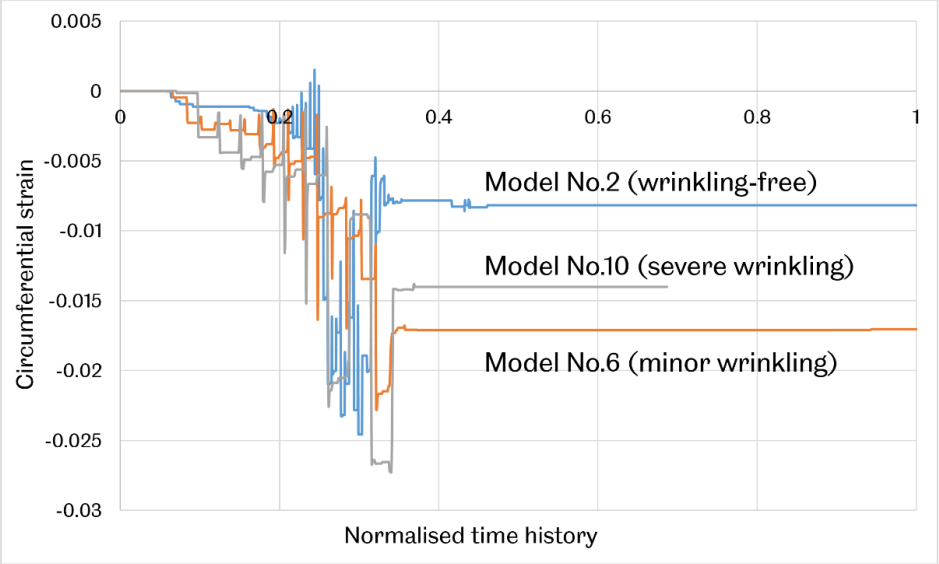

(b)

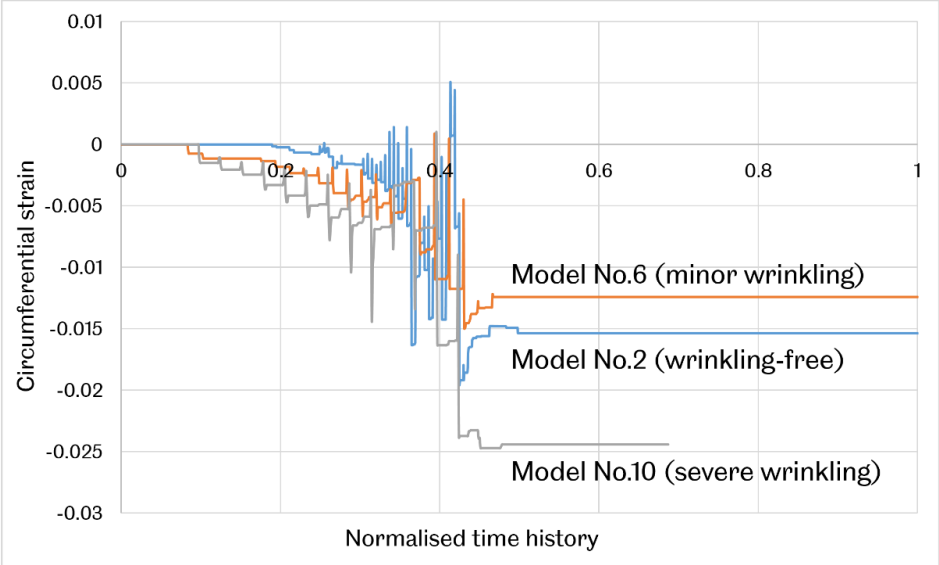

(c)

Figure 3.48 Circumferential strain results of (a) first; (b) second; and (c) third nodes in FE model No.2, model No.6 and FE model No.10.

3.4 Summary of findings

This chapter presents the development of the shear spinning simulation models. The dimensions of the components in the FE model are identical to those in the actual spinning test in Chapter 4. The element type selection, meshing strategy (to prevent hourglass issue), and mass scaling method (to improve computation efficiency) are validated to guarantee the simulation accuracy of the developed models. The Strain results of different models with various mandrel speeds and feed ratios are analysed. The important findings are:

- The circumferential strain on the top surface of the wrinkling wave is used to determine the severity of the wrinkling deformation, and it increases with the severity of the wrinkling deformation. The wrinkling initiates when the circumferential strain cyclically increases and remains tensile. Higher feed ratios result in more rapid circumferential strain accumulation. The circumferential strain remains compressive throughout a wrinkling-free shear spinning process.
- The wrinkling wave amplitude is defined to quantify the severity of the wrinkling deformation, increasing with the severity of the wrinkling deformation. However, the wrinkling wave amplitude and the circumferential strain of the early-stage/minor wrinkling are difficult to measure since the wrinkling wave amplitude and circumferential strain values are small.
- The strain analysis further indicates that the dynamic effect induced to the spinning workpiece due to the high mandrel speeds and strain rates is independent of the wrinkling initiation and other aspects, for example, the wrinkling wave amplitude and the number of wrinkling waves. The wrinkling initiation is the result of the circumferential strain accumulation due to the excessive feed ratio applied to the workpiece. It is the main novelty extracted from the spinning FE modelling for establishing an in-depth understanding of the wrinkling mechanism.

4 Experimental Testing of Wrinkling in Shear Spinning Process

In Chapter 3, FE models are developed for the shear spinning process to investigate material deformation that is nearly impossible to obtain from the experimental testing, for example, the stress results and the strain evolution during the spinning. In this chapter, the shear spinning experimental test is designed to validate the spinning FE models by comparing the FE and experimental test results. As discussed in Chapter 3, the wrinkling phenomenon is extremely easy to trigger when the feed ratio is higher than the wrinkling limit. Although the process can still be successfully finished without excessive distortion/severe wrinkling, the wrinkling that occurs in the early stage of the spinning completely compromises the spun part quality. As a result of the occurrence of wrinkling at the early stage, the spinning experiment may need to be paused because the distorted workpiece might damage the equipment used in the experiment. Due to these two aspects, the spinning experimental tests reported in this chapter focus on wrinkling detection and test results are obtained from successfully finished/slightly wrinkled workpieces produced from the shear spinning process.

Section 4.1 introduces the experiment setup for the spinning tests. Section 4.2 introduces the design of the experiment. Section 4.3 analyses the results obtained from the tests. Section 4.4 presents the conclusion of the main findings.

4.1 Experiment Setup

The forming system used in this study consists of a roller acting as the forming tool, a mandrel and a backplate to clamp and rotate the workpiece. The equipment used to perform the shear spinning process is a CNC-controlled lathe, a modified AJAX Premier 200 CNC turning centre, as shown in Figure 4.1. It can provide axial and radial feed rates up to 3000 mm/min and a mandrel speed up to 2300 RPM, adequately covering the required processing parameter range of the shear spinning process. The experiment setup on the CNC machine is shown in Figure 4.2. The mandrel is clamped by the three-jaw chuck of the machine headstock. The headstock rotates and is driven by the motor of the CNC machine. The tailstock on the other side of the machine provides a compression force for the backplate to

clamp the workpiece onto the mandrel surface, enabling it to rotate with the mandrel. The workpiece is clamped between the mandrel and the backplate throughout the spinning process. The roller is mounted firmly on the CNC-controlled movable grip. The roller moves towards the workpiece and follows a linear one-pass toolpath in the shear spinning. The roller only works over the workpiece linearly for one time, follows the slope of the mandrel surface and keeps a constant pre-set gap between the mandrel surface and workpiece.

Figure 4.1 AJAX Premier 200 CNC turning centre.

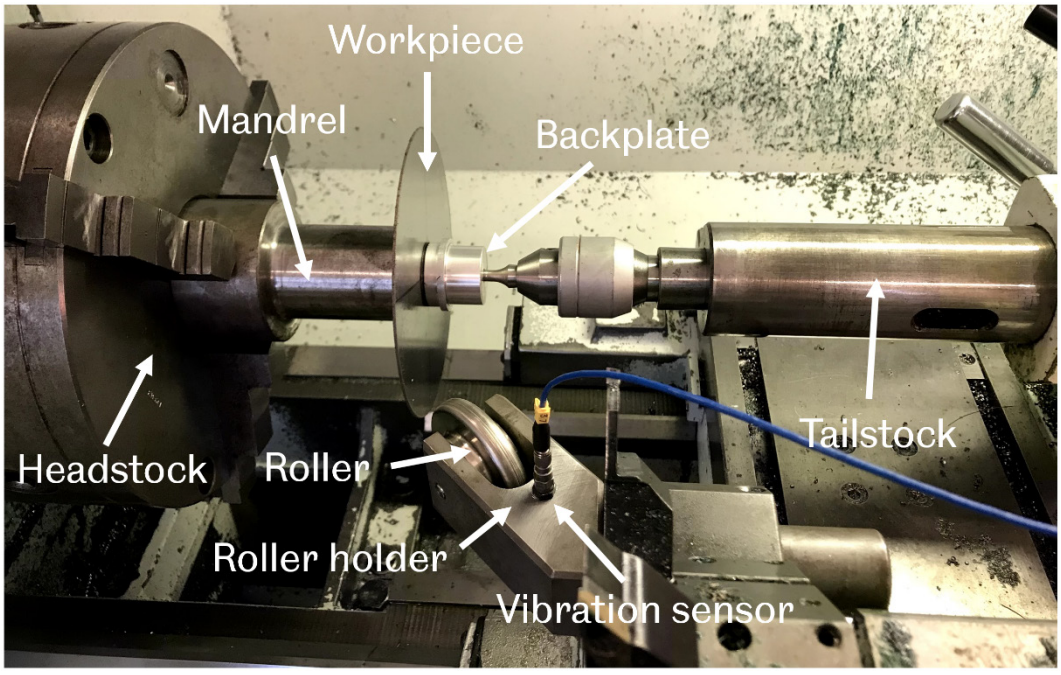

Figure 4.2 The setup of the shear spinning process on the CNC turning machine.

Vibration is generated when the roller works over the workpiece due to the direct contact between the roller and the workpiece surfaces. The vibration is stronger when wrinkling occurs on the workpiece as the roller encounters a less even surface when wrinkling occurs. The vibration measurement system in the spinning test and the measurement principle is illustrated in Figure 4.3. The vibration is transmitted through the hard materials from the roller to the roller holder and detected by the vibration sensor attached to the roller holder. The vibration sensor is a PCB Piezotronics precision vibration sensor. The sensor detects the vibration and transmits the signal to an ICP sensor signal conditioner. The signal conditioner gathers the signal from the sensor and transmits it to a PicoScope 4824 oscilloscope. The oscilloscope interprets the signal into a digital waveform and further transfers the waveform to a PC installed with PicoScope data acquisition software. The vibration can be monitored and recorded continuously throughout the spinning process by processing the data measured between these four devices. The vibration data can be quantified and comparable.

Figure 4.3 The vibration measurement system.

The purpose of quantifying the vibration is to detect the wrinkling initiation timing. For the digital waveform recorded by the software, a greater amplitude means more severe wrinkling occurs in the current spinning process. The workpiece surface in a wrinkling-free process is smoother than the workpiece surface with minor and severe wrinkles. As the roller works over a relatively even surface, less severe vibration is generated between the roller and the workpiece surface. A wrinkling-free process will have a steady waveform that fluctuates within a small range and thus with a much smaller waveform amplitude. Comparing the waveform fluctuation and the amplitude of different spinning experimental tests, the measurement data can be used to determine the severity of the wrinkling of the corresponding spinning experimental test. The time of fluctuation occurrence represents the wrinkling initiation as the roller starts working over a wrinkled workpiece. An example of the digital waveform of wrinkling is shown in Figure 4.4.

The waveform is quantified as voltage, with the unit of mV, and further transferred to the data acquiring software. An example of the waveform recorded from a

spinning process with 1000 RPM mandrel speed and 1.0 mm/rev feed ratio is shown in Figure 4.4. The waveform during the spinning process is recorded over nine seconds and is divided into five phases. For the spinning process of the spinning FE model No.6 in Chapter 3, the spinning time is 3.24s. The spinning time mentioned in Chapter 3 is the sum of the time steps of a spinning FE model. For the spinning time in the spinning test, the recording is started when the roller contacts the workpiece surface. The record is ended when the roller reaches the mandrel slope endpoint and finishes deforming the workpiece. Hence, the spinning time is the sum of phases 2, 3 and 4. Phases 1 and 5 are preparation and post-test phases, and the roller does not contact the spinning workpiece. In phase 1, the process is initiated, and the CNC lathe motor starts to rotate. The roller starts to move towards the starting location of the workpiece determined by the path code input through the CNC control panel. When the roller is about to contact the workpiece surface, neglectable vibration is recorded from the vibration of the CNC machine caused by the motor and mandrel rotation. The moment the roller starts to contact the workpiece surface, the process enters phase 2. Since the vibration sensor is attached to the roller holder and detects the vibration of the roller, the vibration starts to be intensified after the roller is not idle. The roller bends the workpiece and forces it to cling to the mandrel nose. The process of the roller bending the workpiece onto the mandrel is illustrated by the FE spinning modelling in Figure 4.5.

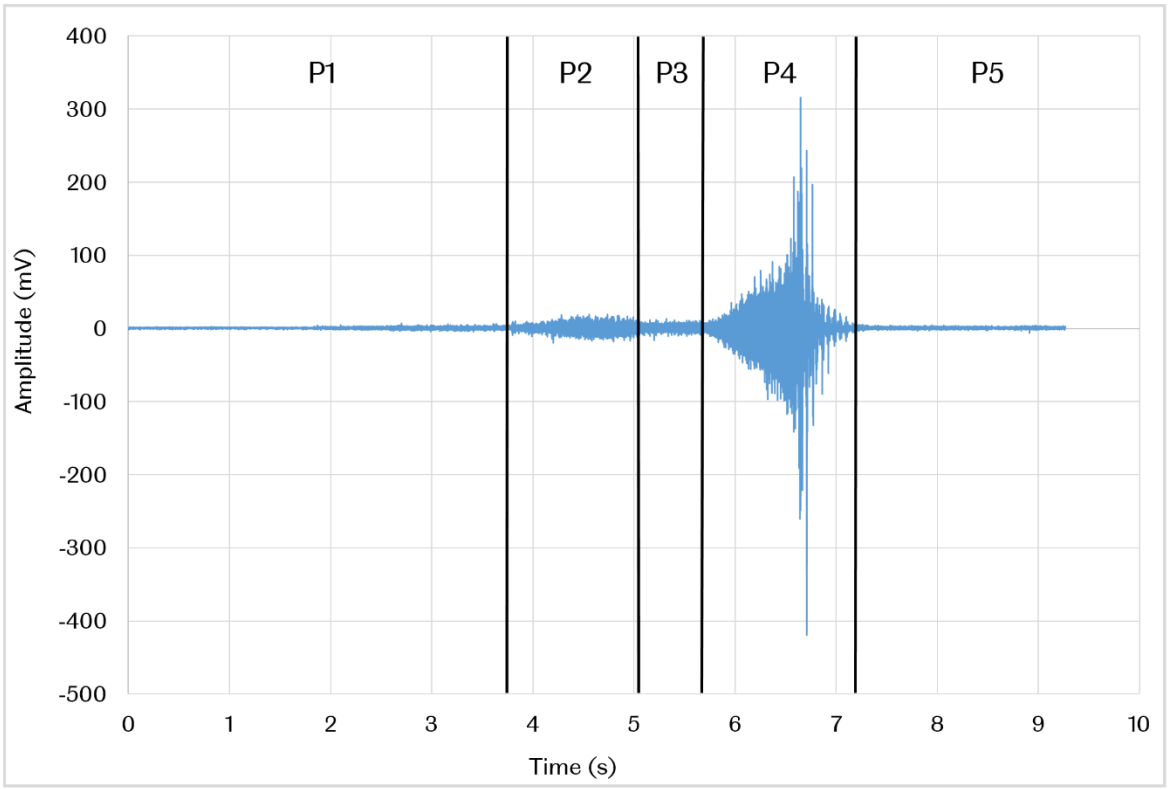

Figure 4.4 An example of the vibration recording as a wrinkling waveform.

In phase 1, the roller moves toward the workpiece surface but has yet to contact it. Towards the end of phase 1, a small distance remains between the roller and the workpiece, as shown in Figure 4.5. The roller contacts the workpiece in the early phase 2 and deforms the workpiece by the shape of the mandrel round nose. The waveform shows higher amplitudes when the roller is deforming the workpiece. The amplitudes increase for a period of time and decrease to a steady processing state in phase 3. The lower amplitudes of the waveform mean the roller does not encounter uneven workpiece surface in phase 3 since the workpiece does not wrinkle in phase 3. When the workpiece starts to wrinkle and the roller contacts the area close to the wrinkled material, the vibration becomes intense, and the amplitudes increase significantly. Visible wrinkling waves around the flange of the workpiece can be observed. The demonstration of mid phase 3 to early phase 4 is shown in Figure 4.6.

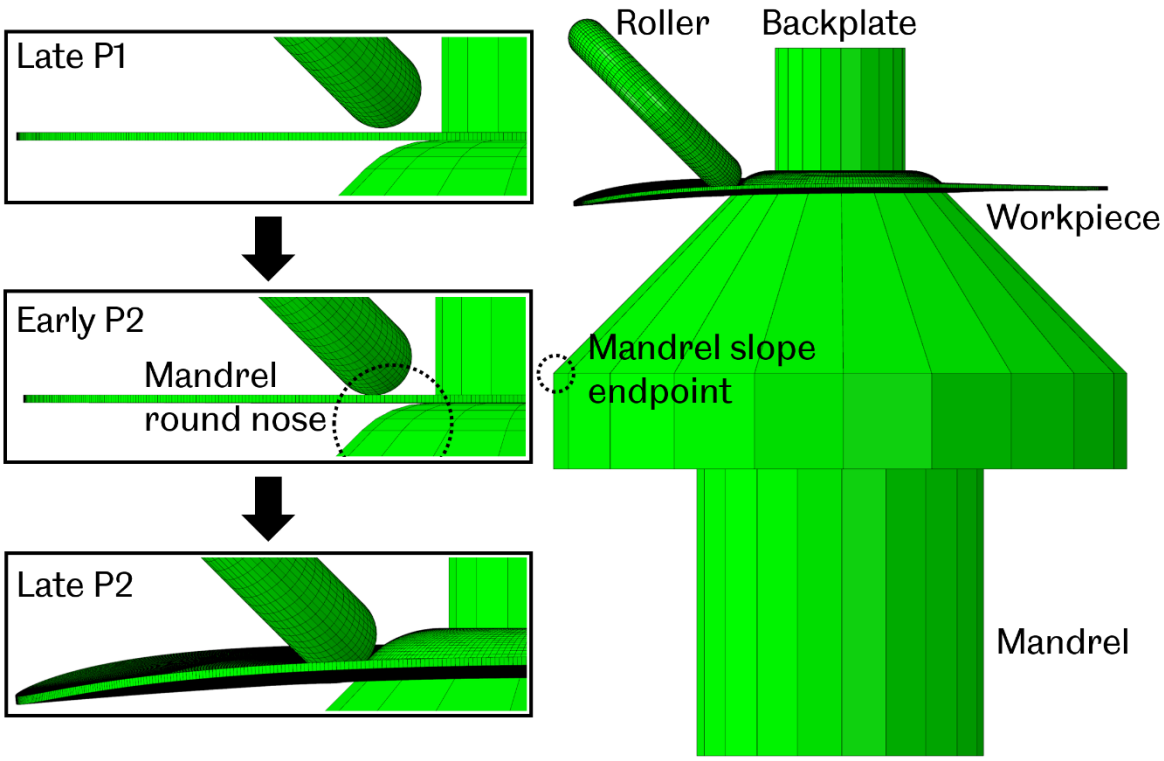

Figure 4.5 Illustration of late phase 1 to late phase 2 in the spinning process.

The workpiece starts to wrinkle, and the wrinkling waves gradually form around the flat flange in early phase 4. The wrinkling wave amplitude of the waves also increases with the process. The vibration waveform amplitude increases to the maximum as the wrinkling becomes the most severe in mid phase 4, as shown in Figure 4.7. The number of wrinkling waves and the wrinkling wave amplitude also increase to the maximum in phase 4. The spinning process with a 1.0 mm/rev feed ratio is minor wrinkled since no excessive distortion occurs. Hence in late phase 4, the roller

flattens the wrinkling waves, and the workpiece surface becomes relatively even. The vibration waveform amplitude gradually decreases from the maximum at mid phase 4 and further decreases in late phase 4. After the roller finishes working over the workpiece and is about to reach the mandrel slope endpoint in phase 5, the vibration returns to the previous neglectable state in phase 1. The roller is floating above the mandrel, does not contact any other components of the CNC machine, and the motor is idling with the mandrel clamp on the headstock of the motor. The illustration of mid phase 4 to phase 5 by FE modelling results is shown in Figure 4.7.

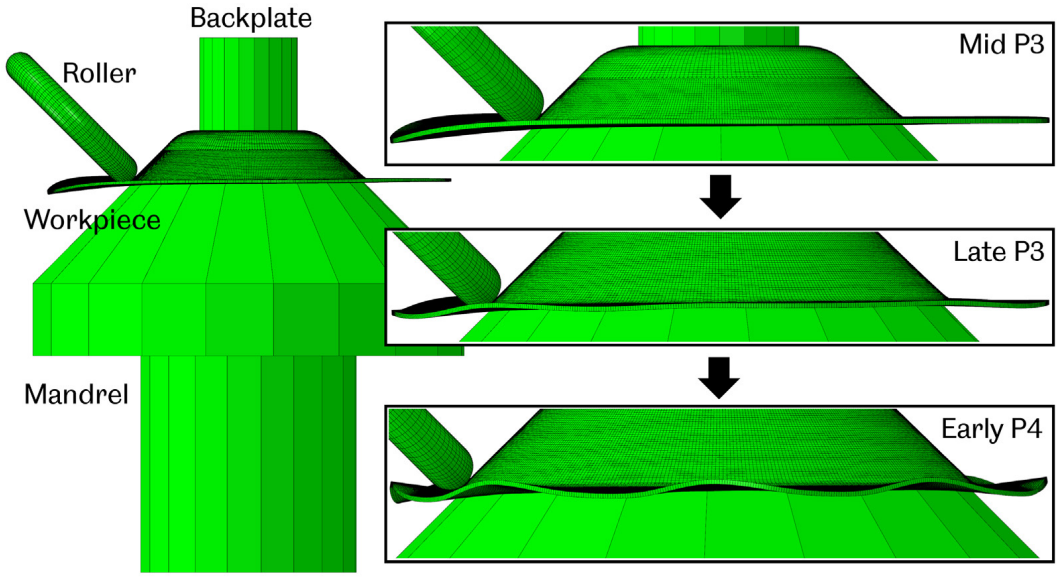

Figure 4.6 Demonstration of mid phase 3 to early phase 4.

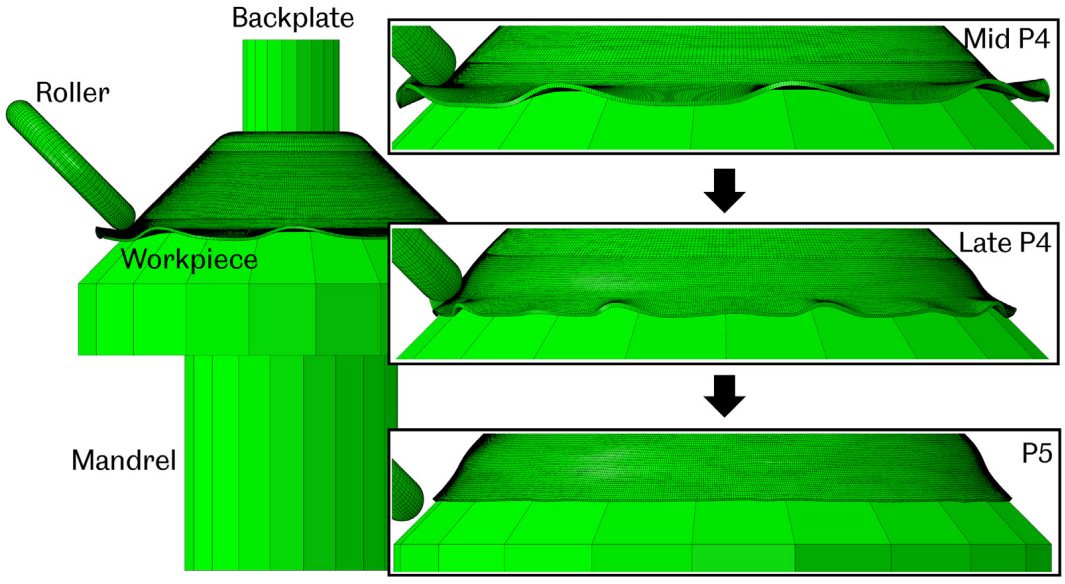

Figure 4.7 Demonstration of mid phase 4 to phase 5.

4.2 Design of the Spinning Experiment and Testing Procedures

Spinning experimental tests are conducted to achieve two objectives:

- To obtain the thickness results in different locations of the deformed workpiece to validate the spinning FE models developed in Chapter 3.
- To obtain the wrinkling initiation timing by analysing the vibration waveform results and comparing them with the spinning testing results.

Several conclusions are obtained in Chapter 3. Comparing the spinning experimental test results with the spinning FE modelling results can validate the FE models and prove that the accuracy of the FE modelling results is acceptable. The experimental test results can also validate the key findings obtained in Chapter 3.

The material to manufacture the spinning workpiece is aluminium alloy AA5251 – H22. The spinning workpiece has a 140 mm diameter and a 1 mm thickness. The dimensions of the mandrel, the roller and the workpiece are identical to the dimensions of the spinning FE models developed in Chapter 3. Spinning experimental tests with different mandrel speeds and different feed ratios are conducted, and the process parameters of the spinning tests are listed in Table 4.1. Tests No.2, No.9 and No.10 have corresponding spinning FE models. Additional tests were performed with different processing parameters for more comprehensive results.

Table 4.1 Process parameters for the shear spinning tests.

Test No.	Mandrel speed (RPM)	Feed ratio (mm/rev)	Corresponding spinning FE model
No.1	200	1.0	-
No.2	200	1.5	Spinning FE model No.1
No.3	200	2.0	-
No.4	500	1	-
No.5	500	1.25	-
No.6	500	1.5	-
No.7	500	2.0	-
No.8	1000	0.25	-
No.9	1000	1	Spinning FE model No.6
No.10	1000	1.25	Spinning FE model No.7

4.3 Experiment Results Analysis and Discussion

In this section, spinning experimental tests are conducted as the test plan shown in Table 4.1. Different results are analysed, including thickness distribution and vibration waveform results. The measured thickness distribution results from the spinning experimental tests are used to validate the spinning FE models developed

in Chapter 3. After the models are validated, the key findings in Chapter 3 are also validated and can be further included in the vibration waveform results analysis.

4.3.1 Thickness Result Analysis for FE Modelling Validation

The FE spinning modelling validation is performed by comparing the thickness distribution results between spinning FE model No.7 and spinning test No.10, and both processes have identical 1000 RPM mandrel speed and 1.25 mm/rev feed ratio. The spinning FE model No.7 is selected because it is severely wrinkled, and comprehensive results are obtained for comparison. As defined in Chapter 3, in a severely wrinkled model, wrinkling occurs in the early stage, and excessive distortion occurs in the late stage of the spinning because the roller does not successfully flatten the severely wrinkled surface of the workpiece. The workpieces of the spinning test and the corresponding FE model No.7 are shown in Figure 4.8.

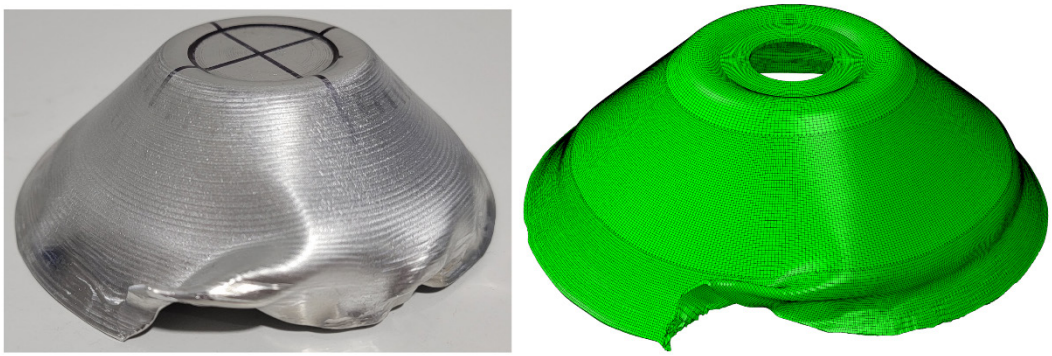

(a) (b)

Figure 4.8 Deformed workpieces of (a) spinning test No.10 and (b) spinning FE model No.7 with 1.25 mm/rev feed ratio.

(a) (b)

Figure 4.9 Deformed workpieces of (a) test No.8 (0.25 mm/rev feed ratio) with high-quality surface finishing and (b) test No.1 (1.0 mm/rev feed ratio) with visible indentations.

The surface finishing of test No.8 with smaller feed ratios (0.25 mm/rev) is better than test No.1 with higher feed ratios (1.0 mm/rev), as shown in Figure 4.9. The

indentations on the workpiece surface of test No.10 are visible. In the spinning process, the roller leaves helix indentation on the workpiece surface if the feed ratio is relatively high, as shown in Figure 4.8 (a) and Figure 4.9 (b). It is a limitation of the spinning FE modelling that the roller indentation cannot be modelled. The Indentation left by the roller also proves that the minor wrinkling has affected surface quality, as stated in Chapter 3, from the aspect of the uneven thickness distribution of the minor wrinkling workpiece.

The original plan to compare the thickness distribution is to select multiple locations along the radius direction from the workpiece centre to the edge and measure the thicknesses in these locations. Due to the limitation of the micrometre, the thickness measurement cannot start from the location close to the workpiece centre. The micrometre to measure the workpiece thickness and the illustration of the thickness measurement is shown in Figure 4.10.

(a)

(b)

Figure 4.10 (a) the micrometre for the thickness measurement and (b) the illustration of the limitation in thickness measurement.

Since the workpiece is eventually excessively distorted, the measurement cannot proceed after the excessive distortion has occurred. Tests with excessive distortion are manually stopped when the workpieces wrinkle most severely. The time point to stop the test is determined by the vibration waveform when it reaches the greatest wrinkling wave amplitude. The timing when the workpiece wrinkles most is determined by the vibration waveform. The process is paused when the amplitude of the vibration waveform reaches the maximum. The unfinished workpiece at the paused timing is considered the most severely wrinkled time and has the greatest wrinkling wave amplitude. The locations to measure the thickness distribution are shown in Figure 4.11 (a). Two straight lines mark the wrinkling bottom and top lines from the workpiece centre point in the radial direction. The dashed lines (blue and red) mark the location where the thickness distribution cannot be measured due to the micrometre limitation. The solid lines (blue and red) mark the location where to measure the thickness distribution. There is a 35 mm distance from the measurement starting point toward the workpiece centre being measurable due to the limitation of the micrometre. To minimise human errors during the measurement, the thickness results are recorded by using the mean values of the measurements from four different locations of the wrinkling top and bottom lines, as shown in Figure 4.11 (a). The schematic diagram of the points to measure is shown in Figure 4.11 (b). Since the workpiece radius is 70 mm, the 35 mm distance starting from the centre is neglected, and the remaining 35 mm is divided by six 5 mm intervals. Thus a total of seven points are measured on each wrinkling top or bottom line.

The thickness results of the locations on the wrinkling top and bottom lines of spinning test No.10 and spinning FE model No.7 are shown in Figure 4.12. Firstly, the spinning experimental tested workpiece and the workpiece modelled by FE are severely wrinkled and excessively distorted, as shown in Figure 4.8. Secondly, the thickness distribution comparison between the experimental test and the FE modelling shows acceptable deviations. The maximum deviation of the thickness results in Figure 4.12 (a) for the wrinkling top line is 8.51% at 55 mm in the radius direction, with 0.86 mm (test) and 0.94 mm (FE modelling). For the wrinkling top line in Figure 4.12 (b), the maximum error is 9.47% also at 55 mm in the radius direction with similar values of 0.86 mm (test) and 0.95 mm (FE modelling). These results indicate that the spinning FE models correlate well with the corresponding spinning experimental test. The similar thickness results on the wrinkling top and bottom lines suggest that the wrinkling top and bottom (wrinkling waves) are symmetrical when considering the thickness aspect, and the thickness distribution comparisons prove the conclusion.

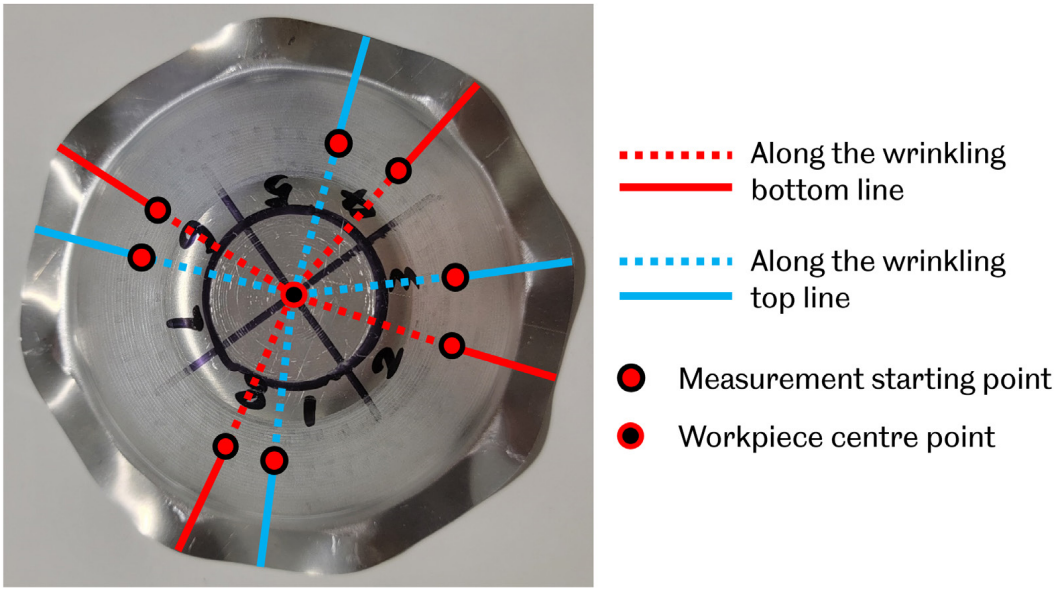

(a)

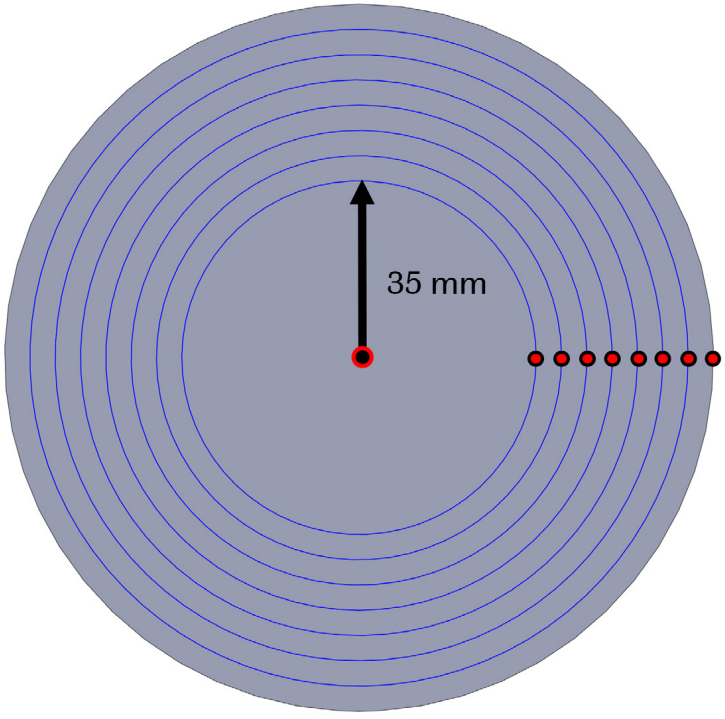

(b)

Figure 4.11 The schematic diagram of (a) the location to measure the thickness and (b) detailed locations as seven points to measure.

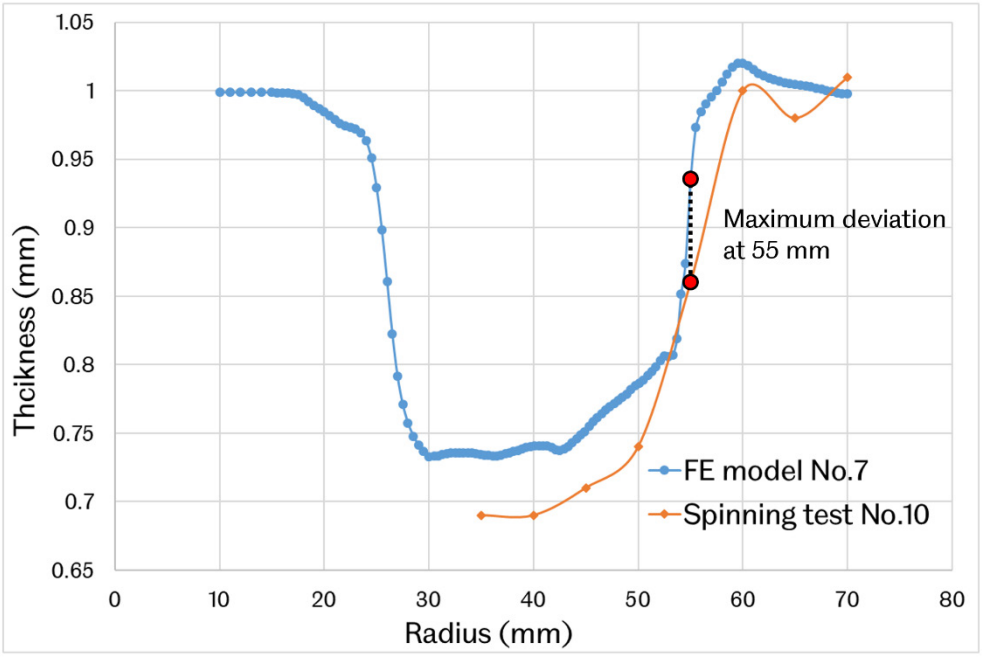

(a)

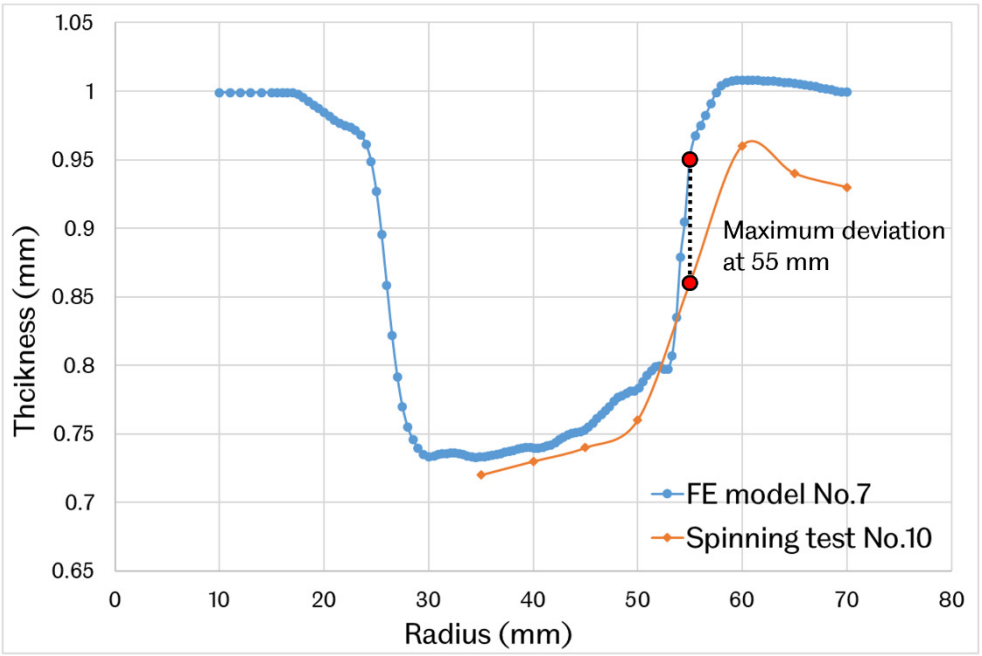

(b)

Figure 4.12 Thickness distribution comparison between spinning FE model No.7 and test No.10 on the (a) wrinkling top lines and (b) wrinkling bottom lines.

4.3.2 Wrinkling wave amplitude analysis

As mentioned in Chapter 3, multiple wrinkling waves always occur around the workpiece flange when the feed ratio exceeds the forming limit feed ratio. This section focuses on analysing the results related to the wrinkling waves of the spun workpiece. Two results from the spinning experimental test are the wrinkling wave

amplitude and the number of wrinkling waves. The results are also compared with the results of the corresponding spinning FE models. The test results are processed and presented in Table 4.2. For test No. 8, the spinning workpiece is wrinkling-free, meaning that the wrinkling does not occur in the test, and the wrinkling wave is not formed. Thus the wrinkling wave amplitude and the number of wrinkling waves cannot be measured. There are spinning models developed for test No.2, test No.9 and test.10. There are no FE models developed for other tests, and the wrinkling wave amplitude of FE models thus can not be compared.

Table 4.2 Wrinkling wave amplitude of spinning tests.

Test No.	Mandrel Speed (RPM)	Feed Ratio (mm/rev)	Spinning outcome (WF/MW/SW)	Wrinkling wave amplitude of tests (mm)	Wrinkling wave amplitude of FE models (mm)	Number of wrinkling waves
1	200	1	MW	4.25	-	8
2	200	1.5	SW	7.69	6.85	8
3	200	2	SW	8.93	-	7
4	500	1	MW	4.06	-	7
5	500	1.25	SW	5.93	-	7
6	500	1.5	SW	7.36	-	7
7	500	2	SW	9.14	-	7
8	1000	0.25	WF	-	-	-
9	1000	1	MW	3.44	3.48	8
10	1000	1.25	SW	6.75	6.24	8

* WF – wrinkling-free; MW – minor wrinkling; SW – severe wrinkling

Wrinkling wave amplitude is determined from a mean value calculated from the sum of all the wrinkling waves on a spinning workpiece for both spinning FE modelling and test. The method to measure the wrinkling wave amplitude of a wrinkling wave is shown in Figure 4.13. The wrinkling wave amplitude is also measured by the micrometre when the deformed workpiece is placed on the table. For the wrinkling wave amplitude of FE models presented in Table 4.2, the results are obtained similarly by calculating the difference between the horizontal coordinates of the wrinkling tops and bottoms in the spinning FE models. The horizontal table surface acts as the dashed line in Figure 4.13 between the two wrinkling bottoms. An example of test No.9 and test No.10 with different wrinkling wave amplitudes is shown in Figure 4.14.

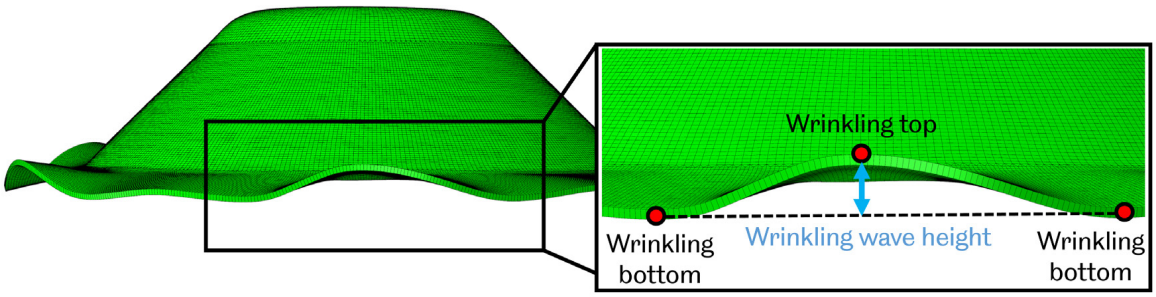

Figure 4.13 The schematic diagram of the wrinkling wave amplitude.

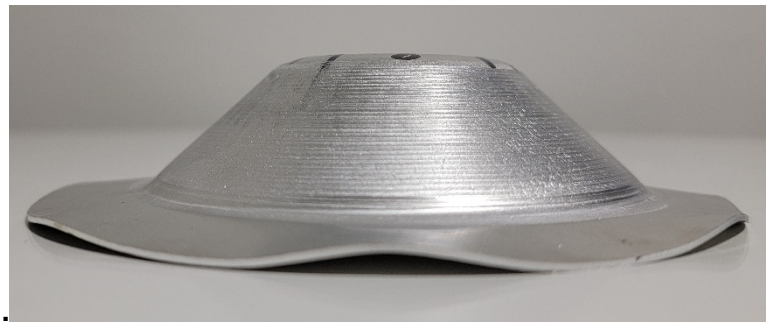

(a)

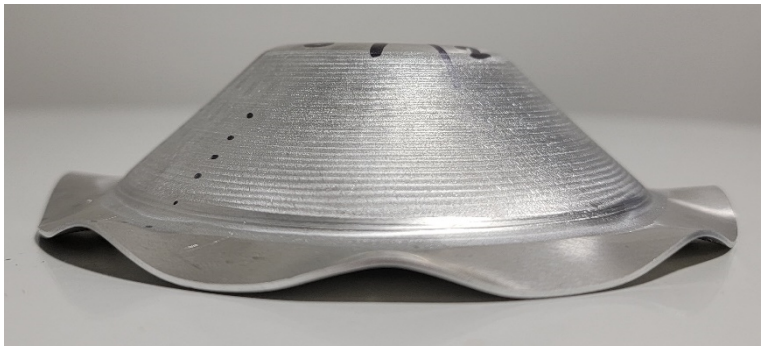

(b)

Figure 4.14 Two wrinkled workpieces of (a) test No.9 with relatively small wrinkling wave amplitude and (b) test No.10 with relatively large wrinkling wave amplitude.

For the number of wrinkling waves, no obvious difference between the tests is found. All the minor and severe wrinkling tests have seven and eight wrinkling waves on the flange. The workpieces with seven wrinkling waves are produced by using low to high feed ratios (1.0 to 2.0 mm/rev) with different mandrel speeds (200 RPM and 500 RPM). Hence, the mandrel speeds and the feed ratios in the spinning experimental tests completed do not affect the number of wrinkling waves. The wrinkling waves in the spinning test are similar to the number of waves obtained from the spinning FE modelling. Only severely wrinkled waves are visible enough to be detected in the spinning test. As summarised in Chapter 3, wrinkling is defined to be formed if the circumferential strains become tensile. However, some of the

wrinkling waves have relatively low circumferential strains. The small wrinkling waves cannot be classified into the number of wrinkling waves. These small wrinkling waves are not detectable since the strain results can not be measured in the spinning experimental tests.

A very obvious pattern is that the wrinkling wave amplitude increases with the feed ratio. A higher feed ratio results in a great wrinkling wave amplitude. Also, the wrinkling wave amplitude increases with the feed ratios for tests with all three mandrel speeds: tests No.1 to No.3 with 200 rpm mandrel speed; tests No.4 to No.7 with 500 rpm mandrel speed; and tests No.9 to No.10 with 1000 rpm mandrel speed. Also, the wrinkling wave amplitude results are similar for tests with the same feed ratio but different mandrel speeds: test No.1 (4.25 mm); test No.4 (4.06) and No.9 (3.44 mm), with the same feed ratio of 1.0 mm/rev but different mandrel speeds of 200, 500 and 1000 RPM. Tests No.1 and No.9 have the greatest wrinkling wave amplitude difference of 23.5%. However, the wrinkling wave amplitudes for test No.1 and test No.9 are relatively small, and human errors in height measurement might cause a greater result deviation. Wrinkling wave amplitude results deviation between other tests with the same feed ratios is much smaller than that 23.5%. Only 4.48% deviation is found between test No.2 and test No.6; 2.35% between test No.3 and test No.7; 18% between test No.4 and test No.9; and 13.8% between No.5 and No.10. Hence, it can be concluded that the mandrel speed does not affect the wrinkling wave amplitude, and the feed ratio is the determining factor. The wrinkling wave amplitude also represents the wrinkling severity in the spinning test. This observation is also summarised from the spinning FE models in Chapter 3. In spinning FE models, the circumferential strains on the wrinkling tops and bottoms, as well as the wrinkling wave amplitudes, increase with the feed ratios; thus, these FE models are validated by the spinning experimental test results. The wrinkling wave amplitude results of the FE models corresponding to test No.2, test No.9 and test No.10 also indicate a very agreeable correlation between the results of FE models and the tests. Thus, it can be further concluded that the feed ratio determines the wrinkling severity. The dynamic effect due to different strain rates in material deformation caused by the different mandrel speeds also does not affect the wrinkling severity.

4.3.3 Vibration Result Analysis

Previous literature did not investigate the connection between the dynamic effect and the wrinkling initiation. Spinning processes with identical feed ratios but different mandrel speeds have identical outcomes in wrinkling. For example, if a process with a feed ratio is wrinkling-free, the outcome of any other processes with

the same feed ratio but proportional changes in the mandrel speed and feed rate will eventually be wrinkling-free. The same conclusion is true for minor or severe wrinkling cases, respectively. The vibration waveform results are collected from the spinning experimental tests to further investigate the connection between the dynamic effect and the different strain rates induced by the various mandrel speeds. The vibration waveform results of nine spinning tests, except test No.8, are shown in Figure 4.15, Figure 4.16, Figure 4.17 and Figure 4.18. Various mandrel speeds and feed ratios result in different spinning times. The spinning time is normalised to make the results comparable between the tests with different mandrel speeds. The wrinkling initiation timing of each spinning test is marked in the corresponding diagram. The summary of the timing is presented in Table 4.3.

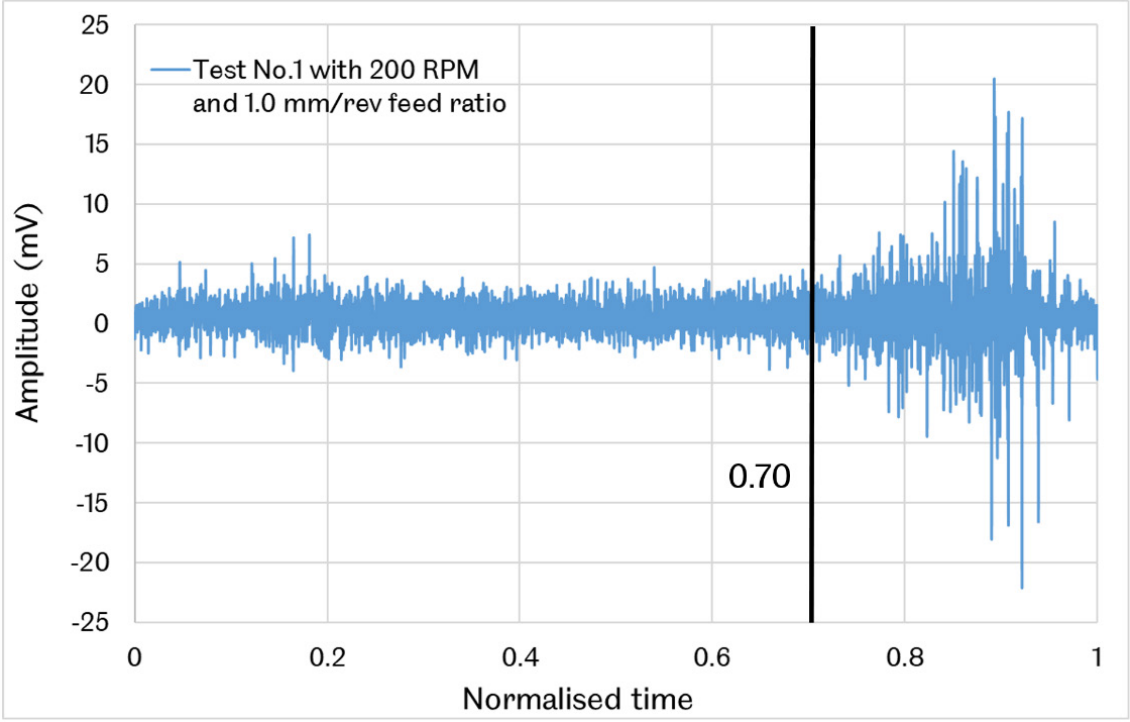

(a)

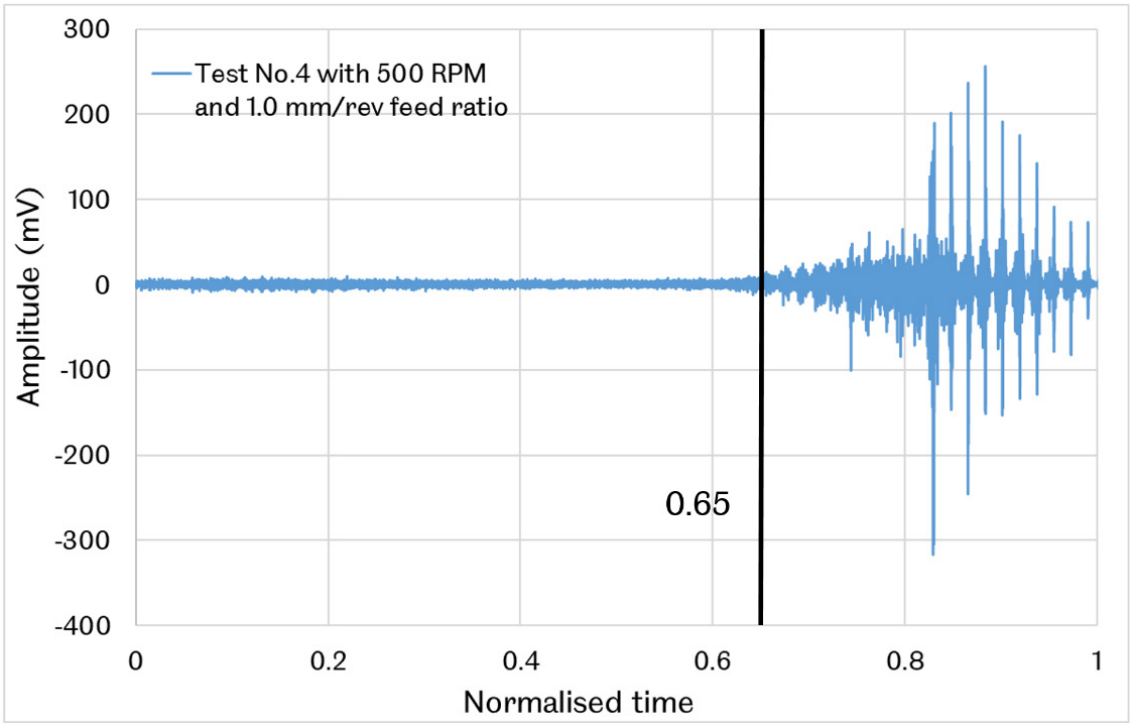

(b)

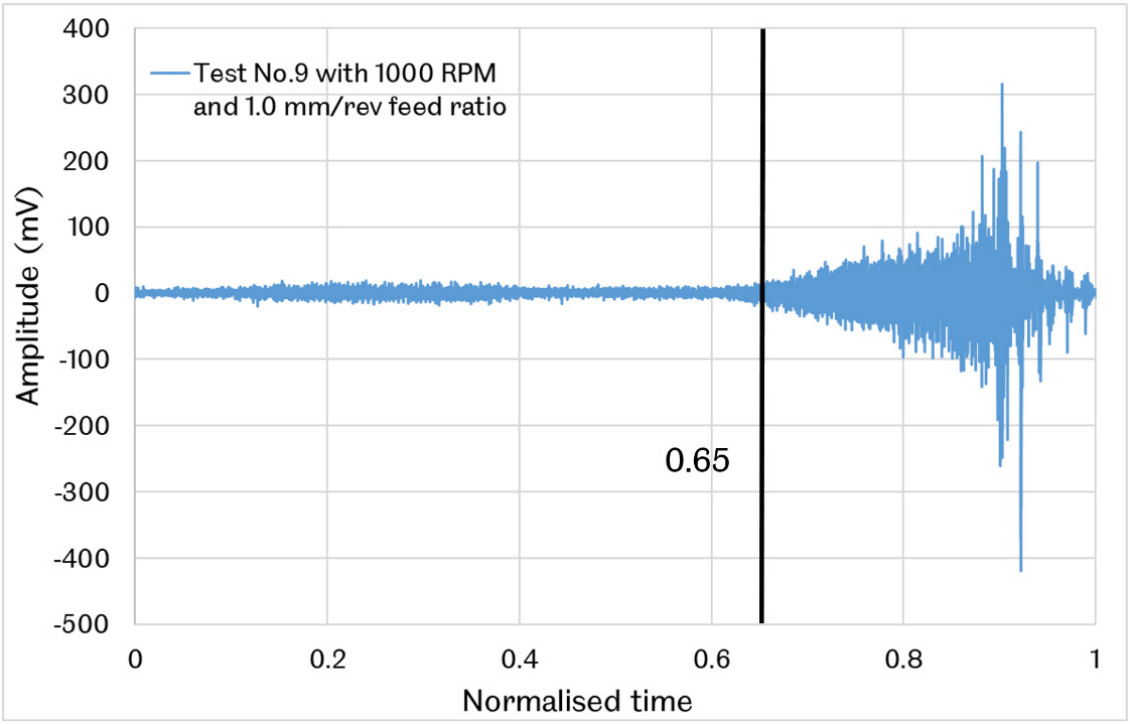

(c)

Figure 4.15 Vibration waveforms of tests with 1.0 mm/rev feed ratio and (a) test No.1 with 200 RPM; (b) test No.4 with 500 RPM; and (c) test No.9 with 1000 RPM mandrel speeds.

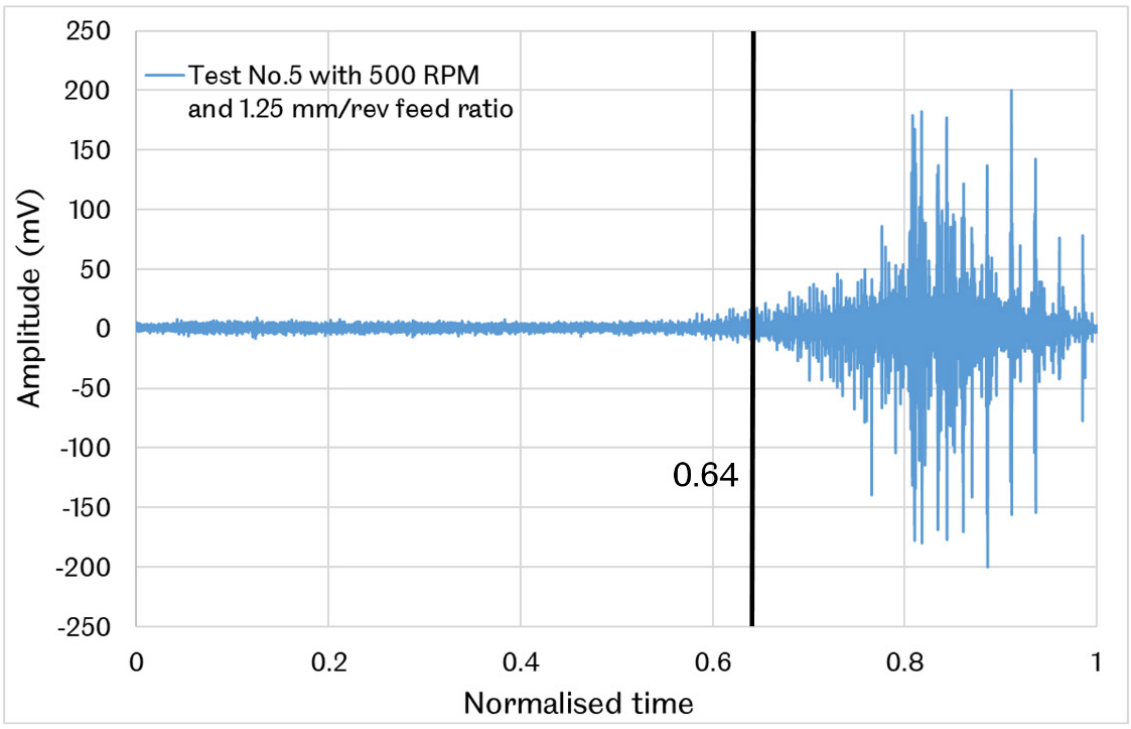

(a)

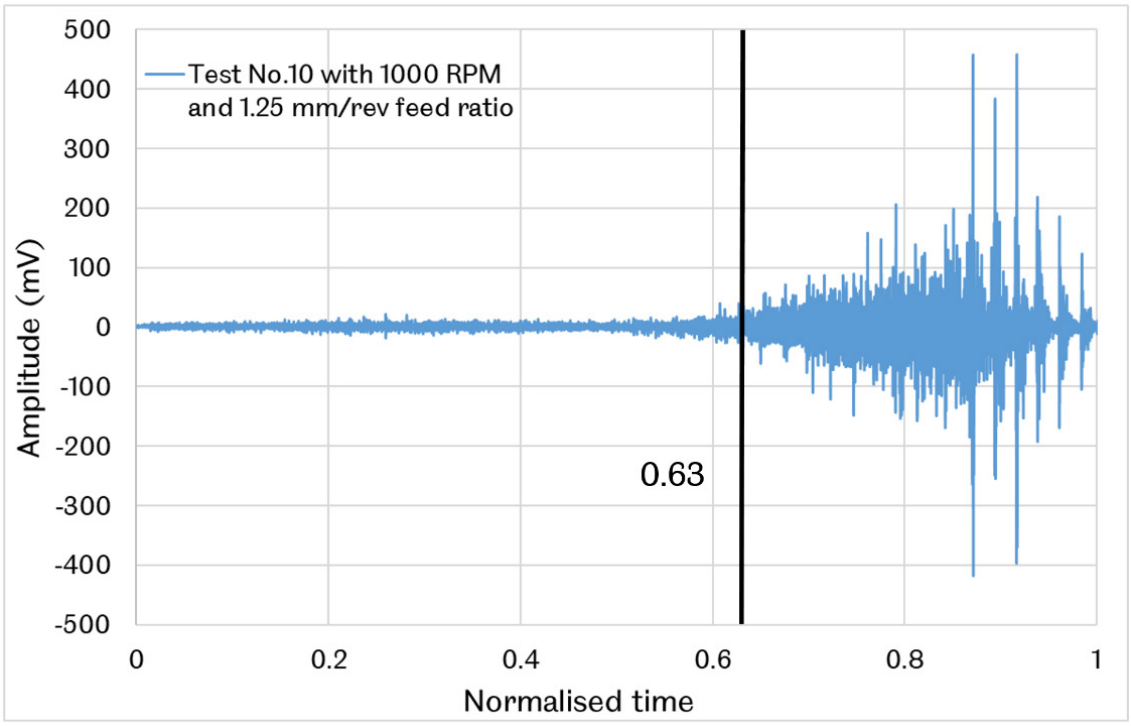

(b)

Figure 4.16 Vibration waveforms of tests with 1.25 mm/rev feed ratio and (a) test No.5 with 500 RPM and (b) test No.10 with 1000 RPM mandrel speeds.

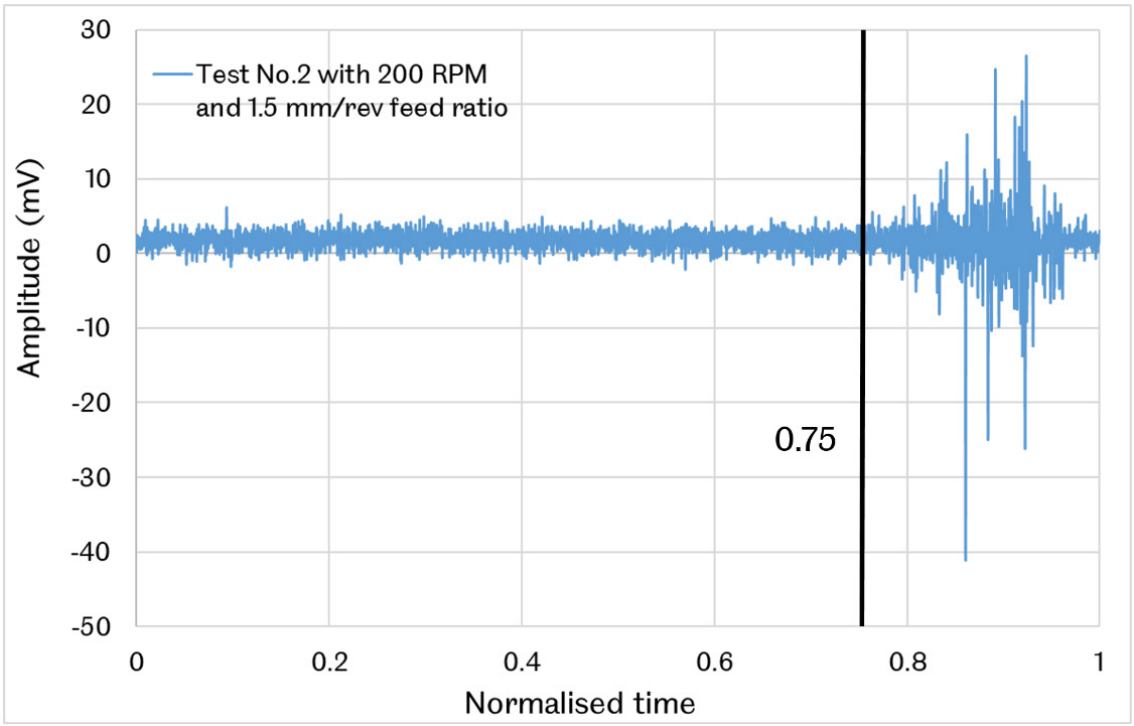

(a)

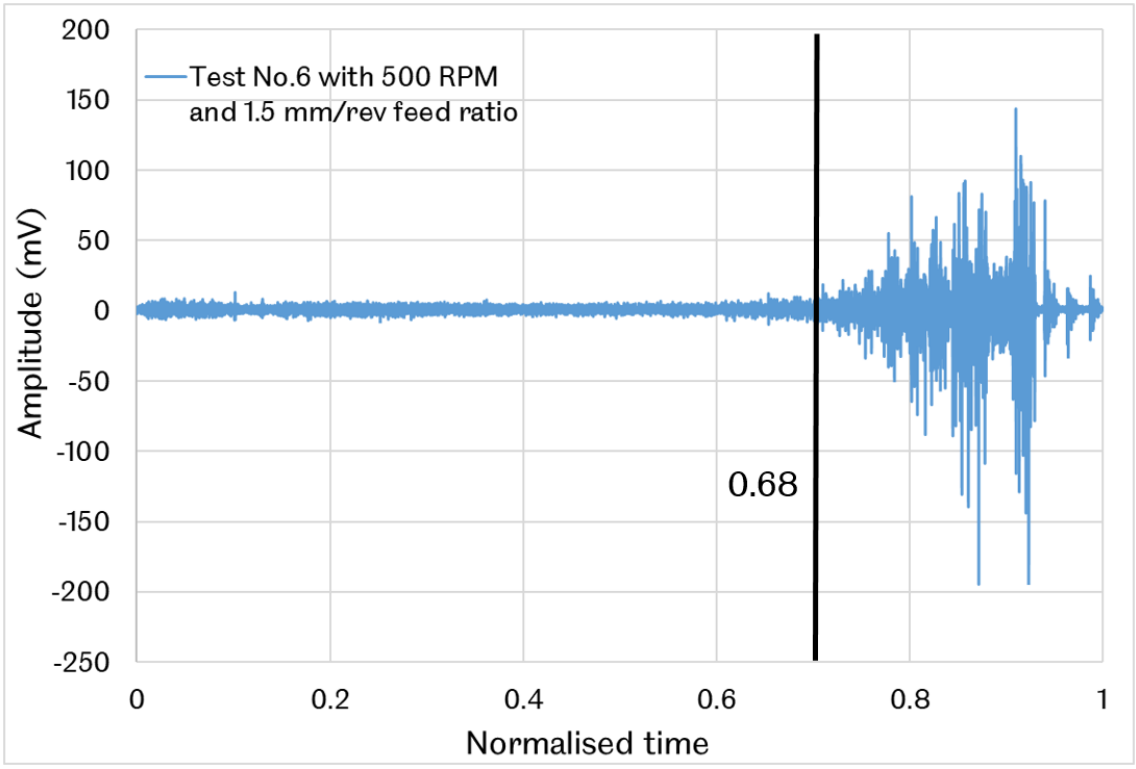

(b)

Figure 4.17 Vibration waveforms of tests with 1.5 mm/rev feed ratio and (a) test No.2 with 200 RPM and (b) test No.6 with 500 RPM mandrel speeds.

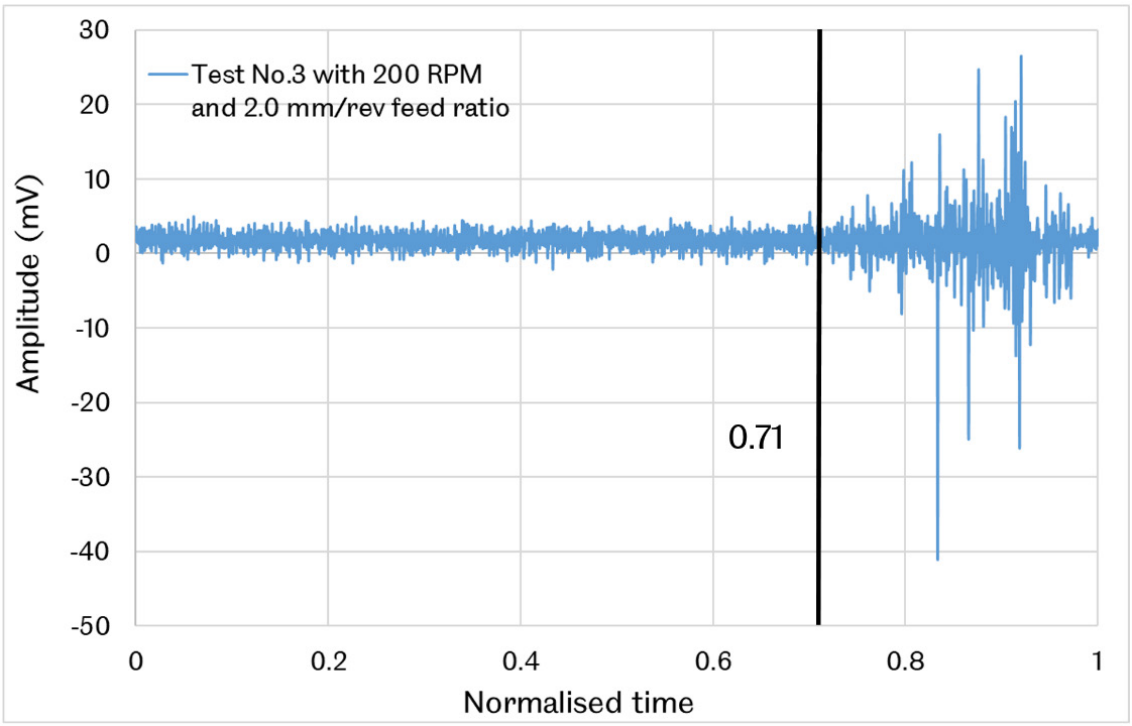

(a)

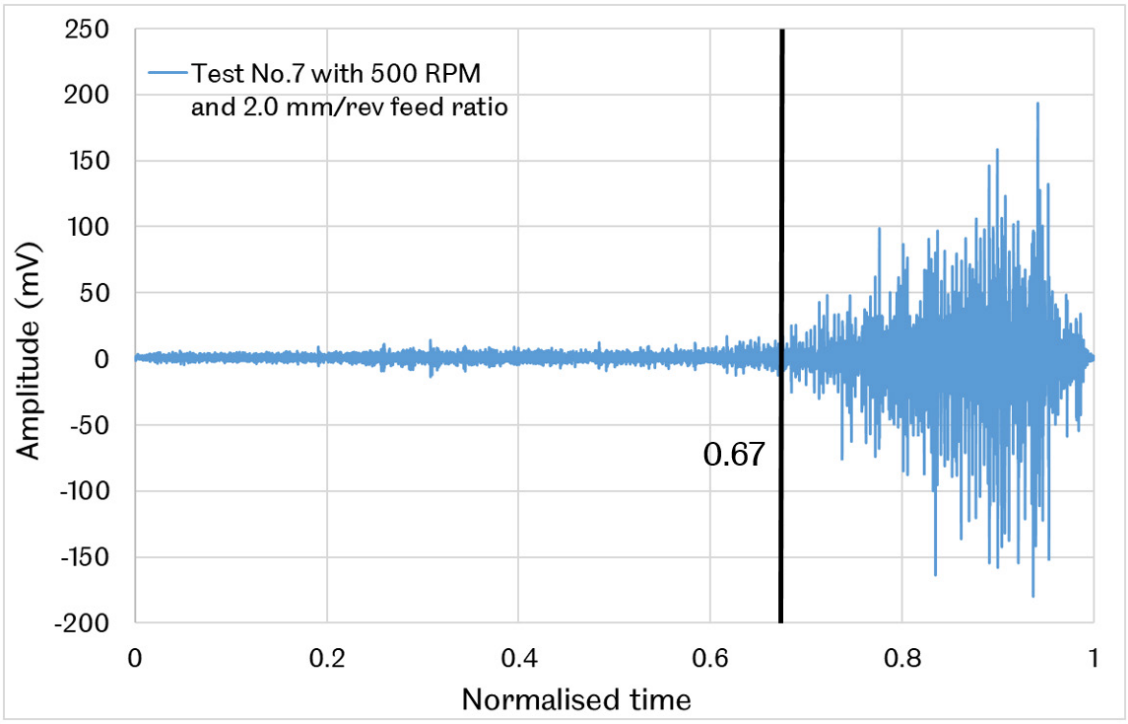

(b)

Figure 4.18 Vibration waveforms of tests with 2.0 mm/rev feed ratio and (a) test No.3 with 200 RPM and (b) test No.7 with 500 RPM mandrel speeds.

Table 4.3 Wrinkling initiation timing of the spinning test.

Test No.	Mandrel Speed (RPM)	Feed Ratio (mm/rev)	Normalised wrinkling initiation timing	Normalised wrinkling initiation timing in spinning FE modelling
1	200	1	0.70	-
2	200	1.5	0.75	0.46
3	200	2	0.71	-
4	500	1	0.65	-
5	500	1.25	0.64	-
6	500	1.5	0.68	-
7	500	2	0.67	-
8	1000	0.25	-	-
9	1000	1	0.65	0.52
10	1000	1.25	0.63	0.56

The method to determine the wrinkling initiation timing is introduced in section 4.1 as the vibration waveform amplitude starts to increase beyond the normal values of the steady process state. There are good correlations between the spinning tests for the normalised wrinkling initiation timing, as shown in Table 4.3. The timing results vary in a range from 0.63 to 0.75. The maximum result deviation of the wrinkling initiation time for all the tests is 19.04% between test No.5 and test No.6. For the tests with identical feed ratios, the maximum result deviation is 15.3% between test No.2 and test No.6. The minimum result deviation is 3.1% between test No.3 and test No.7. Tests No.2, No.9 and No.10 have their corresponding FE models. The results of normalised wrinkling initiation timing of spinning tests are greater than in the FE modelling, and the maximum deviation is 63% in test No.2. In the FE modelling, the wrinkling is determined when the circumferential strain becomes tensile. At the early stage of wrinkling, the strains are insignificant to cause detectable unevenness on the workpiece surface. The vibration waveform amplitude only increases when the surface unevenness is significant enough to be detected by the vibration sensor. Hence the normalised wrinkling initiation timing is delayed in the spinning test. FE modelling captures the negligible tensile circumferential, which cannot be detected in the test by the vibration sensor at the early stage of wrinkling.

As shown in Figure 4.15 (a), Figure 4.17 (a) and Figure 4.18 (a), spinning tests No.1 to No.3 with 200 RPM mandrel speed has the lowest vibration waveform amplitudes ranging from –40 to 30 mV. Although a slower mandrel speed does not affect the wrinkling initiation, with a lower strain rate, the roller processes the workpiece slower, and the vibration is less intense. This pattern also can be found in the tests

with 500 and 1000 RPM mandrel speeds. For spinning tests No.4 to No.7 with a 500 RPM mandrel speed, the waveform amplitudes range from –200 to 200 mV, as shown in Figure 4.15 (b), Figure 4.16 (a), Figure 4.17 (b) and Figure 4.18 (b). For spinning tests No.9 to No.10 with a 1000 RPM mandrel speed, the waveform amplitudes range from –500 to 500 mV, as shown in Figure 4.15 (c) and Figure 4.16(b). The test results correlate very well with the FE modelling results, with a maximum of 6% deviation.

To summarise, the vibration waveform results further prove that the wrinkling initiation timing is not affected by the dynamic effect and different strain rates induced due to different mandrel speeds. Hence, the strain rates in the wrinkling test developed in Chapters 5 and 6 are unnecessary to be as high as in the spinning tests. The loadings applied to the wrinkling test specimen only need to be converted from the feed ratios in the shear spinning process. The wrinkling testing method can be considered successful if the loadings representing the corresponding feed ratios can cause similar wrinkling deformation on the specimen.

Currently, the vibration is quantified and recorded as the voltage waveform (mV). The amplitude intensifies and fluctuates when wrinkling occurs. The waveform maintains a stable state without intense fluctuation in a wrinkling-free spinning process. Due to this characteristic, a waveform amplitude limit can be set to distinguish whether wrinkling occurs as a quality control method in the industry. For example, a CNC spinning process can be designed to stop automatically when excessive vibration is detected. A wrinkled spun part can be detected early in the manufacturing process without a post quality check. Generally, the automatic quality control method of setting a vibration waveform amplitude limit will improve manufacturing efficiency and lower the overall cost.

4.4 Summary of Conclusion

In this Chapter, the spinning experimental tests with the mandrel speed of 200, 500, and 1000 RPM and the feed ratios of 1.0, 1.25, 1.5, and 2.0 mm/rev are performed. Based on the experimental test results, the following key points are concluded:

- The thickness results of the spun workpiece are measured, and the spinning FE models are validated by a good correlation between the spinning experiment and FE simulation.
- The wrinkling wave amplitudes are measured from the wrinkled spun workpiece and compared with the spinning FE results. The results confirm that the dynamic effect and various strain rates induced by different mandrel speeds do not affect the wrinkling wave amplitude. Furthermore, it is

observed that the wrinkling wave amplitude increases with the increasing feed ratio.

- The vibration waveforms are obtained, and the wrinkling initiation time results are compared with spinning FE results. The results further prove that the wrinkling initiation is not affected by the dynamic effect and different strain rates induced by different mandrel speeds in the spinning process. The vibration waveform results also indicate that the vibration is less intensive for tests with relatively lower mandrel speeds.

5 FE Modelling of Specimen Design for the New Wrinkling Testing Method

This chapter develops the FE models for the new wrinkling testing method. Section 5.1 introduces the concept of the new wrinkling testing method and the BTBC rig for the test. Section 5.2 presents the six most meaningful FE models developed for developing the testing method and specimen design, including the modifications of the specimen geometry and the boundary conditions of the test. Section 5.3 discusses the FE modelling results of the six models and the main findings. Section 5.4 presents the summary of this chapter.

5.1 Concept of the New Wrinkling Testing Method

As previously discussed in Chapter 2, the uniaxial and biaxial tensile and other conventional testing methods cannot test the material formability for wrinkling failure in the shear spinning process. These testing methods cannot apply the deformation modes relative to wrinkling deformation to their specimens. Thus, a new testing method is required to apply the corresponding deformation modes on the newly designed specimens to test the wrinkling failure. The new testing method is developed in this chapter based on a previously developed biaxial tension under the bending and compression (BTBC) rig. The specimen and the boundary conditions are aimed at that can be achieved in the experiments. The rig was initially developed to apply different loadings to a cruciform specimen biaxially. The rig has been modified for the wrinkling test. In order to create wrinkling deformation of a specimen to represent an accurate condition in the shear spinning process, the design of the specimen geometry should be optimised. The geometry of the specimen has gone through multiple iterations by developing many FE models to optimise the specimen design.

As previously stated, the BTBC rig is selected as the testing platform. The photo of the BTBC rig, including the annotations of the key components, is shown in Figure 5.1. Two rails and motors control the axial movements of the four clamps, which constrain the four arms of the cruciform specimen. Thus the loadings, both axial compression and tension, can be applied to the specimen. The original purpose of the BTBC rig was to test the material formability under different deformation modes

with a cruciform specimen design for the incremental sheet forming process, developed by a previous PhD student [2]. The CAD drawing of the BTBC rig to illustrate the material deformation is shown in Figure 5.2 (a). The bending is applied as the bending depth by adjusting the threaded hand wheel on the bending tool above the centre of the two intersected loading axes. Normal compression is applied by the spring and the cap on the lower side of the specimen. The rig successfully tested specimens under various loading conditions with adjustable strain ratios by changing the compression and elongation speeds of the clamps on the two axes, as shown in Figure 5.2 (b).

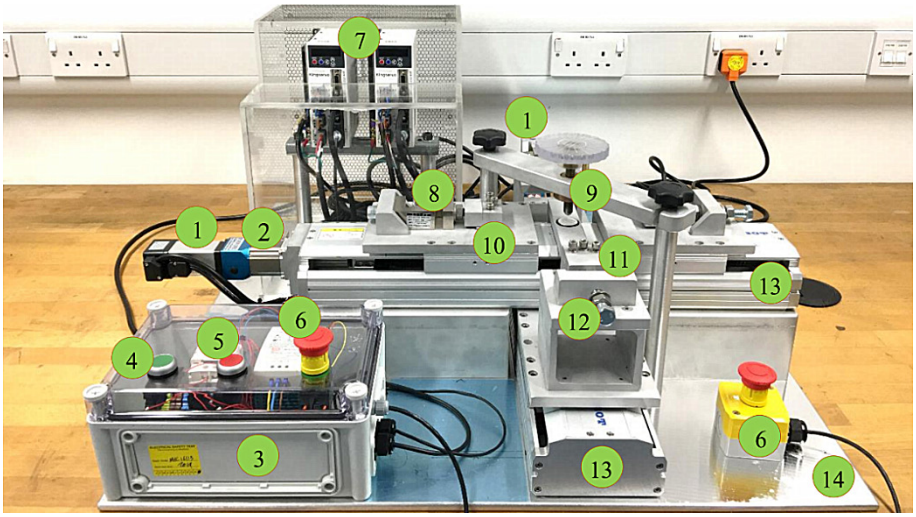

Figure 5.1 Critical components of the BTBC rig: 1. motor; 2. gearbox; 3. power control box; 4. power-on button; 5. power-off button; 6. emergency stop button; 7. motor speed control units; 8. load cell; 9. bending tool; 10. spring; 11. clamp; 12. clamp location adjusting screw; 13. bi-directional linear screw (inside) and 14. base plate [89]**.**

Table 5.1 The applicable loadings of the BTBC rig on axis 1 and 2.

Loading condition No.	Axis 1	Axis 2
Loading No.1	Compression	Compression
Loading No.2	Elongation	Compression
Loading No.3	Compression	Elongation
Loading No.4	Elongation	Elongation
Loading No.5	Elongation	Idle
Loading No.6	Compression	Idle
Loading No.7	Idle	Elongation
Loading No.8	Idle	Compression

The BTBC rig can apply different loadings simultaneously on axes 1 and 2. These loadings are also separately controlled and adjustable. The loading conditions

applied to the cruciform specimen are shown in Figure 5.2 (b). The applicable loading conditions that the BTBC rig can provide are listed in Table 5.1.

There are four clamps to fix the four arms of the cruciform specimen on the BTBC rig. These four clamps further control the loadings, axial elongation, and compression applied to axis 1 and 2, respectively, as shown in Figure 5.2 (b). The loadings are controlled by the input moving speeds and directions to the clamps. The two clamps on the same axis can only move towards or away from the axes centre with the same speed, as well as the two clamps on the other axis. The moving speeds are also constant after commencing the test. However, the moving speeds and the directions on the different axes can be different. The speeds and directions can only be adjusted before the test and remain constant throughout the test.

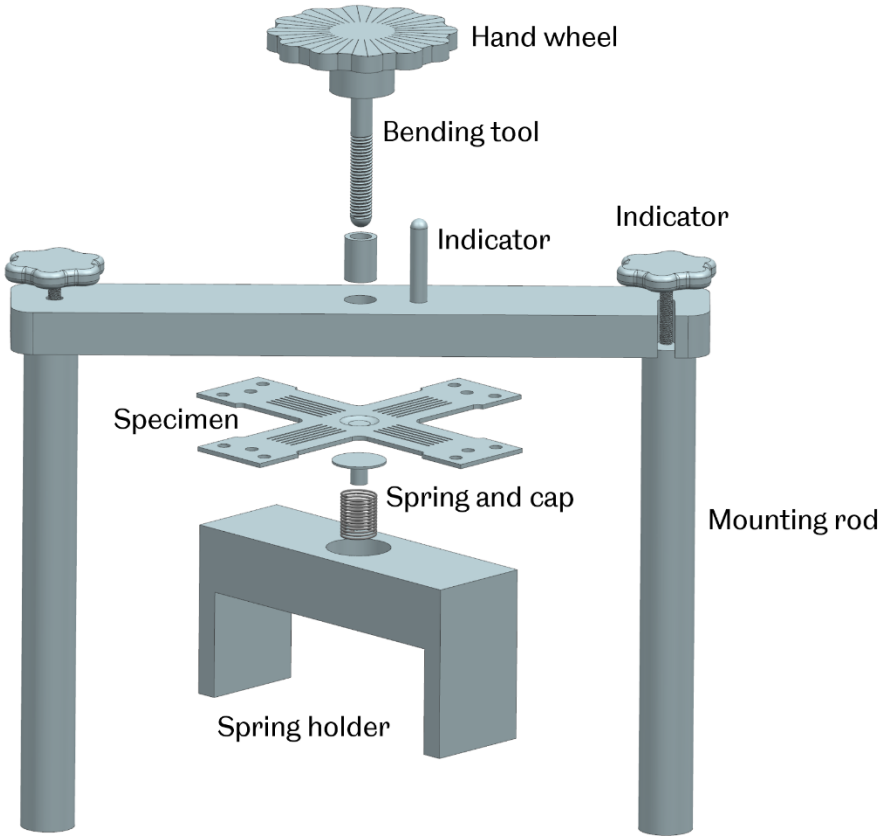

(a)

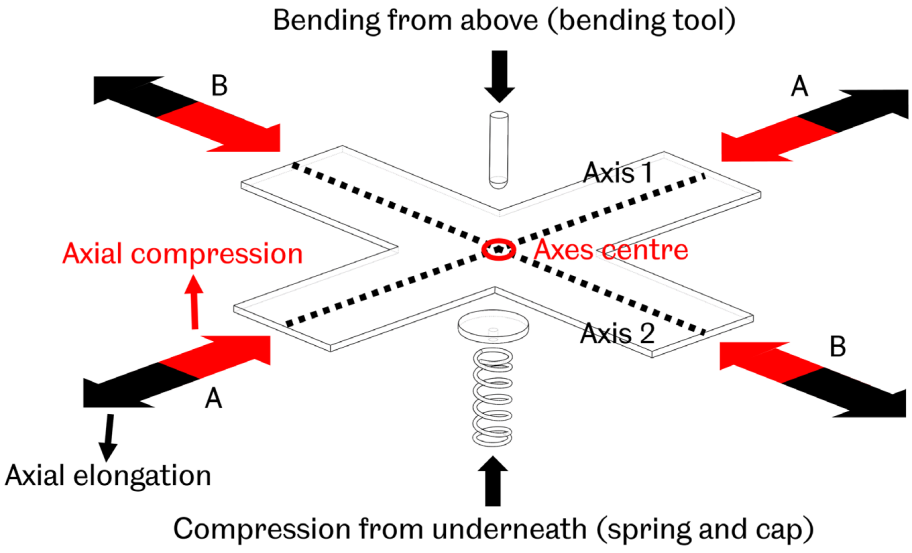

(b)

Figure 5.2 Schematic diagrams of the BTBC rig for multiaxial material deformation: (a) the assembly of the bending tool and (b) different loadings applied to the specimen.

The first reason to choose the BTBC rig as the testing platform is that the rig can apply the corresponding deformation modes to cause wrinkling deformation, which cannot be achieved by existing testing methods. The second reason is that the test conducted on the BTBC rig is much less dynamic than the spinning process conducted on the CNC lathe. The BTBC wrinkling test is also safer and less complicated without the highly rotational components like the mandrel and backplate on a CNC lathe. The third reason is that wrinkling deformation can be achieved without performing a complete spinning process to achieve wrinkling deformation. The deformation is isolated on the BTBC rig and can be further quantified and studied, which has never been done in the previous investigation.

To summarise, the aim of this study is to develop a wrinkling testing method, reproducing the deformation modes on the wrinkling testing specimen as that occurring in the shear spinning process. As a result, the strains on the wrinkling testing specimen should be similar to the strains on the spinning workpiece if similar deformation modes could be achieved on the wrinkling testing specimen. Comparing the strains on the wrinkling testing specimen and spinning workpiece can determine whether the deformation modes in the shear spinning are reproduced on the wrinkling testing specimen under certain loading conditions. These are applied as the boundary conditions in FE Models and will be studied in this chapter. The testing method simplifies the loadings induced by the rotating mandrel and the moving roller in spinning, isolating the wrinkling deformation from the highly dynamic spinning process. The objectives of this chapter are :

- To determine the boundary conditions applied to the wrinkling testing specimen. The boundary conditions should represent the boundary conditions in the shear spinning process, which cause wrinkling on the spinning workpiece.
- To determine the geometry of the wrinkling testing specimen. The geometry to achieve wrinkling deformation under applied boundary conditions in the wrinkling test should represent that in the shear spinning process.

5.2 FE Optimisation of Wrinkling Testing Design

The current section develops a number of BTBC FE models for the wrinkling test. The geometry of the wrinkling testing specimens and the boundary conditions applied to these specimens are gradually improved through iterations of these FE models. The current section introduces six FE models to illustrate the most significant findings in the study.

As mentioned in section 5.1, the ultimate objective is to design the wrinkling testing specimen and apply the corresponding boundary conditions to cause similar deformation modes in the shear spinning, thus, achieving similar strain results. The boundary conditions applied to the wrinkling test FE models are taken from spinning FE model No.10 as it is a model with severe wrinkling since the results obtained from this model are considered the most comprehensive in Chapter 3. To determine whether the strain results in the wrinkling FE test model represent spinning, the strain results in spinning FE model No.10 are considered reference strain results in the wrinkling test FE models to compare. If a good agreement between the results is found, the corresponding wrinkling test FE model/test design/specimen design can be considered a successful representation of the spinning process. Hence, the aim of developing FE models is to improve the specimen design through iterations and ultimately achieve similar wrinkling and strain results on the specimen. Also, the wrinkling test specimen and boundary conditions must be adaptable by the BTBC rig to test.

For the clarity of the discussion of the results, six FE models are named from wrinkling test designs A to F. For each model, the discussion is presented in four stages: 1. Aim of test design; 2. Specimen geometry and testing boundary conditions; 3. FE results and discussion; and 4. Modification and improvement are required for test design.

5.2.1 Wrinkling Test Design A

As a start of the testing method development, the geometry of the specimen in wrinkling testing FE model A is derived from the previous cruciform incremental sheet forming (ISF) specimen. Some of the features from the previous ISF specimen design remain in the current wrinkling test specimen A. For example, the overall geometry of specimen A is cruciform, and the method to reduce the strength of a certain section is to cut slots on the specimen.

Aim of test design A

The aim of the current model is to achieve wrinkling on the curved sections (gauge areas) of the test specimen, as shown in Figure 5.3 (a). Yoshida [105] test proved that applying compression to the specimen could cause wrinkling. As the first step of the study, specimen A is to test whether the BTBC rig can successfully cause wrinkling to the specimen.

Specimen geometry and boundary conditions of test design A

The specimen is cruciform with a cruciform central cut to reduce the strength of the specimen and make it easier to wrinkle when applying loadings to the four arms. The geometry of specimen A is shown in Figure 5.3 (a). The thickness of the specimen is 1 mm, and it is uniform across the entire specimen. The side view of the specimen is shown in Figure 5.3 (b). There are three screw holes on each end of the arm for fixing the specimens onto the clamps and allowing the screws to tighten the clamps on the arms to provide elongation or compression by friction between the contacting surfaces of the specimen and clamps.

For the geometry of the FE model, the screw holes are neglected. Screw holes do not affect the FE results as they are located at a noticeable distance from the curved sections (gauge areas) near the centre of the specimen. The prediction is that the curved sections will wrinkle upwards when applying loadings to the four arms of the specimen in axes 1 and 2. The FE model of the specimen is shown in Figure 5.4. Since the aim of the current model is to test whether the wrinkling deformation can be achieved on the BTBC rig, the boundary condition applied to the specimen is 0.2 mm/s compression speed on the four arms for 10 seconds toward the axes centre, shown in Figure 5.4. The compressing speed of 0.2 mm/s and compression time of ten seconds is selected as appropriate and controllable by the BTBC rig.

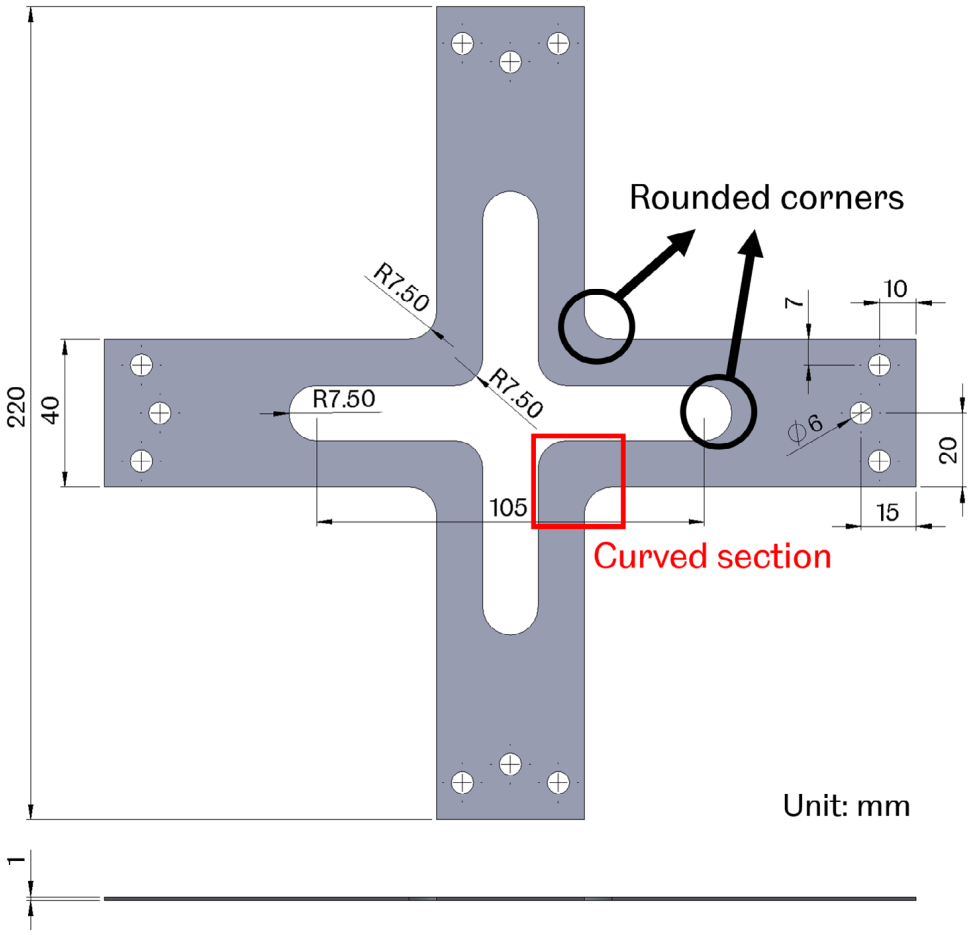

(a)

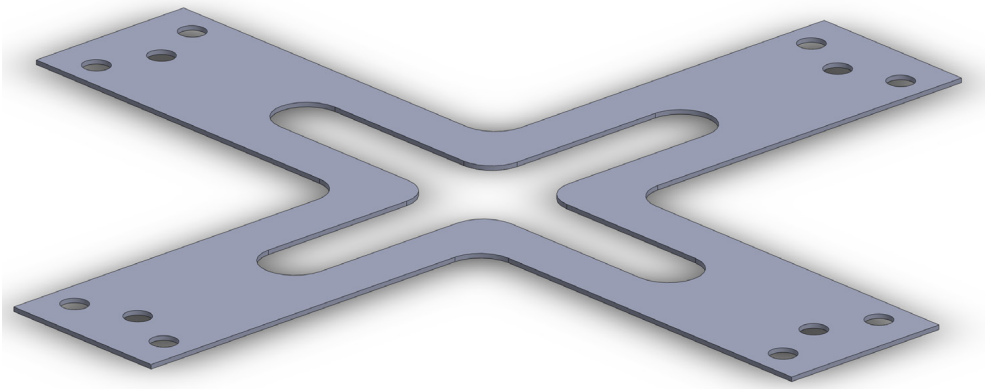

(b)

Figure 5.3 (a) Dimensions of the cruciform specimen A and (b) a side view to illustrate the uniform thickness.

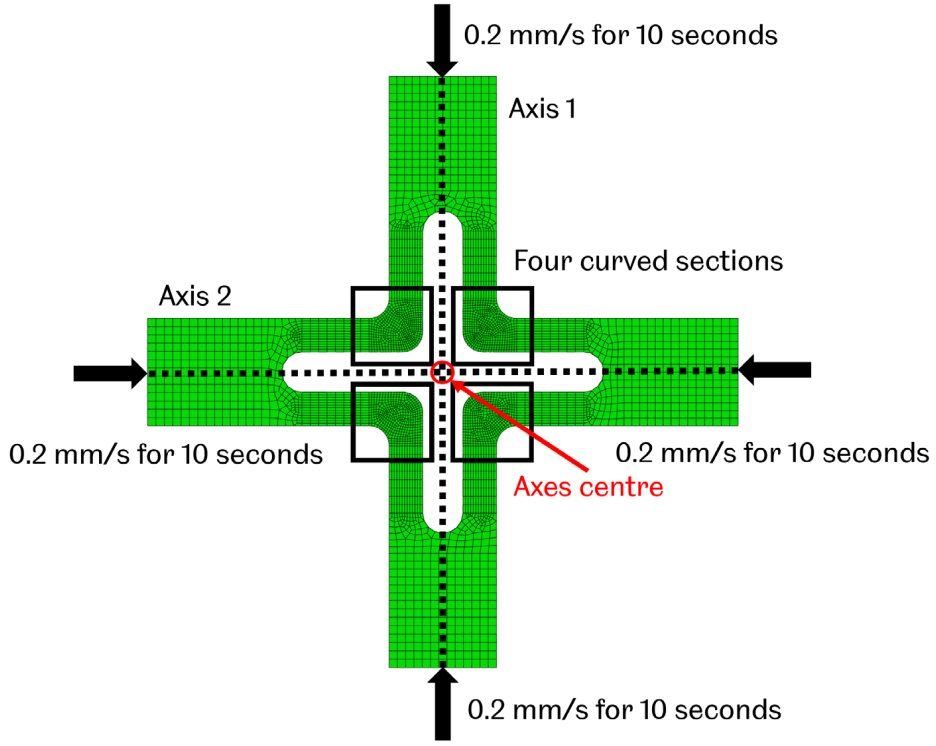

Figure 5.4 Top view of FE model A with curved sections (gauge areas) and the boundary conditions applied to the four arms.

FE results and discussion of test design A

There is a 4 mm compression displacement on each axis after applying 0.2 mm/s compression speed for ten seconds on axes 1 and 2. The compressing boundary conditions have successfully caused the specimen to wrinkle on the curved sections, as shown in Figure 5.5. However, the wrinkling is not ideal and is different from the wrinkling that occurred in the shear spinning process. The first drawback is that the specimen is symmetric with uniform thickness. The upwards and downwards wrinkling occur simultaneously, causing the wrinkling to be unpredictable. In the FE modelling, the specimen is perfectly uniform with no manufacturing deviations, for example, thickness unevenness. However, in experiments, the result will highly rely on the manufacturing quality of the specimen. Whether certain curved section wrinkles upwards or downwards will be unpredictable. The wrinkle direction needs to be unified to fully control the test result, at least making all the curved sections wrinkle in the same direction.

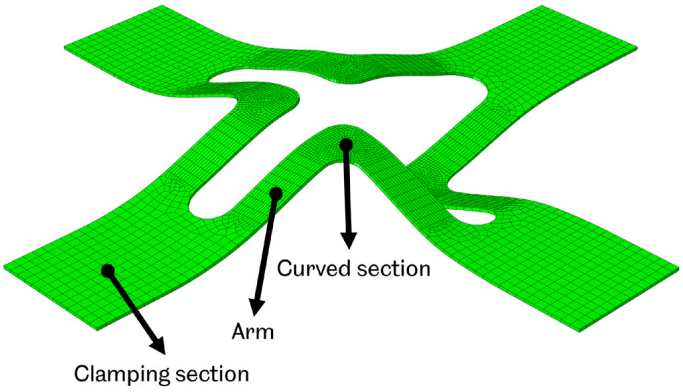

Figure 5.5 Specimen wrinkles on the curved sections.

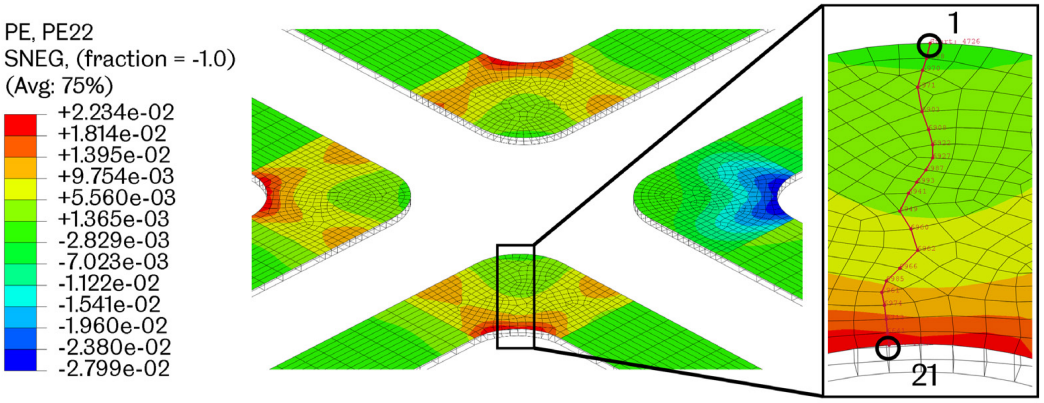

Figure 5.6 Circumferential strain of the FE model A and nodes selection for result output.

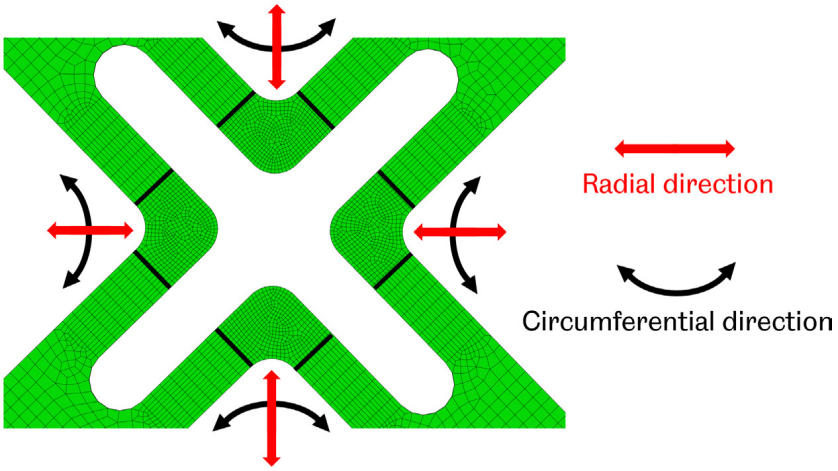

Figure 5.7 Definition of the circumferential and radial directions.

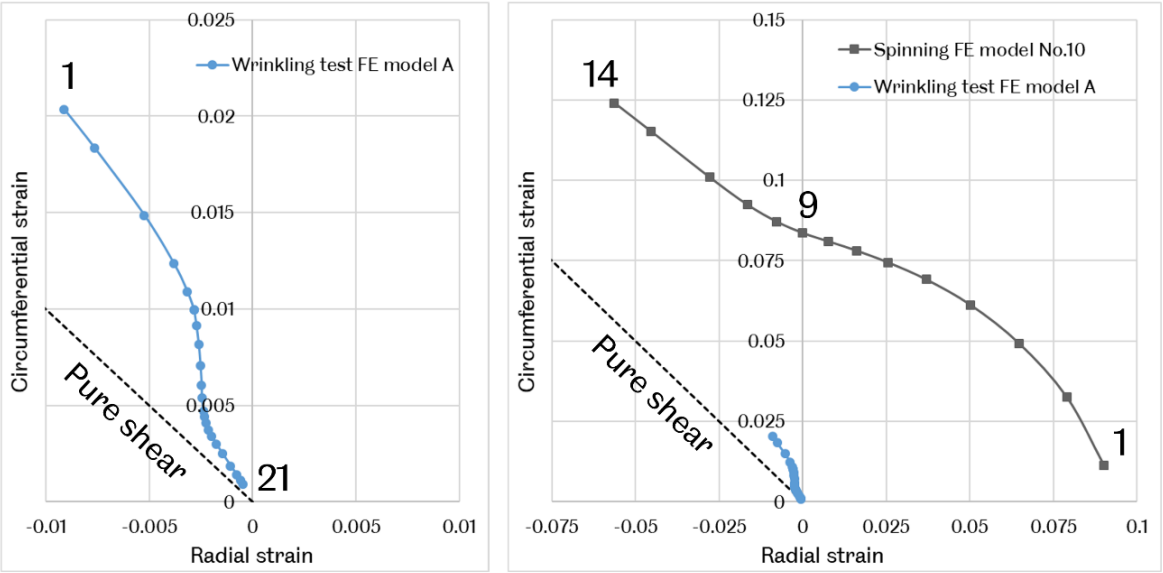

Figure 5.8 Circumferential and radial strains of wrinkling test FE model A and spinning FE model No.10.

For FE model A, local coordinate systems are established for every curved section. The strain results are output from the noded selected on the curved section, as shown in Figure 5.6. The definition of circumferential and radial directions follows the curvature of each curved section, as shown in Figure 5.7. The circumferential and radial strain results of selected nodes are shown in Figure 5.8. Since the thickness is uniform, the deformation is likely to be distributed evenly throughout the specimen, causing some sections of the specimen to be even less resistant to deformation. The wrinkling is supposed to only occur near the curved sections. However, the arms between the clamping areas and the curved sections are also deformed, as shown in Figure 5.5. Because a part of the compressing displacement applied to the specimen has been distributed to the arms, it results in very small strains on the curved sections, as shown in Figure 5.8. The circumferential and radial strains in spinning FE model No.10 are approximate 0.125 and –0.06 as the maximum values, but the wrinkling test FE model A achieves only 0.02 and –0.01.

Nevertheless, the strain signatures of the wrinkling test FE model A and the spinning FE model No.10 (nodes No.9 to 14) are in the same region. The circumferential to radial strain ratios are also similar since the strain signatures of both models are not beyond the dashed line (pure shear) with a –1 strain ratio. The deformation in the wrinkling test FE model can be considered as wrinkling as in the spinning FE model. Fourteen nodes are selected in the spinning model, and the strains increase from node No.1 to No.14. Twenty-two nodes are selected in the wrinkling test model, and the strains decrease from node No.1 to No.22. The patterns of the wrinkling test FE model A and the spinning FE model No.10 are opposite. The compression is created

from the clamping section through the arm, compressing the inner and outer edges, as shown in Figure 5.9. However, there is an additional material between the compressed clamp and the outer edge. This results in the outer edge being less compressed than the inner edge since the compressing displacement has to compress the additional material. The strain results demonstrate the same pattern: when closer to the outer edge, the material is compressed more, thus the greater strains. Hence the patterns of the strain results between the spinning and wrinkling test models are opposite.

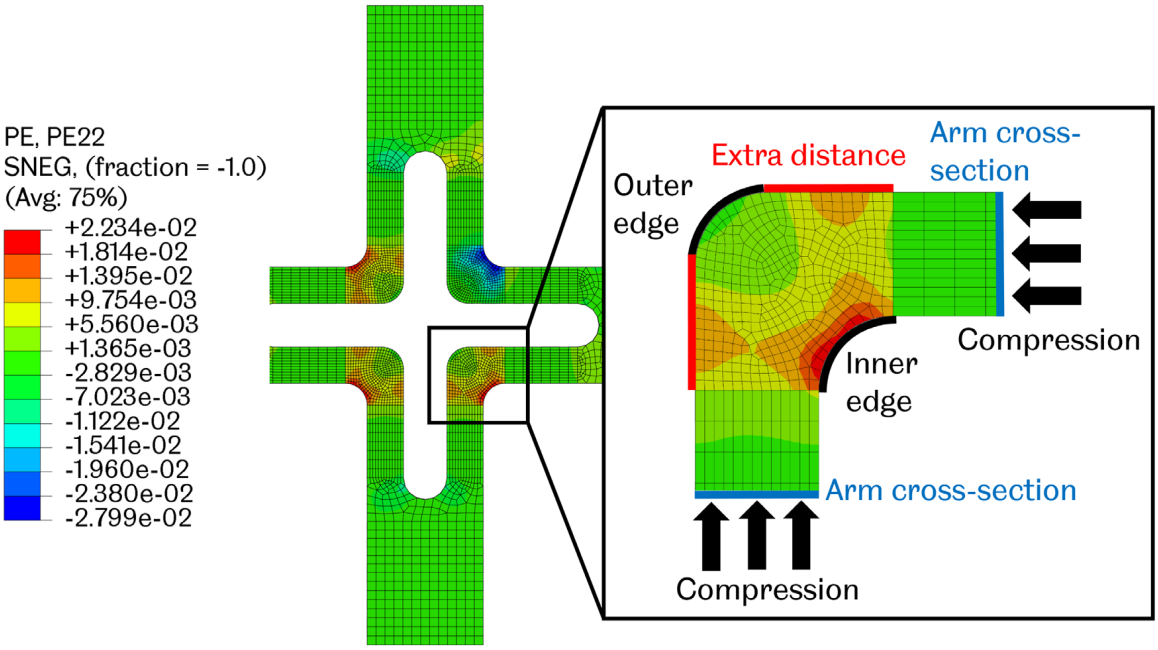

Figure 5.9 Detailed view of circumferential strain results on the curved section.

To summarise, the wrinkling testing model A has proved that wrinkling can be achieved by applying compression to the specimen. However, the strain results are smaller than the target wrinkling strains in the spinning FE model. The strain signature patterns of both models are not similar either. Modifying the specimen geometry and boundary conditions is necessary to eliminate the abovementioned problems.

Modification and improvement required for test design A

- The specimen geometry design needs to reduce the strength of the gauge area rather than cutting slots.
- The boundary conditions need to be modified according to the actual boundary conditions in the shear spinning process.

5.2.2 Wrinkling Test Design B

The strain results in the FE model test design A do not match the spinning process.

The next step of the study is to improve the strain results by increasing the similarity of the results between the spinning FE model and the wrinkling test FE model. The specimen geometry and the boundary conditions of wrinkling test FE model B are greatly different from specimen A since the geometry of the gauge area (curved section) in specimen A is flawed.

Aim of test design B

By modifying the wrinkling test FE model, the geometry of the specimen and boundary conditions, it aims to achieve a more similar wrinkling deformation in the test specimen as in the spinning FE model.

Specimen geometry and boundary conditions of test design B

A straight shape specimen with a thickness-reduced gauge area, wrinkling test FE model B, is developed in the current section. The idea is to improve the similarity between the wrinkling deformation in the wrinkling testing specimen and the wrinkling deformation in shear spinning. As a result, the results will be more similar/closer in these two processes.

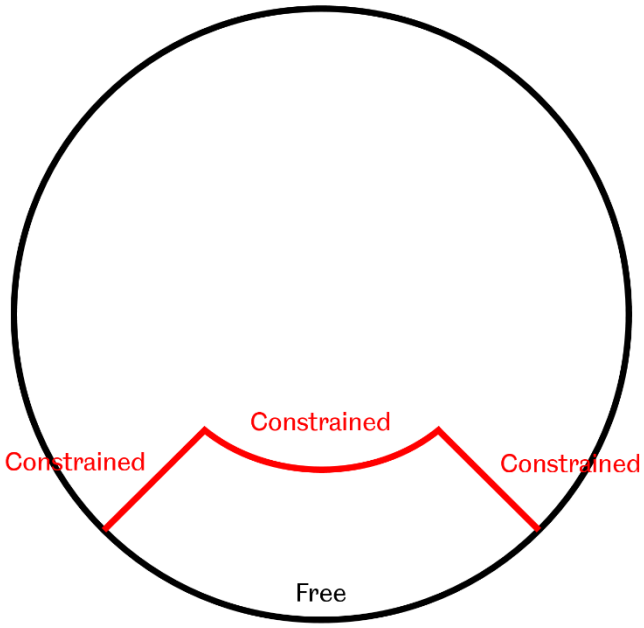

Figure 5.10 An arc section on the circular workpiece in the spinning process.

The gauge area of the specimen in FE model B is designed to have similar geometry to the actual wrinkled section in the spinning process, illustrated in Figure 5.10. In spinning, three sides of the arc section of the spinning workpiece are constrained by the adjacent material marked as red boundaries, while the edge is free from constraint. As discussed in section 5.2.1, the thickness-reduced gauge area section should be created in the wrinkling test specimen.

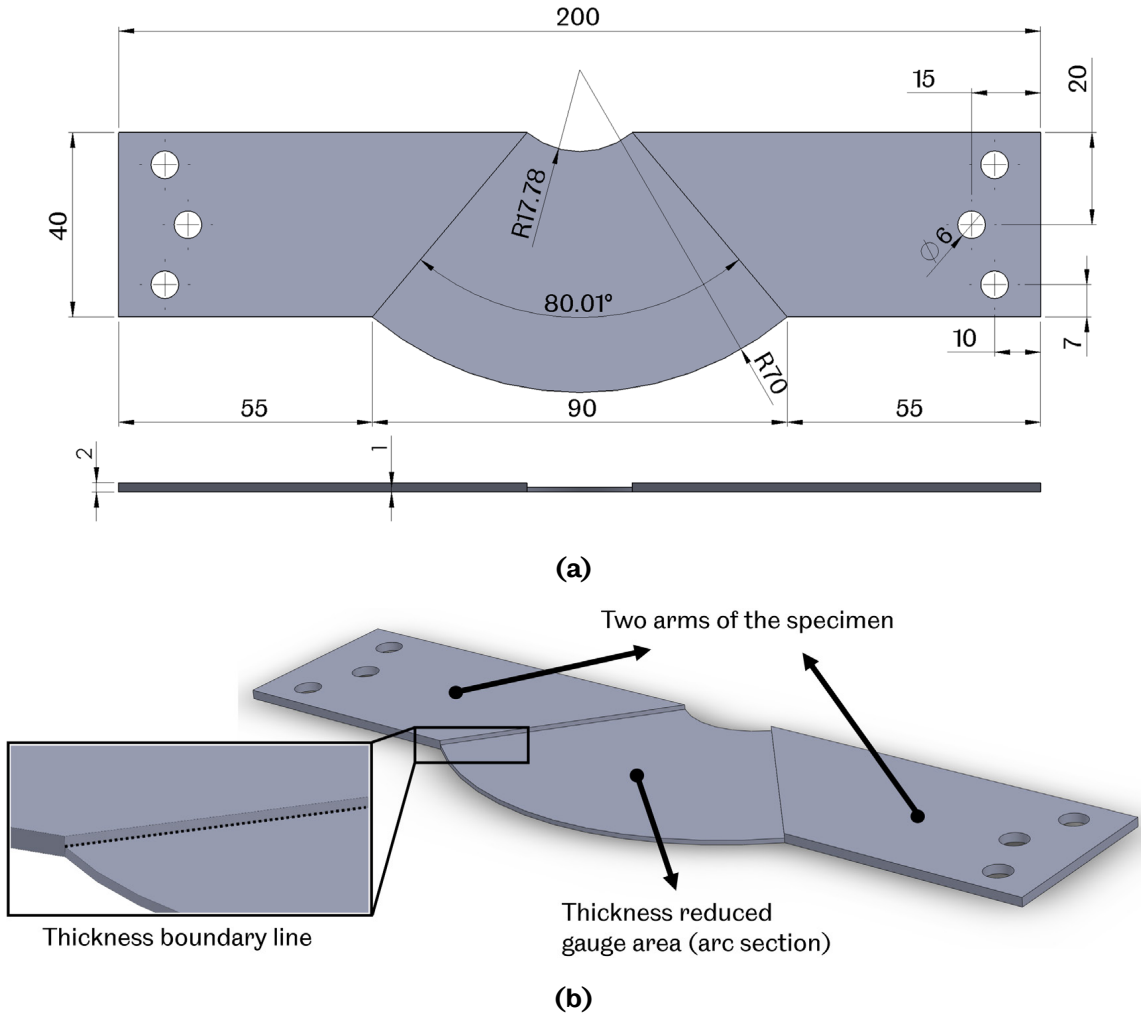

Figure 5.11 Dimensions of the straight shape specimen B and (b) a side view to illustrate the uniform thickness feature.

The geometry of the arc gauge area in the test specimen represents the arc section on the spinning workpiece. Specimen design B is developed based on this idea, and the dimensions of specimen B are shown in Figure 5.11 (a). A side view of specimen B is shown in Figure 5.11 (b) to illustrate that the thickness of specimen B is 2 mm with a 1 mm thickness-reduced gauge area. The gauge area is supposed to be less resistant to compression. If the thickness is uniform or the structure is symmetrical, the specimen will have equal chances of wrinkling in both directions. Whether the specimen wrinkles upwards or downwards will become unpredictable and uncontrollable. There is a boundary line between the arm and the gauge area, causing a sudden change in the thickness. The sudden thickness change ensures the specimen is always wrinkled in one direction, even if there are imperfections due to manufacturing. Ideally, the wrinkling on the specimen will only occur in the gauge area. The deformation on the arms in FE model A will be eliminated, and there will be no strain concentrations near the material between the clamps and the arms.

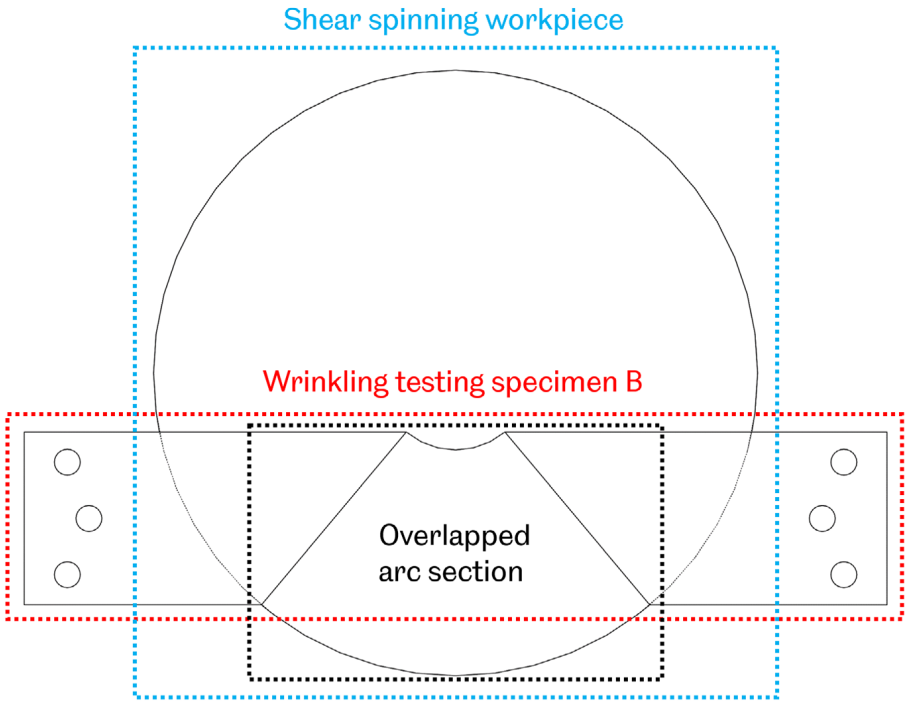

Figure 5.12 The wrinkling testing specimen overlaps with the shear spinning workpiece.

In Figure 5.12, the CAD design of the wrinkling testing specimen is placed on top of the CAD design of the shear spinning workpiece for a better visual illustration of the specimen gauge area related to the arc section of a round spinning workpiece. The gauge area of the specimen overlaps with the arc section on the workpiece, and the loadings are applied through the two arms of the specimen. The perfectly overlapped section is shown in Figure 5.12.

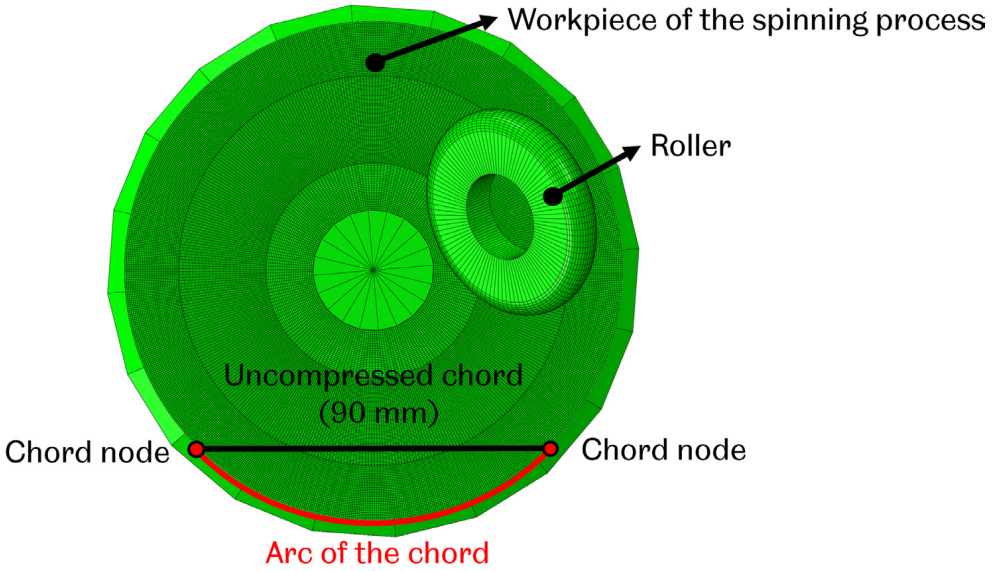

(a)

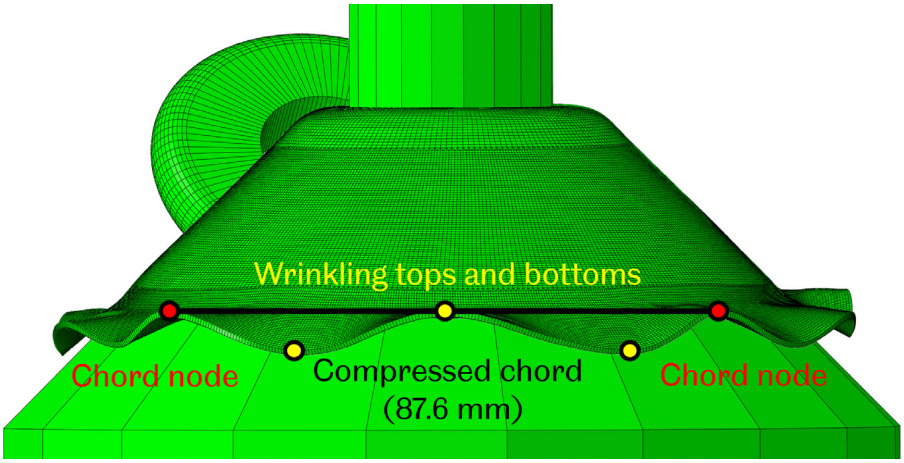

(b)

Figure 5.13 An illustration of the chord on the spinning workpiece of (a) uncompressed before the process and (b) compressed after the process.

Since compression is the only loading applied in wrinkling test FE model B, the compressing displacement must be determined by considering the compressing speed and time for the BTBC rig to implement. In Chapter 3, the shear spinning process model No.10 with 1000 RPM mandrel speed and 1.5 mm/rev feed ratio is analysed in detail for comprehensive results since this model involves both wrinkling and excessive distortion. Hence, for the wrinkling test in the current chapter, the boundary conditions applied to the specimen are derived from shear spinning model No.10 for the same reason. In spinning FE model No.10, the workpiece excessively distorts at 1.373s of the process, and the two nodes, marked red in Figure 5.13 (a), are compressed. These two nodes are selected as the two ends of the chord in the arc gauge area. The compressing distance between these two nodes is converted to the boundary condition to be applied to the wrinkling test specimen. The location of the chord is determined by the distance between the two wrinkling tops, as shown in Figure 5.13 (b). The purpose is to make the wrinkling test specimen present more features after applying the boundary conditions. Two wrinkling bottoms and one wrinkling top within the chord length are marked yellow in Figure 5.13 (b). The idea is that more than one wrinkling wave should be achieved in the wrinkling test. According to the calculations, the boundary conditions are applied to the specimen on axis 1, as shown in Figure 5.14.

The compression displacement in the wrinkling test is calculated by comparing the coordinates of the two nodes of the spinning workpiece before and after the deformation in spinning. The initial distance between the two nodes is 90 mm as the chord length of the arc gauge area, as marked in Figure 5.13 (a). At 1.373s in the spinning model No.10, the distance between the two nodes reduces to 87.6 mm;

there is 2.4 mm of chord compression throughout the spinning process, as marked in Figure 5.13 (b). Chapter 3 also proves that only the feed ratio affects the wrinkling in the spinning process, and the strain rate does not. Hence, the ideal outcome is that the same wrinkling deformation can be reproduced on the wrinkling test specimen B after the 2.4 mm compression displacement is completely applied to the wrinkling specimen. Since the deforming time is proven not to affect the result, 10 seconds of compressing time are selected as an appropriate and controllable duration for the BTBC rig. The compression speed is applied in model B, illustrated by the black lines shown in Figure 5.15 (a).

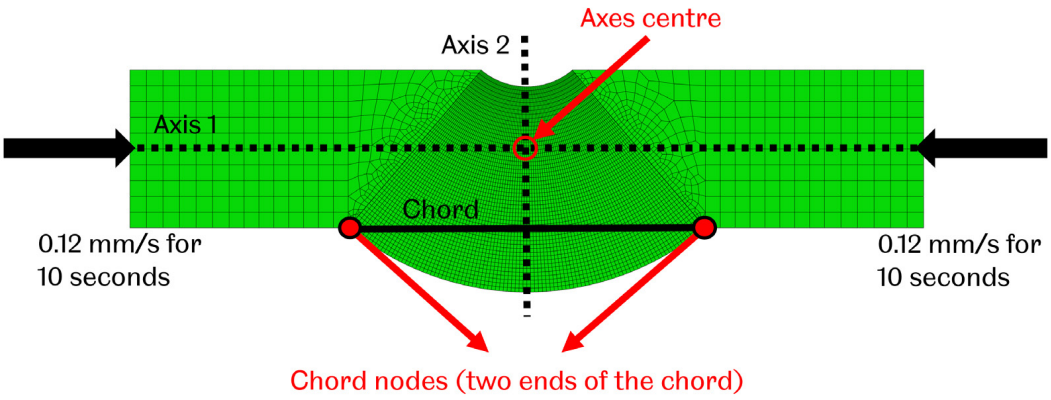

Figure 5.14 Top view of specimen B with applied boundary conditions.

The original element type selected for FE model B is the C3D8 solid element. However, the strain results are much smaller than the experiment results. The element type is changed to the SC8R shell element, the same as that used in the shear spinning modelling in Chapter 3. Since the deformation modes in the wrinkling testing are expected to be the same as that in the spinning process, employing the SC8R shell element with nine integration points to the model should achieve a higher FE modelling accuracy when the test involves bending deformation mode. When employing the SC8R shell element in the model, elements cannot be constructed with different thickness values, for example, a thickness-reduced section of the gauge area in the centre. Hence, only the arc gauge area is constructed in FE model B, and the two arms of the specimen are neglected. The model is shown in Figure 5.15 (a) with a side view for a better visual illustration, as shown in Figure 5.15 (b).

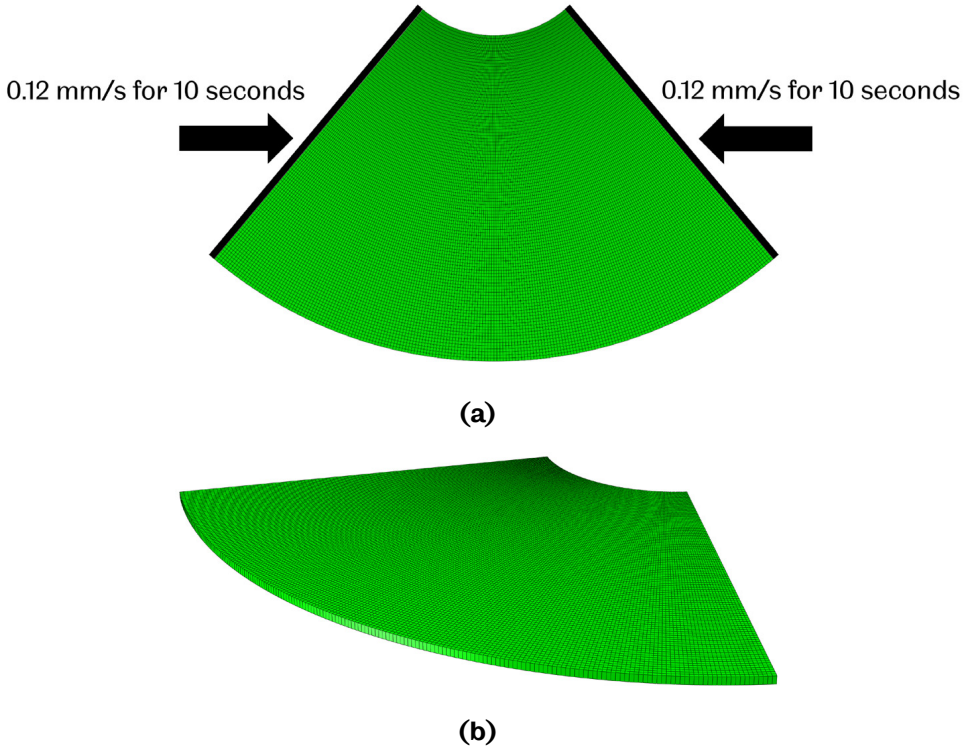

Figure 5.15 (a) top view and (b) side view of the FE model B with the simplified specimen and an arc gauge area with the boundary conditions.

FE results and discussion of test design B

The specimen has wrinkled upwards after 2.4 mm compressing displacement is applied to specimen B, as shown in Figure 5.16 (a). There are 105 nodes selected on the specimen for strain results output, numbered from No.1 to No.105, as shown in Figure 5.16 (b). These nodes are selected on the wrinkling top of the wrinkling wave as the most wrinkled locations with the greatest circumferential strains.

The circumferential strain contour of the gauge area is shown in Figure 5.17. The strains gradually decrease along with the selected node set numbers. The maximum strain is 0.23 at node No.1, the closest node to the centre point of the arc. The minimum circumferential strain is 0.018 of No.94. Node No.105, as the last node of the selected node set, is on the edge of the arc with 0.026 circumferential strain. The circumferential strains of nodes No.80 to No.105 are similar, from 0.018 to 0.028. A decreasing trend of the circumferential strains can be observed from near to far away from the centre point of the arc.

The strain signature of the wrinkling test model B is generated and compared with the spinning FE model No.10 (1000 RPM mandrel speed and 1.5 mm/rev feed ratio) in Figure 5.18. Both strain signatures are located between plane strain and the pure shear region. For wrinkling test FE model B, most nodes are located very close to the circumferential strain axis as the plane strain condition. Nodes near No.38 in

wrinkling test FE model B achieve similar values around 0.125 as node No.14 in the spinning FE model. It is a major improvement of FE model B compared with FE model A. The strains in FE model A are too small compared with the spinning FE model as the maximum circumferential strains are 12.5 in spinning FE model No.10, but it is only 0.026 in the wrinkling test FE model A.

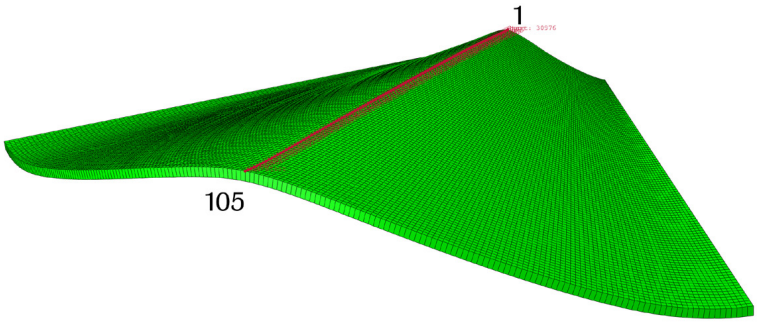

Figure 5.16 FE model B after 2.4 mm compressing displacement applied and nodes selected for results output.

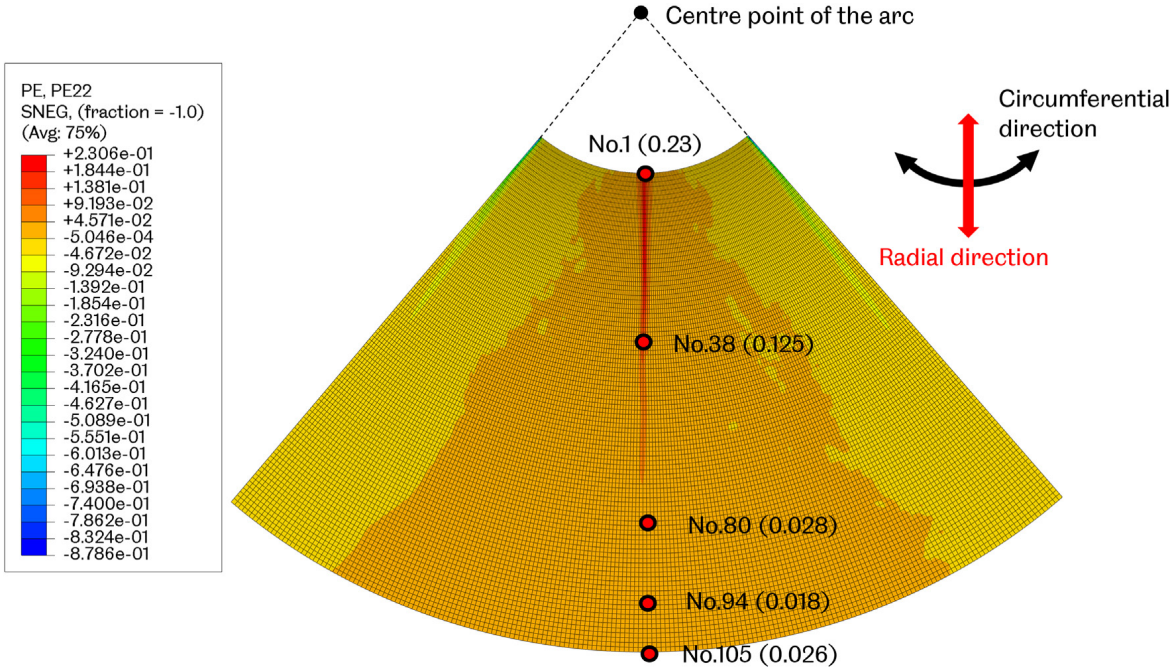

Figure 5.17 Circumferential strain results of the FE model B.

However, in the spinning FE model, the node with the greatest circumferential strain is on the edge as the furthest node from the centre point of the workpiece. Similar to the wrinkling test FE model A, model B strain signature pattern is also opposite to the spinning FE model No.10, as shown in Figure 5.18. In FE model B, node No.1 with the greatest circumferential strain is the closest node to the centre point of the arc in model B, and node No.105 on the edge is the furthest node to the centre point with almost the smallest circumferential strain. Although model B is constructed to reproduce the spinning process as much as possible, the model B strain signature

pattern is still the opposite of the spinning FE model. However, wrinkling test FE models A and B patterns are similar. The assumption is that the compression displacement applied to the arc gauge area is still unevenly distributed as in model A, shown in Figure 5.19. Although the compression displacements applied, shown in Figure 5.15 (b), are identical throughout the side of the arc section, the ratios between arc length and compression displacement at the different locations are different. For example, the lengths of the short/intermediate/long chords marked in Figure 5.19 are different, and the deformations induced to these chords by 2.4 mm compression displacement are also different. The compression to the chord is reflected on the corresponding arc and generated strains. Hence the strain on the arc decreases as the chord length increases.

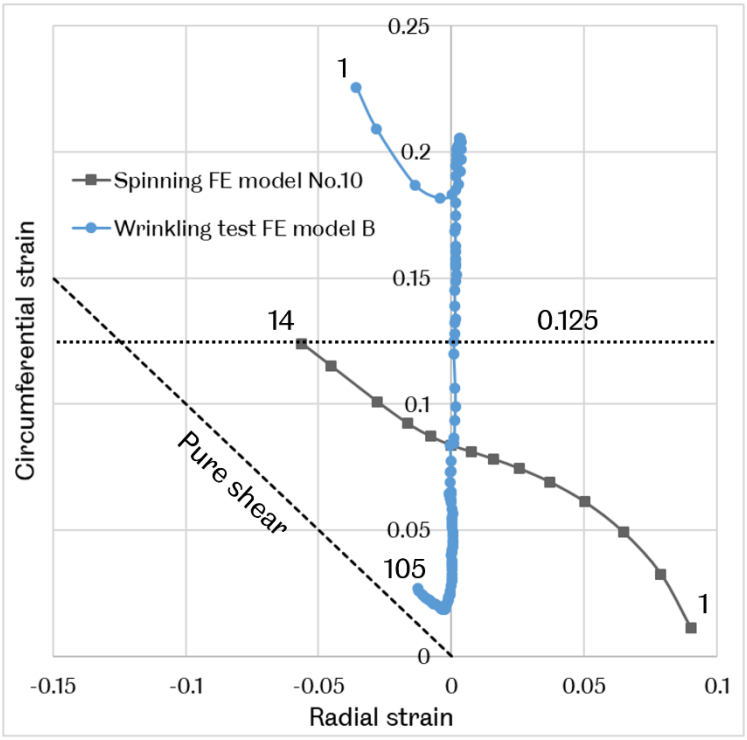

Figure 5.18 Comparsion of the circumferential strain results of spinning FE model No.10 and wrinkling test FE model B.

In wrinkling test FE model B, some nodes wrinkle severely enough to produce the strains as in the spinning FE model. However, the overall strain signature pattern is still the opposite of the spinning FE model. However, at least some similar circumferential strains can be found in the spinning FE model and FE model B. FE model B proves that the direction of the study is correct. In the next step of the study, the boundary conditions need to be modified to eliminate this phenomenon. The geometry of the specimen may need to be modified as well. For now, the geometry of specimen B does not need to be modified since the strain results are

improved when compared with FE model A. Boundary conditions modification is always considered before the specimen geometry modification. Because the specimen geometry modifications will increase the workload and induce unnecessary complexity to the FE modelling.

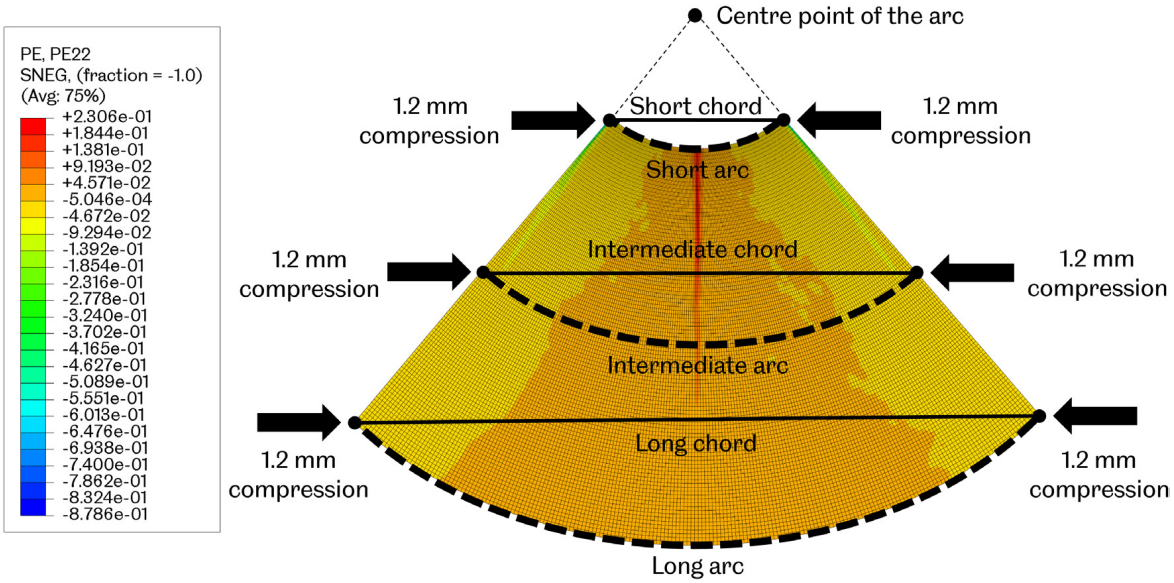

Figure 5.19 Compression displacements applied to the various locations of the arc gauge area.

Modification and improvement required for test design B

The boundary conditions applied in the wrinkling test FE model B need to be improved to achieve a more similar strain result and strain signature compared to spinning FE model No.10.

5.2.3 Wrinkling Test Design C

Wrinkling test design B has improvements, but the FE strain results do not achieve a satisfying level. As mentioned in section 5.2, the strain results in the spinning process are considered reference values to determine whether strain results in the wrinkling test FE modes are ideal. In FE model B, strains of some nodes are below the ideal strains, and some are above the ideal strains. The nodes with excessive strains are distributed in the upper section of the arc gauge area that is close to the centre point of the arc, as shown in Figure 5.19. In model B, compression is the only boundary condition applied. The effect of the roller on the spinning process is not considered. The roller will work over already wrinkled areas of the spinning workpiece in the late stage of the spinning process. The strains will decrease as the roller flattens the wrinkled material since the roller tends to restore the wrinkled material into a well-deformed state. The roller will reduce the circumferential strain and increase the radial strain, as discussed in Chapter 3. Also, the roller will induce compression in

the thickness direction. Hence, if bending or compression can be induced in the thickness direction of the wrinkling test specimen, excessive circumferential strains in model B may be reduced to ideal strains or closer to the strains in the spinning process.

Aim of test design C

The aim of the wrinkling test design C is to prove the assumption that bending or compression in the thickness direction of the test specimen can properly reduce the excessive strains in wrinkling test FE model B to be closer to the ideal strains. The specimen geometry remains unchanged, and the bending tool in the BTBC rig is added to apply additional boundary conditions.

Specimen geometry and boundary conditions of test design C

Since the geometry of the specimen does not change, details of the geometry follow section 5.2.2, shown in Figure 5.11. The compression boundary conditions to the test specimen also follow section 5.2.2, shown in Figure 5.15. A bending tool is involved in the wrinkling test FE model C, and the details are shown in Figure 5.20. The bending tool is at the centre of the axes centre on the BTBC rig, as shown in Figure 5.20 (a). Boundary conditions are applied in three steps (A, B and C), as shown in Figure 5.20 (c). The bending tool has a pre-set 10 mm distance above the specimen, as shown in Figure 5.20 (c). The head of the bending tool is a hemisphere with a 5 mm radius. For the actual bending tool in the BTBC rig, the cylinder section is covered with threads for adjusting the location in the vertical direction. In the FE modelling, threads are neglected as they do not affect the deformation of the specimen. A 2.4 mm compression displacement is applied to the specimen arc gauge area in 10 seconds as step A. The bending tool moves downwards in step B and forces the wrinkled material back to horizontal level. The bending tool is to reproduce the effect of a roller as it will bend the wrinkled material towards the mandrel in the spinning process. The bending tool moves upwards in step C as the roller works over the wrinkled area on the workpiece and leaves this area in the spinning process.

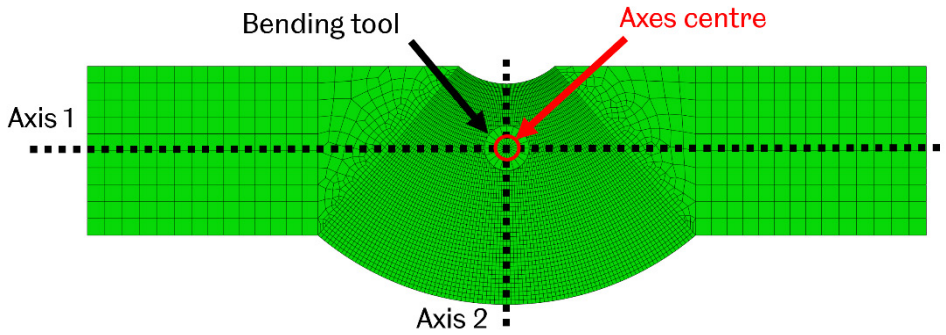

(a)

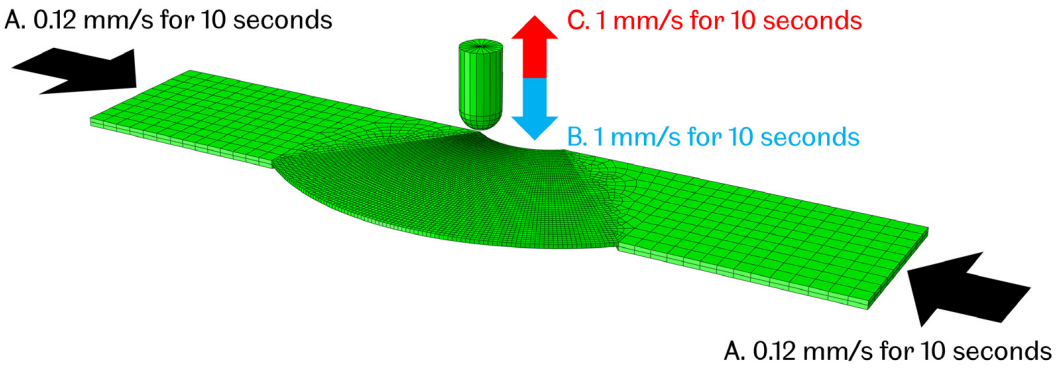

(b)

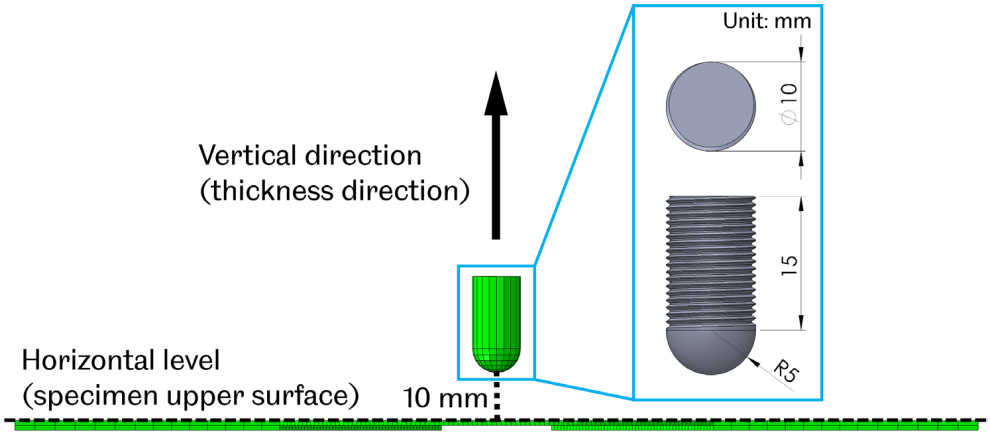

(c)

Figure 5.20 (a) top view of the wrinkling test FE model C; (b) front view of the model C with the bending tool 10 mm above the specimen; and (c) the boundary conditions applied in the model C.

Wrinkling test FE model C is simplified, similar to model B. The two arms of the specimen are removed, and boundary conditions are only applied to the arc gauge area and the bending tool. Model C without the two arms of the specimen is shown in Figure 5.21. The compression is applied to the two sides of the arc gauge area.

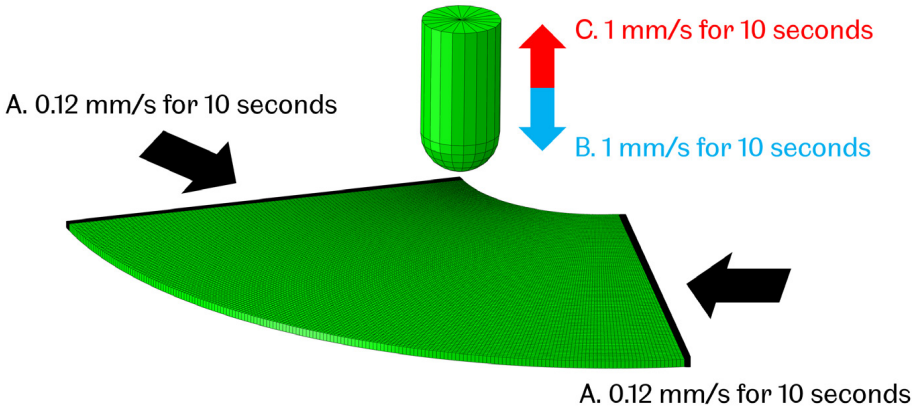

(a)

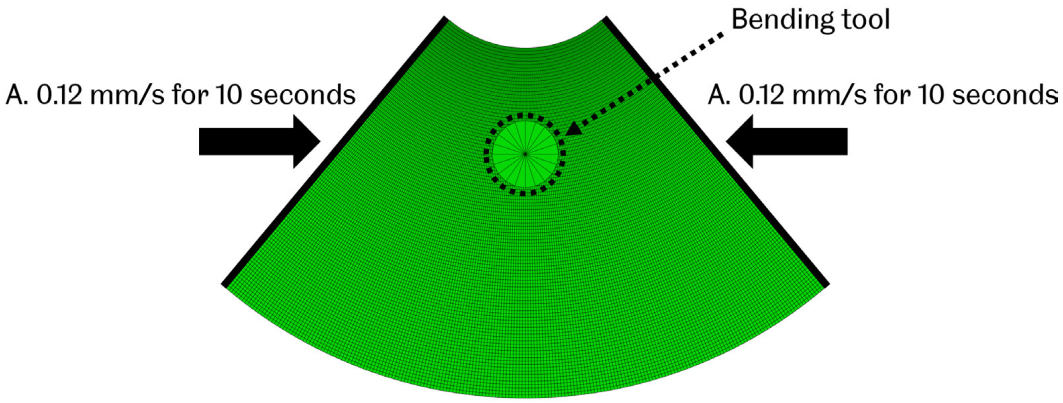

(b)

Figure 5.21 (a) FE model C with the bending tool and the simplified specimen as an arc gauge area and (b) the boundary conditions applied on the two sides of the gauge area.

FE results and discussion of test design C

In FE model C, the bending tool is involved in the modelling. The test specimen deformation in FE model C after the compression on the specimen and the effect of the bending tool in the vertical direction is shown in Figure 5.22. The bending tool leaves a dent on the specimen and changes the location of the wrinkling top. The bending tool pushes the wrinkling top off the centre to the left-hand side shown in the front view. Compared with FE model B, the material in FE model C is further deformed by the bending tool. However, FE Model B only includes a single wrinkling wave with a wrinkling top, as shown in Figure 5.22 (c).

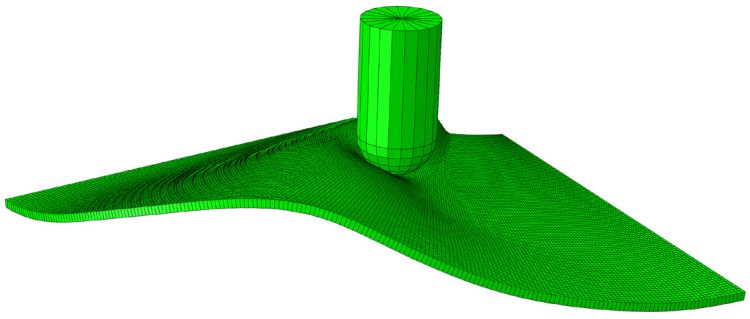

(a)

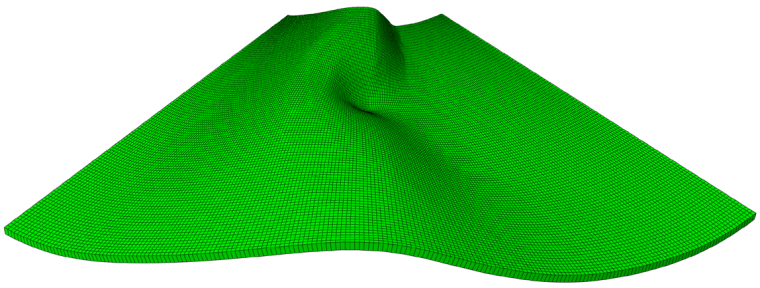

(b)

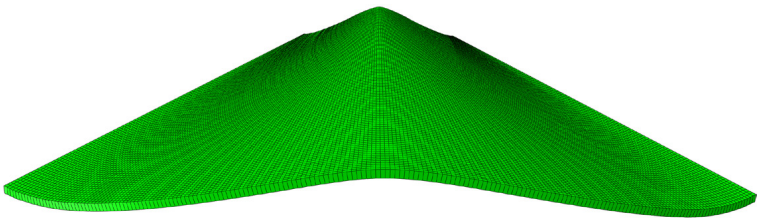

(c)

Figure 5.22 (a) FE model C after the boundary conditions are applied to the specimen, (b) the front view of FE model C after the bending tool leaves the area and (c) the front view of FE model B as a comparison.

There are 105 nodes selected to output the strain results, as shown in Figure 5.23. The node set involves the dent created by the contacting of the bending tool. As previously mentioned, involving the bending tool contacting with the specimen to reproduce the effect of the roller on the workpiece in the spinning process. The bending tool creates a dent in specimen C as the roller contacts the workpiece, as shown in Figure 5.24. The overall circumferential strain results contour of model C is shown in Figure 5.25. The minimum circumferential strain is on node No.95, with 0.023 near the edge in the selected node set, and node No.105 on the edge is 0.028. The strain slightly increases from No.95 to No.65 (0.058) through No.75 (0.037). The strains become compressive on the bending tool contacting area, and the most compressive strain is on node No.34 (–0.13). Node No.46 is considered the boundary node that separates the dented area, as the strain is the closest to zero.

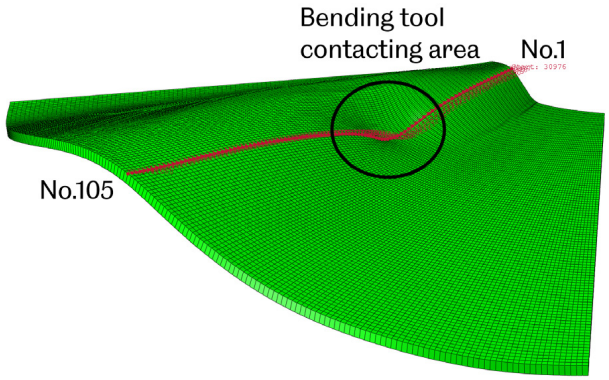

Figure 5.23 Illustration of the 105 nodes selected on the deformed specimen C.

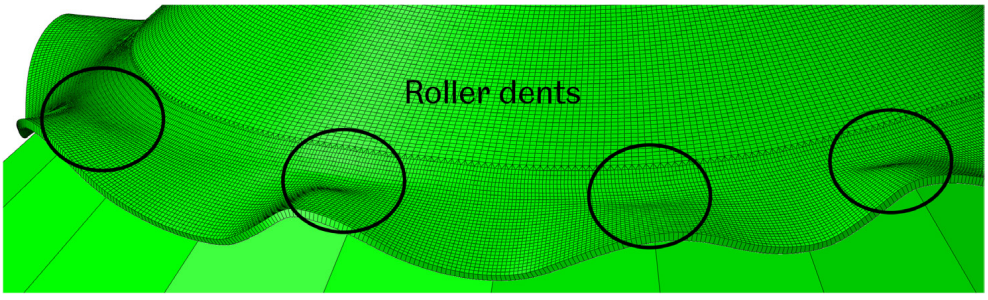

Figure 5.24 Roller dents created in the spinning process.

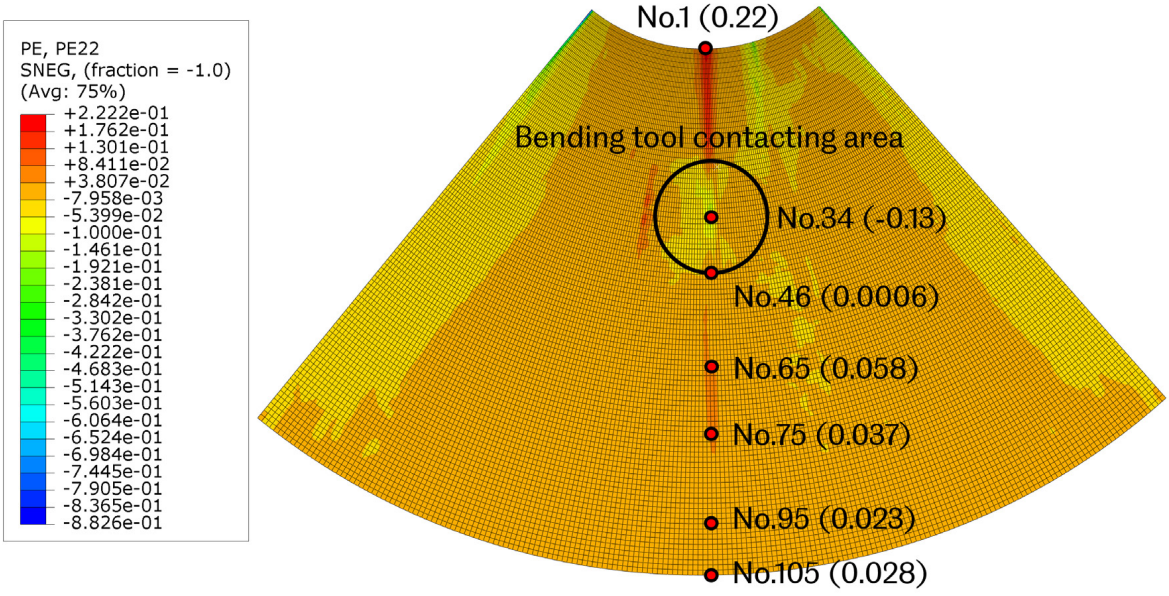

Figure 5.25 Circumferential strain contour of FE model C.

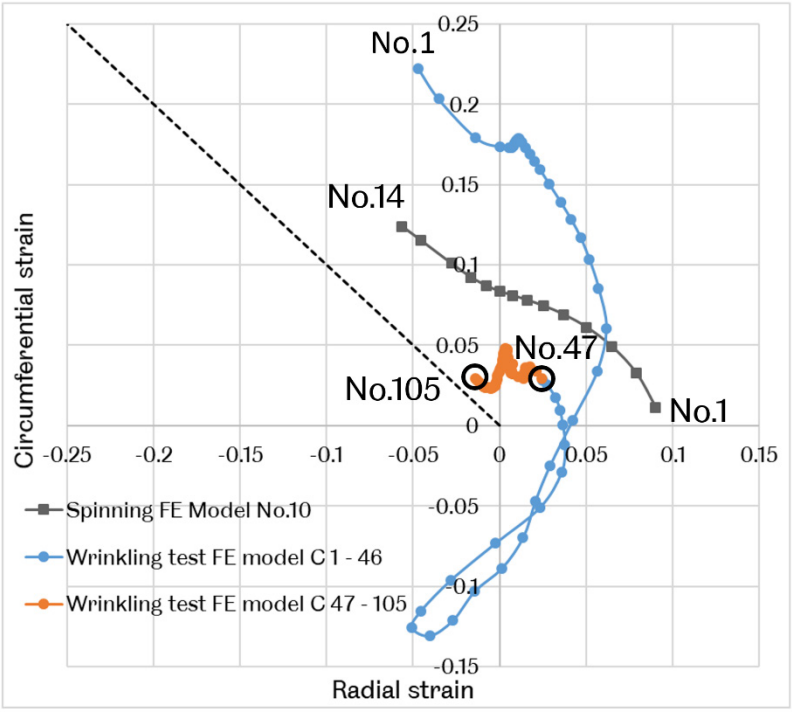

(a)

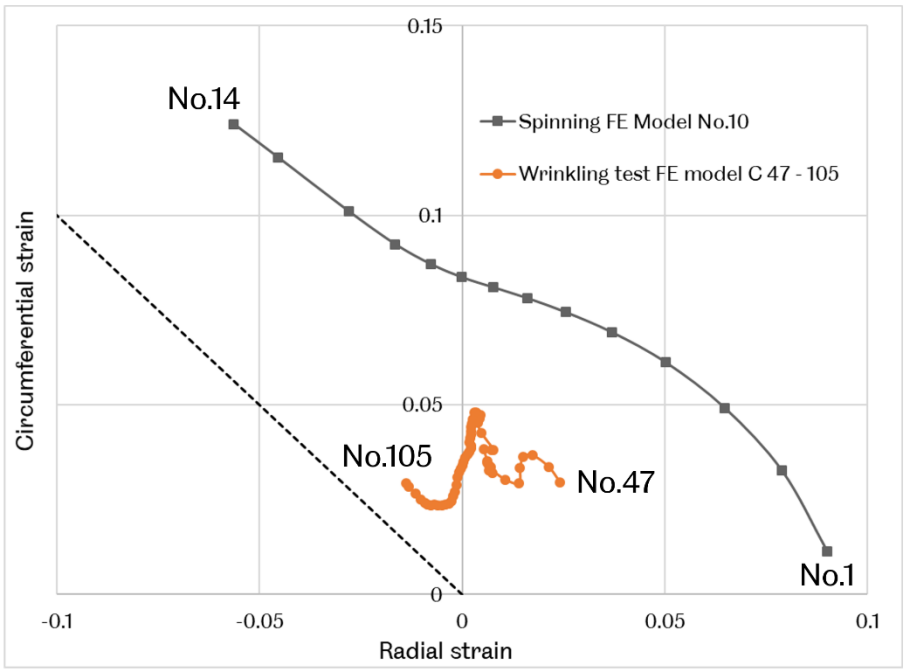

(b)

Figure 5.26 Circumferential and radial strain results comparison between the ideal strain results in spinning FE model No.10 and (a) node No.1 to No.105 and (b) node No.47 to No.105.

By comparing the circumferential and radial strain results, model C is not ideal. Node No.1 to No.105 includes the bending tool dented area, with inconstant strain distribution between tensile and compressive states. Hence the strain signature of FE model C is disordered, as shown in Figure 5.26 (a). However, fourteen nodes (No.1 to No.14) selected in the spinning process do not include the roller dented area. In the spinning process, as demonstrated in section 3.3.4, node No.1 is near the roller dented area, and No.14 is on the edge of the workpiece. Correspondingly, nodes No.47 (near the bending tool dented area) to No.105 (on the edge of specimen C) are selected in the test model C to compare with the spinning process results in Figure 5.26 (b). Although the strain results in FE model C are much smaller, the similar trend distributed from the first to the second quadrant by the node selecting sequence is an improvement for FE model C.

The involvement of the bending tool and the compression boundary conditions on the current straight specimen with an arc gauge area have utilised the full potential of the BTBC rig. But the strain results are still not satisfying. For the next step of the study, the geometry and the boundary conditions of the FE model may need major modifications to generate satisfying strain results to that in spinning.

Modification and improvement required for test design C

Modify the geometry and the boundary conditions for the next FE model to lower the strains in the area close to the centre point of the arc gauge area (nodes close to node No.1). The geometry of the specimen may need major modifications to include a constraint to the target area for lowering the strains. Also, the next model needs to focus on solving the problem that the strain results close to the edge of the arc (nodes No.105) are smaller than the strains on the edge of the workpiece in the spinning process.

5.2.4 Wrinkling Test Design D

Although the bending tool is involved in the wrinkling test FE model C and the strains of some nodes are successfully lowered after the bending tool compresses the specimen in the thickness direction, the strain results are still not ideal. The strains of the nodes close to the centre point of the arc are still excessively greater than the ideal strains. These nodes must be constrained in some ways to lower the strains to match the ideal strains.

The easiest method to control the strains of certain nodes is to apply relatively complex boundary conditions to the gauge area on one axis, for example, reducing compression boundary conditions on the sides of the gauge area, as shown in Figure 5.27. In this way, the strains of the area, which are close to the centre point of the arc gauge area with the greatest strain in model C, will be reduced. Although the current compression boundary conditions are more similar to the boundary conditions in the spinning process, the BTBC rig has limitations in that only one boundary condition can be applied on each axis. In other words, only one compressing speed can be applied to the sides of the arc gauge area. Lowering the strains under such limitations is a major problem that needs to be overcome in the wrinkling test FE model D.

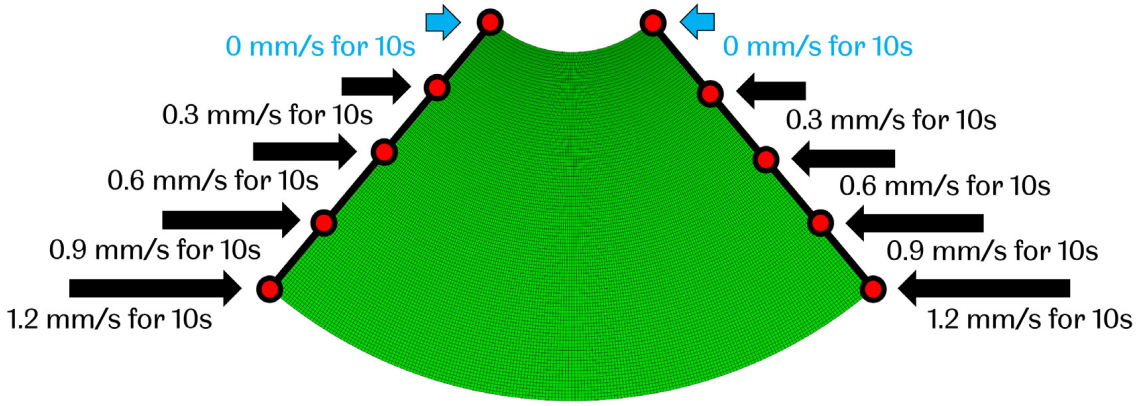

Figure 5.27 Descending compression boundary conditions to the gauge area.

Aim of test design D

The aim of the wrinkling test FE model D is to develop a constraint and modify the geometry of specimen D to lower the strains of the target area. The boundary conditions must be compatible with the BTBC rig for future experiments.

Specimen geometry and boundary conditions of test design D

The modified specimen D based on specimen C is shown in Figure 5.28. The thickness of specimen D is 2 mm with a 1 mm thick arc gauge area. The amount of arms has been increased to three for three clamps of the BTBC rig to provide the corresponding boundary conditions.

After the major modification to the geometry of specimen C, the specimen in design D becomes a T-shape with a thickness-reduced arc shape gauge area constrained by three arms, as shown in Figure 5.28 (b). The thickness difference in the junctions between the gauge area and the arms is shown in the detailed figures in Figure 5.28 (b), which should produce the focused deformation on the gauge area. The width of the two arms as axis 1 is modified to only cover the partial length of the side of the arc gauge area. As shown in Figure 5.29, the red line marked sections are not covered by the arms on axis 1. The compression is only applied on the black line marked sections of the specimen compressed by the arms. Although the red line marked section is free, they will still be compressed since they are near the black line marked sections compressed by the arms. As a result, the red line marked sections will be slightly compressed. The existence of the arm on axis 2 constraints the red line marked area; unlike specimens B and C, the area is free without any constraint on axis 2 direction.

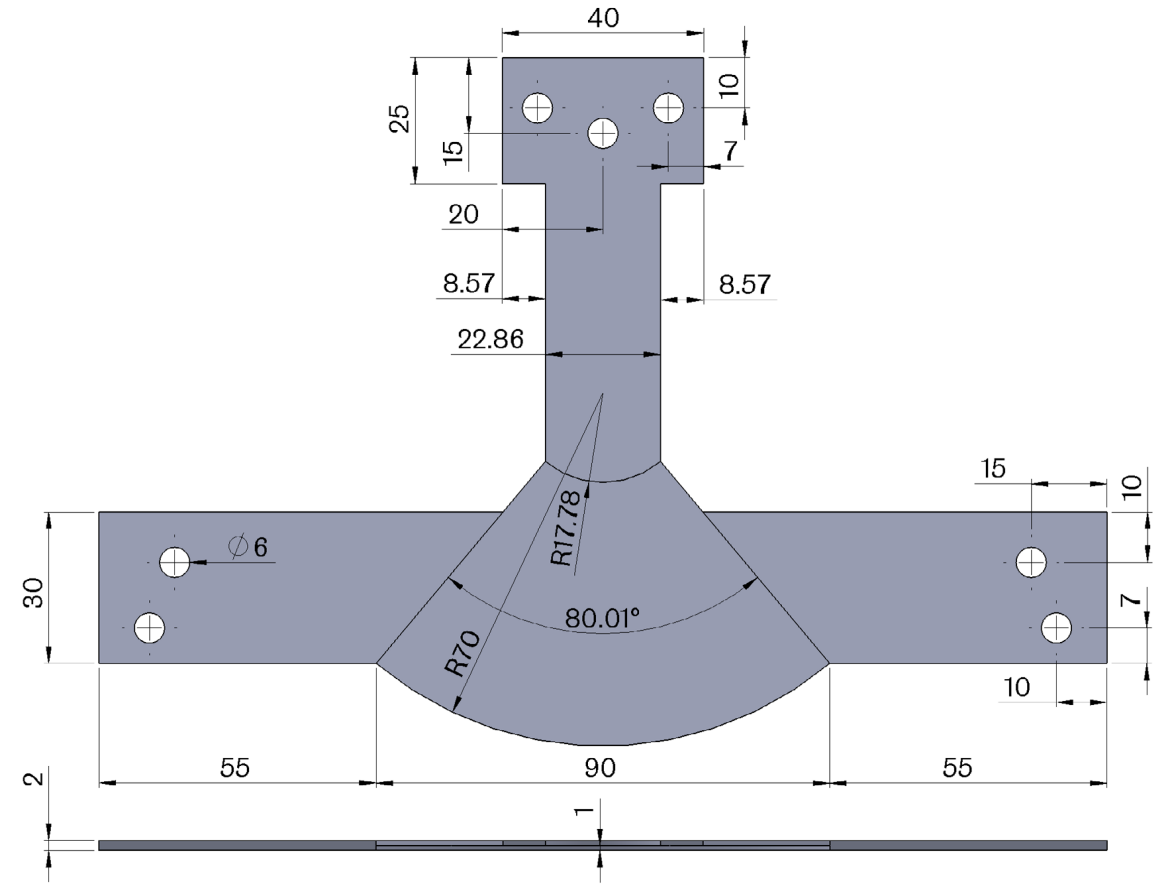

(a)

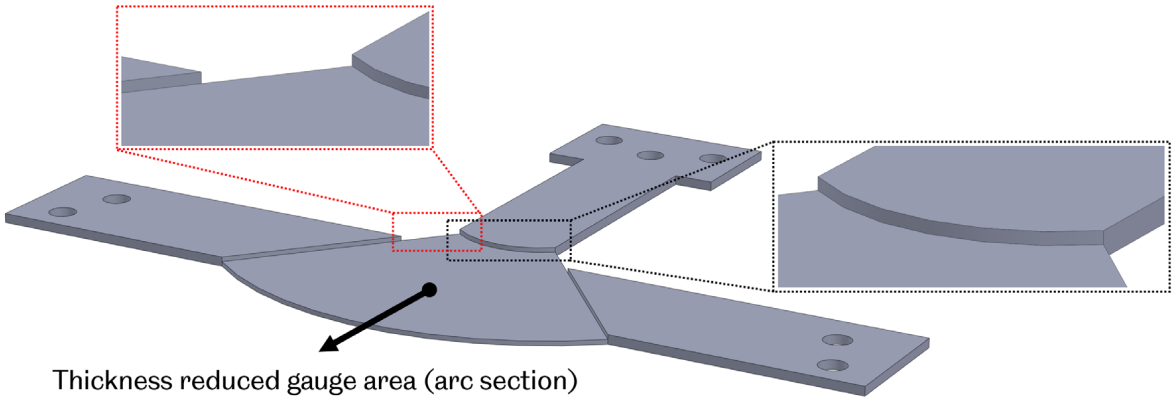

(b)

Figure 5.28 (a) geometry of specimen D and (b) the side view of specimen D with a 1 mm thickness arc gauge area.

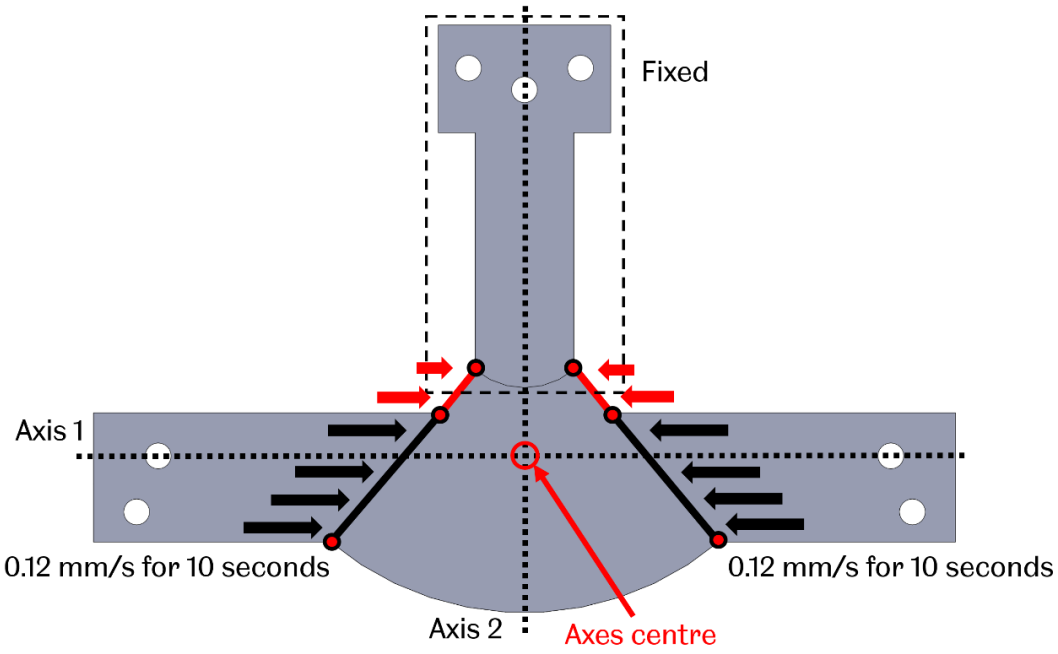

Figure 5.29 Illustration of the boundary conditions applied in the wrinkling test FE model D.

SC8R shell element is selected due to the involvement of bending deformation mode in the FE modelling. The thickness difference and the majority of the arms are neglected to reduce the calculation time. The FE model is shown in Figure 5.30. Three arms are partial remained for applying the boundary conditions. Compression is applied at 0.12 mm/s compression speed for 10 seconds on both sides of the gauge area, and another arm is fixed throughout the modelling, as shown in Figure 5.30 (a). The side view of the model with uniform thickness for a better illustration of the simplified FE model is shown in Figure 5.30 (b).

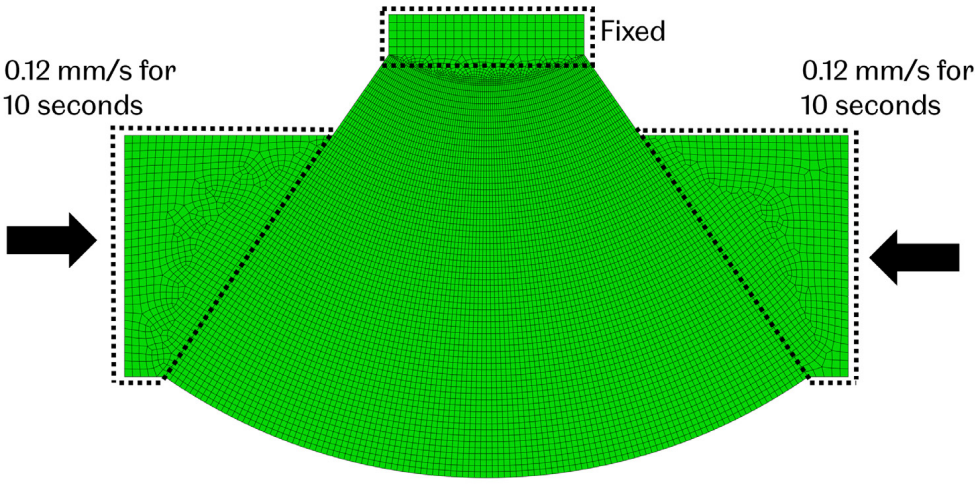

(a)

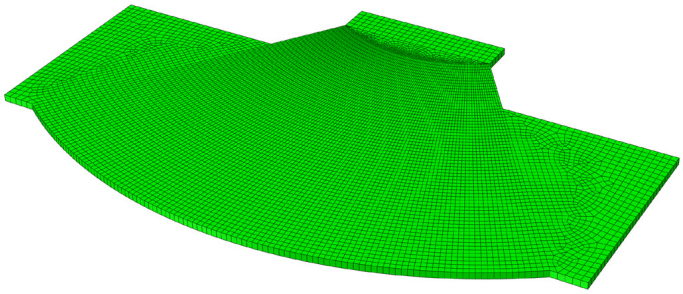

(b)

Figure 5.30 (a) top view and (b) side view of the FE model D with the simplified specimen.

FE results and discussion of test design D

After a 2.4 mm of compression displacement is applied to the specimen, the specimen wrinkled upwards, as shown in Figure 5.31. Seventy nodes along the radius direction are selected to output the strain results.

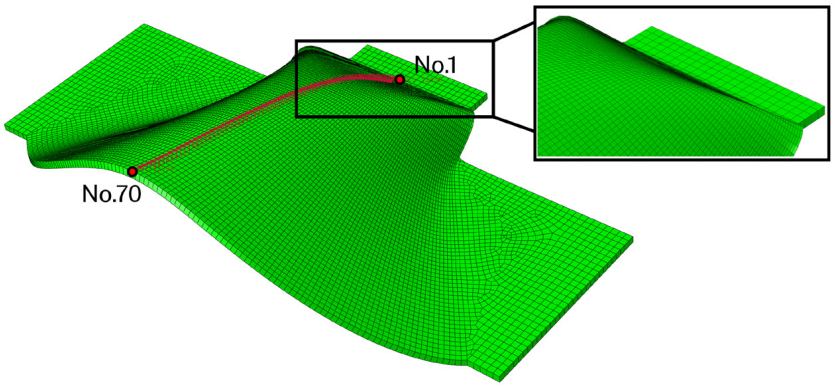

Figure 5.31 Specimen D wrinkles upwards under the compression boundary conditions on axis 1 and enlarged view of the near-flat area on the specimen on axis 2.

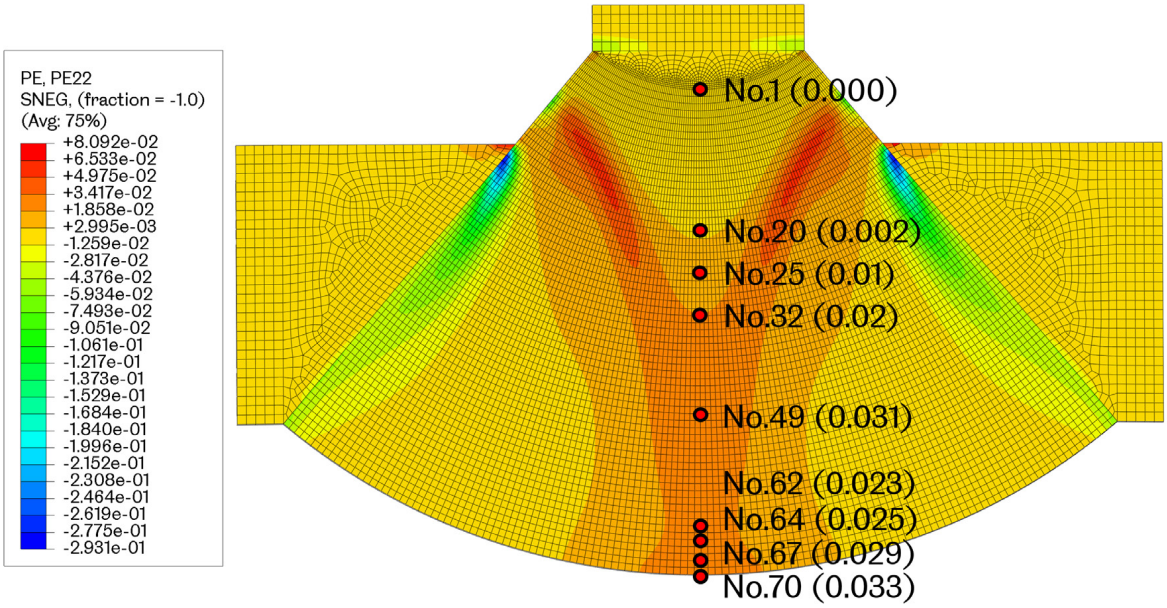

Figure 5.32 Circumferential strain contour of FE model D.

The circumferential strains of nodes No.1 to No.20 on a near-flat specimen area are almost equal to zero. The strain increases to 0.031 on node No. 49 and slightly decreases to 0.023 on node No.62. The circumferential strain eventually reaches the maximum of 0.033 at the edge of the specimen on node No.70. As a constraint, the newly added arm on axis 2 successfully lowers the strains of nodes near node No.1 as that in FE models B and C. However, the overall strain values still do not match the ideal strains in spinning FE model No.10.

The strain signatures of wrinkling test FE model D and spinning FE model No.10 are shown in Figure 5.33. Nodes No.1 to No.20 are in the near-flat area, and the strains of these nodes are very small. The strain signature of FE model D is slightly improved to be more similar to that of the spinning FE model. The strains are distributed from the first to the second quadrant, the same as the spinning FE model. Nodes No.21 to No.49 have a similar increasing trend to nodes No.1 to No.8 in the spinning FE model. The strains start with near-zero radial strain and small circumferential strain on No.1 of the spinning FE model and No. 21 of the wrinkling test model. The radial strain decreases to near zero, and the circumferential strain increases to a certain level on nodes No.49 in the wrinkling test FE model D and No.9 in the spinning FE model. The number sequences of these two nodes are beyond and not far from the median nodes of their corresponding node sets. The median node of FE model D and the spinning model is node No.45 (between nodes No.70 and No.20) and No.7 (between nodes No.1 and No.14), respectively. This means the nodes near the middle area of the wrinkled material are always in plane strain deformation mode, and this conclusion can be found in both FE model D and spinning FE model results.

Despite all these similarities between the two models, the circumferential strains in FE model D are still much smaller than the circumferential strains in the spinning FE model. The circumferential strains in the spinning model can reach a maximum of 0.125. In FE model D, the maximum is only 0.033, much smaller than the spinning model. The compression boundary conditions with a total of 2.4 mm compression displacement may not be adequate to deform the specimen. As previously stated, the 2.4 mm compression displacement is derived from the spinning process.

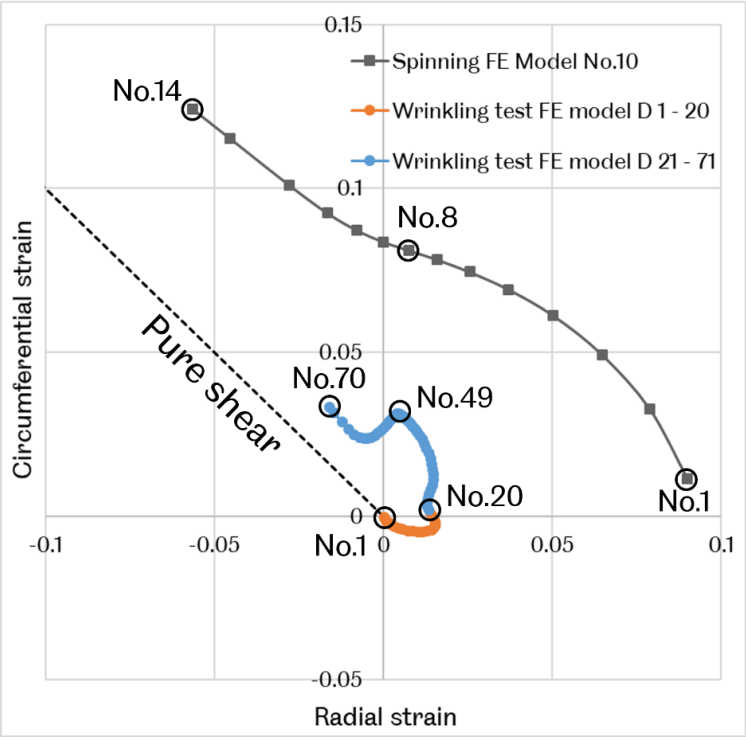

Figure 5.33 Comparison between the circumferential and radial strains of wrinkling FE model D and spinning FE model No.10.

The strain signature has a turning point on node No.49, which means that the compression boundary conditions are not following an increasing trend as predicted in Figure 5.27 when designing the specimen with width reduced arms. Since the limitation of the BTBC rig is that only one compression boundary condition can be applied on one axis, the geometry of the specimen may need further modifications in future FE modelling. If an increasing trend of compression boundary conditions cannot be achieved, turning points like node No.49 in FE model D will occur in future FE models.

Modification and improvement required for test design D

Before major modifications to the specimen geometry and the boundary conditions, the next step of the modification is to include the bending tool in the FE modelling. Since the strain signature of wrinkling test FE model D is slightly more similar to the spinning FE model, the specimen geometry modifications are proved effective. The bending induced by the bending tool may further improve the strain results since FE model C shows some positive effects from the involvement of the bending tool. Hence the involvement of the bending tool is very likely to improve the strain results in FE model D.

5.2.5 Wrinkling Test Design E

Although the modification to the geometry of specimen D successfully lowers the strains on target nodes, the overall strains of FE model D are still far from the ideal strains. The bending tool in FE model C is a factor worth involving in the modelling as the effect of the bending tool is a representation of the roller in the spinning process. The strain results of the FE model E after involving the bending tool are valid results to compare with the results without the bending tool of model D and the ideal strain results in spinning model No. 10.

Aim of test design E

Improve the strain results by involving the bending tool in the FE modelling. The geometry of the bending tool and the specimen will not be modified from model D. The specimen is directly using specimen D, and the bending tool is also using the bending tool from FE model C. Also, the boundary conditions must be feasible to be implemented by the BTBC rig.

Specimen geometry and boundary conditions of test design E

As mentioned in the previous section, the geometry of the specimen and the bending tool are identical to the previous models. The FE model is shown in Figure 5.34. The bending tool is located at the axes centre on the BTBC rig, as shown in Figure 5.34 (a). The arm on axis 2 is simplified, the length and thickness of the arm on axis 2 are reduced, and the remaining section marked by the dashed lines is fixed throughout the modelling process. The first step, step A, is to apply the compression boundary condition to the specimen on axis 1. The compression is applied to the identical arc gauge area at a 0.12 mm/s compression speed for 10 seconds, similar to the previous models B, C and D. The bending tool is located above the specimen to create room for the specimen to wrinkle upwards, as shown in Figure 5.34 (b). The second and third steps, steps B and C, are only related to the bending tool. The bending tool moves downwards, inducing bending to the specimen in the vertical (thickness) direction. After the bending tool reaches the original horizontal level in step B, it moves upwards and ceases to contact the specimen, the same as the roller leaving an area on the workpiece that the roller has just worked over. There is a 15 mm distance between the bending tool and the specimen, as shown in Figure 5.34 (c). The boundary conditions applied to the bending tool are a moving speed of 1.5 mm/s for 10 seconds downwards in step B and upwards in step C, respectively.

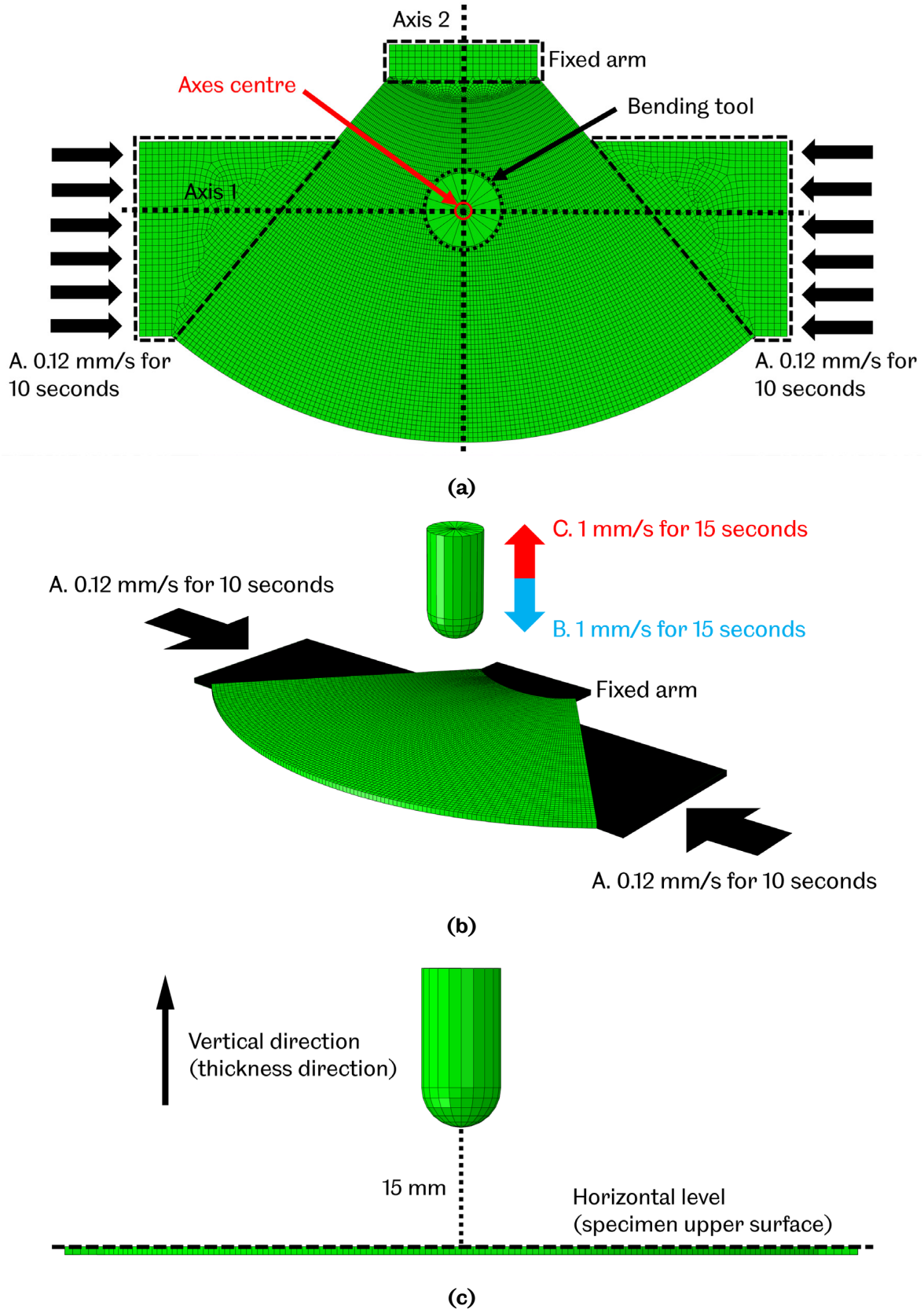

Figure 5.34 (a) top view of wrinkling test FE model E and boundary conditions; (b) side view of the FE model E with the bending tool and the simplified specimen, and (c) the distance of the bending tool above the specimen.

FE results and discussion of test design E

FE model E after the compression boundary conditions and the bending tool is applied to the specimen is shown in Figure 5.35. The early stage of the modelling is identical to FE model D, with only compression boundary conditions applied to the specimen. In the late stage of the modelling, the bending tool reaches the horizontal level and is about to leave the specimen, as shown in Figure 5.35 (a). Different from the results without the bending tool in model D, model E creates more than one wrinkling wave with wrinkling top and bottom, as shown in Figure 5.35 (b). The bending tool induces bending to the specimen, and with the constraint provided by the newly added arm on axis 2, the bending is concentrated on material near the edge of the specimen. In FE models B and C, with no constraint from the added arm on axis 2, the bending induced by the bending tool does not cause an extra wrinkling bottom like that in FE model E.

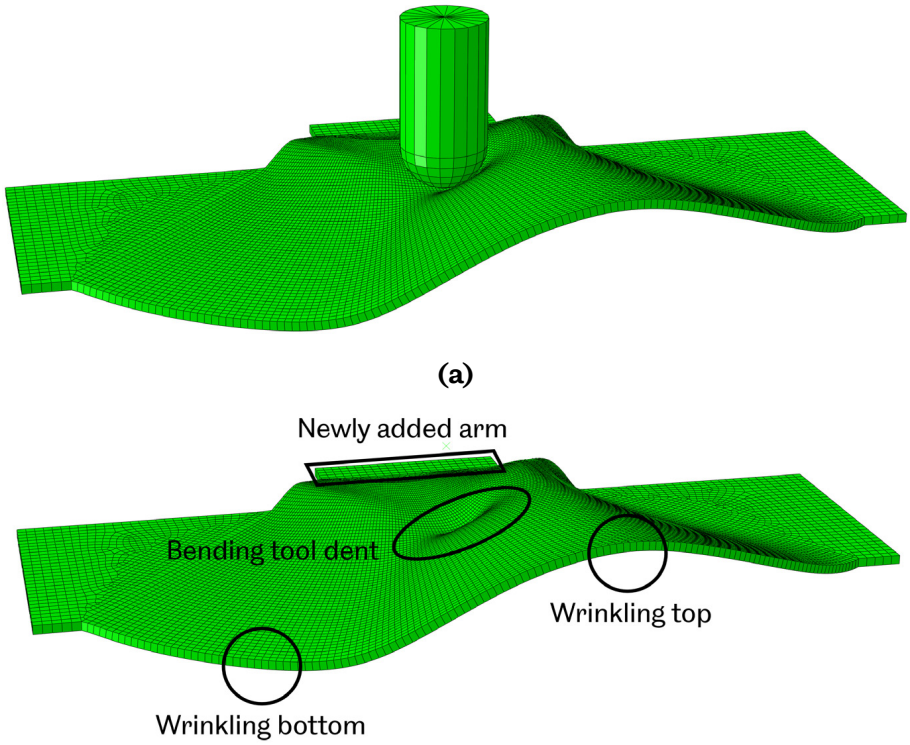

Figure 5.35 (a) FE model E after the bending tool contacts specimen E and (b) after the bending tool leaves specimen E.

The circumferential strain contour is shown in Figure 5.36. There is a distortion area on the left side of the specimen. The area is the thickness reduction junction between a 2 mm thick arm and a 1 mm thick gauge area. Without the newly added arm, FE models B and C do not have an area distorted like FE model E. FE model D does not either. In conclusion, the bending tool and the constraint provided by the

newly added arm on axis 2 cause distortion with a 0.105 circumferential strain. The elements are more elongated in the circumferential direction than in FE models B, C and D.

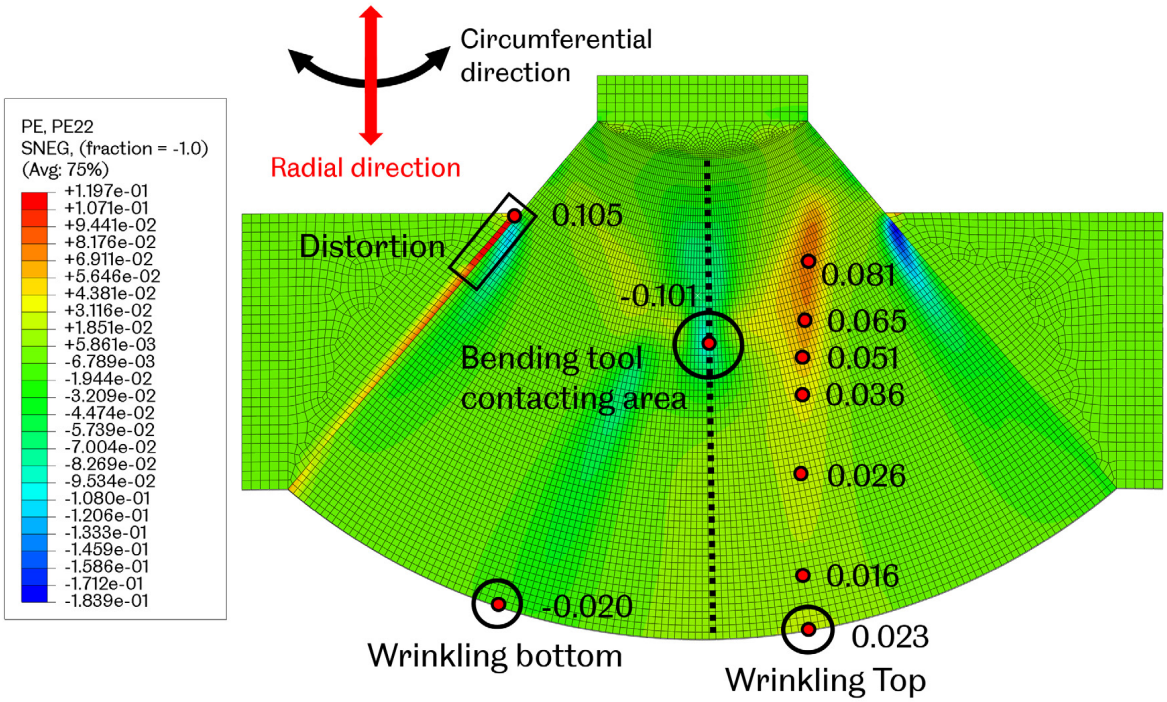

Figure 5.36 Circumferential strain contour of FE model E.

It is obvious that the strain results of the FE model E are not satisfying. As mentioned in section 5.2.4, circumferential strains of the wrinkling wave in spinning FE model No.10 are much greater than the strains in FE model E. As shown in Figure 5.36, the node with –0.02 circumferential strain on the lower left is the wrinkling bottom, with the most compressive circumferential strain on the edge of the specimen. The node with 0.023 circumferential strain on the lower right is the wrinkling top, with the most tensile circumferential strain on the edge of the specimen. The bending tool contacting area (dent) is not even in the same radius direction, marked by the black dashed line, with the wrinkling bottom or top. The node with the greatest tensile strain (0.081) is far from the edge on the top right side. These nodes show a similar trend with FE model D; the strain decreases from 0.081 to 0.016 and increases from 0.016 to 0.023 in FE model E. In the spinning FE model, the strain on the wrinkling top lines is with an increasing trend only with no turning point on any of the node sets.

For FE model E, with the constraint from the newly added arm on axis 2 and the bending deformation mode induced by the bending tool, the specimen successfully achieved multiple wrinkling waves with one wrinkling top and bottom. However, similar to all the previous FE models, the strains are much smaller than the strains

in the spinning FE model. The fixed bending tool is considered inadequate to induce the necessary boundary conditions to achieve similar wrinkling deformation by the BTBC rig. In conclusion, certain constraints are necessary, for example, the newly added arm, to constrain the deformation of the area near the newly added arm. In other words, the arm increases the strength of the nearby section. This conclusion further interprets that even though the gauge area has thickness reduced (initially to reduce the strength of the gauge area and make it easier to deform), there are still constraints that might be needed to increase the strength of certain areas on the gauge area for a similar strain results as that of the spinning FE model. The BTBC rig has explored its full potential to achieve a wrinkling deformation in the spinning process. However, the current capability of the BTBC rig is inadequate. Major modifications to the boundary conditions are necessary. For the next wrinkling test FE model, the idea must be explored beyond the capability of the current BTBC rig and include any other feasible modifications (new functions) to the BTBC rig.

Modification and improvement required for test design E

Major changes are necessary for future modifications to the specimen geometry and the boundary conditions, including modifications to the structure and components of the BTBC rig. New functions can be added to the test design model, such as a movable bending tool to include more actions similar to the roller in the spinning process and extra clamps as constraint boundary conditions to the specimen.

5.2.6 Wrinkling Test Design F

After numerous FE model modifications on the BTBC rig, the original BTBC rig is considered inadequate to reproduce the wrinkling deformation in the spinning process. In general, the specimen geometry is much easier to modify since the only design limitation is whether the specimen can be fit onto the BTBC rig. There is great potential for developing various specimens corresponding to spinning workpieces with different geometries. However, in the previous FE models, the boundary conditions are limited by the current capability of the BTBC rig. In FE model F, the limitations are slightly eased to develop a new set of boundary conditions that can provide much more similar deformation modes to the specimen as in the spinning process.

Aim of test design F

Modify the specimen geometry and design the boundary conditions that include more features of the spinning process. The aim is to achieve more than one wrinkling wave, at least including wrinkling top and bottom like FE model E. The strain results

of the wrinkling wave should be ideally similar to the strains in spinning FE model No.10.

Specimen geometry and boundary conditions of test design F

The geometry of specimen F is shown in Figure 5.37. The detailed dimensions of specimen F are shown in Figure 5.37 (a). The gauge area of specimen F is identical to the previous models. The width of the arm is further reduced based on specimens D and E. The purpose is to focus compression boundary conditions more toward the edge of the arc gauge area. The strategy to increase the strength of the arm is identical to the previous modes. The deformation can be focused on the gauge area by increasing the thickness of the arm to 2 mm. There is a sudden thickness change on the junction as the thickness boundary line between the arm and the gauge area. The detail of the thickness boundary line is shown in Figure 5.37 (b). The general design rewinds to specimens B and C, with only two arms on the two sides of the arc gauge area, without the arm on axis 2. Although the arm on axis 2 does strengthen the gauge area near this arm and improves the strain results, the deformation and even distortion occur in some unexpected areas and cause abnormally great strains, as shown in Figure 5.36. Hence in FE model F, the gauge area is partially strengthened by using the upper and lower clamps as a constraint. The purpose is the same as the previous specimens, to ensure the wrinkling occurs in the same direction.

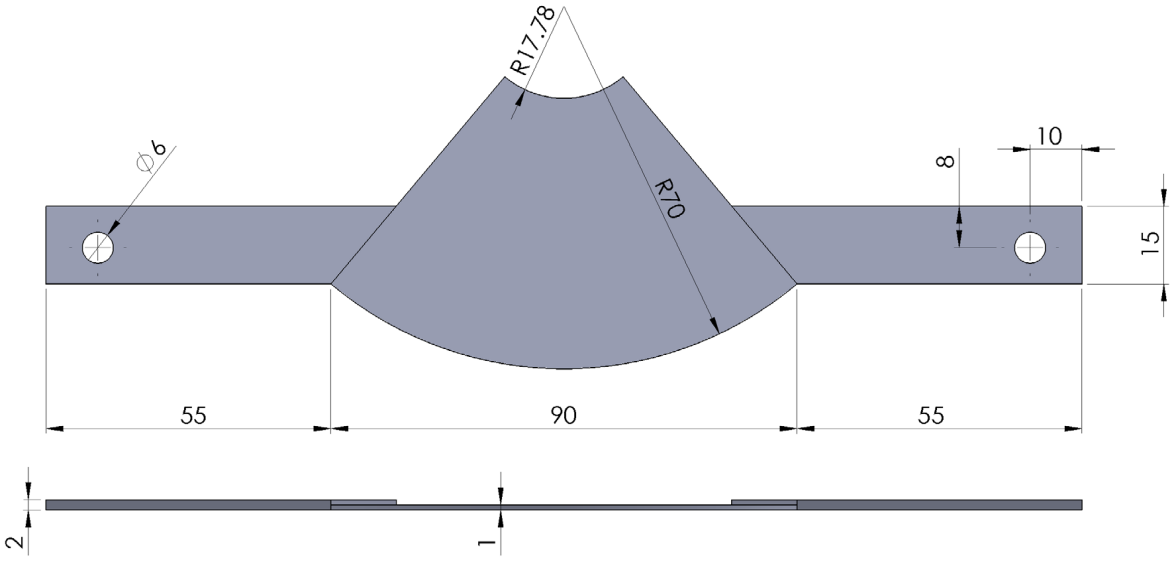

(a)

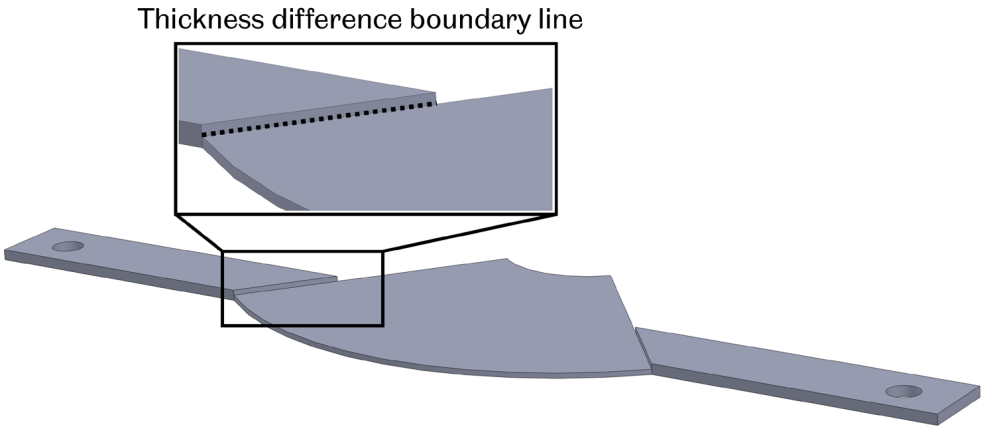

(b)

Figure 5.37 (a) geometry of the specimen F and (b) enlarged view of the junction between the arm and gauge area.

The elements of the specimen are assigned with the SC8R shell element as in the previous FE models. The mesh is refined on the area that contacts the bending tool in the modelling. The detailed meshing strategy is shown in Figure 5.38. Since the element type is the SC8R shell element, the thickness must be uniform in the modelling. Hence the thickness is uniform at 1 mm, and the effect of the increased strength by thicker arms will be reproduced by the boundary conditions applied to the arms.

The boundary conditions applied in FE model F are shown in Figure 5.39. Since the fixed bending tool in the BTBC rig is inadequate to reproduce a similar scenario as that in the spinning process, the boundary conditions for the bending tool are changed with the location. Originally, only the height of the bending tool could be changed by adjusting the downwards and upwards displacement. The location of the bending tool cannot be changed, and the bending tool stays on the axes centre point. In FE model F, the bending tool moves on an arc toolpath with the compression applied on both sides of the specimen by two fixed clamps, as shown in Figure 5.39 (a). The boundary conditions are applied to the specimen in three steps. In step A, the bending tool moves downwards for 2.96 mm, at a speed of 0.296 mm/s for 10 seconds. The bending tool induces bending to the specimen and compresses the specimen with the lower clamp. In step B, the bending tool works over the specimen on an arc path with a 55 mm radius and a 65-degree subtending angle at a constant speed, as shown in Figure 5.39 (b). The compression on both arms of the specimen is also applied in step B. After the bending tool finishes working over the specimen, it moves upwards and stops contacting the specimen. This step is similar to the roller leaving a certain area on the workpiece after finishing working over the area in the spinning process. The upper and lower clamps are fixed throughout the

process, constraining the gauge area and preventing excessive strains from occurring on the area close to the centre of the arc, as in FE models B and D, which constrain the gauge area by using the arm on axis 2.

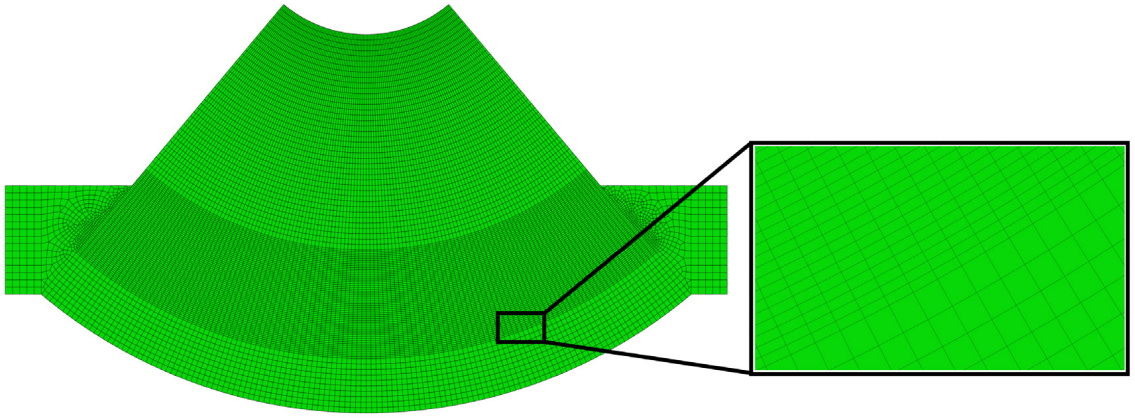

(a)

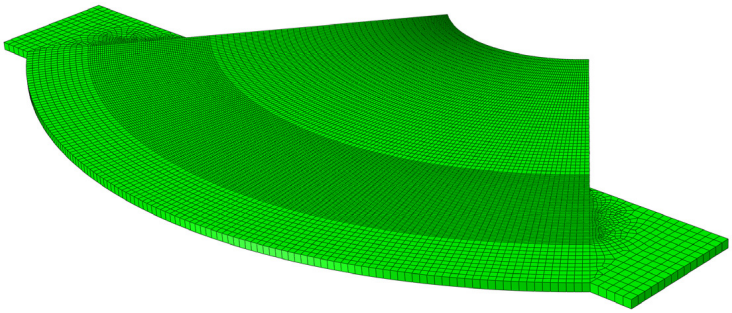

(b)

Figure 5.38 (a) the simplified specimen in FE model F with an enlarged view of meshing strategy and (b) a side view of the specimen with uniform thickness.

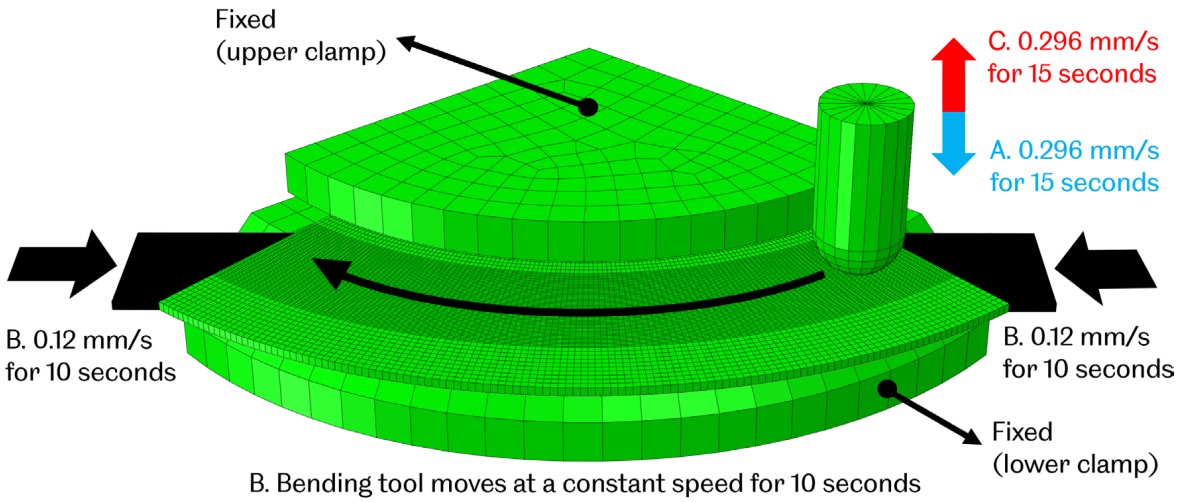

(a)

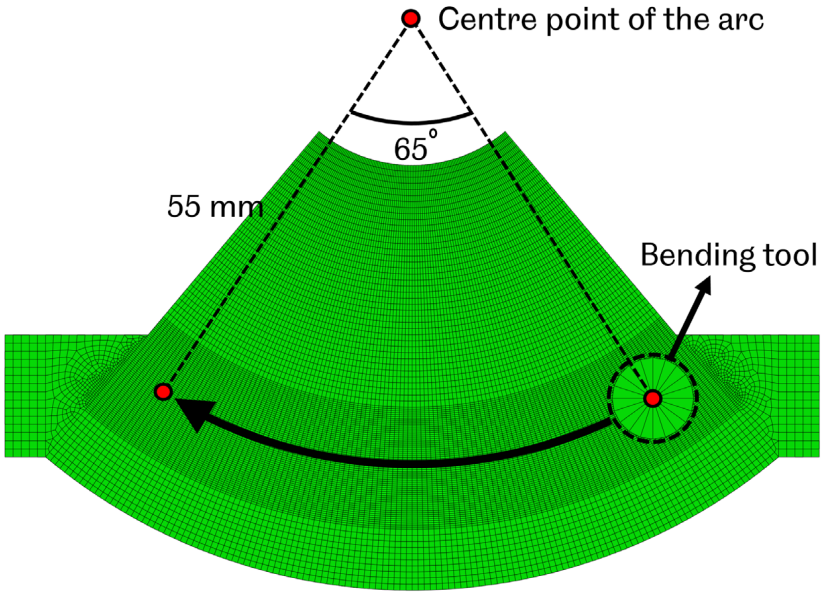

(b)

Figure 5.39 (a) an illustration of the boundary conditions applied to the FE model F and (b) the top view of the bending tool toolpath.

Since the geometry of the arc gauge area is identical to the previous FE model B to E, the compression boundary conditions applied to the gauge area are also identical. A 2.4 mm compression displacement is applied to the gauge area after 10 seconds of compression. The major changes to the boundary conditions of the bending tool and the involvement of newly designed upper and lower clamps are to reproduce the features in the spinning process using the BTBC rig for maximum similarity. The workpiece thickness in the spinning process is reduced to a certain value by the roller, determined by the sine law. The effect of the specimen thickness reduction is not included in FE models B to E. In step A of FE model F, the bending tool is applied with the boundary conditions of moving downwards for 2.96 mm and compresses the specimen with the lower clamp, creating a reduced thickness by the sine law, $\sin(45^{\circ})$, as shown in Figure 5.40. The side view of the FE model F is shown in Figure 5.40 (a). The schematic diagrams of before and after the bending tool compresses the specimen are shown in Figure 5.40 (b) and Figure 5.40 (c), respectively. The thickness of the section compressed by the bending tool and the lower clamp is reduced to 0.71 mm. In step B, the bending tool works over the specimen, inducing bending and compression to the specimen and creating a series of sections with the same thickness reduction. The radius of the arc toolpath is determined by the actual wrinkling forming location in the spinning process. The wrinkling usually forms on the flange areas 40 to 70 mm away from the workpiece centre, varied by the feed ratios. Hence, a 55 mm radius of the arc toolpath is determined as an average value

to locate the initial point of the toolpath. The initial and finishing points form a toolpath as a 65-degree arc. In the spinning process, the workpiece is considered a 360-degree arc with six to nine wrinkling waves, varied by the feed ratio. The toolpath determined as a 65-degree arc is to ideally include more than one wrinkling wave with a wrinkling top and a wrinkling bottom.

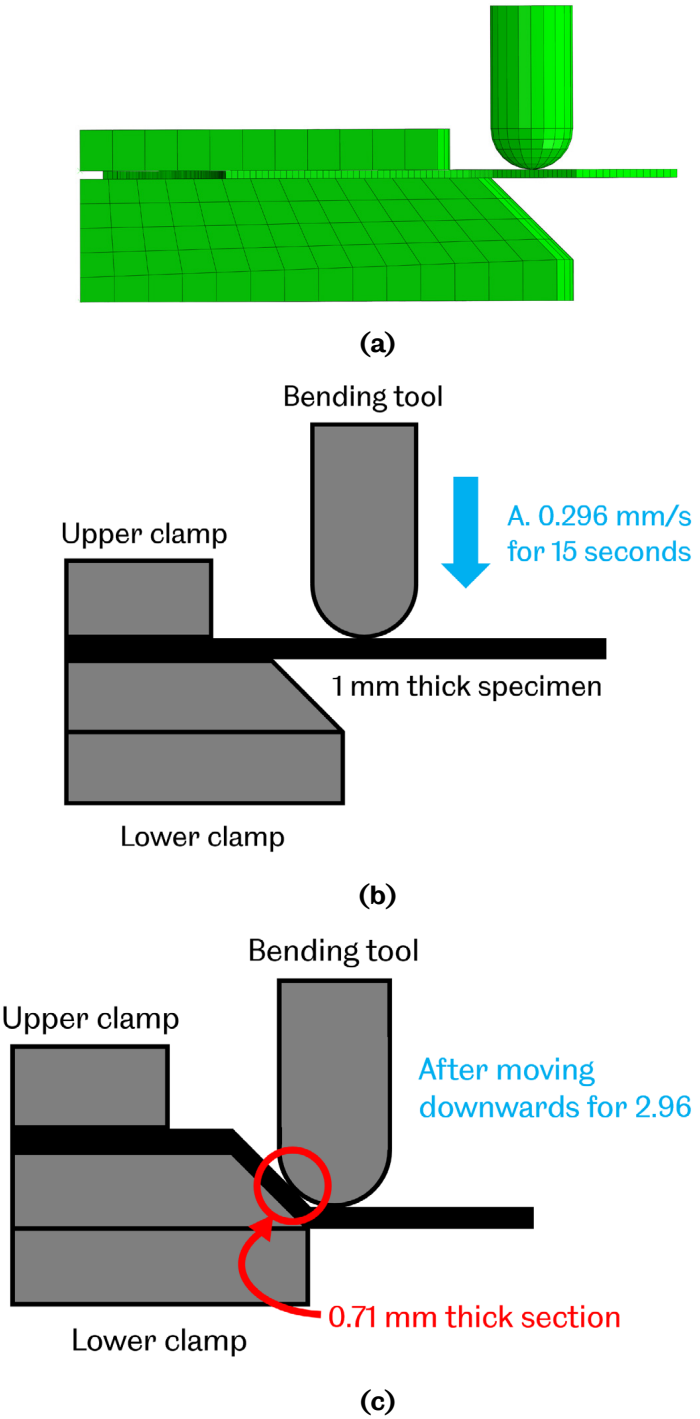

Figure 5.40 (a) side view of the FE model F, (b) schematic diagram of the FE model F before the bending tool moves downwards and (c) schematic diagram of the FE model F after the bending tool moves downwards for 2.96 mm.

FE results and discussion of test design F

The material deformation in the wrinkling test FE modelling is illustrated in Figure 5.41. The bending tool moves downwards and compresses the specimen with the lower clamp. The roller works over an arc area on the specimen, as illustrated in Figure 5.41 between figures No.2 to No.6. The thickness contour of the specimen is shown in Figure 5.42. The bending tool produces a reduced thickness, shown by the blue trail after the process is finished, as shown in Figure 5.42 (a). The thickness of the compressed area is around 0.75 mm, as the dark blue contour indicated. The bending tool gradually reduces the 1 mm thick specimen to around 0.75 mm throughout the process, as shown in Figure 5.42 (a). The theoretical thickness is 0.707 mm after the process, determined by the sine law (sine 45-degree). Only a 6.1% deviation between the theoretical and FE modelling results. The strain contour with only the specimen is shown in Figure 5.42 (b). The node sets are selected in the circumferential and radial directions to output the results. The node sets A, B and C are illustrated in Figure 5.43. Node set A is selected in the radial direction with 110 nodes. Node set B is selected in the circumferential direction with 130 nodes, and these nodes are with the smallest thickness. Node set C is on the edge of the arc gauge area with 130 nodes. Nodes set A, B and C are selected when the bending tool is at its initial location. Node No.1 of node sets B and C is on the right-hand side of the bending tool.

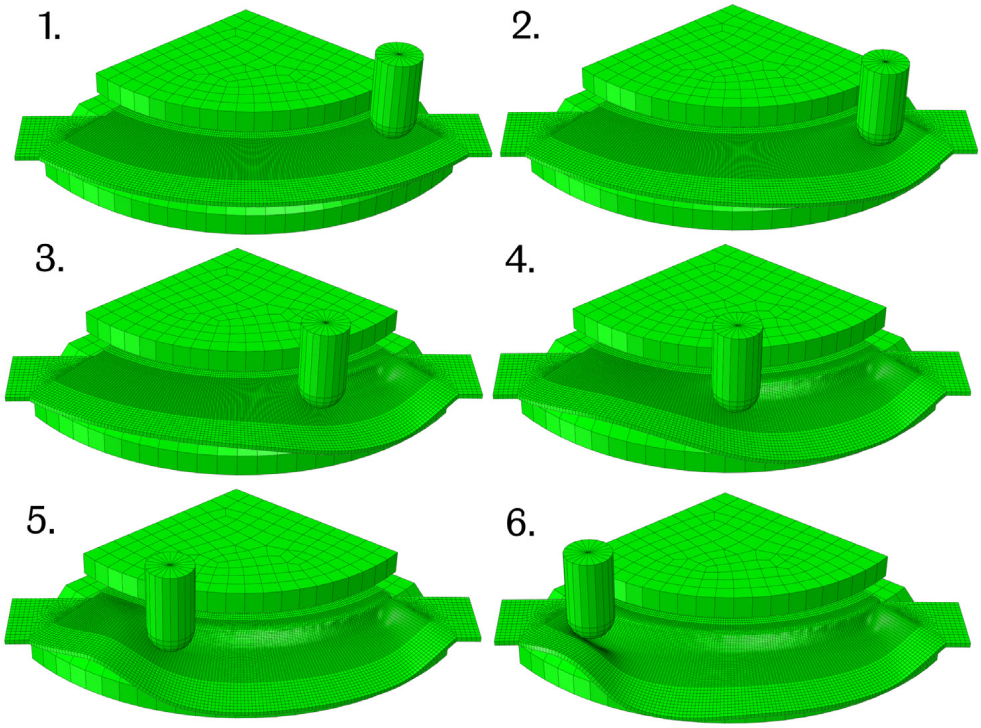

Figure 5.41 Wrinkling test FE model F process.

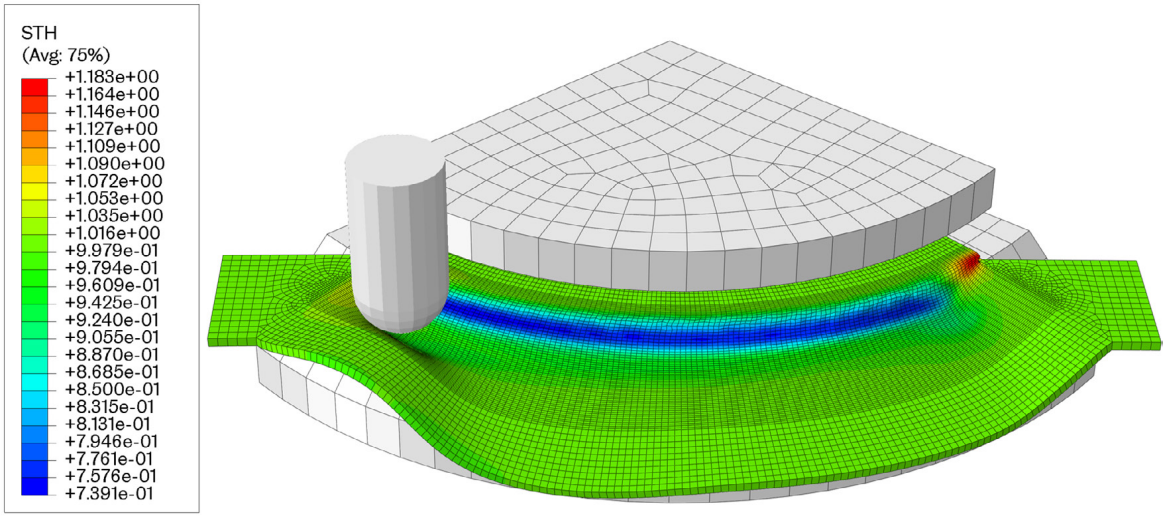

(a)

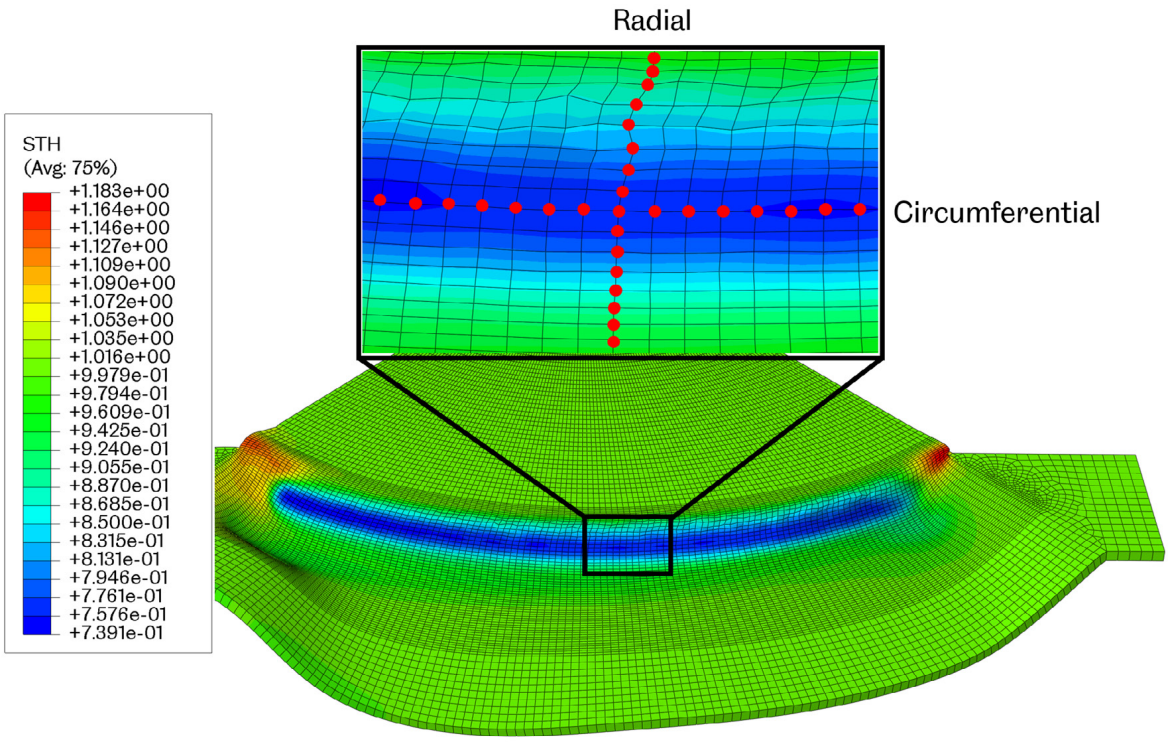

(b)

Figure 5.42 Thickness contour of the wrinkling test FE model F (a) with tool and clamps and (b) without tool and clamps.

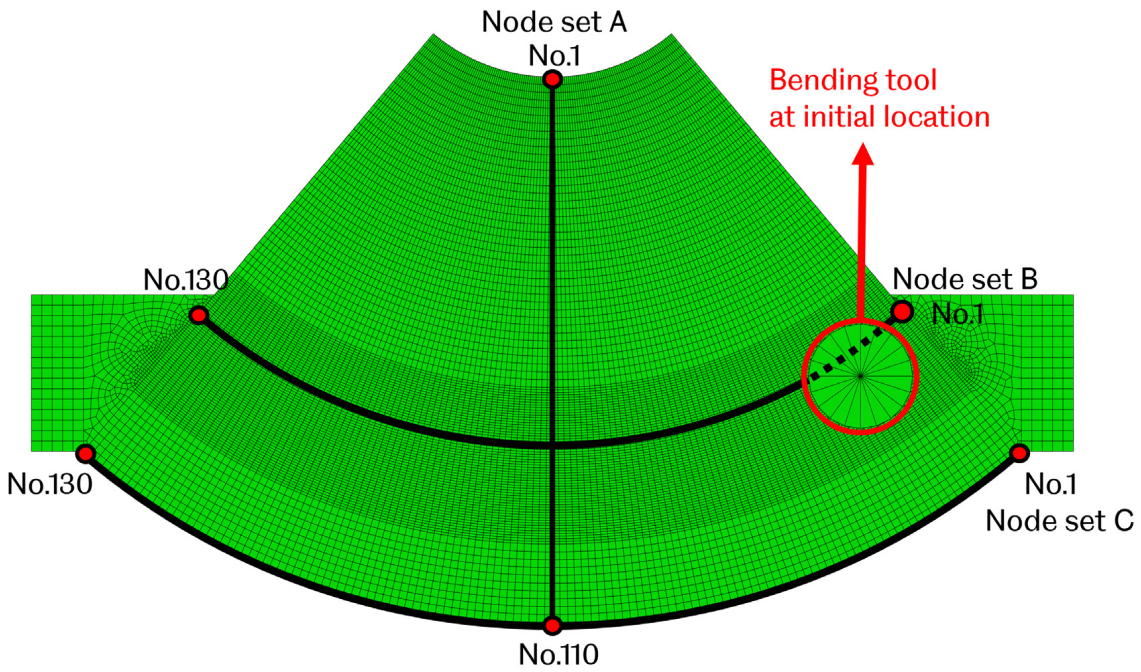

Figure 5.43 Illustration of node sets A, B and C selected on the specimen.

The thickness results of the node set A and B are shown in Figure 5.44 and Figure 5.45, respectively. The smallest thickness on node set A is 0.758, as shown in Figure 5.44. There is an obvious bending tool working zone marked by two dashed lines in Figure 5.44. The average thickness of nodes No.20 to No.110 is 0.758 mm. Nodes No.1 to No.20 and No.110 to No.130 are too close to the arms on the two sides of the gauge area and the bending tool location when the modelling is finished. The thickness results in FE model F are very close to the theoretical sine law thickness of 0.707 mm. The average thickness is only 6.1% greater than the theoretical value. The thickness reduction feature in the spinning process has been achieved in the wrinkling test FE model F. However, the thickness of the workpiece in the spinning process is reduced gradually. In FE model F, the thickness only around node No.57 of node set A is reduced. Nodes before and after the bending toll contacting zone are not being deformed by the bending tool. Assume the node set A is being worked over by a roller in the spinning process; the thickness of nodes No.1 to No.56 will be reduced by the cyclical loading of the roller before node No.57.

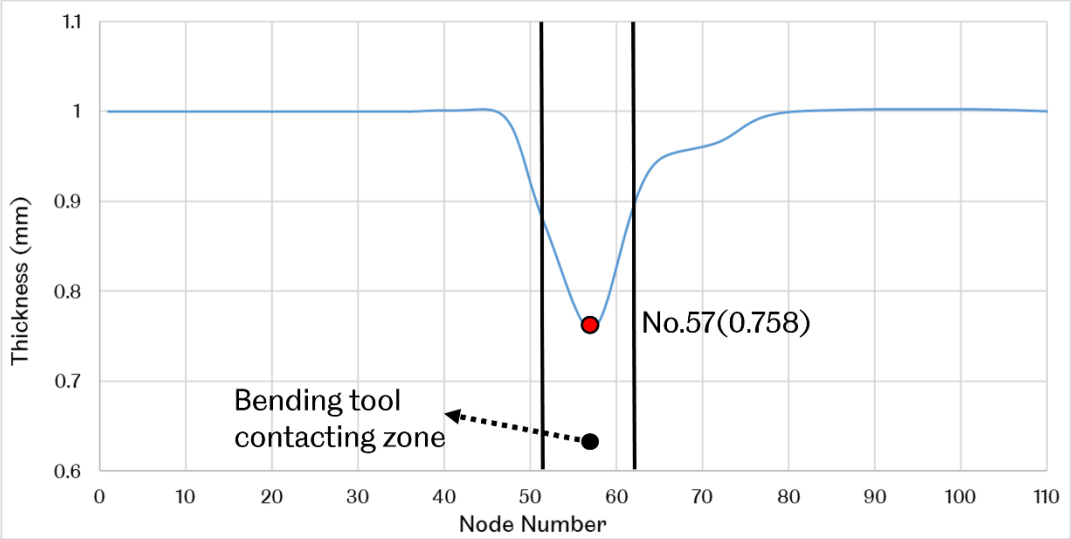

Figure 5.44 Thickness result of node set A.

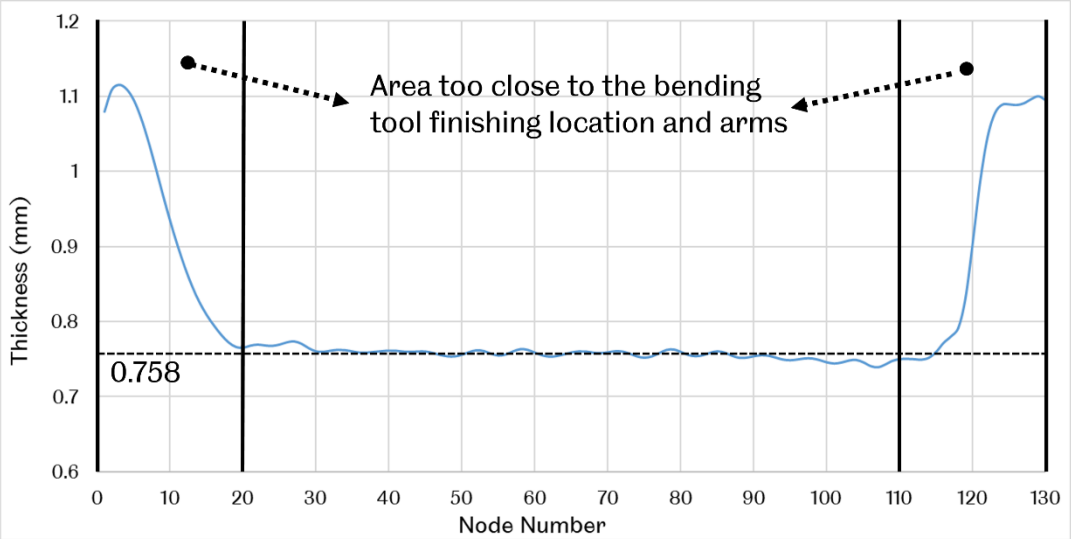

Figure 5.45 Thickness result of node set B.

The circumferential strain results of node set C on the edge of the arc gauge area are shown in Figure 5.46. Similar to the previously analysed thickness results, the strain results are extracted after the process is finished and the bending tool moves to the finishing location. There are two wrinkling tops and two wrinkling bottoms formed on the edge of the specimen, determined by whether the strains are tensile or compressive. It is a huge improvement to achieve more than one wrinkling wave with multiple wrinkling tops and bottoms. However, the strains of the wrinkling tops and bottoms are still much smaller than the strains in spinning FE model No.10 (0.125 on the workpiece edge as wrinkling top). The compression is still inadequate and unevenly distributed on the specimen. The compression only induces greater strains to the first several nodes (node No.1 to No.4) and the last (node No.125 to No.130) in node set C, as shown in Figure 5.46.

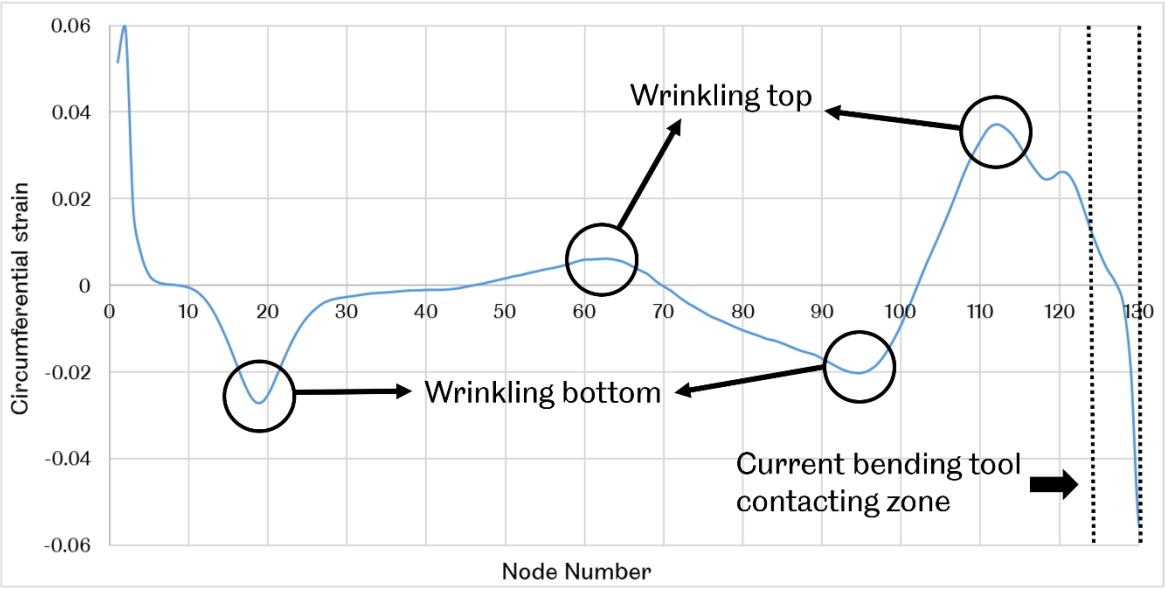

Figure 5.46 Circumferential strain results of node set C.

There is compression that causes the nodes in the middle of the edge of the specimen to be displaced and created circumferential strains. This compression is created by the effects of the bending tool working over the specimen and the downwards 2.96 mm displacement boundary conditions assigned to the bending tool before it starts to work over the specimen. The bending tool creates tensile circumferential stress and compressive radial stress, as shown in Figure 5.47. The compression boundary conditions applied to the arms did not transmit to the middle of the specimen; they only compressed the areas close to the arms. The compression that causes the circumferential strains and stresses results from the bending tool only, similar to the roller in the spinning process, as shown in Figure 5.48. The time point to output the stress and strain results is the modelling midpoint of both processes, 5s for wrinkling test FE model F and 0.75s for spinning FE model No.10. Five areas for each model are selected, and the maximums around the white marking points are extracted. The stress and strain results comparison and analysis are listed in Table 5.2.

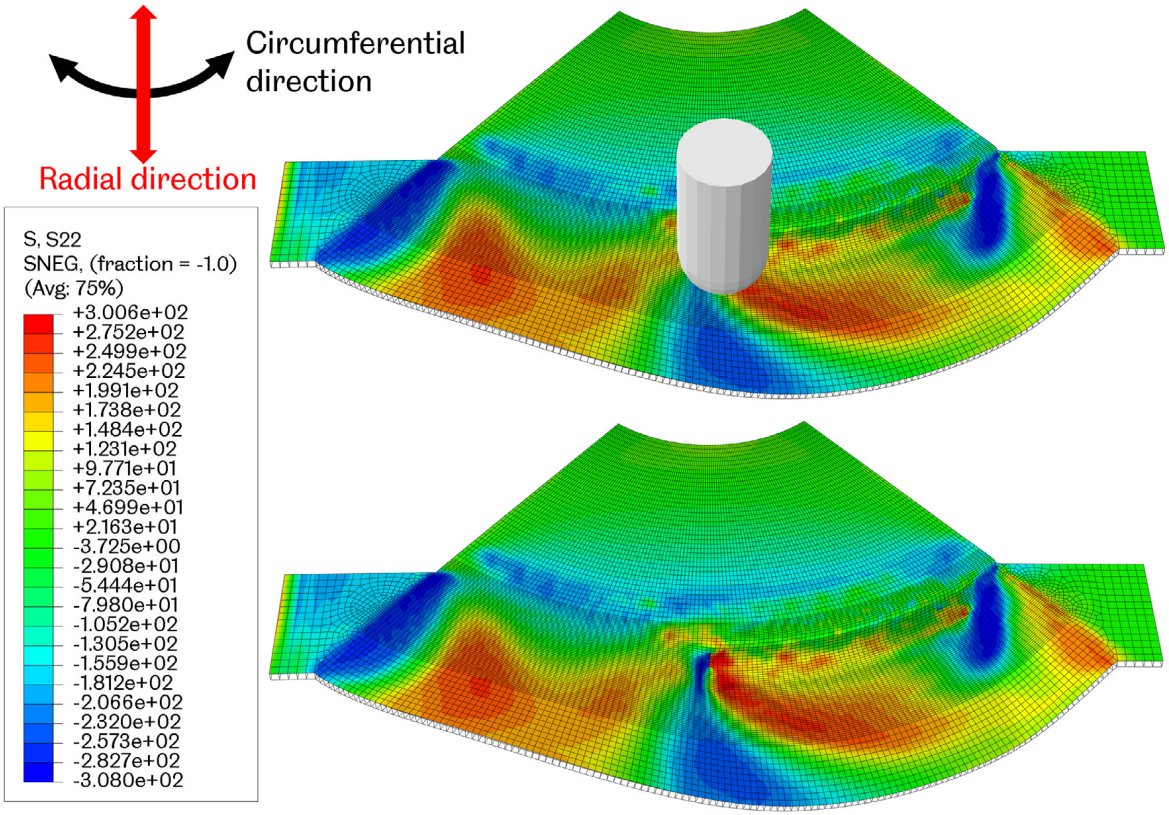

Figure 5.47 Circumferential stress contour of wrinkling test FE model F at 5.0s of step B.

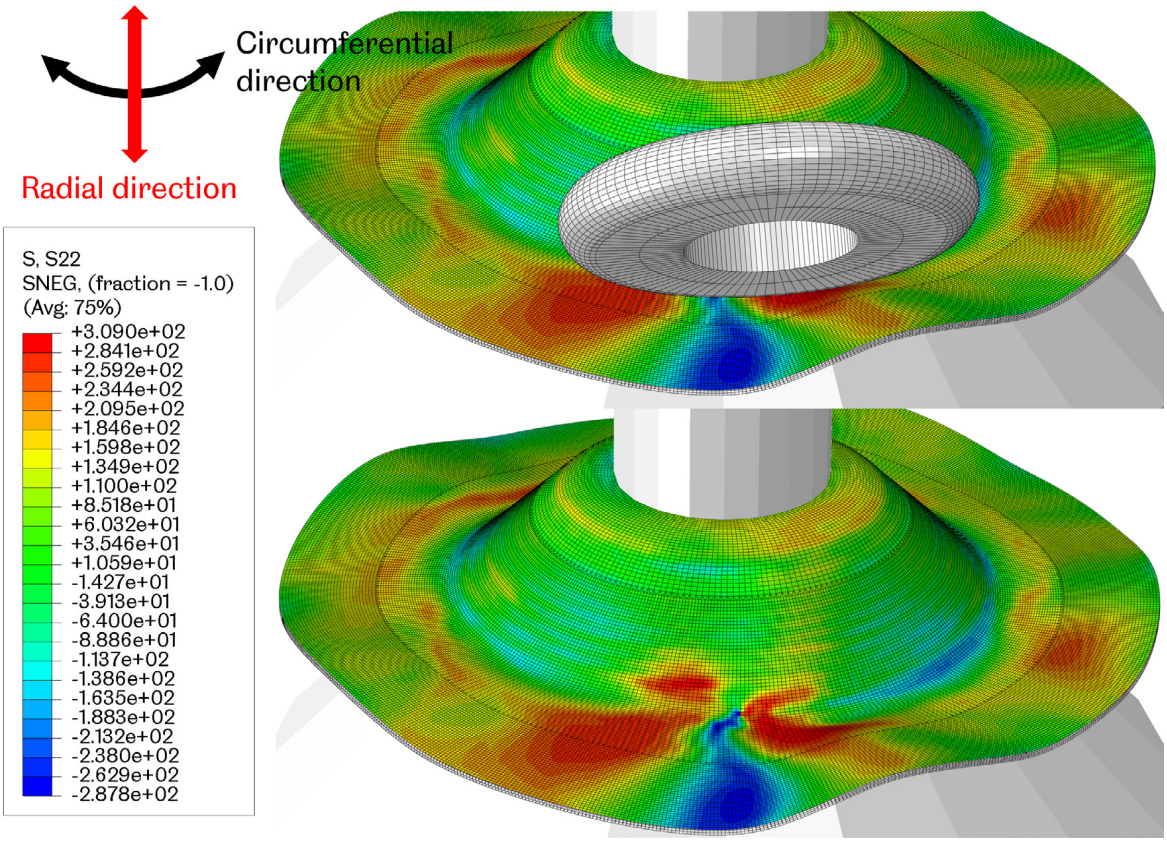

Figure 5.48 Circumferential stress contour of spinning FE model No.10 at 0.75s.

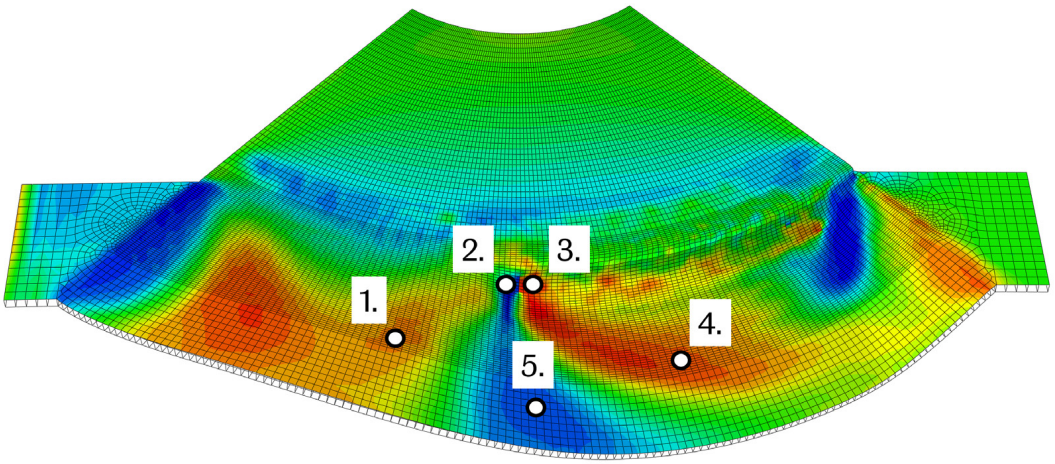

(a)

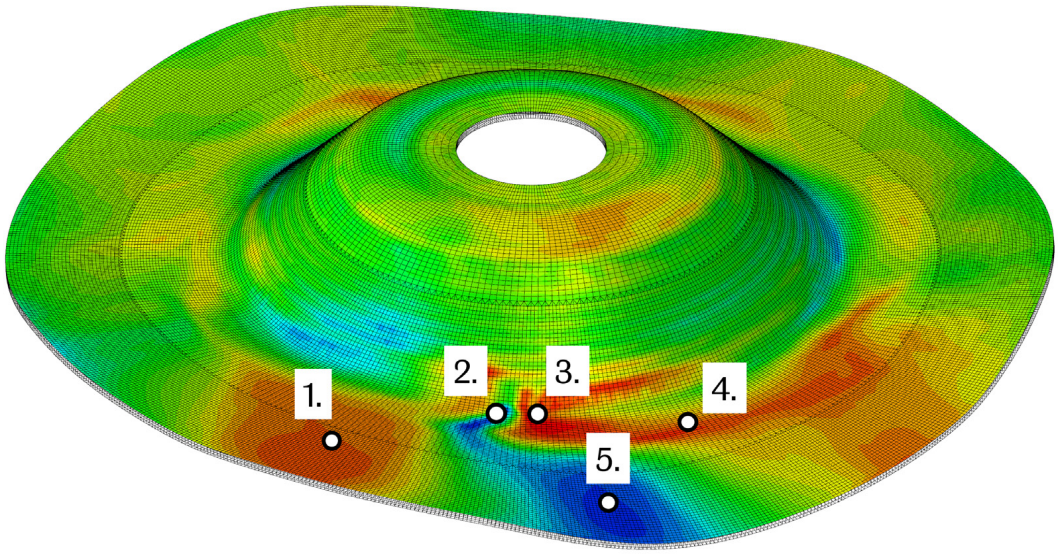

(b)

Figure 5.49 Selected areas on two specimens of (a) wrinkling test FE model F and (b) spinning FE model No.10.

Generally, the stress results correlate well between the wrinkling test FE model F and spinning FE model No.10, as shown in Table 5.2. Both models also indicate a similar pattern of compressive circumferential stresses in area No.2 with tensile stresses in the other four areas. The maximum results deviation is 13.8% between area No.1 of the two models. The strains of area No.1 and area No.3 are tensile, and the other three areas are compressive. The patterns between both models are identical. However, the circumferential strain results correlation between wrinkling test FE model F and spinning FE model No.10 is much worse than the circumferential stress results correlation, as shown in Table 5.3. Results deviations are much greater, and even in area No.2, the circumferential strain result deviation is greater than 100%.

Table 5.2 Circumferential stress of wrinkling test FE model F and spinning FE model No.10.

Area No.	Circumferential stress of wrinkling test FE model F (MPa)	Circumferential stress of spinning FE model No.10 (MPa)	Stress results deviation
1	223.5	254.4	13.8%
2	−293.5	−306.8	4.53%
3	294.2	312.4	6.19%
4	261.5	272.2	4.09%
5	259.9	262.5	1.00%

Table 5.3 Circumferential strain of wrinkling test FE model F and spinning FE model No.10.

Area No.	Circumferential strain of wrinkling test FE model F	Circumferential strain of spinning FE model No.10	Stress results deviation
1	0.0028	0.0023	21.7%
2	−0.2446	−0.0547	>100%
3	0.0088	0.0072	22.2%
4	−0.0161	−0.0159	1.26%
5	−0.0073	−0.0066	10.6%

In the shear spinning process, the feed ratio (mm/rev) is a processing parameter to determine the depth for the roller presses into the workpiece during each mandrel rotating revolution. The feed ratio in spinning FE model No.10 is 1.5 mm/rev, which means the roller presses a total of 1.5 mm distance into the workpiece in one revolution. In wrinkling test FE model F, the bending tool presses into the specimen in step A for 2.96 mm to simulate the pressing movement of the roller in the spinning process and achieve a thickness that follows the sine law. A 2.96 mm pressing distance is almost twice the depth for one revolution in spinning FE model No.10 (1.5 mm). Hence, the deformation caused by the bending tool in wrinkling test FE model F is more severe than the deformation caused by the roller in spinning FE model No.10. Thus, the circumferential strains of both models in area No.2 have excessively great deviation. The other areas (area No.1, No.4 and No.5) are far away from area No.2, and the bending tool finishes working over area No.3. The circumferential strain results of these areas have smaller results deviation compared with spinning FE model No.10.

A node as the wrinkling top is selected, as shown in Figure 5.50. The node is selected with the greatest circumferential strain after the bending tool finishes step B (deforming step). The circumferential strain of this node with the time history is shown in Figure 5.51.

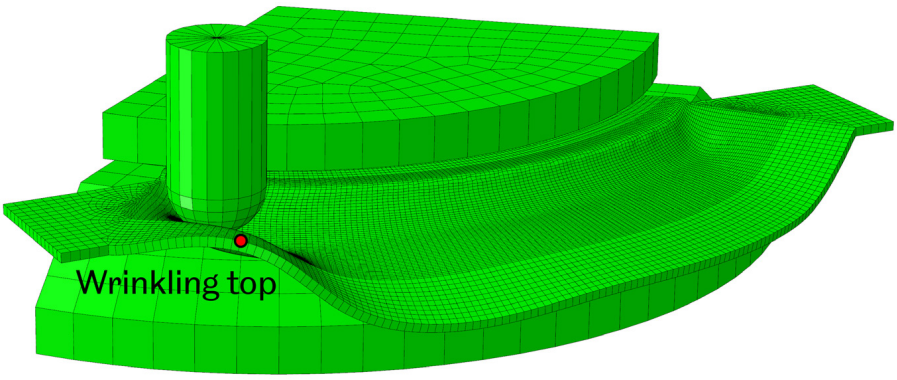

Figure 5.50 The selected node as a wrinkling top on the specimen at the end of step B.

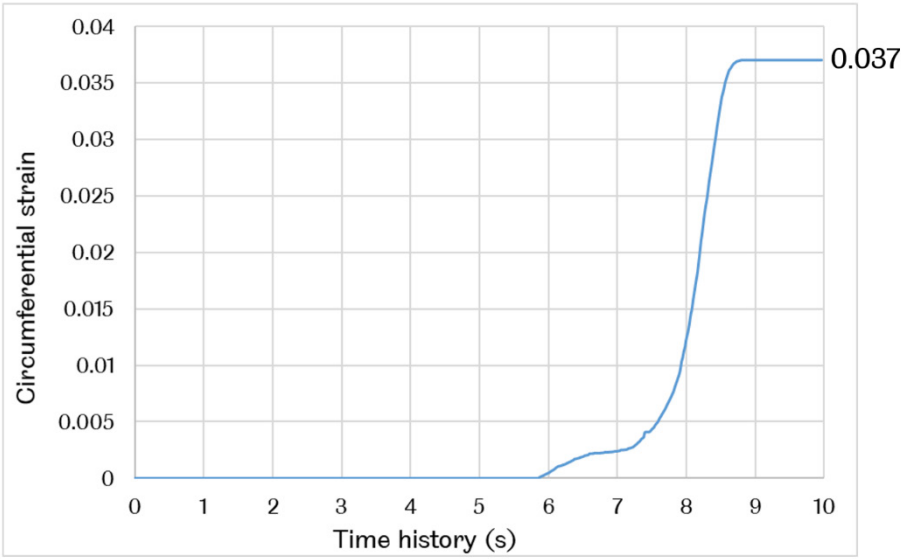

Figure 5.51 Circumferential strain of the wrinkling top in FE model F with time history.

The circumferential strain of the selected node is zero until step B nearly reaches the sixth second. The strain increases along the step and reaches a maximum of 0.037 at 8.8s, and the strain has not changed until the end of step B. However, the circumferential strain of the wrinkling top in spinning FE model No.10 is 12.5, much greater than 0.037.

Although wrinkling test FE model F has tried to reproduce the boundary conditions in the shear spinning process as similar as possible, the strain results still cannot correlate well with the spinning process. The circumferential strains in wrinkling test FE models B to F are much smaller than the strains in spinning FE model No.10. Only model A achieves the strain results with similar values to spinning model No.1 than the other wrinkling test FE models. But there is almost no similarity between wrinkling test FE model A and spinning FE model No.10 since the strain signature of FE model A is far from matching with spinning FE model. Wrinkling test FE model F still needs further modifications to improve the strain results for better corealation with the spinning FE modelling results.

Modification and improvement required for test design F

Wrinkling test FE model F has achieved many similarities to the spinning process, for example, multiple wrinkling waves and similar circumferential strain and stress patterns. Although it is the last model developed in Chapter 5, it is still not fully satisfying. Since there is no further development after completing FE model F in this study, modifications to FE model F can be considered further work. The geometry of the specimen needs to be changed for the modified compression loadings. The compression boundary conditions in the spinning process are always normal to the two sides of the arc gauge area. The compression loadings are not in a straight line (axis 1) as in the six wrinkling test FE models in this chapter. A pre-set angle is formed between the two loading axes. The sum of pre-set angle and the arc angle is 180°. The modified compression loadings are shown in Figure 5.52.

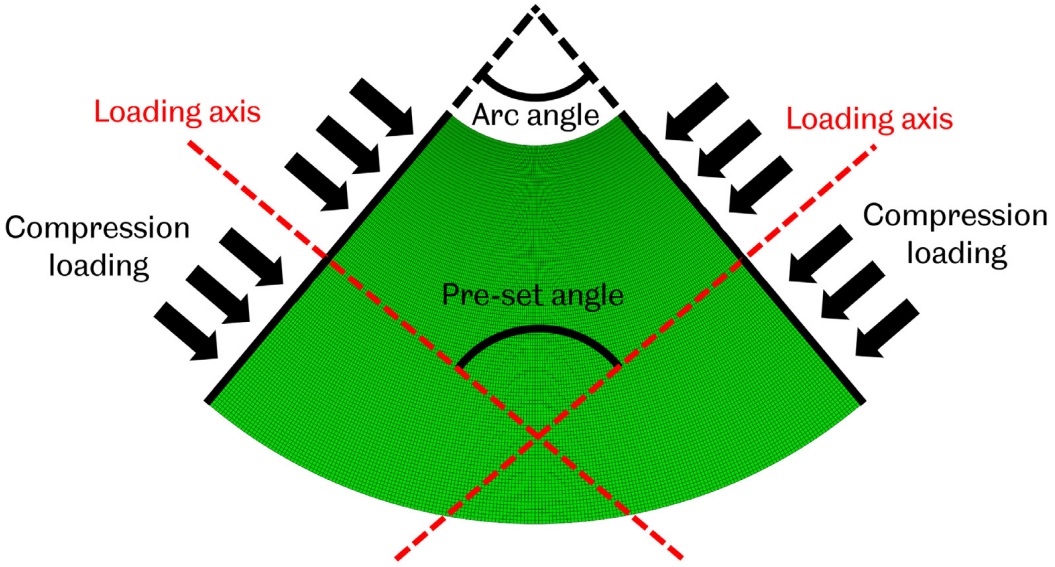

Figure 5.52 Modified compression loadings normal to the sides of the arc gauge area.

In wrinkling test FE model F, the deforming tool presses downwards 2.96 mm into the specimen, inducing bending deformation in step A before working over the specimen on an arc toolpath. Even if the bending tool presses deeper than the roller in the spinning FE model No.10 (1.5 mm for one revolution), the circumferential strain results are still smaller than the results in the spinning FE model No.10. The toolpath of the bending tool in wrinkling test FE model F is a one-pass, meaning the bending tool only works over and deforms the specimen once. In spinning FE model No.10, the roller works over a rotating workpiece is more similar to cyclic deformation since the roller deforms the workpiece multiple times. Hence, the toolpath can be modified, and the cyclical toolpath can be involved in the modelling. The bending tool can be designed to work over the specimen cyclically rather than only once, as in wrinkling test FE model F. Also, different initial downwards pressing displacements

can be applied to the bending tool, derived from the corresponding spinning FE models.

5.3 Summary of Conclusion

Six wrinkling test FE models are developed based on the BTBC rig to reproduce the wrinkling deformation in the spinning process. Each model is an improved version of the previous one. The stress and strain results of the six wrinkling test models are analysed and compared with the results of the spinning FE model to determine whether the wrinkling test FE models successfully reproduce the wrinkling deformation. Based on the FE results obtained from these six models, the following conclusions are drawn:

- The BTBC rig is capable of producing wrinkling deformation on the specimens that developed to fit onto the rig. Boundary conditions applied to the specimen and the geometry of the specimen are developed. The wrinkling deformation is successfully achieved.
- The wrinkling test aims to achieve similar wrinkling deformation in the spinning process on the BTBC rig with converted boundary conditions. It has been modified five times from the first wrinkling test FE model, and the wrinkling deformation still does not match the spinning FE model. The strain results of six wrinkling test FE models are much smaller, and the strain signatures have limited similarities because the test method only achieved early-stage/minor wrinkling deformation.
- Among the six wrinkling test FE models, the results of FE model F are the most similar to the spinning FE model. The stress and strain results are compared, and the stress results show a better correlation with the spinning FE model. The strain results are not as good as the stress results.
- The most important feature of the specimen is the thickness-reduced arc gauge area. The thickness reduction allows the deformation to occur only on the gauge area, and the arc geometry represents the workpiece flange in the spinning process.
- The capability of the initial BTBC rig is inadequate for providing the necessary boundary conditions to cause wrinkling deformation similar to the spinning process. From the wrinkling test FE model F, it has been found that the toolpath by the bending tool should be cyclically applied rather than one-pass because the wrinkling deformation is a result of strain cyclical accumulation in the spinning process. The two compression conditions should be applied

perpendicularly to the two sides of the gauge area, as in the spinning process. A pre-set angle is needed between the directions of the two compression boundary conditions. However, the BTBC rig cannot apply compression with pre-set angles due to the limitation of its design.

6 Experiment of New Wrinkling Test Method

In Chapter 5, six wrinkling test FE models are developed. However, the circumferential and radial strains are always much smaller than that from the spinning FE model. In this chapter, four wrinkling test FE models are experimentally tested and compared with the corresponding wrinkling test FE results presented in Chapter 5. Specimens of AA5251 aluminium alloy are used in the tests, similar to that used in the FE models. Section 6.1 presents a detailed introduction of the BTBC rig and the testing concept of the wrinkling test method. Section 6.2 introduces the geometry of the specimens, the test setup and the test parameters used. Section 6.3 is the result analysis and discussion of the wrinkling experimental tests. Section 6.4 is the summary of the main findings of Chapter 6.

6.1 Concept of the New Wrinkling Testing Method

The aim of this chapter is to perform the newly developed wrinkling experiment on the BTBC rig. The new wrinkling testing method is to test formability related to the wrinkling in the spinning process by the specimen designed to fit onto the BTBC rig. The applied loadings on the BTBC rig are derived from the spinning process. Although the wrinkling test FE modelling results in Chapter 5 are not ideal, performing the experimental tests developed in Chapter 5 will expose the details that are not considered in the FE models and support the future development of the wrinkling testing methods.

Several modifications are made to the BTBC rig, as shown in Figure 6.1. Critical components and devices are indicated as No.1 to No.10. As mentioned in Chapter 2, the original BTBC rig was designed to apply elongating loadings to the cruciform specimen to test the formability of the incremental sheet metal forming process [89]. The compression and bending deformation can be applied to the specimen by the bending system (component No.6) with a bending tool of 5 mm radius semispherical head to apply the bending deformation. The CAD drawings of the bending system with specimens B and D are shown in Figure 6.2. The hand wheel controls the movement of the bending tool, the bending depth (downward displacement of the bending tool), and two mounting rods as the general structure to support the bending tool.

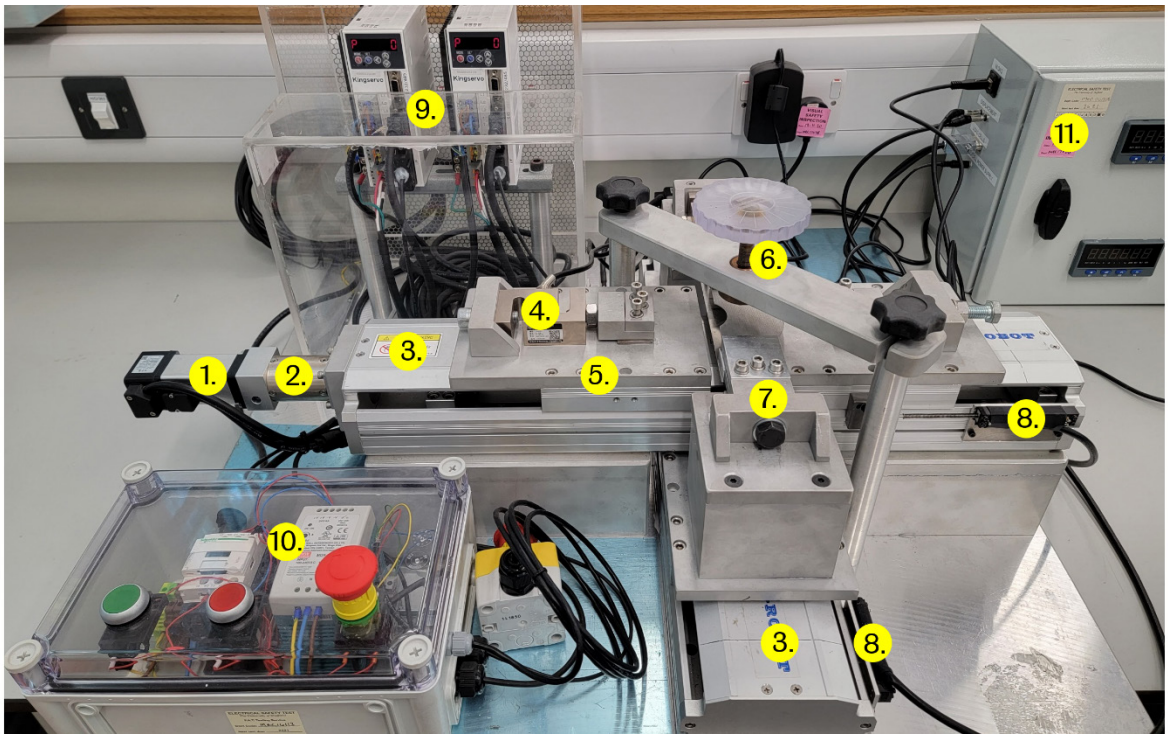

Figure 6.1 Critical components of the BTBC rig: 1. motor; 2. gearbox; 3. slider; 4. load cell; 5. carriage; 6. bending system; 7. clamp; 8. displacement sensor; 9. motor speed control units; 10. power control box with power on and off bottoms and 11. signal interpreting unit.

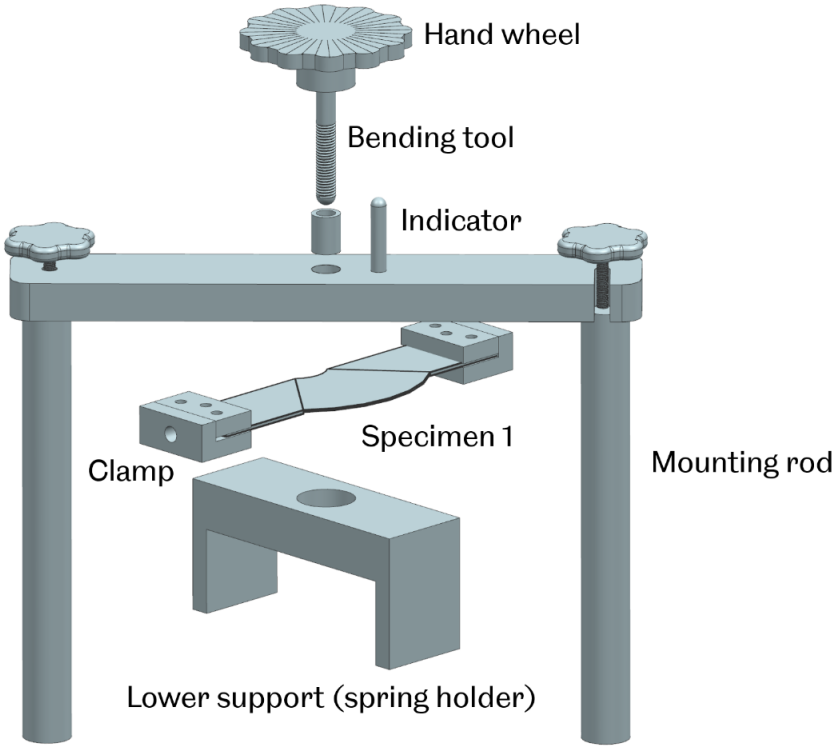

(a)

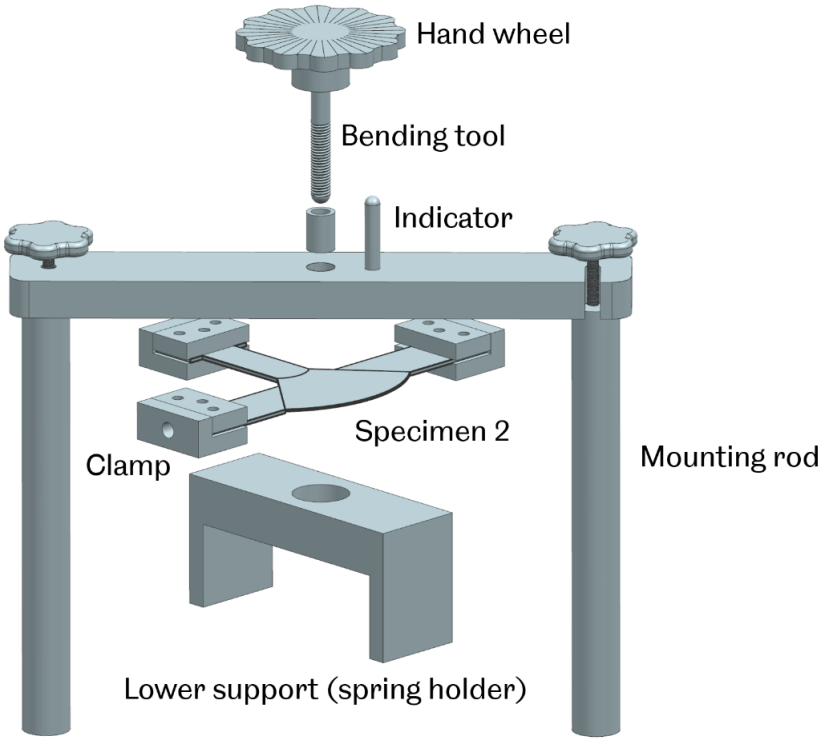

(b)

Figure 6.2 CAD drawings of the bending system in the BTBC rig with (a) specimen No.1 and (b) specimen No.2.

There are two perpendicularly installed linear sliders in the BTBC rig. These two sliders intersect and form two axes, axis 1 and 2, with an intersection point named axes centre, as shown in Figure 6.5. In commercial biaxial tensile machines, four motors are commonly used on four ends of two sliders. In this way, the compression and elongation speeds of four ends can be adjusted separately. Also, there are four screw shafts connected to the motors to drive the four (two for each slider) carriages that mount the four clamps. The BTBC rig uses only two motors to drive each screw shaft in two sliders, one on each end of the two screw shafts. Threads on the screw shaft are in opposing directions, as shown in Figure 6.4. In this way, the axes centre maintains its position throughout the test, as shown in Figure 6.5. Also, the elongation and compression speeds in the opposite directions on axes 1 and 2 are identical. Using the BTBC rig, the calibration work of constructing and specimen installing is greatly simplified. The cost of the BTBC rig is also reduced by using two motors instead of four. The lead of the screw shaft is 5 mm, meaning that for every revolution of the screw shaft, the two carriages move 5 mm towards or away from each other simultaneously. In other words, one revolution of the screw shaft results in a total 10 mm displacement on the two carriages. Two motors drive the movement of the carriages, and each motor is responsible for movement in one planar direction.

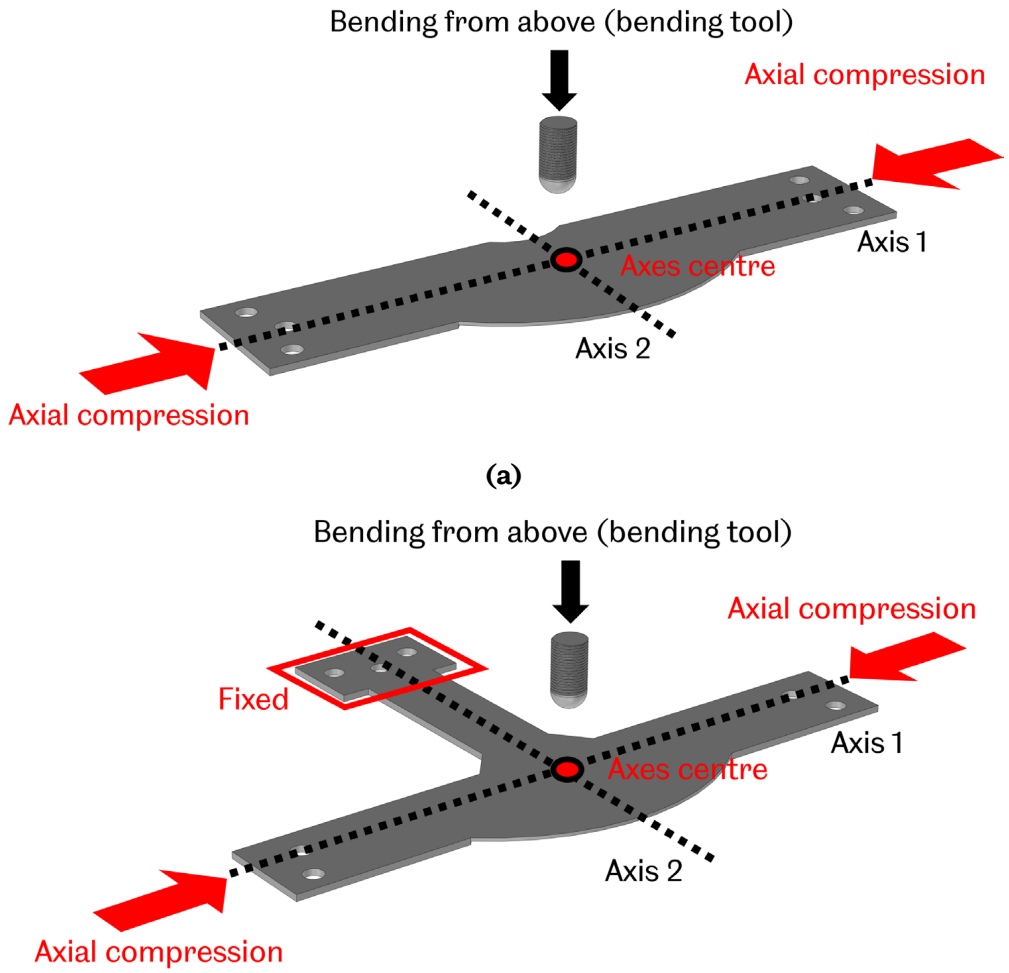

Figure 6.3 Schematic diagrams of (a) specimen No.1 and (b) specimen No.2.

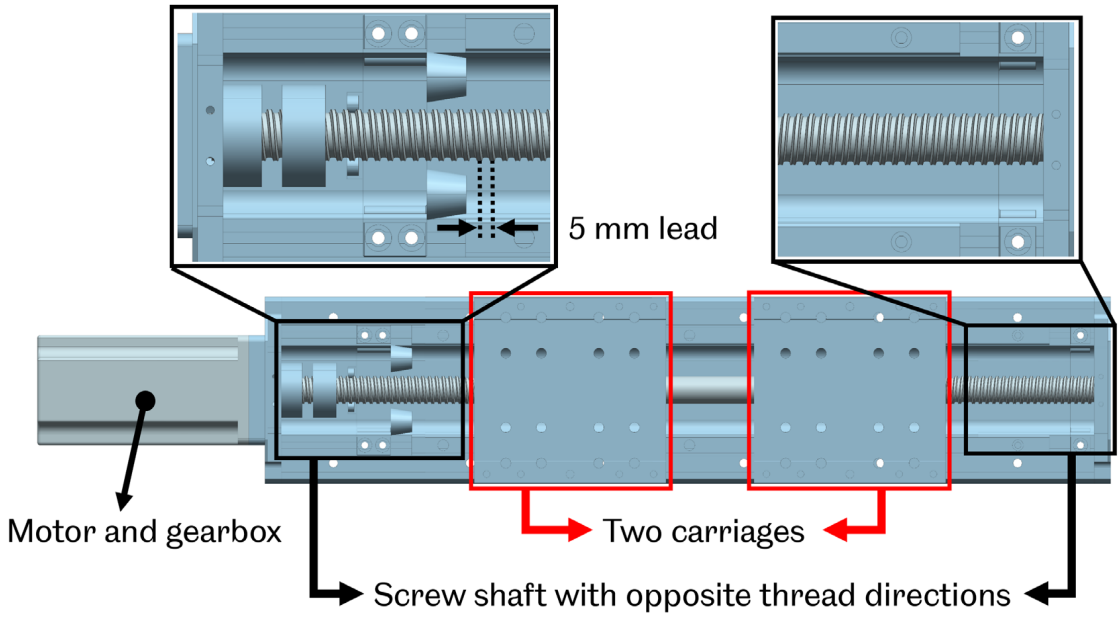

Figure 6.4 Slider with carriages driven by motor with opposite threads on the two ends.

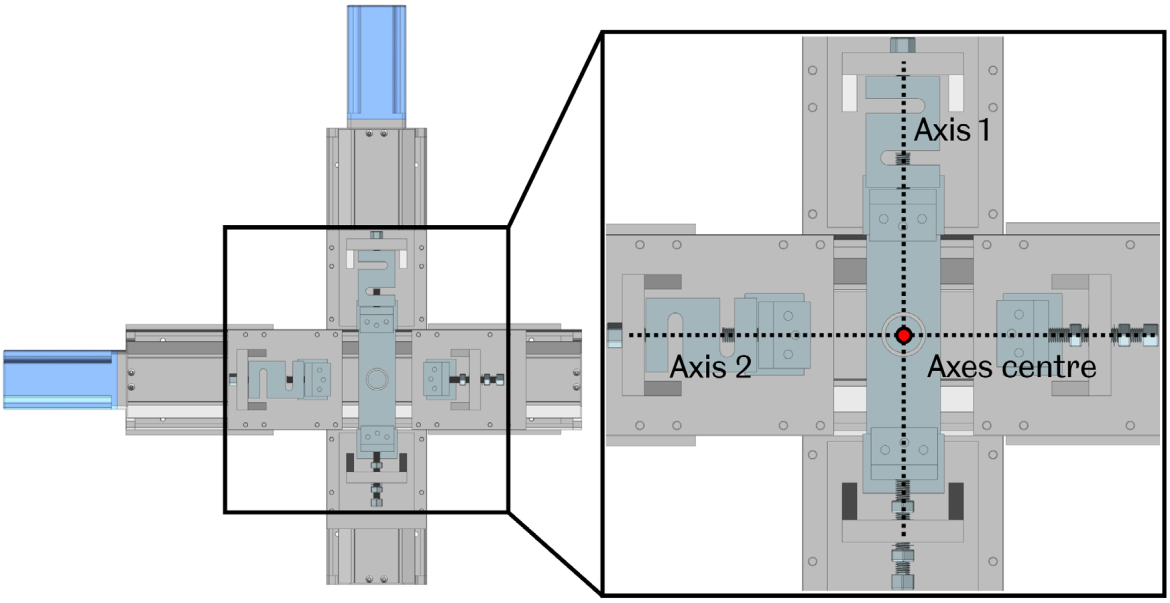

Figure 6.5 Detailed view of two axes with specimen No.1 on the BTBC rig.

After the tests have been done, the strain results are analysed and compared with the FE results. However, the original BTBC rig cannot successfully induce wrinkling deformation in the specimen due to the limitations found in the preliminary tests. As the BTBC rig is originally designed for biaxial tensile loadings, the strength of some components and the general structure is inadequate to stably provide compression loadings to the specimen. Details are explained in section 6.2 about modifications to the BTBC rig. The objectives are determined for this chapter:

- Modify the original BTBC rig to make it capable of reproducing wrinkling deformation in the spinning process by using the wrinkling test specimen on the BTBC rig. Use an electrochemical etching machine to apply circular grid patterns to the specimen surface for strain results measurement.
- Carry out the experiment of the wrinkling tests by applying the loadings to achieve wrinkling deformation of the test specimen. Obtain the strains and compare the wrinkling test results with spinning FE modelling results.

6.2 Experiment Setup

The details about modifications to the BTBC rig and the etching circular grid patterns on the specimens are introduced in this section. The corresponding experimental tests of wrinkling test FE models from B to E are performed after the BTBC rig modification, and gird etching works have been completed. This section further introduces the wrinkling test concept by presenting the information about the modifications to the BTBC rig and the gird etching method.

6.2.1 Modification to the BTBC rig

Several problems are found in the preliminary experimental tests when assessing whether the BTBC rig can provide compression loadings and induces wrinkling deformation to the specimen. Modifications are made to solve the problems in the preliminary experimental tests.

Gearbox

The sliders are driven by an HML40-01030LI servomotor with a maximum 3000 RPM rotational speed and 0.32 Nm torque output. The planetary gearbox DS042-L2 is installed between the screw shaft and the motor. The gearbox ratio is 70:1, resulting in a lower maximum rotational speed of 43 (2000/70) RPM and a higher torque output of 22.4 (0.32*70) Nm. The torque and the rotational speed are transmitted to the screw shaft, driving the carriages on the screw shaft that mount the clamps, thus providing compression or elongation to the specimen fixed by the clamps. As mentioned in the previous section, each revolution of the screw shaft equals 10 mm displacement to the carriages (1 RPM motor rotational speed converts to 10 mm/min compression or elongation speeds), and the rotational speed of the motor controls the compression or elongation speed. The rotational speeds of the two motors are controlled separately by the two motor speed control units. Two motors are set to be started and stopped simultaneously, controlled by the power control box.

However, the 70:1 gear ratio is considered inadequate to perform the wrinkling test after conducting the preliminary experiment. AA5251-H22 and DC01 steel are used in the preliminary experimental tests. The specimens have three thicknesses: 1 mm, 2 mm and 3 mm, respectively. The 22.4 Nm torque is inadequate to deform the specimens with 3 mm. For BTBC rig assessment purposes, compression and elongation loadings are applied to the specimens. The BTBC rig successfully deforms the specimens with 1 mm and 2 mm. However, the screw shaft could not drive the carriages and the clamps to deform the 3 mm thickness specimens, especially for DC01 specimens, which are much stronger than AA5251 aluminium. The connection joint between the gearbox and the screw shaft slips, and the motor rotates idly when the strength of the specimen is excessively great. Hence, a new gearbox with a 200:1 gear ratio is installed to replace the original 70:1 gearbox, as shown in Figure 6.6.

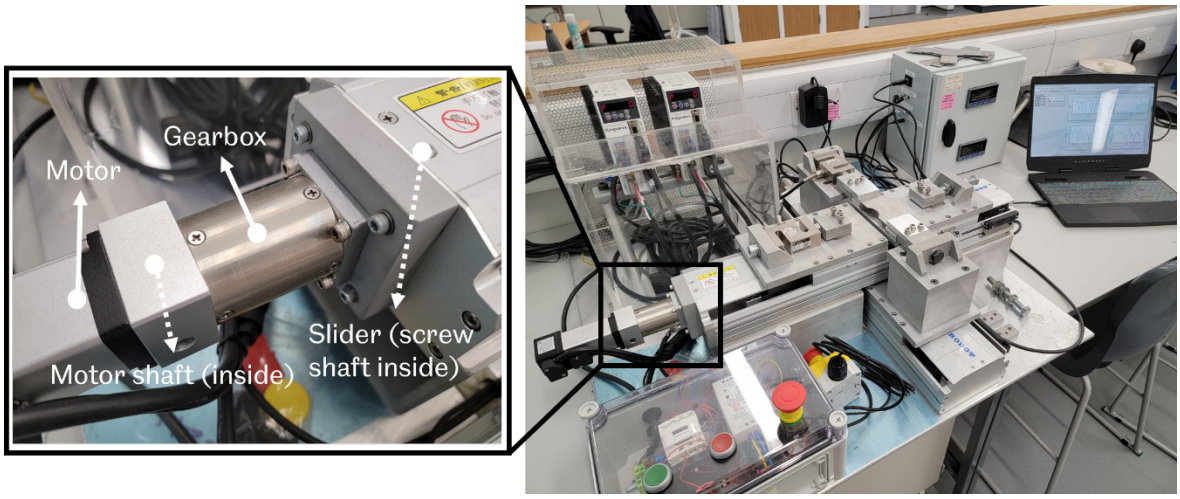

Figure 6.6 Gearbox with 200:1 gear ratio.

The motor control unit controls the rotational direction of the motor shaft, clockwise or anti-clockwise, thus determining whether the loading applied to the specimen is compression or elongation. After the gearbox has been changed, the output torque from the motor increases to 64 (0.32*200) Nm, and the maximum rotational speed is reduced to 15 (3000/200) RPM. Hence, the maximum compression or elongation speed provided by the clamps is 150 mm/min since one revolution of the screw shaft with a 5 mm lead will result in 10 mm displacement between the two carriages on the same slider. After changing the gearbox, the BTBC rig can stably induce deformation to much stronger specimens, whether the specimen is 3 mm thick or DC01 steel.

Clamps

The original BTBC rig is designed to only apply elongation loading to the specimen. There is a clearance between the clamp location adjusting screw and the hole on the carriage top for the screw to pass through. The clamp locating screw is located by the two washers and two locating nuts, tightened on the left and right sides of the carriage top, as shown in Figure 6.8.

When the original BTBC rig is used for elongating loading to the specimen, the clamp location adjusting screw aligns itself with the direction of the elongating loading, moving away from the axes centre. Every component involved in the elongating loading is adequately strong to be kept on the horizontal reference line. However, when the carriages are under compressive loading for the specimen, they move towards each other and the axes centre. The clamp and location adjusting screw become unstable and bend upwards, as shown in Figure 6.8.

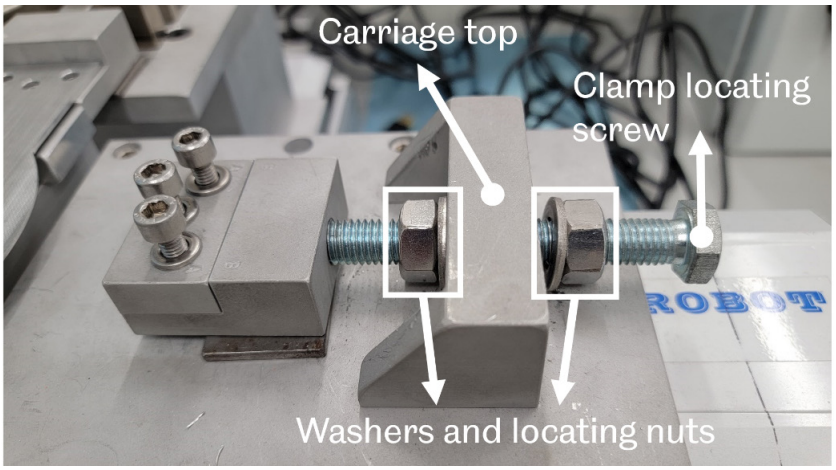

Figure 6.7 The original clamp with the clamp location adjusting screw and nuts.

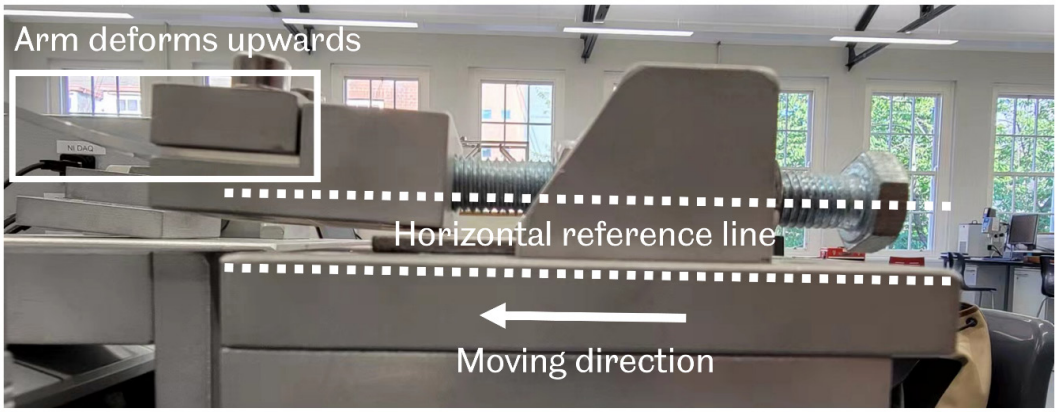

Figure 6.8 The bent clamp location adjusting screw in the wrinkling test when applying compression to the specimen.

To solve the problem with minimum effort and cost, the carriage top is relocated, and the clamp is directly in contact with it, constrained by it, as shown in Figure 6.9 (a). Also, a longer clamp, shown in Figure 6.9 (b), is manufactured to replace the short clamp to constrain the arm of the specimen, and the deformation will only occur on the specimen gauge area. The clearance between the clamp and the carriage top is eliminated.

Any other clearance around the clamp and the carriage top is filled by the supporting pad and block. An example of clearance is shown in Figure 6.10. It will be filled with a supporting pad before the test. Also, supporting pads and blocks with different thicknesses are manufactured to fill the clearance with different heights.

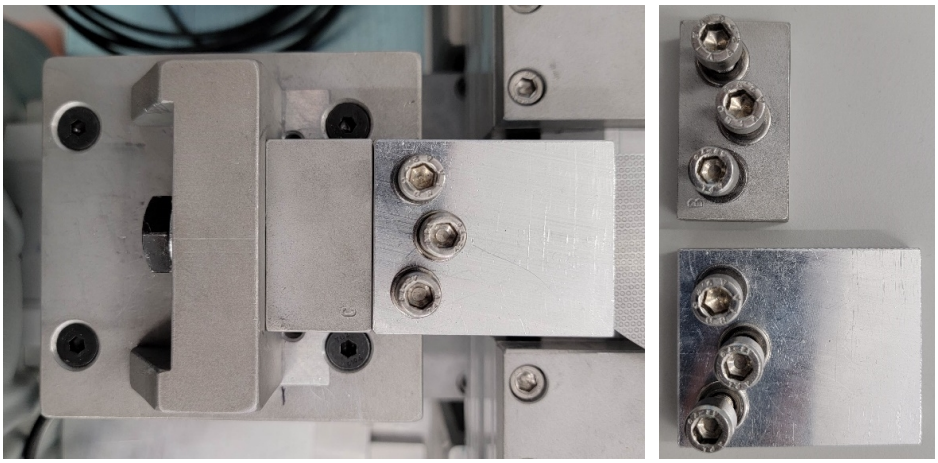

(a) (b)

Figure 6.9 (a) the top view of the modified clamp and (b) the comparison of two clamps.

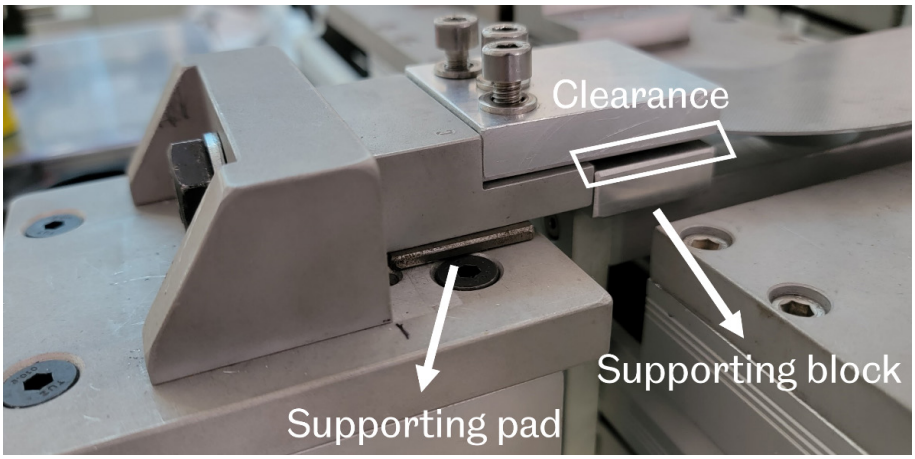

Figure 6.10 The side view of the clamp with the supporting pad and block.

The CAD drawings of the original clamps of specimens B and D on the BTBC rig are shown in Figure 6.11. Two clamps are involved in the experimental test related to specimen No.1 (specimen B). The bending tool is located above the gauge area. Also, the specimen will always wrinkle upwards and towards the bending tool due to the thickness-reduced surface facing downwards. Because of the original clamp design, only the areas near the end of the arms of specimen No.1 are clamped. Even with a thickness-reduced gauge area in the middle of the specimen, the deformation is still not concentrated on the gauge area. The CAD drawings of specimen No.1 (specimen B) and specimen No.2 (specimen D) after the modification to the clamp and nearby components are shown in Figure 6.12. Almost all the areas other than the gauge area are constrained by the supporting blocks and the long clamps.

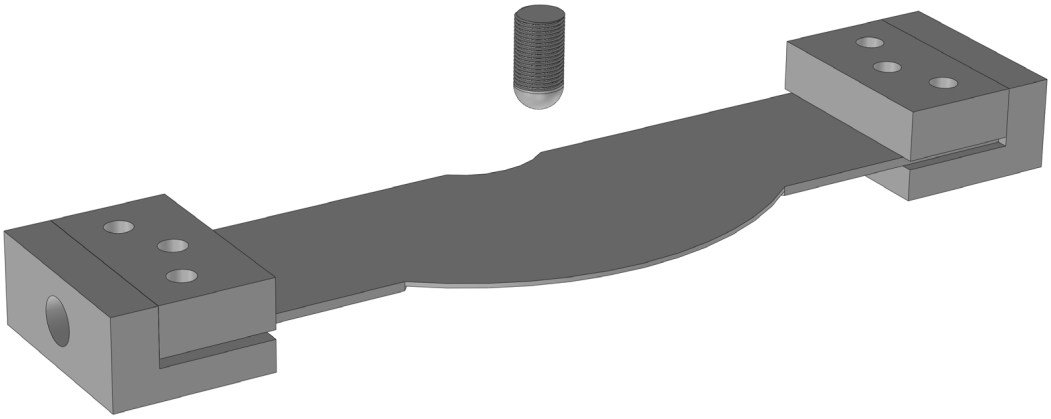

(a)

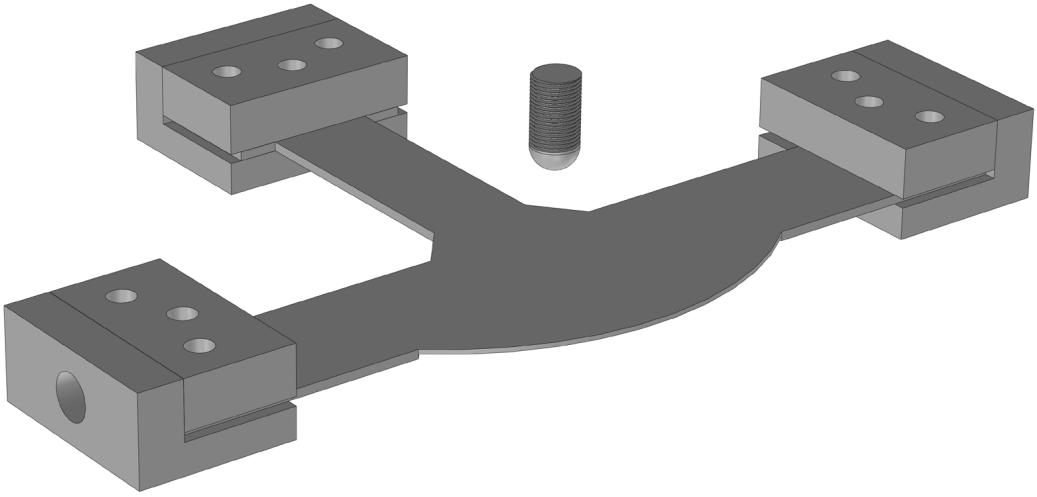

(b)

Figure 6.11 Original BTBC clamps and bending tool with (a) specimen No.1 and (b) specimen No.2.

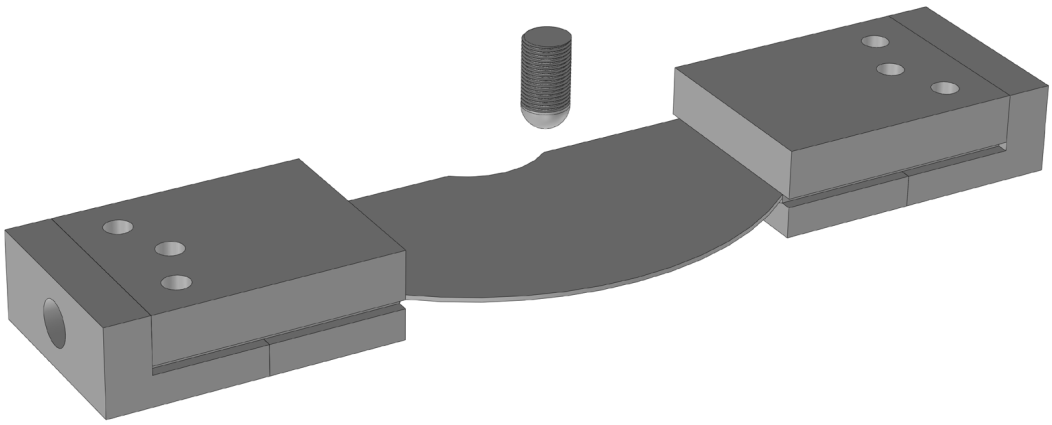

(a)

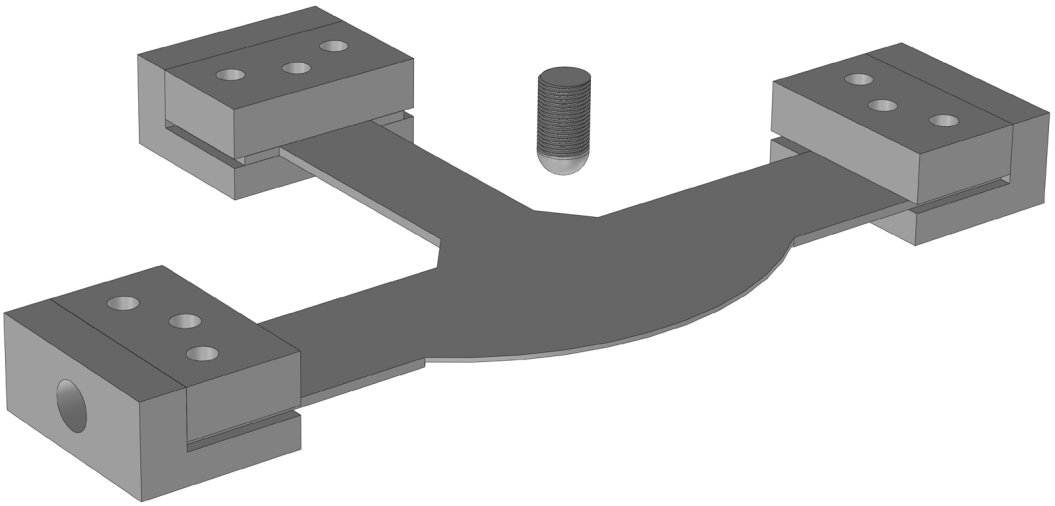

(b)

Figure 6.12 Modified BTBC clamps and bending tool with (a) specimen No.1 and (b) specimen No.2.

Displacement sensors

There is no displacement measurement device installed on the original BTBC rig. However, the displacement measurement is essential to monitor whether the compression loading applied to the specimen correctly follows the requirement. Two displacement sensors, shown in Figure 6.13, and two signal interpreting units, shown in Figure 6.14, are installed on the BTBC rig to achieve a real-time displacement measurement. Each displacement sensor is installed on the outer side case of the slider. It does not integrate within the structure of the BTBC rig or inside the slider to reduce the workload and cost. The displacement measurement device consists of three components: the blocker, the sensor rod and the signal transmitter, as shown in Figure 6.13. The blocker is installed on the carriage, sharing the identical movement with the carriage, either elongation or compression. The signal transmitter is installed on the outer case of the slider, and it is immobilised. The movement of the carriage directly determines the loading applied to the specimen since the clamp is installed on the carriage and moves with it. The identical movement transmits to the sensor rod by the blocker, and the signal transmitter outputs the corresponding signal to the signal interpreting unit, as shown in Figure 6.14.

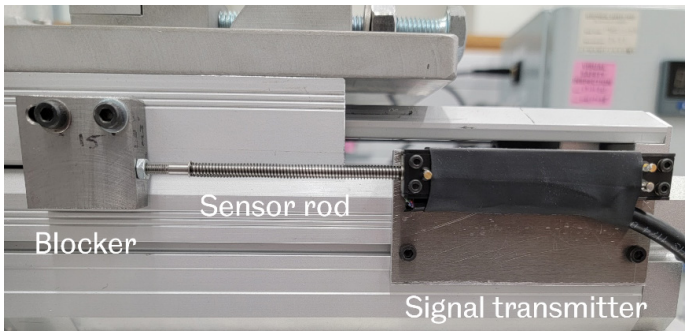

Figure 6.13 The displacement sensor on the side of the slider.

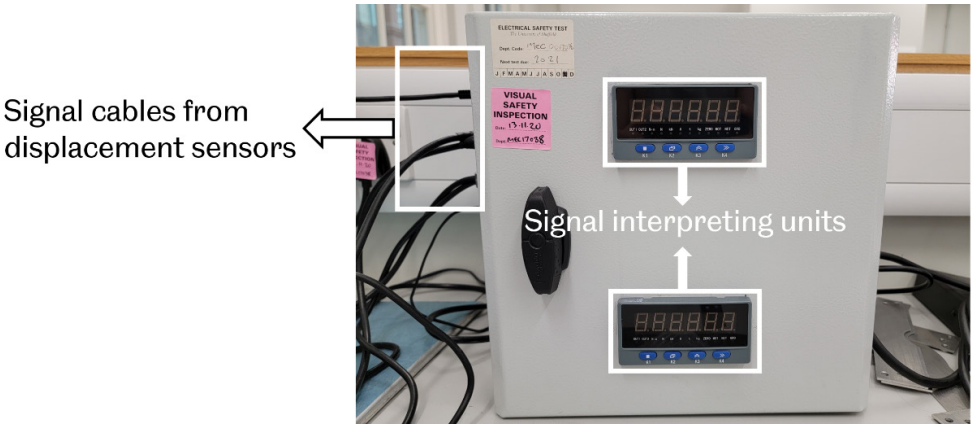

(a)

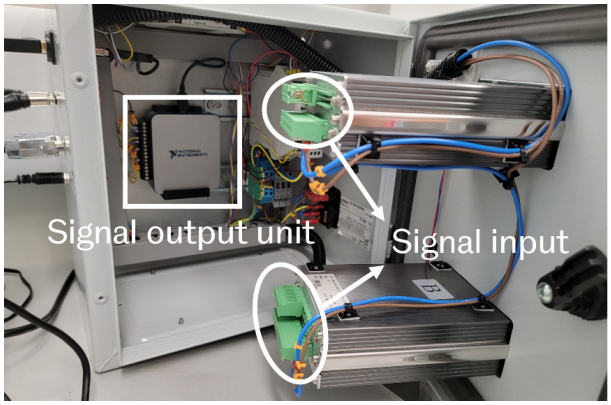

(b)

Figure 6.14 (a) the layout and (b) the inside layout of the signal interpreting units.

The signal interpreting unit receives the signal from the displacement sensor through the cables, and the signal output unit transmits the signal to the LABVIEW software on the laptop. The signal interpreting units also display the displacement value in real-time.

To summarise, after the modifications to the gearbox and the clamps and installing the displacement sensors, the BTBC rig can stably inducing wrinkling deformation to the specimen and measuring the compression applied to the specimen in the form of displacement (mm).

6.2.2 Grid Etching on the Specimen

The grid etching method is applied to the specimen using a ME96SP-V2 electrochemical etching machine, as shown in Figure 6.15. Rolling the electrified roller over the stencil soaked in the etching liquid with the specimen underneath will etch the circular patterns onto the specimen, and the stencil is reusable.

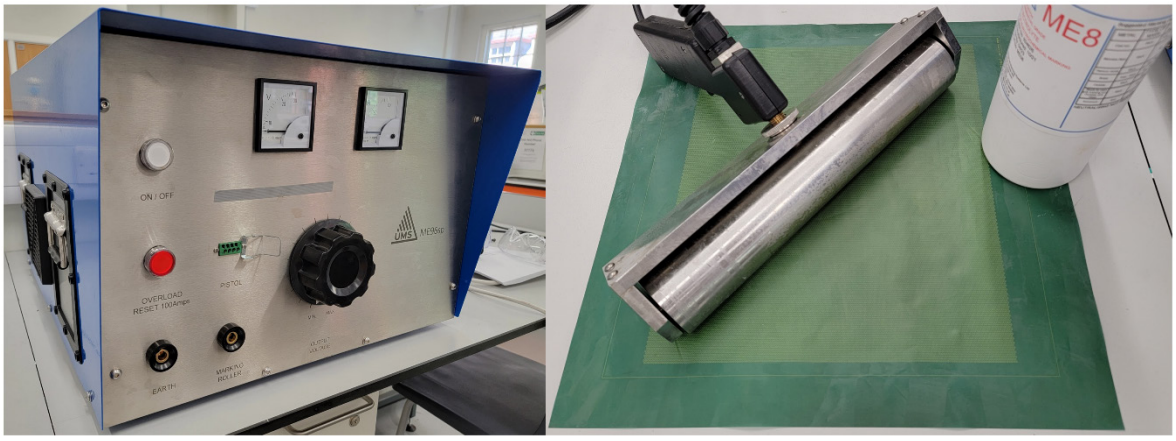

Figure 6.15 The etching machine, the roller, the stencil with circular grid patterns and the liquid etching solution.

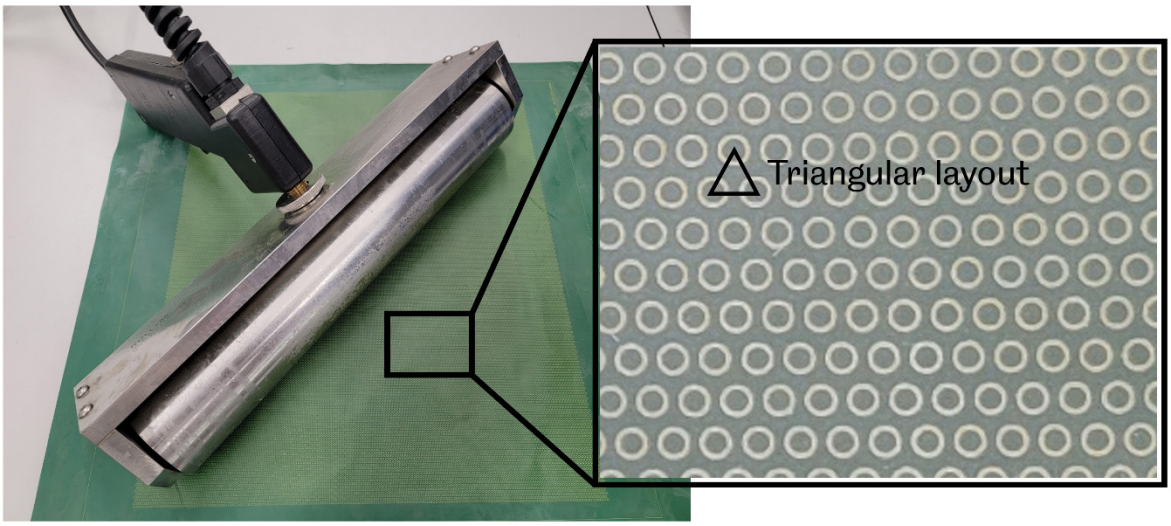

Figure 6.16 The detailed view of the circular gird patterns on the stencil.

The detailed circular grid pattern on the stencil is shown in Figure 6.16. The radius of the circular patterns is 1 mm, arranged in triangles on the stencil. The circular pattern allows for measuring the major and minor strains of the wrinkling test specimen after deformation since a circle will deform into an eclipse, and the direction of the major and minor strains can be determined by the major and minor axis of an eclipse. The circular patterns etched on the specimen are shown in Figure 6.17.

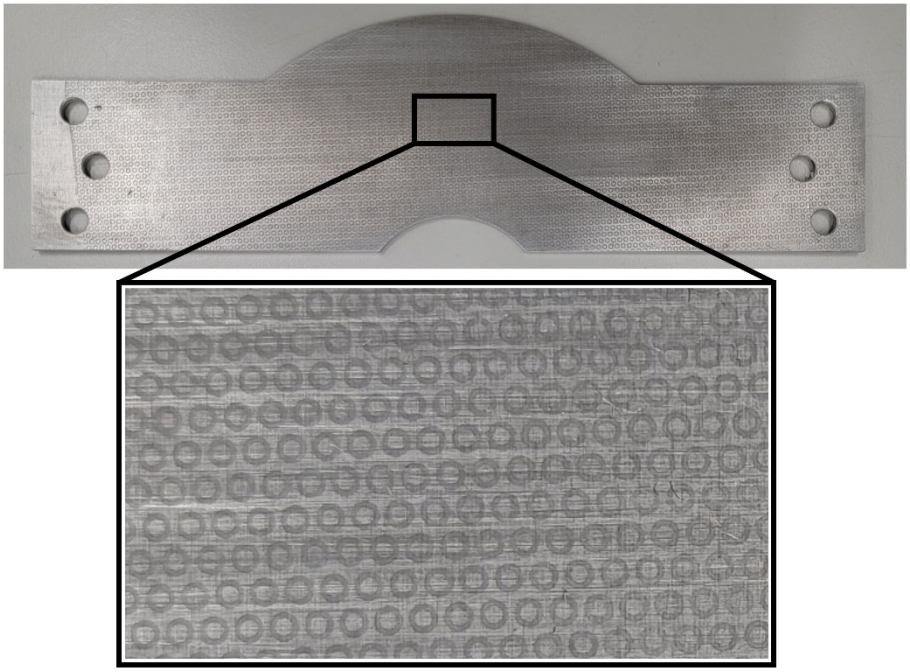

Figure 6.17 The detailed view of the circular grid etched on specimen No.1.

As shown in Figure 6.17, the circumference of each circular pattern has a visible thickness. It is the main disadvantage of this etching machine. The advantage of this etching machine is that it is easy to use and is a small machine compared to a laser engraving machine. However, the thickness of the circular lines etched by a laser machine will be much thinner than this electrochemical etching machine. It is an alternative to the expensive laser engraving machine with a much greater footprint.

Several problems are noticed after finishing the etching process. Firstly, the roller cannot evenly roll on the stencil. Human error cannot be prevented in this process. The roller is handheld, and the force exerted on the roller through the hand is inconstant throughout the rolling process. This drawback unavoidably results in the circular patterns etched on the specimen surface are not identical. For example, some circular patterns have blurry circular lines, and some are clear. Secondly, the stencil is a soft plastic film paper. When rolling the roller on the stencil, the friction between the surfaces slightly displaces the stencil, and in the worst situation, the roller wrinkles the stencil. Under this circumstance, some of the circular patterns also become blurry. However, at least the circular grid patterns are successfully etched on the specimen, and they can be observed by the microscope to determine major and minor strains of the specimen. An electronic microscope is used to observe the deformed circular patterns on the specimen, as shown in Figure 6.18.

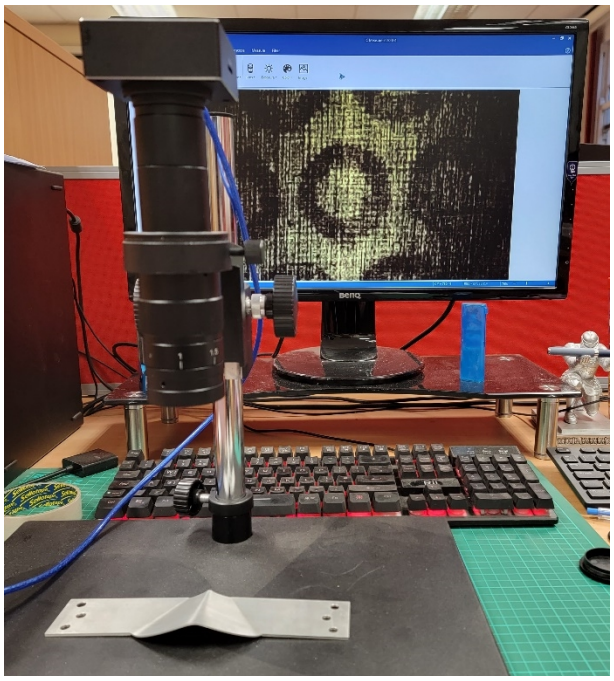

Figure 6.18 Electronic microscope and the deformed specimen.

6.3 Test Design and the Result Analysis

After finishing the BTBC rig modification and preparation, the wrinkling experimental tests based on wrinkling test FE models B, C, D and E are performed. After the tests have been completed, the strain results are obtained by measuring the deformed circular grid patterns and compared with the spinning FE results. Furthermore, the wrinkling wave amplitude results are obtained and compared with the wrinkling test FE modelling results.

6.3.1 Design of the Experimental Test

The four wrinkling experimental tests are performed and briefly introduced in Table 6.1. The four tests correspond to four FE models B, C, D and E in Chapter 5. The compression loading is applied by a 0.12 mm/s compression speed on both arms of the specimen along axis 1 for 10 seconds. A total of 2.4 mm compression displacement is applied to the specimen. The specimen clamping condition employed in tests No.3 and No.4 is to maintain the initial location of the arm fixed by the clamp on axis 2 throughout the testing process. The bending loading is applied using the bending tool via the handwheel by applying a downward movement. This loading bends the wrinkled material of the specimen back to the initial horizontal location as the bending loading is applied after the compression loading. The schematic diagrams of tests No.1 to No.4 are shown in Figure 6.19. The compression and bending loadings applied in the tests are identical to the loadings in the wrinkling test FE modelling. In the FE specimen and test design models that involve the

bending tool, the downward speed is 1 mm/s. However, the downward speed of the bending tool in the BTBC rig is controlled manually by the handwheel. The speed is not a constant speed of 1 mm/s. As discussed in Chapter 3 and Chapter 4, the strain rate does not affect the wrinkling initiation and propagation. Hence, the unconstant bending speed does not affect the wrinkling deformation in the tests.

Table 6.1 Experimental plan of the wrinkling tests.

Test No.	Specimen No.	Corresponding FE design model	Loading on axis 1	Loading on axis 2	Loading from bending tool
No.1	1	B	Compression	-	-
No.2	1	C	Compression	-	Bending (after compression)
No.3	2	D	Compression	Fixed	-
No.4	2	E	Compression	Fixed	Bending (after compression)

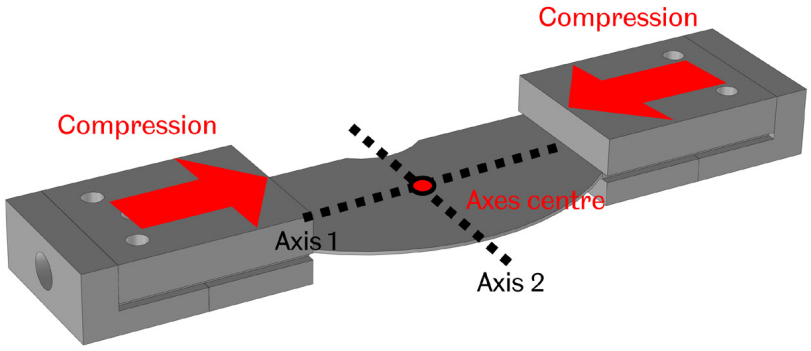

(a)

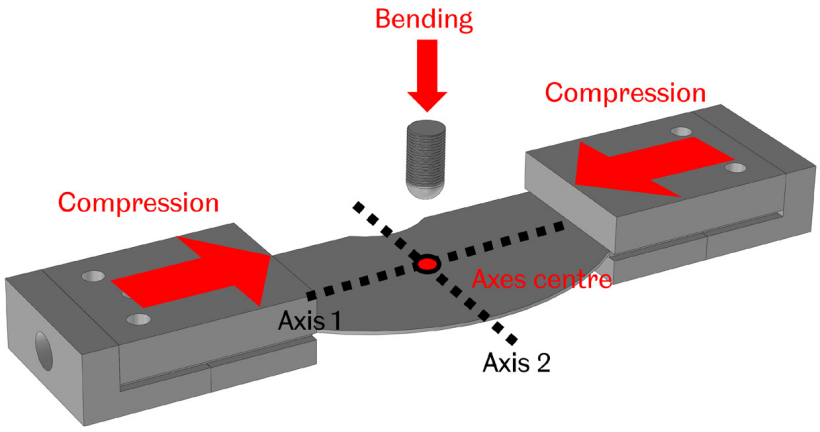

(b)

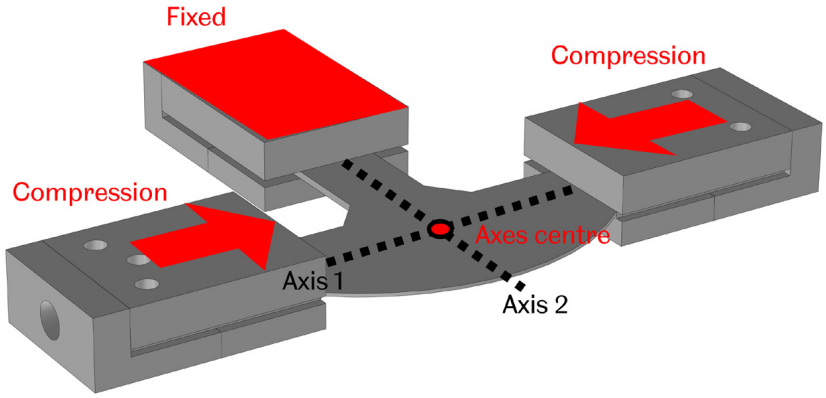

(c)

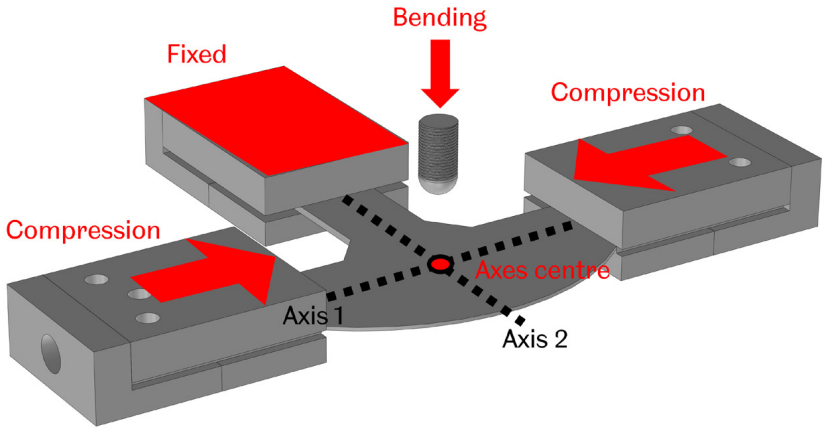

(d)

Figure 6.19 Schematic diagrams of the loadings applied in the tests (a) No.1; (b) No.2; (c) No.3; and (d) No.4.

6.3.2 Strain Results Analysis

Specimen No.1 and specimen No.2 used in the wrinkling tests are shown in Figure 6.20. They are identical to the specimens designed and simulated in wrinkling test FE models B, C (with specimen No.1) and D, E (with specimen No.2) in Chapter 5. The material of the specimen is AA5251-H22 aluminium alloy.

(a)

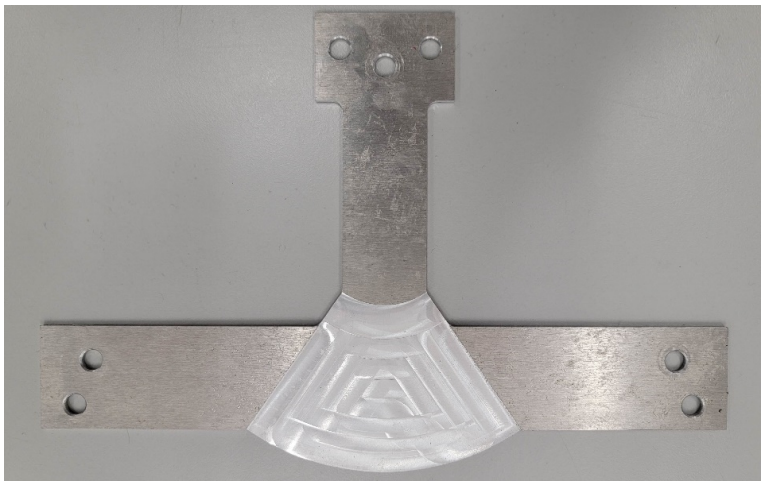

(b)

Figure 6.20 Photos of (a) specimen No.1 (wrinkling test FE models B, C) and (b) specimen No.2 (wrinkling test FE models D, F).

An example of deformed circular patterns etched on the specimen surface under the microscope is shown in Figure 6.21. The diameter of the circular pattern is 1 mm. The circumference of the circular pattern has a uniform thickness, and the deformed diameter of the circular pattern is calculated as the average value between the outer and inner diameters of the circumference. For example, in Figure 6.21, the elongation in the circumferential direction is 0.071 mm, calculated by [(1.36+0.782)/2–1.0]=0.071 mm. The compression in the radial direction is calculated similarly by [(0.719+1.277)/2–1.0]=–0.002 mm. Circumferential and radial strains are calculated by Equation 6.1 as true strains based on these measurements. For example, the circular gird with a 0.071 mm circumferential elongation and –0.002 mm radial compression, and the engineering circumferential and radial strains, ε_{EC} and ε_{ER}, are 0.071/1=0.071 and –0.002/1=–0.002. The true circumferential and radial strains, ε_{TC} and ε_{TR}, are ln(1+0.071)=0.069 and ln(1–0.002)=–0.002. Since engineering strains are only used to calculated the true strain and not mentioned in the following strain results analysis, the true circumferential and radial strains are abbreviated as circumferential strain and radial strain in the following study.

$$\varepsilon_T = \ln(1 + \varepsilon_E)$$

Equation 6.1

The circular patterns on the wrinkling top lines in the radius direction are selected. The selected patterns to measure the strain results on specimen No.1 and specimen No.2 are shown in Figure 6.22 (a) and Figure 6.22 (b). The selected patterns on both specimens follow a serrated line, not a straight line, due to the triangular layout of the grid, as shown in Figure 6.16.

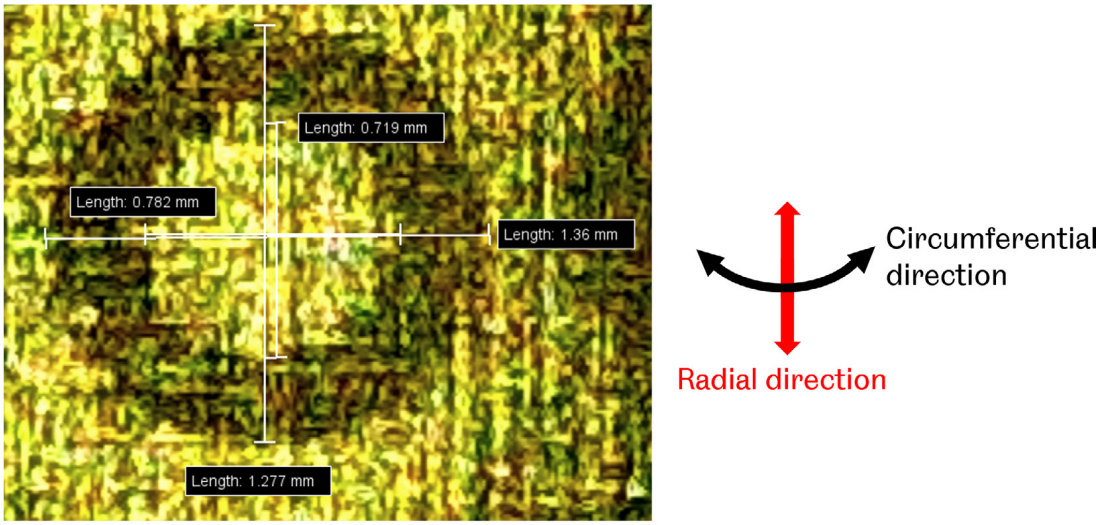

Figure 6.21 Deformed circular pattern under the microscope.

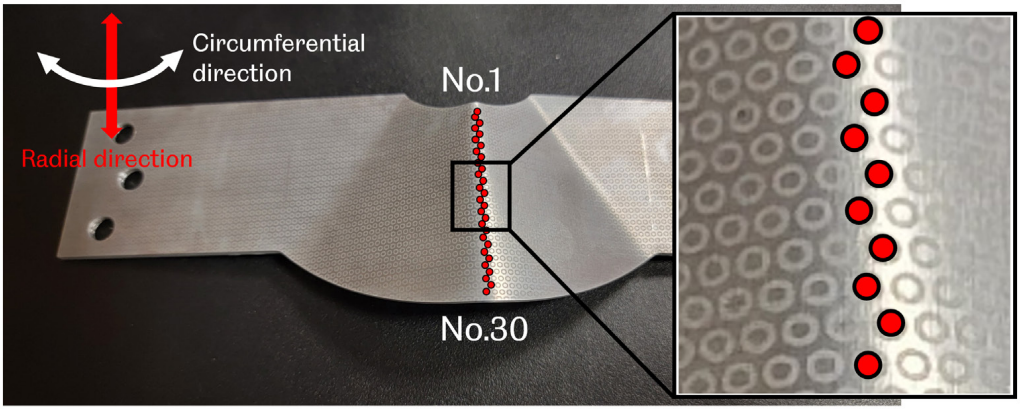

(a)

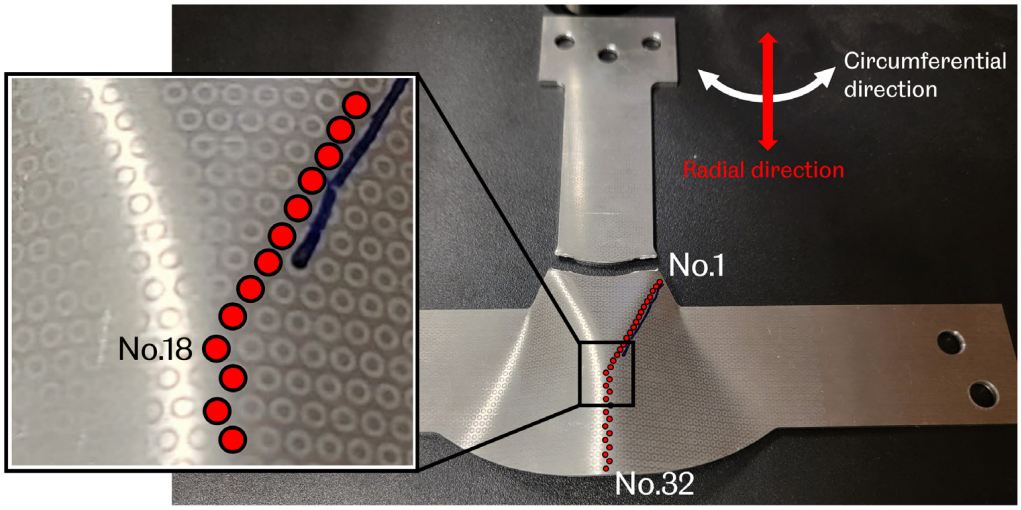

(b)

Figure 6.22 Circular patterns selected on (a) specimen No.1 and (b) specimen No.2.

Test No.1 results analysis and discussion

The deformed specimen in test No.1 is shown in Figure 6.23 (a). Thirty circular patterns are selected on the specimen. However, the strains calculated from these patterns are not distributed continuously in the circumferential-radial strain diagram, unlike the data points from FE model B, which forms a continuous strain signature. To minimise the discontinuity of the strain signature of the test, thirty patterns are divided into three sets: set 1 (No.1 to No.10), set 2 (No.11 to No.20) and set 3 (No.21 to No.30), as shown in Figure 6.23 (b). The corresponding node selection in FE model B to extract the strain result for comparison with the test is shown in Figure 6.24. Fourteen nodes are selected in the spinning FE model on the wrinkling top line on the wrinkled workpiece, as shown in Figure 6.25. There are 105 nodes selected on the specimen in FE model B, node No.1 has the greatest circumferential strain located on the top side of the diagram, and the strain signature propagates downwards, as shown in Figure 6.26.

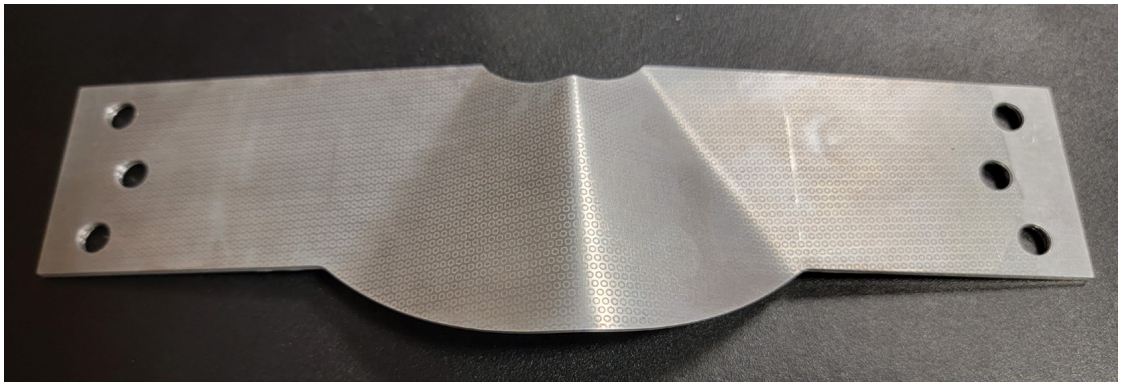

(a)

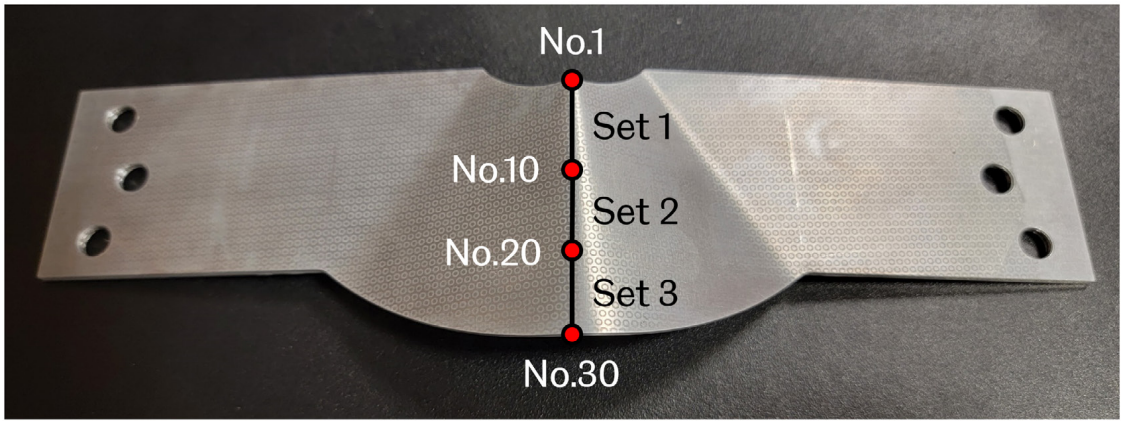

(b)

Figure 6.23 (a) deformed specimen and (b) set 1 to 3 on the most severely wrinkled area (wrinkling top line) in test No.1.

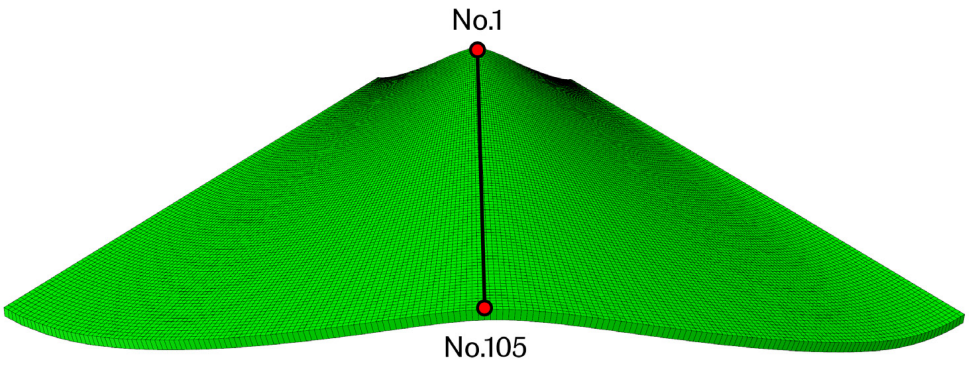

Figure 6.24 Nodes No.1 to No.105 to output strain results in wrinkling test FE model B.

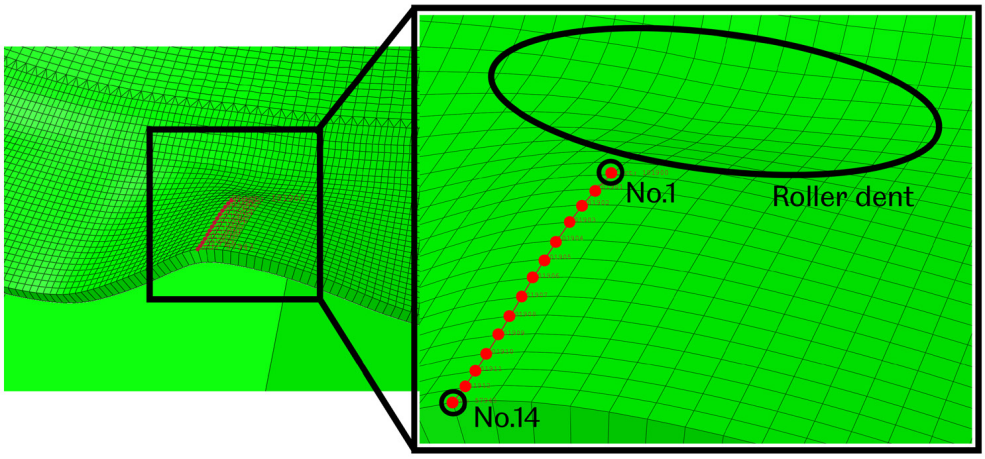

Figure 6.25 Nodes selected on the wrinkled workpiece in the FE spinning model.

The general pattern of the strain results in wrinkling test No.1 is similar to the results of FE model B. Data points of set 1 is located the highest, set 2 is in the middle and set 3 is the lowest. Some data points are located excessively diverged from others; for example, two orange points which belong to set 1 are located around set 3. There is no continuity of the strain signature. The only pattern is that these sets follow a descending sequence from set 1 to set 3.

In general, the strain results of wrinkling test No.1 do not correlate well with the spinning FE results. As mentioned in section 6.2.2, the etching machine is an alternative to the expensive laser engraving machine. The limitation of this electrochemical etching machine is obvious: the circumference of the circular pattern has an unneglectable thickness, which is the most probable cause of the diverged data point distribution. The strain is calculated by the initial diameter and the deformed diameters of a circular pattern as the true strain. When the deformation of a circular pattern occurs, it deforms into an ellipse with the major axis (the diameter being elongated) and the minor axis (the diameter being compressed), as shown in Figure 6.27. The thickness of the circumference produces errors when measuring the deformed diameters of the circle (ellipse) in major and

minor axes. The greater the diameter elongates, the smaller the ratio between the circumference thickness and diameter. Hence, the errors in measuring a severely deformed diameter are smaller than in a less severely deformed diameter.

The specimen wrinkles upwards under the compression loadings applied in test No.1, and the circumferential strains on the most wrinkled/deformed area (wrinkling top line) have tensile strains with greater values in the range from 0.05 to 0.19. The radial strains are much smaller than the circumferential strains in a range from –0.005 to 0.025. Human error in result measurement and the error due to the circumference thickness greatly affect the strain results on the minor axis. The circumferential strains are less affected by human errors as the material severely deforms on the major/circumferential axis, while radial strains are more severely affected by errors. These factors cause the circumferential strains of test No.1 to follow a similar descending pattern on the circumferential strain axis as FE model B, while the radial strains are distributed divergently along the radial strain axis.

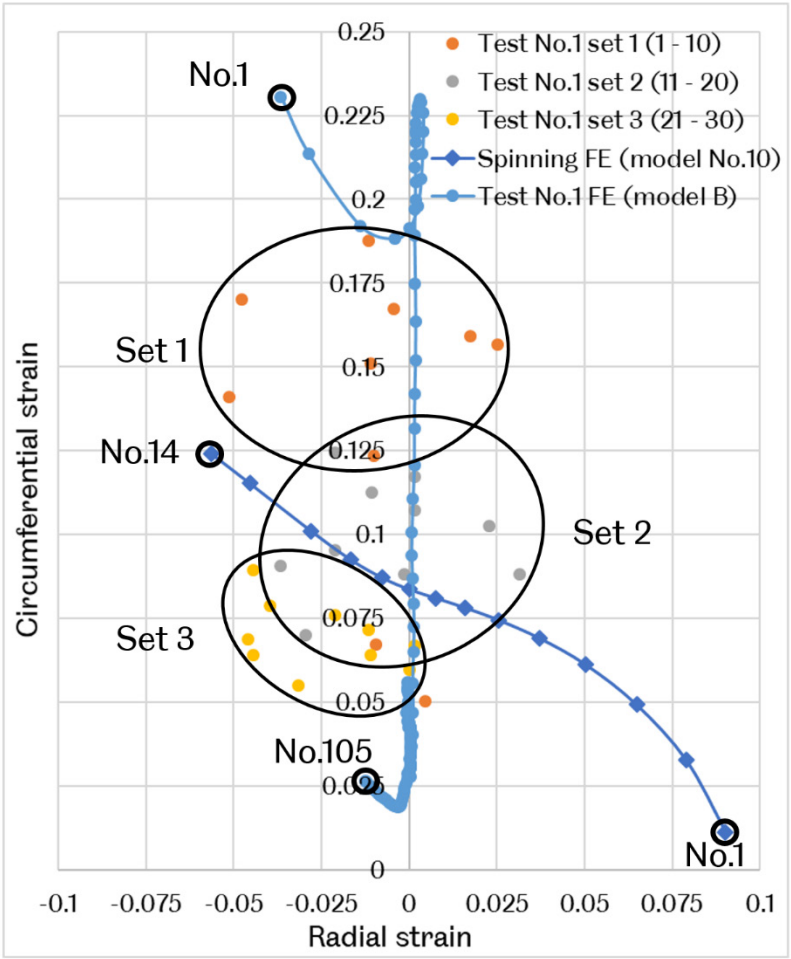

Figure 6.26 The strain results comparison of wrinkling test No.1, wrinkling test FE model B and spinning FE model No.10.

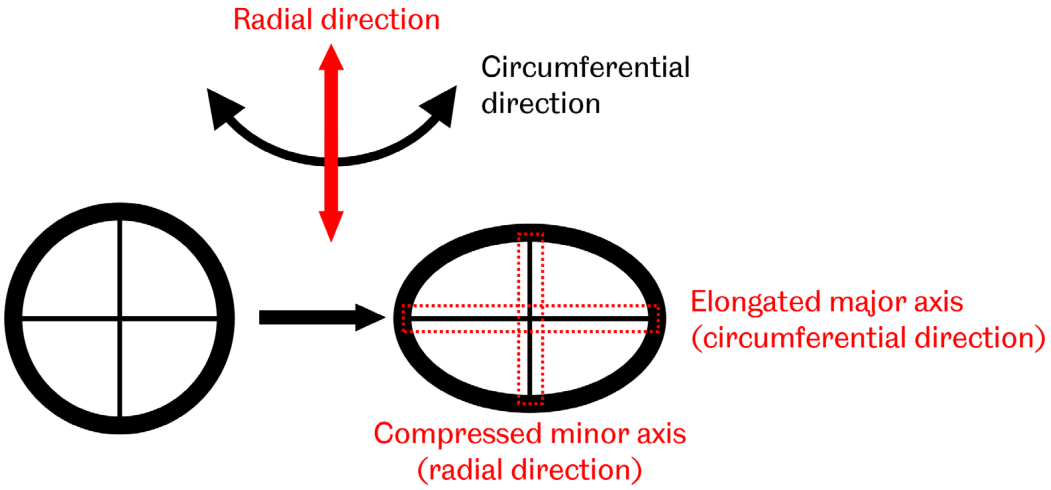

Figure 6.27 The schematic diagram of the initial and the deformed circular pattern.

Test No.2 results analysis and discussion

In test No.2, the bending tool produces bending deformation to the specimen after the specimen wrinkles upwards under the compression loadings. The deformed specimen in test No.2 is shown in Figure 6.28 (a). Thirty-two circular patterns on the specimen are divided into three sets, as shown in Figure 6.28 (b).

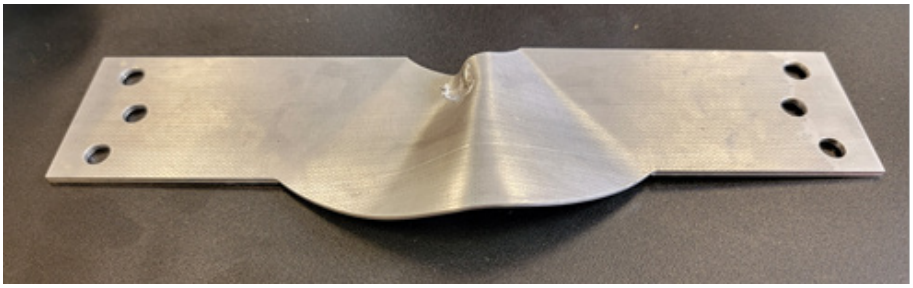

(a)

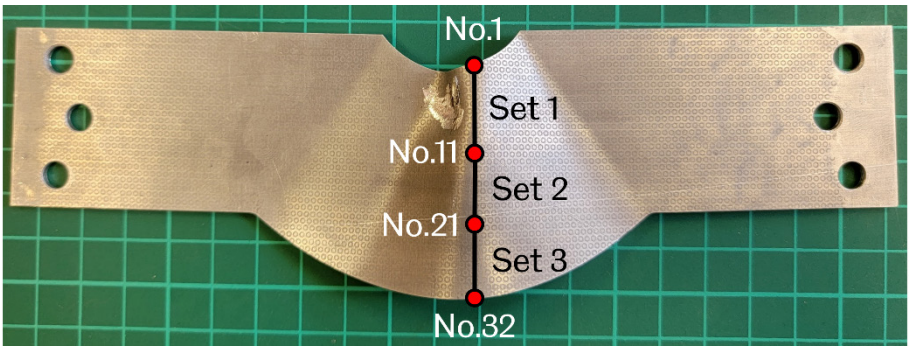

(b)

Figure 6.28 (a) deformed specimen and (b) set 1 to 3 on the most severely wrinkled area (wrinkling top line) in test No.2.

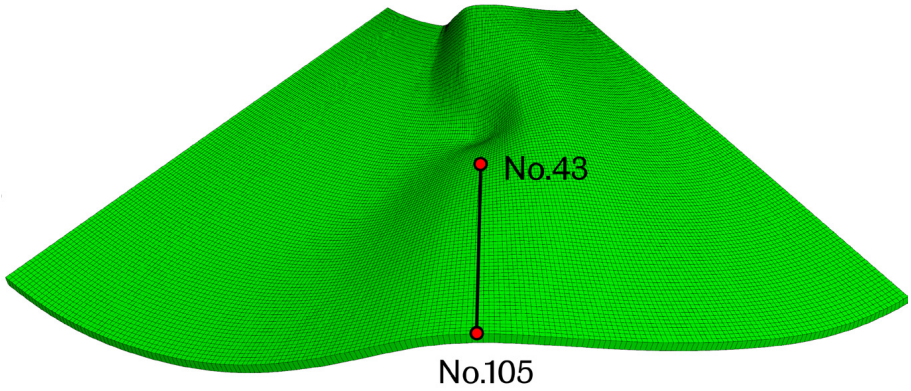

Figure 6.29 Nodes No.43 to No.105 to output strain results in FE model C (test No.2).

The corresponding node selection in FE specimen design model C is shown in Figure 6.29. The strain results of test No.2 and FE model C are shown in Figure 6.30. The bending tool has caused a dent on the wrinkled specimen, and the strain results are only obtained from the wrinkling top line that is free from the effect of the dent. Hence, only the strain results of nodes No.43 to No.105 are included in the diagram shown in Figure 6.30. The circumferential strains of these nodes are tensile, indicating that the wrinkling deformation is achieved. The nodes at the dented area have compressive circumferential strains caused by dominating bending and a little compression deformation. For wrinkling test FE model C, the nodes not affected by the dent are selected to output the strain results to analyse the wrinkling. Node set 1 in wrinkling test No.2 is close to the dent and affected by it. Hence, the strain results of set 1 are excluded, and only results of set 2 and set 3 are included in Figure 6.30.

The data points show divergent distributions, similar to test No.1 results, as shown in Figure 6.30. The strain results of test No.2 do not correlate with the spinning FE results. There is no obvious pattern of wrinkling test No.2 data points. The spinning FE modelling strain signature starts from the right-hand side and propagates to the left-hand side of the diagram as the radial strains decrease from positive to negative values while the circumferential strain gradually increases. The data points of set 2 and set 3 are on the right-hand side and left-hand side, respectively. The strain results of wrinkling test No.2 propagate from the right-hand side to the left-hand side. It is the only similarity with the spinning FE modelling. The circumferential strains of wrinkling test FE model C are all lower than 0.05, and the radial strains vary from –0.025 to 0.025. The test No.2 strain results are much greater than the FE model C results. Although the data points of test No.2 test results are scattered around the strain curve of the spinning FE modelling results, test No.2 is improved and closer to the spinning process model compared with test No.1.

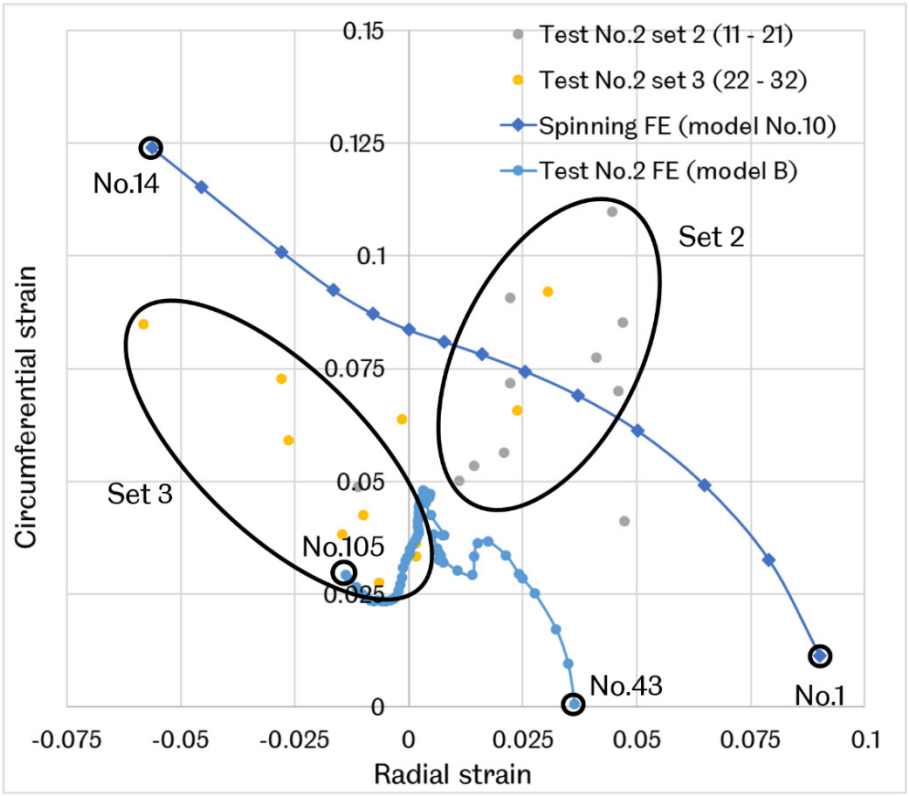

Figure 6.30 The strain results comparison of wrinkling test No.2, wrinkling test FE model C and spinning FE model No.10.

Test No.3 results analysis and discussion

In test No.3, the loadings are applied to specimen No.2 to test wrinkling deformation. The deformed specimen is shown in Figure 6.31 (a). Thirty-two circular patterns are divided into three sets, as shown in Figure 6.31 (b). Similar to test No.2, only the strain results of set 2 and set 3 are output to compare with the results in wrinkling test FE model D and the results in spinning FE model No.10. The corresponding node selection, nodes No.19 to No.70, on the specimen in FE model D is shown in Figure 6.32. The strain results comparison between wrinkling test No.2, wrinkling FE model C and spinning model No.10 is shown in Figure 6.33.

Test No.3 shows some similarities and improvements in comparison with test No.2. Similar to test No.2, the circumferential and radial strains of wrinkling test FE model D are in the ranges of 0 to 0.04 and –0.02 to 0.02, and they are much smaller than spinning FE model No.10. The strain results of test No.3 are much greater than the FE wrinkling test results, and the data points are distributed around the spinning FE data points. Although the data points of test No.3 still have divergent distributions, they are more similar to the spinning FE results compared with test No.2. The data points gather more around the spinning strain signature and are less diverged than that of test No.2. However, set 2 and set 3 are more likely to gather around the

middle section of the spinning strain signature. No data points cover the areas close to node No.1 on the right-hand side and node No.14 on the left-hand side of the spinning strain signature. In general, the strain results of wrinkling test No.3 do not correlate with the spinning FE modelling results. Nevertheless, test No.3 further improves the strain results and achieves its design purpose as an improvement of test No.2.

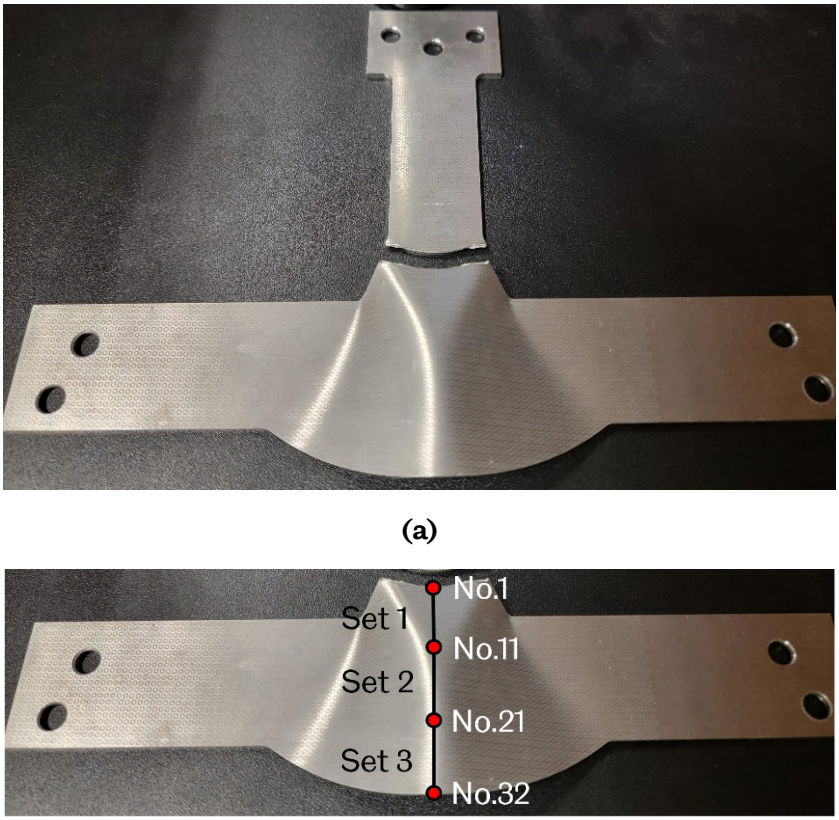

(a)

(b)

Figure 6.31 (a) deformed specimen and (b) set 1 to 3 on the most severely wrinkled area (wrinkling top line) in test No.3.

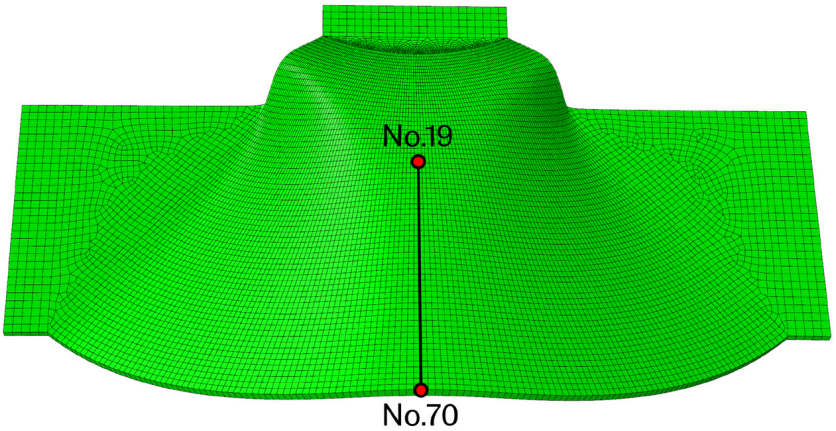

Figure 6.32 Nodes No.19 to No.70 to output strain results in wrinkling test FE model D.

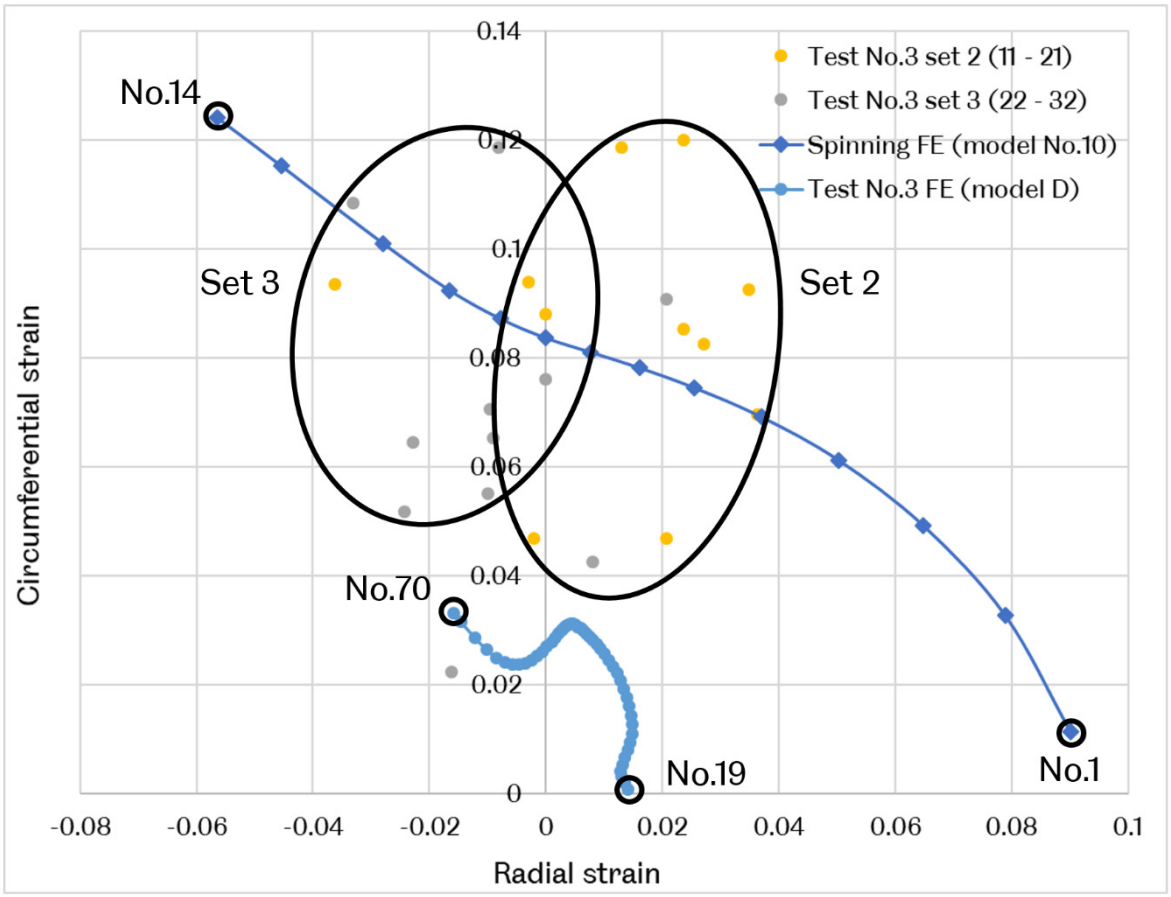

Figure 6.33 The strain results comparison of wrinkling test No.3, wrinkling test FE model D and spinning FE model No.10.

Test No.4 results analysis and discussion

The deformed specimen in test No.4 is shown in Figure 6.34 (a). Similar to the previous tests, thirty-one circular patterns on the specimen are divided into three sets, as shown in Figure 6.34 (b). The corresponding nodes not affected by the dent are selected in the wrinkling test FE model E, as shown in Figure 6.35.

(a)

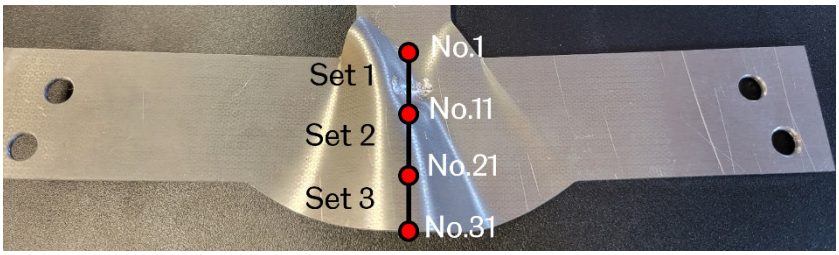

(b)

Figure 6.34 (a) deformed specimen and (b) set 1 to 3 on the most severely wrinkled area (wrinkling top line) in test No.4.

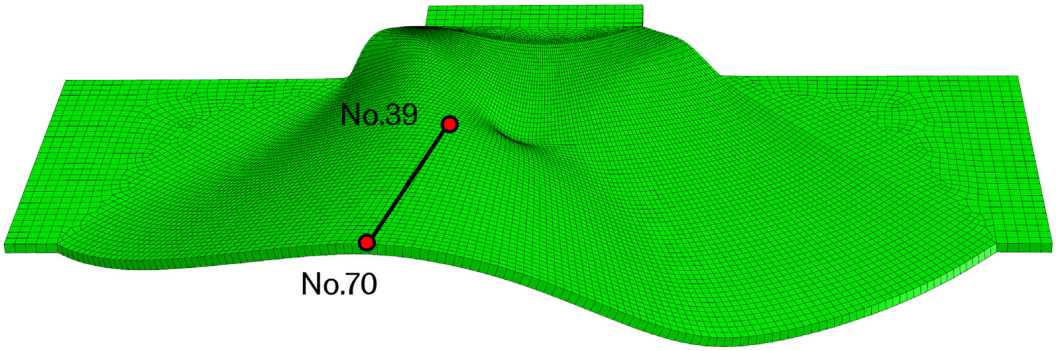

Figure 6.35 Nodes No.39 to No.70 to output strain results in wrinkling test FE model E.

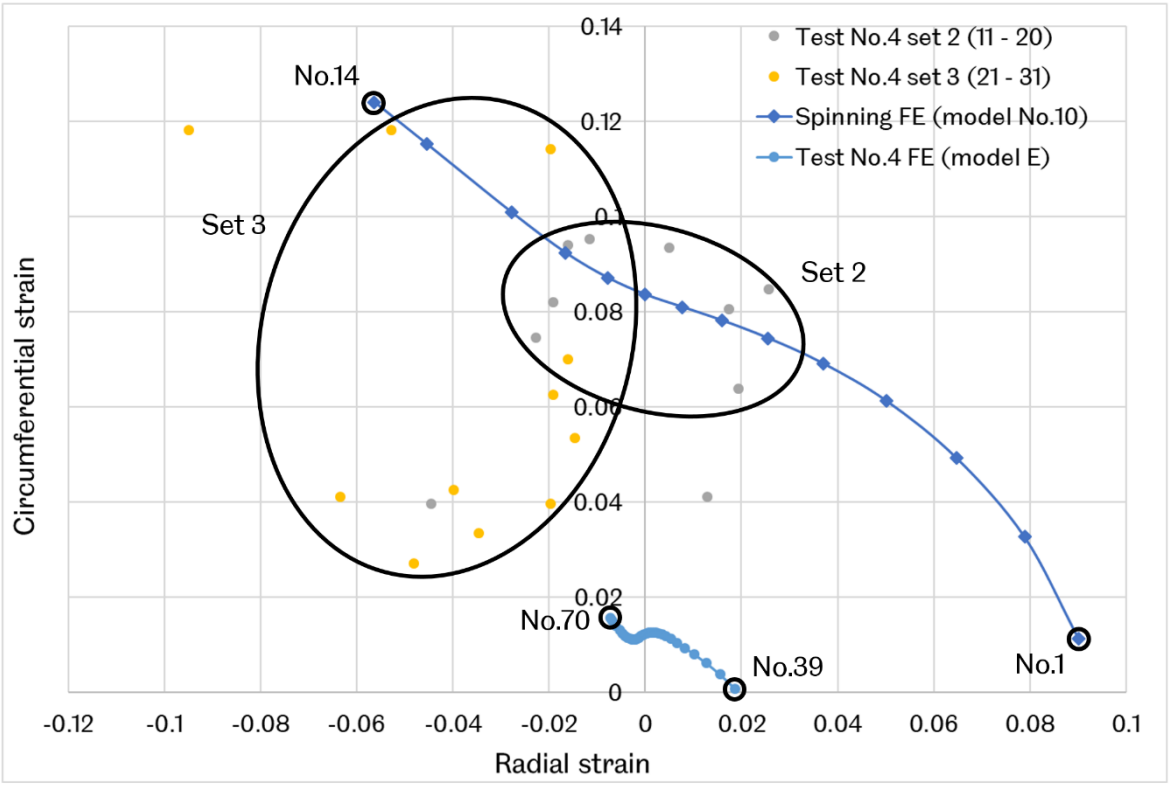

Figure 6.36 The strain results comparison of wrinkling test No.4, wrinkling test FE model E and spinning FE model No.10.

Similar to test No.3, the strain results of test No.4 are much greater than the wrinkling test FE model E. Also, the strain results from set 2 and set 3 are scattering around the strain signature of spinning FE model No.10, gradually propagating from the right-hand side to the left-hand side. Furthermore, test No.4 further improves the strain results compared with test No.3. In test No.3, the strain results gather around the middle section of the spinning strain signature. For test No.4, the data points in set 2 distribute around the middle section of the spinning strain signature and set 3 covers the left-hand side section of the strain signature. Although there are no data points distributed close to the right-hand side of the signature, there are some improvements to the strain results in test No.4. However, the results of test No.4 still do not correlate with the results of spinning FE model No.10.

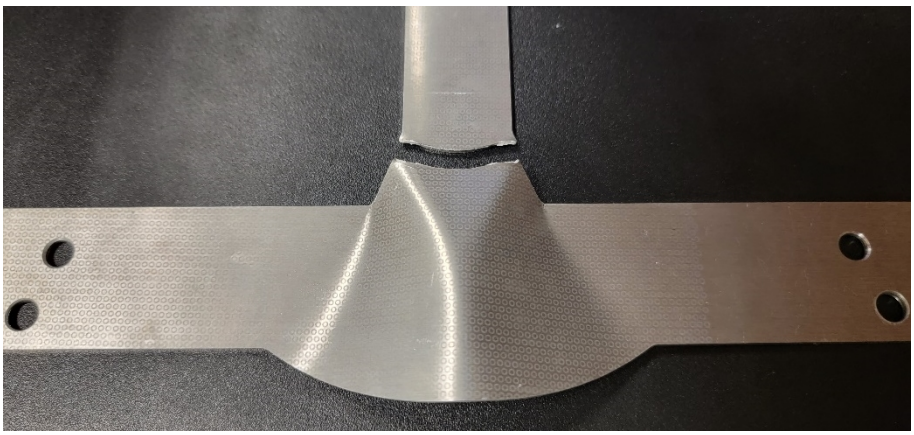

(a)

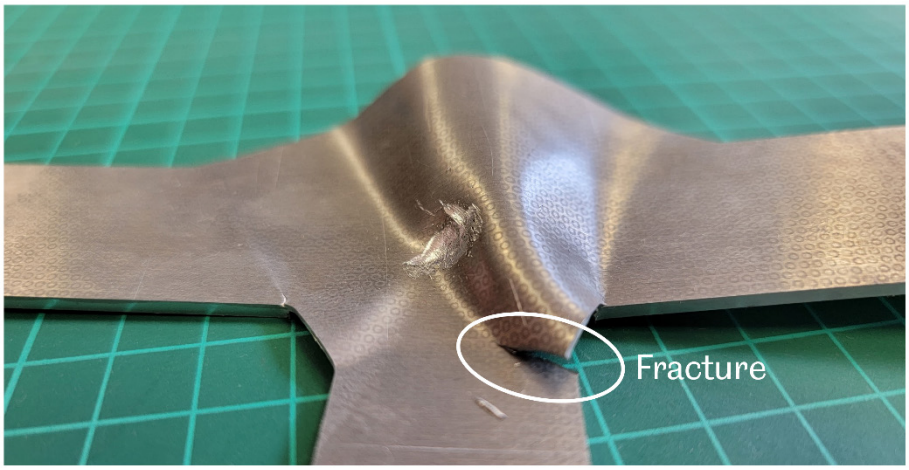

(b)

Figure 6.37 Fracture on the deformed specimen in (a) test No.3 and (b) test No.4.

Another problem for the wrinkling test No.3 and No.4 is the fractures shown in Figure 6.37, which are not supposed to occur in the test. The fracture in Figure 6.37 (a) occurs when unloading the specimen from the BTBC rig. Although it does not

occur during the test, the facture indicates that the test lowers the strength of the fractured area, and thus it fractures when relatively small loadings are applied. The fracture in Figure 6.37 (b) is discovered during the test. The fracture occurs when the bending tool pushes the wrinkled material downwards.

As mentioned in chapter 5, the purpose of the thickness reduction on the gauge area and the width reduction on the two arms on axis 1 is to reduce the strength of the corresponding locations to ensure the loadings concentrate on the gauge area. However, the end of the gauge area is over-weakened. The loadings applied by the BTBC rig are still not entirely concentrated on the gauge area and fracture the weak junction between the arm and the gauge area. Fracture is not expected since the wrinkling test FE models developed in Chapter 5 do not involve fracture modelling. In the current BTBC rig, the location of the bending tool is fixed and targets the centre of the two axes. Hence, the bending tool can only induce the bending deformation to the axes centre. Further modification can be focused on the bending tool mounting system, improving the flexibility of the bending system so that it can apply the bending deformation at different locations on the specimen instead of only at the centre of the axes. More complex loadings can be applied by the bending tool can better represent the roller movement in the spinning process.

6.3.3 Strain Results Analysis of Additional Wrinkling Tests

The strain results do not correlate with the FE modelling results since the wrinkling tests are conducted with coarsely etched specimens. Additional wrinkling tests are conducted with improved etching patterns processed by the laser engraving machine at the University of Birmingham. The improved patterns with 1 mm diameter and neglectable circumference thickness are shown in Figure 6.38.

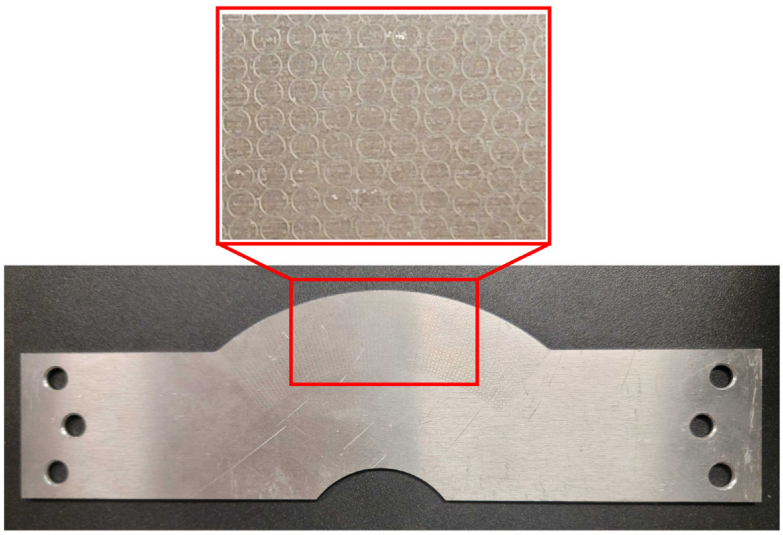

Figure 6.38 Circular patterns etched by the laser engraving machine.

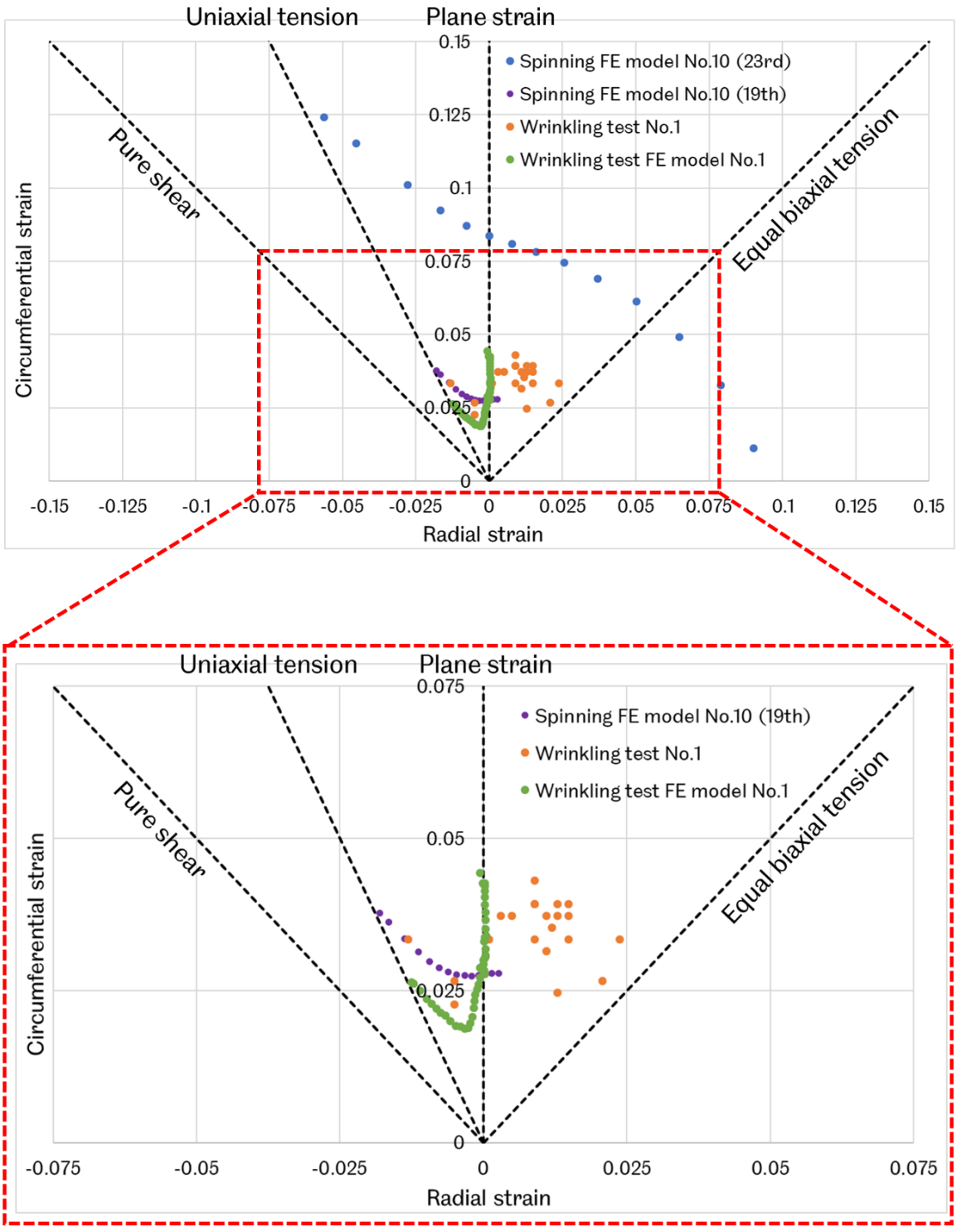

Figure 6.39 Strain results comparison between wrinkling test No.1, wrinkling test FE model No.1 and spinning FE model No.10.

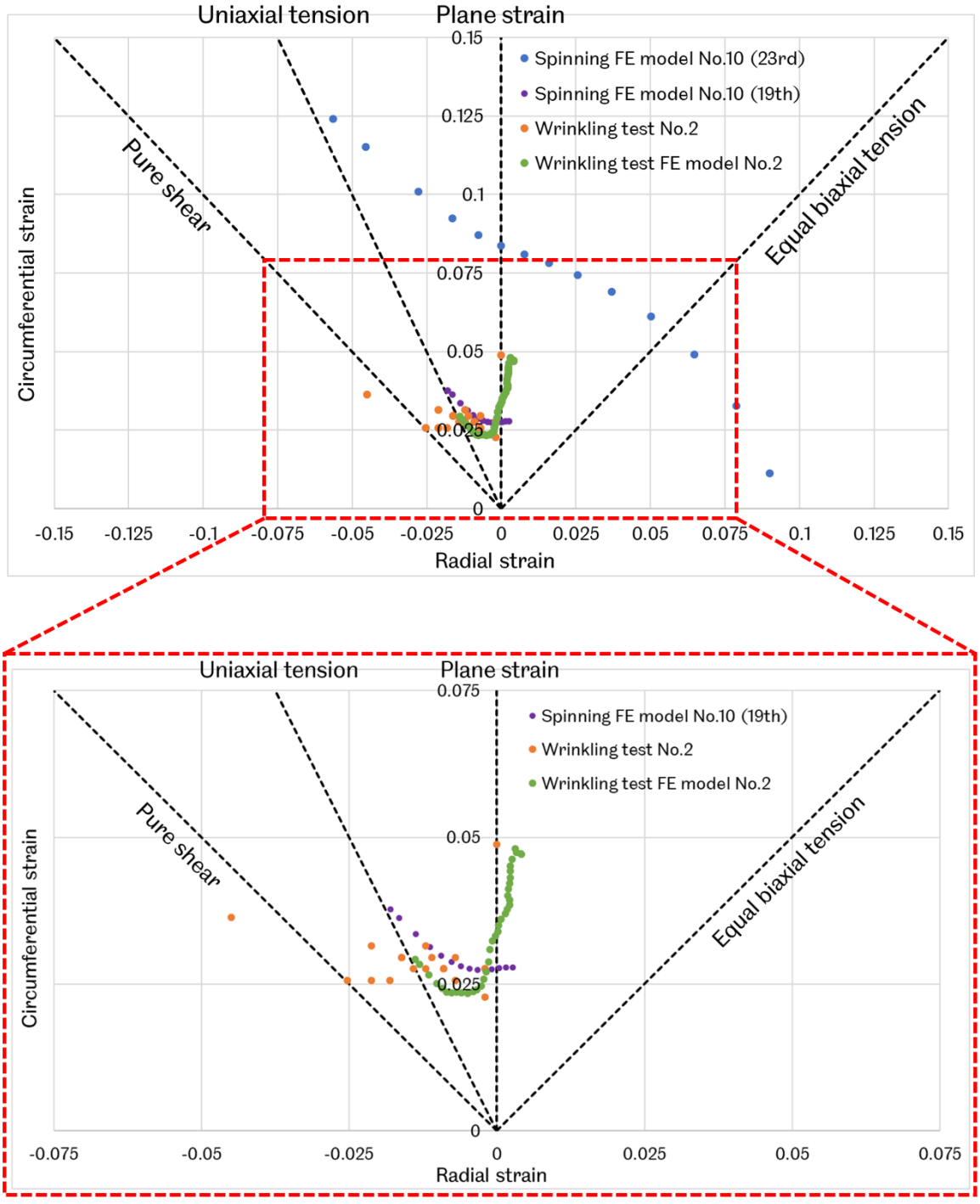

Figure 6.40 Strain results comparison between wrinkling test No.2, wrinkling test FE model No.2 and spinning FE model No.10.

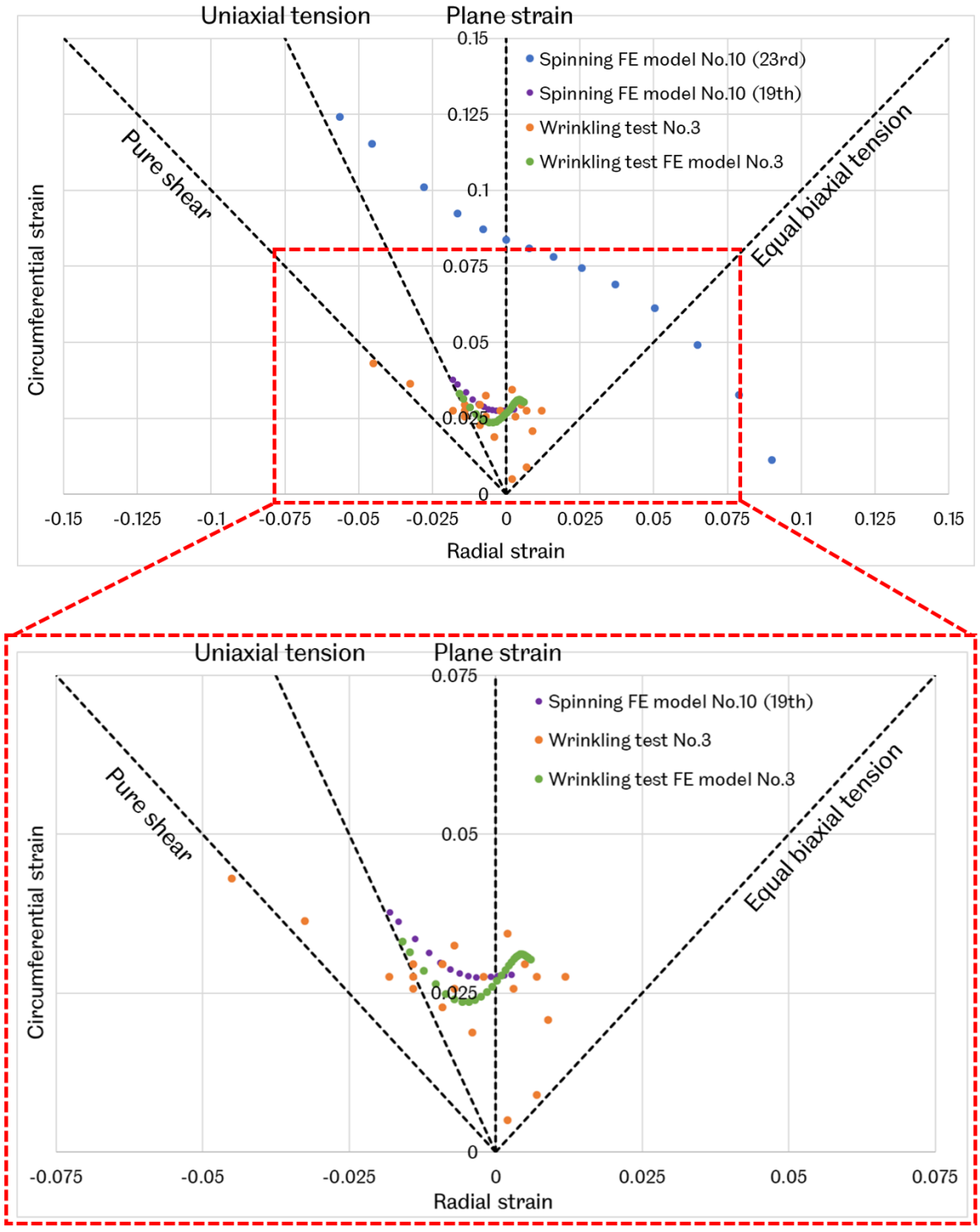

Figure 6.41 Strain results comparison between wrinkling test No.3, wrinkling test FE model No.3 and spinning FE model No.10.

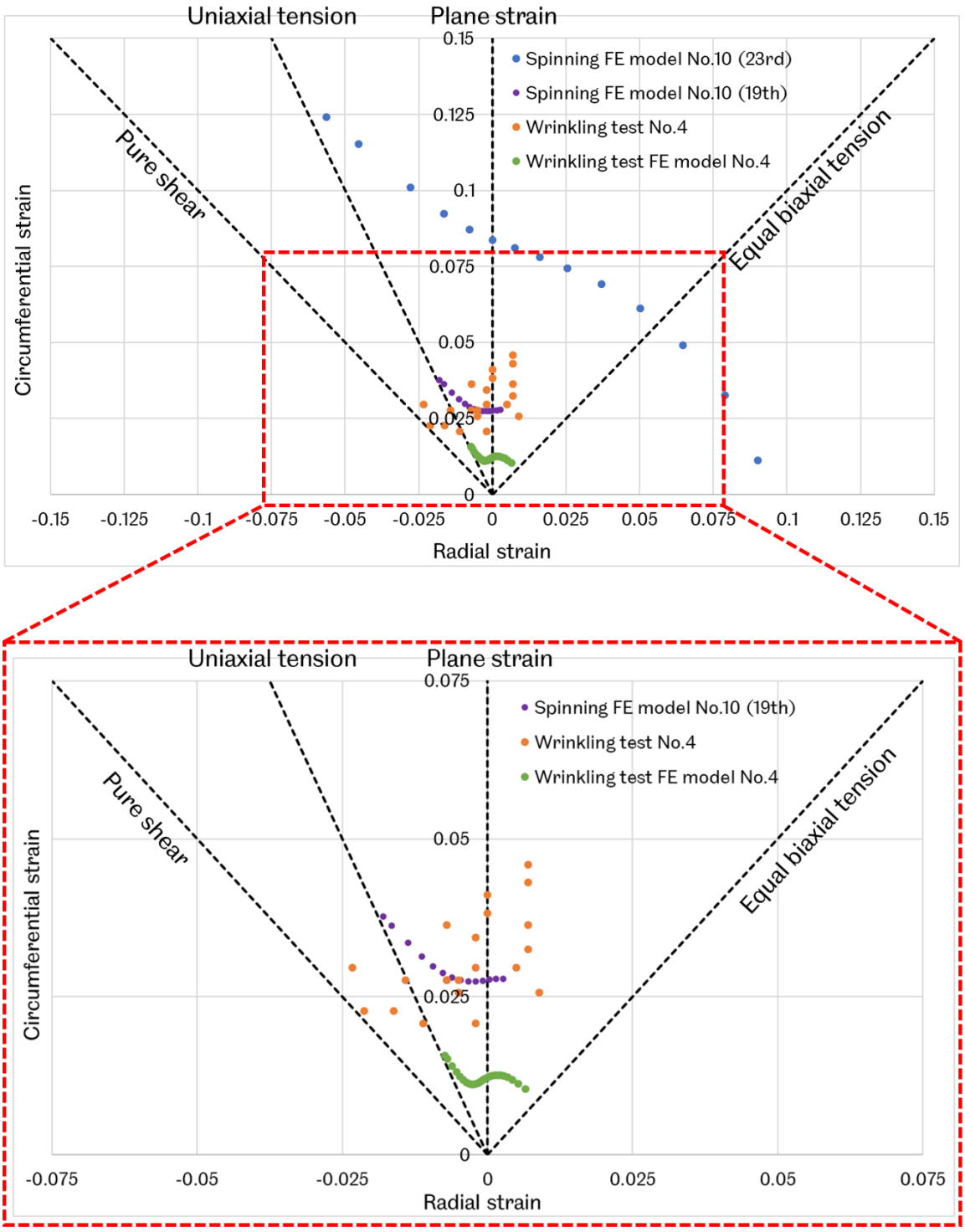

Figure 6.42 Strain results comparison between wrinkling test No.4, wrinkling test FE model No.1 and spinning FE model No.10.

In the spinning FE model No.10, the roller works over the workpiece 23 revolutions before the excessive distortion occurs, and the strains reach maximum on the 23rd revolution. Also, the strains of the 23rd revolution are regarded as reference strains for wrinkling tests to achieve and compare with. The comparison of the strain

results between wrinkling FE modelling and tests No.1 to No.4 with spinning FE model No.10 are shown in Figure 6.39, Figure 6.40, Figure 6.41 and Figure 6.42.

The results of wrinkling tests No.1 to No.4 are all improved compared with the previous wrinkling tests as the data points distribute much closer around wrinkling FE modelling data points. Wrinkling tests No.2 and No.3 correlate better than tests No.1 and No.4 as the data points distribute. However, the test results are still much smaller than the spinning FE modelling results on the 23rd revolution, so comparing them with the strain results of the 23rd revolution is meaningless. Hence, the strain results of the 19th revolution are added to the diagram to illustrate a better correlation between the wrinkling test and the spinning FE modelling. The 19th revolution in the spinning process is in an early stage wrinkling /minor wrinkling with smaller strains, correlating much better with the wrinkling tests. Wrinkling tests No.2 and No.3 correlate better than tests No.1 and No.4. The data points of tests No.2 and No.3 have similar trends with the data points of spinning FE modelling. The data points distribute between the uniaxial tension and the plane strain deformation modes with approximately 0.025 to 0.04 circumferential strain and −0.025 to 0 radial strain. The human errors in the additional wrinkling tests are greatly reduced due to the laser-processed specimens with high-quality etched patterns. The wrinkling tests correlate much better with the spinning FE modelling, and the tests achieve the early stage wrinkling.

The wrinkling test specimens are designed to achieve multiple wrinkling waves on the arc gauge area. It is the first reason that the dimensions of the arc gauge area are larger than a single wrinkling wave in the spinning process. The second reason is to match the specimen with the BTBC rig clamping system since the smaller specimen may not be compatible. However, the compression loadings are inadequate to cause multiple wrinkling waves. Even if multiple wrinkling waves were achieved (like in the photo of test No.4), the severity of these waves is minor, resulting in smaller circumferential and radial strains. But the wrinkling tests can still be considered successful as the early stage wrinkling /minor wrinkling was achieved. There is potential to achieve severe wrinkling with further modification to improve the compression loading and the bending tool movement discussed in Section 6.3.2.

6.3.4 Wrinkling Wave Amplitude Result Analysis

As mentioned in section 6.3.1, the compression loading applied to the wrinkling test specimen is 1.2 mm over 10 seconds on each side of the arm. The wrinkling wave amplitude results of test No.1 and test No.3 are measured ten times by a vernier scale, as shown in Figure 6.43, at one-second intervals. Since test No.2 and test No.4

are identical to test No.1 and test No.3 before the bending tool is involved and further deforms the specimen, the wrinkling wave amplitude results are only measured from test No.1 and test No.3, and the results are shown in Figure 6.44.

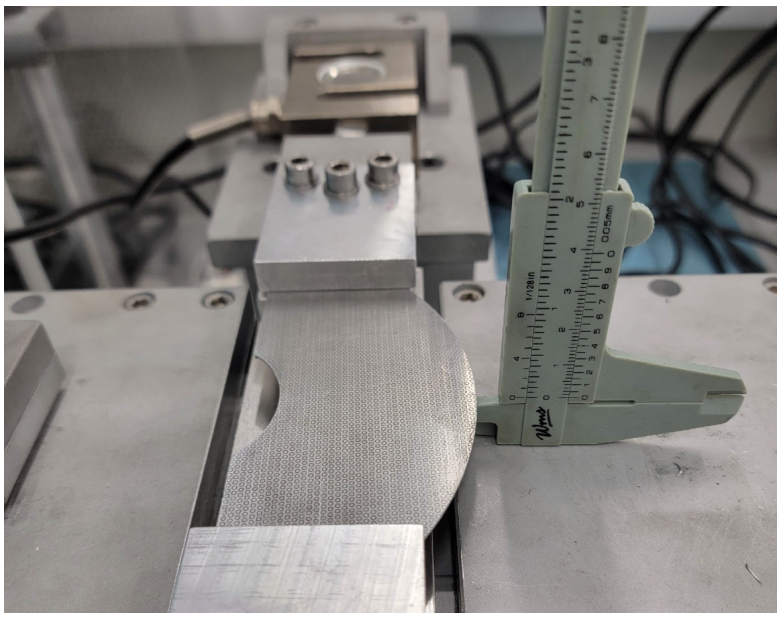

Figure 6.43 A demonstration of measuring wrinkling wave amplitude with a vernier scale.

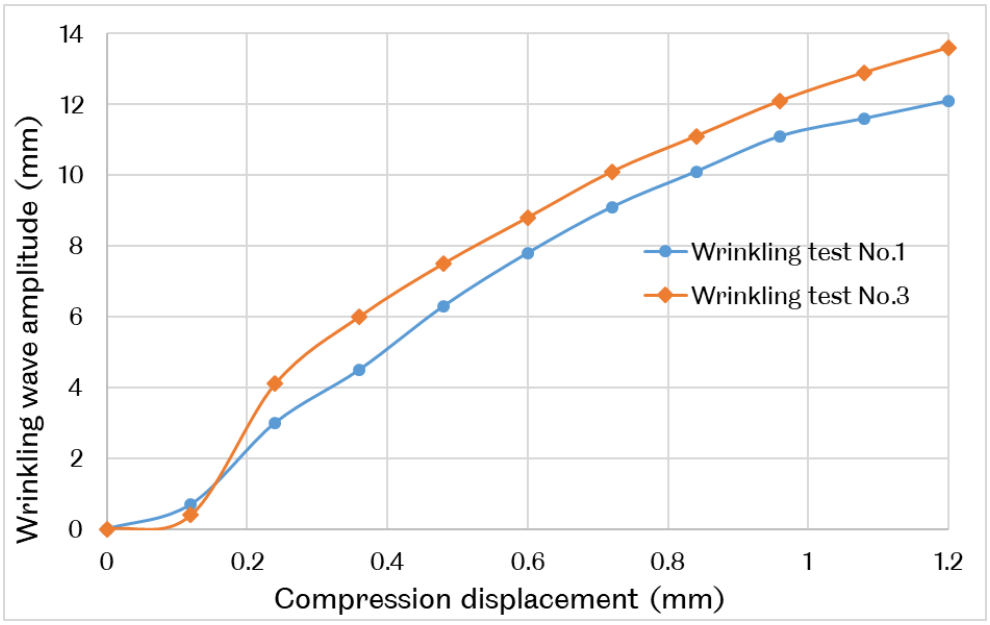

Figure 6.44 The wrinkling wave amplitude results in the compression displacement history of tests No.1 and No.3.

Tests No.1 and No.3 have a similar increasing pattern of wrinkling wave amplitudes. The amplitude almost does not increase for the first 0.12 mm compression of the test, which rapidly increases in the next 0.12 mm compression. After the second 0.12 mm compression, the amplitude increases less rapidly. The final wrinkling wave amplitudes are 12.1 mm for test No.1 and 13.6 mm for No.3. The comparisons between

wrinkling tests No.1, No.3 and FE model B, and FE model D results are shown in Figure 6.45 and Figure 6.46, respectively.

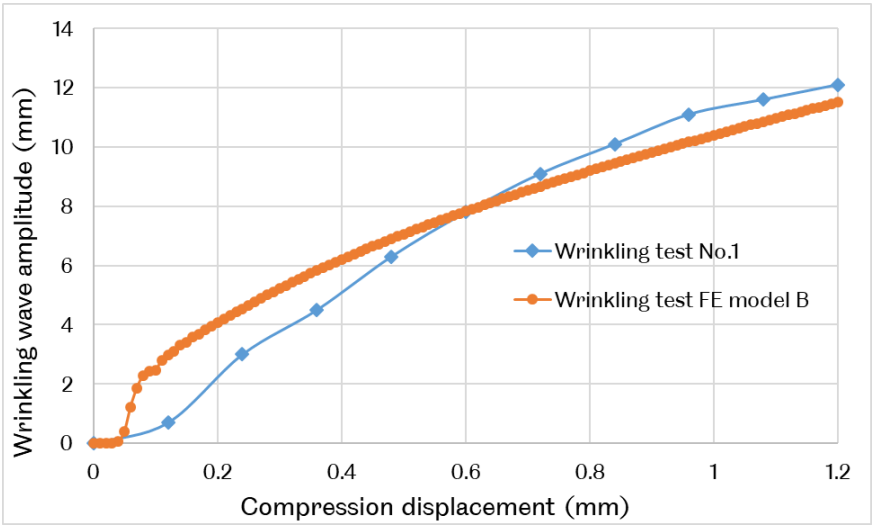

Figure 6.45 The wrinkling wave amplitude of wrinkling test No.1 and FE model B.

The wrinkling wave amplitude results of the test and the FE modelling demonstrate a similar pattern that the amplitude does not increase for a period of time at the beginning of the test. The FE model demonstrates the pattern more clearly. The amplitude increases after 0.05 mm of compression is applied to specimen No.1 in FE model B. The result deviation is huge in the early stage of the test. The deviation becomes smaller with increasing time and only 4.6% at the end of the test (12.1 mm in test No.1 and 11.57 mm in FE model B).

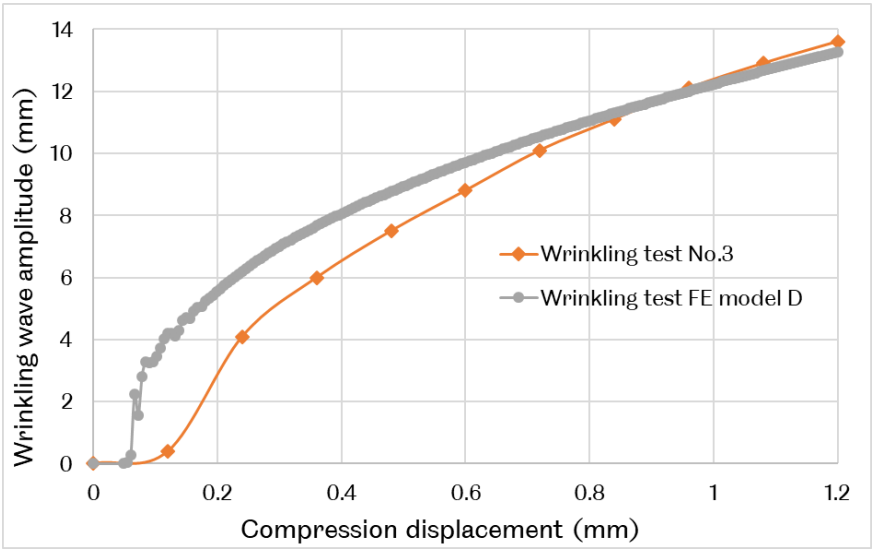

Figure 6.46 The wrinkling wave amplitude of wrinkling test No.3 and FE model D.

Wrinkling test No.3 and wrinkling test FE model D indicate similarly to test No.1 and FE model B, as shown in Figure 6.46. The wrinkling wave amplitude does not increase until 0.06 mm compression is applied to specimen No.2. The result deviation is also

great at the early stage of the test. The deviation is smaller in the late stage, and the amplitude results eventually achieve a very agreeable 2.4% deviation of the maximum wrinkling wave amplitude.

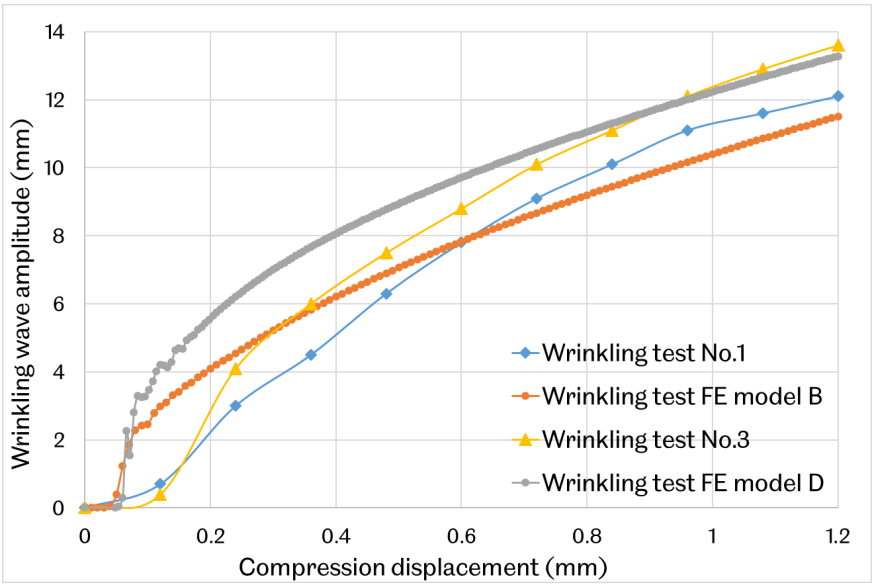

Figure 6.47 Wrinkling wave amplitude results of wrinkling test No.1, test No.3, wrinkling test FE model B and model D.

The wrinkling wave amplitude results of wrinkling test No.1, FE model B, test No.3 and FE model D are displayed in Figure 6.47 for a comprehensive comparison. The test and the FE modelling results achieve very agreeable correlations. The final wrinkling wave amplitude results have the smallest deviations. Both FE models show a pattern that the wrinkling wave amplitudes do not change for a short period of time in the early stage. The data collecting frequency of the wrinkling tests is inadequate to record similar results, only reflecting a similar pattern that the wrinkling wave amplitudes rapidly increase after the first and second data points. Also, the wrinkling wave amplitudes of the spinning tests in Chapter 4 (smaller than 8 mm for tests with a 1.5 mm/rev feed ratio) are much smaller than the wrinkling tests (over 12 mm), in which the test loadings correspond to the 1.5 mm/rev feed ratio. The reason for such great result deviation is that the gauge area of the wrinkling test specimen is much bigger than the wrinkling wave in the spinning test. The original purpose of the excessively big gauge area is to achieve multiple wrinkling waves (tops and bottoms). However, only one wrinkling wave is achieved on specimen No.1 and two (one wrinkling top and one bottom) on specimen No.2. Hence, the loadings for multiple wrinkling waves focus on one wrinkling wave, resulting in a much greater wrinkling wave amplitude than the spinning test. Also, the direction of the compressive loadings applied to the specimen is along axis 1

throughout the test. In the spinning process, the compressive stress is always normal to the two sides of a wrinkling wave, as shown in Figure 6.48.

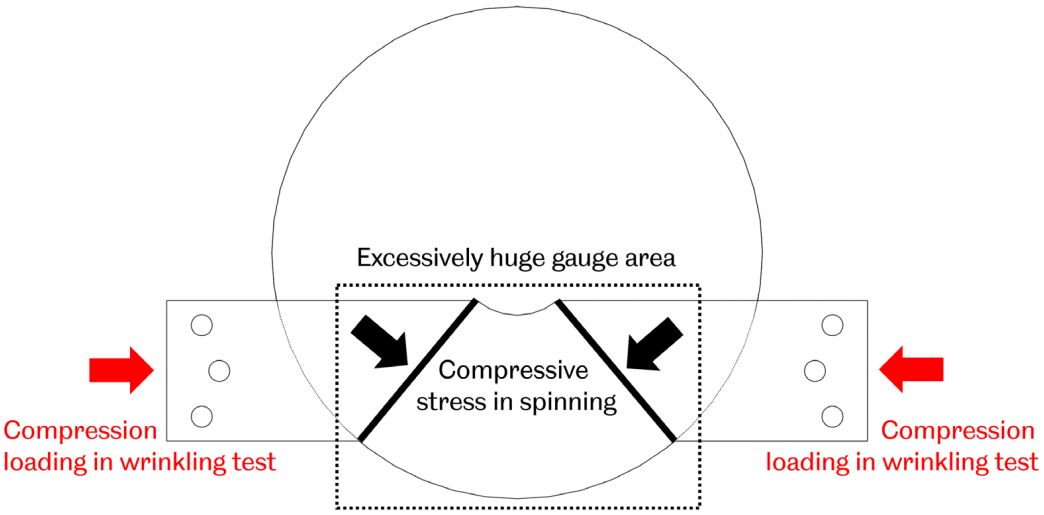

Figure 6.48 Schematic diagram of the compression loadings in the wrinkling test and compressive stress in the spinning process.

(a)

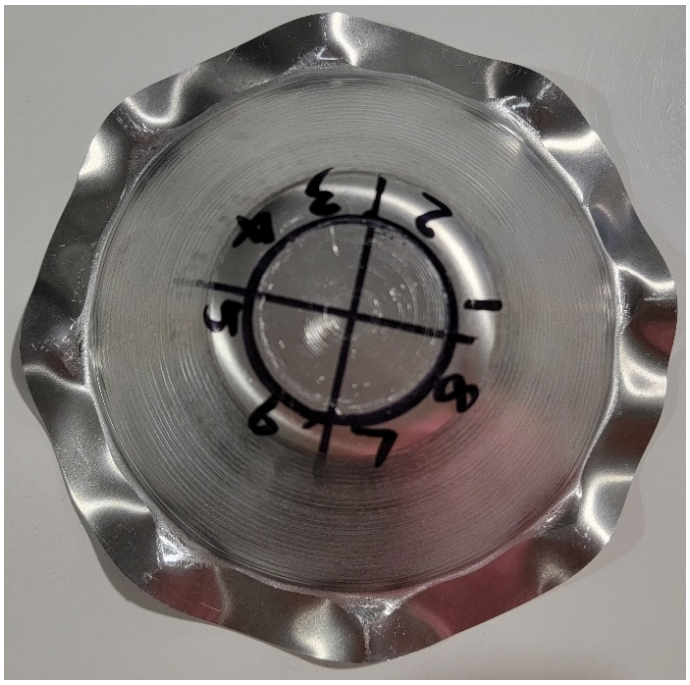

(b)

Figure 6.49 The example of the relatively smaller wrinkling waves from 1.5 mm/rev feed ratio (a) FE model No.10 and (b) spinning test No.1.

The example of the relatively smaller wrinkling waves from spinning FE model No.10 and spinning test No.1 is shown in Figure 6.49. The wrinkling test specimen design has been compromised. For example, the dimensions of the specimen need to be adequately large to fit in the BTBC rig. Hence the specimen design aims to achieve multiple wrinkling waves on a great gauge area. The wrinkling waves in the spinning FE model and test are narrower and similar to a strip shape distributed on the flange of the workpiece. Further modifications are required to the wrinkling test specimen to achieve similar wrinkling deformation as the spinning test. For example, a smaller gauge area may be practical to reduce the final wrinkling wave amplitude.

6.4 Summary of Conclusion

In this chapter, the BTBC rig is modified to perform the wrinkling tests developed in Chapter 5. Circular grid patterns are etched on the specimen by using the electrochemical etching machine. The purpose is to induce wrinkling deformation to the specimen and measure the strain results through the deformed patterns. The strain results are obtained by using the electron microscope. Based on the results, key findings are outlined as follows:

- The modifications to the BTBC rig are successful. The BTBC rig can stably provide compression loadings to the specimen. The compression

displacement is controllable and can be monitored in real-time. The specimens are manufactured, and four tests are performed on the BTBC rig.

- The wrinkling wave amplitude and strains of the wrinkling test results correlate with the wrinkling test FE models developed in Chapter 5. However, only early-stage/minor wrinkling deformation is achieved in the wrinkling test due to the limited movement of the bending tool and clamps.

7 Conclusion and Future Work

This chapter summarises the main findings and future improvements of this project. Section 7.1 is the conclusion of all the results obtained throughout the project, including the important contribution to existing knowledge. 7.2 is the improvements to tackle the limitations of the current research.

7.1 Conclusion

This PhD research focuses on two investigations: 1. investigating the mechanism of wrinkling failure in the shear spinning process and 2. developing the wrinkling testing method on the BTBC rig. This section introduces the main findings and the research novelty around these two investigations.

7.1.1 Summary of the research findings

Main findings of the shear spinning investigation

The wrinkling deformation behaviour of material AA5251-H22 is investigated. The shear spinning FE models are developed, and comprehensive strain results are obtained. The feed ratio and the mandrel rotational speed as two important processing parameters are investigated. The shear spinning tests are conducted, and vibration results are recorded as waveforms. The wrinkling initiation timing is obtained by analysing the vibration waveforms. The wrinkling wave heights of the wrinkling waves on the workpiece flange are measured. The thickness distribution results of the spun part are measured and used to validate the FE modelling results. Based on the experimental and FE modelling results of the shear spinning process, the key findings are concluded as follows:

- The wrinkling deformation is the result of circumferential strain accumulation by the cyclical loadings induced to the workpiece by the roller. Excessive feed ratio causes circumferential strain accumulation and, thus, wrinkling initiation. The wrinkling occurs when the circumferential strain on the top surface of the wrinkling wave starts to increase cyclically and permanently becomes positive/tensile. Higher feed ratios result in more rapid circumferential strain accumulation.
- The different strain rates caused by the different mandrel speeds do not affect the wrinkling initiation. The strain rate also does not affect the circumferential strain accumulation and, thus, wrinkling propagation.

- For the shear spinning process with the experiment setup in this study, the wrinkling limit as the maximum feed ratio applied to the workpiece that does not cause wrinkling throughout the entire process is 0.5 mm/rev. The circumferential strain remains compressive throughout a wrinkling-free shear spinning process.

Main findings of the wrinkling testing method development

The FE models of the new wrinkling testing method are developed, and the wrinkling tests are conducted on the modified BTBC rig. The material used in the FE model and the wrinkling tests is AA5251-H22. The testing specimens are manufactured and etched with circular grid patterns for strain measurements. According to the experimental and FE modelling results of the new wrinkling testing method, the main findings are concluded as follows:

- Although the BTBC rig is modified and the new wrinkling testing method is developed based on the capability of the rig, the strain results do not correlate well with the shear spinning FE and experimental test results. Human error in strain measurement is unavoidable due to the limitation of the electrochemical etching machine.
- The most important feature of the specimen design is the thickness-reduced arc gauge area. The thickness reduction guarantees that the deformation only occurs on the gauge area rather than partially distributed on the arms of the specimen.
- The most important boundary condition is the compression on the two sides of the gauge area. The compression causes tensile circumferential strains on the top surface of the specimen and triggers wrinkling deformation.
- The one-pass toolpath is not sufficient for triggering the wrinkling deformation on the specimen to fully match spinning wrinkling because the wrinkling deformation in the shear spinning process is a result of cyclical strain accumulation.

7.1.2 Research novelty

Research novelty of the shear spinning investigation

For the FE models of the spinning process, the meshing strategy that divides a circular workpiece into three areas to reduce the number of elements and maintain an overall sweep strategy is not reported in the previous literature. This strategy eliminates the hourglass problem and achieves an optimised balance between the CPU calculation cost and the accuracy of results.

The investigation of the wrinkling deformation by studying the strain results of the wrinkled material is also not reported in the previous literature. The strain result analysis defines the wrinkling initiation and propagation. The wrinkling deformation also has been quantified by the wrinkling wave amplitude as a universal and measurable method for industry. The vibration detection of the surface unevenness will benefit the industry in distinguishing whether the wrinkling occurs on a spun part before the spinning process finishes, increasing manufacturing efficiency and lowering costs.

The strain analysis also proves that the dynamic effect induced to the spinning workpiece due to the high mandrel speeds does not affect the wrinkling initiation. The wrinkling initiation is caused by the excessive feed ratio applied to the workpiece. The compression to the workpiece surface induced by the roller causes the circumferential strain beThe wrinkling initiates when the circumferential strain on the top surface of the wrinkling wave cyclically increases and remains positive/tensile. A higher feed ratio causes a more rapid circumferential strain accumulation. The circumferential strain remains compressive throughout a wrinkling-free shear spinning process.

Research novelty of the wrinkling testing methods development

The wrinkling testing method developed in this project for the spinning process has never been reported in the existing literature. The BTBC rig has been modified and successfully caused wrinkling deformation by applying compression and bending to the specimen. Although the strains of the wrinkled material are smaller than the maximum strains of spinning FE models, the wrinkling tests achieve early stage wrinkling/minor winkling and correlate well with the wrinkling FE and spinning FE modelling strain results. The wrinkling test can also prove that compression and bending can cause wrinkling deformation on the specimen with a thickness-reduced arc gauge area. The BTBC has the potential to achieve severe wrinkling deformation and obtain more similarities in the circumferential strain and wrinkling wave amplitude results.

7.2 Future Work

As concluded in section 7.1, this project consists of two main parts: an investigation of the shear spinning process and the development of the wrinkling testing method. This section introduces the future work around these two parts.

Future work on the shear spinning investigation

The workpiece is clamped in the shear spinning test by the mandrel and the

backplate, as described in section 4.1. The centre of the workpiece is located by the centre finder, as shown in Figure 7.1. However, the centre finder is operated by humans, and human error is involved. The centre of the workpiece is marked by a marker pen, as shown in Figure 7.2.

Figure 7.1 Centre finder to locate the centre of the workpiece [119].

The friction between the backplate, mandrel, and workpiece may not be enough to stop the workpiece from moving slightly along its radial direction during the spinning test. The workpiece is off-centre in test No.8, as shown in Figure 7.2 (a). Figure 7.2 (b) is an example of an in-centre workpiece from test No.1. For a workpiece that retains an in-centre state throughout the test and is fully formed by the roller and eventually becomes a cone shape spun part. Some of the excessive result deviations in section 4.3 may be caused by the off-centre workpieces, resulting in unexpected deformation as the roller is not following the designed toolpath on the workpiece, and thus abnormal vibrations waveforms are recorded. The roller works over an unsymmetrical workpiece and impacts the edge, causing unnecessary wrinkling and excessive distortion.

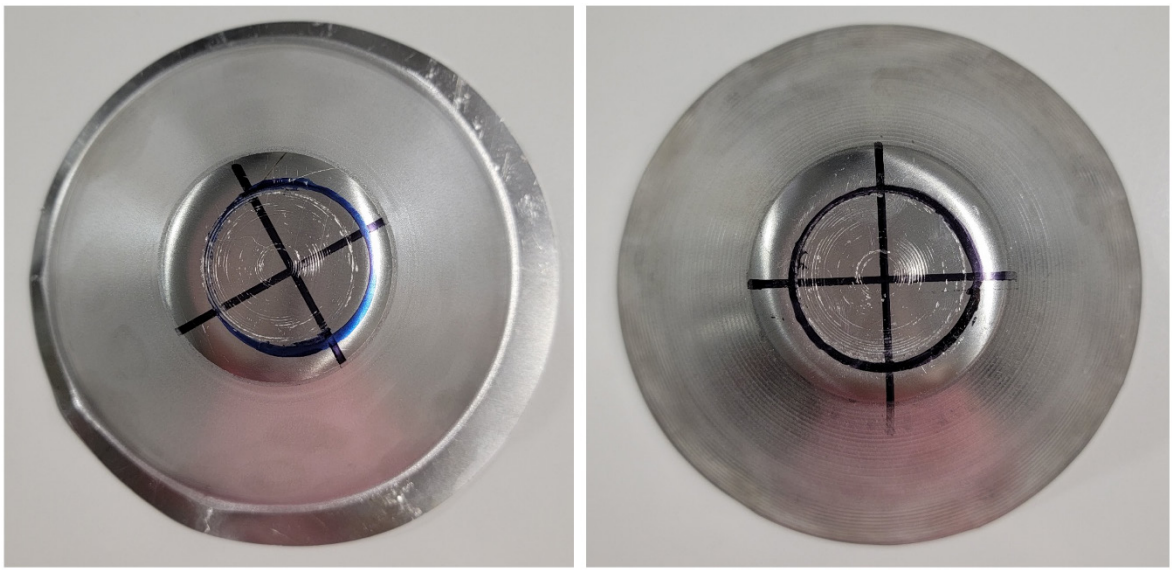

(a) **(b)**

Figure 7.2 Deformed workpieces of (a) test No.8 off-centre and (b) test No.1 in-centre.

Modifications have been made to the backplate, mandrel and workpiece related to the spinning test set up. The locating hole method is developed, as shown in Figure 7.3. Two locating holes are drilled in the backplate, the mandrel and the workpiece, as shown in Figure 7.3 (a), Figure 7.3 (b) and Figure 7.3 (c). The mandrel is fitted with two location poles with corresponding dimensions. The workpiece is automatically located by the mandrel and the backplate, and an illustration of the auto locating is shown in Figure 7.3 (d). The workpiece does not rely on the frictional force produced to stop the workpiece from moving. Two locating poles prevent the workpiece from sliding off-centre effectively. However, spinning tests with improved components are not conducted due to the prohibition of conducting further spinning tests on the existing CNC lathe and the inefficiency of repairing the other lathe in the university workshop.

(a)

(b)

(c)

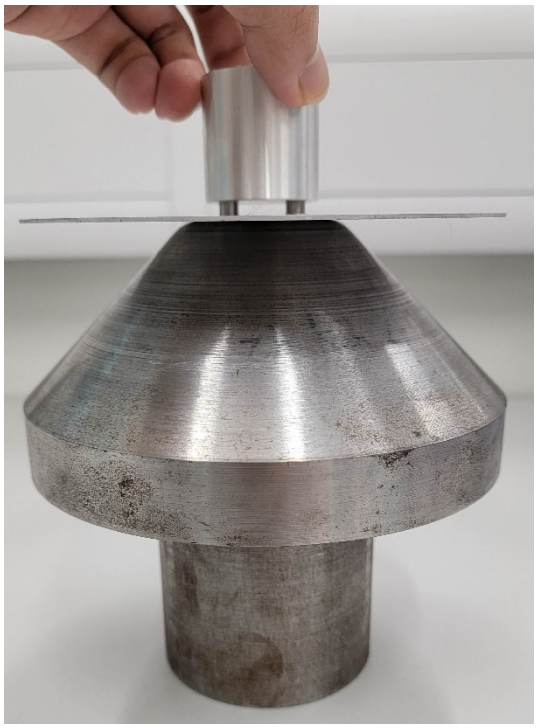

(d)

Figure 7.3 Modifications to the spinning test (a) backplate with two locating holes; (b) mandrel with two locating poles; (c) workpiece with two locating holes and (d) the illustration of spinning setup assembly.

To summarise, the wrinkling wave heights, the wrinkling vibration waveforms and the wrinkling initiation timing were obtained, but the strain related results were not. The current electrochemical etching machine has limitations in etching high-quality patterns. Also, the shear spinning testing machine, for example, the CNC lathe, the mandrel and the backplate have limitations in clamping and locating the workpiece. Hence, future work to perfect the shear spinning experimental investigation includes:

- Improving the quality of the etched circular grid patterns by using a more advanced laser engraving machine, performing preliminary tests to check if the modifications to prevent the workpiece from sliding are reliable and validating the spinning FE modelling using the preliminary test results;
- Performing more shear spinning tests to obtain vibration waveforms and strain results under more comprehensive processing parameters, for example, mandrel speeds over 1000 RPM and feed ratios over 2.0 mm/rev, to obtain more comprehensive results like the wrinkling initiation timing and strain results of the wrinkling waves under different processing parameters.

Future work on the new wrinkling testing method development

Although the new wrinkling testing method is developed based on the modified BTBC rig, which successfully applied multiple deformation modes to the specimen, the strain results still do not correlate well with the shear spinning FE modelling and experimental test results. Due to the limitation of the electrochemical etching machine used in this project, human error in strain measurement greatly influenced the analysis of the strain results. The bending tool on the BTBC rig cannot achieve a complex toolpath requiring cyclic loading. Thus it cannot simulate the cyclical strain accumulation effect induced on the workpiece by the roller in the shear spinning process. Also, the compression applied to the arc flange section of the workpiece in the shear spinning process is different from the BTBC rig. The BTBC rig applies compression to the specimen on a straight axis, and the compression to the arc section in the shear spinning process always has an angle. Hence, the future work for the wrinkling testing methods development are:

- Improving the quality of the pattern etched on the specimen using a laser engraving machine;
- Modifying the bending tool holding system on the BTBC rig to allow the bending tool moves on a cyclical toolpath;
- Modifying the compression loadings system and allowing the clamps to apply compression to the specimen from different directions instead of on a straight axis.

Reference

[1] M. Kleiner, R. Göbel, H. Kantz, C. Klimmek, and W. Homberg, "Combined methods for the prediction of dynamic instabilities in sheet metal spinning," *CIRP Ann. - Manuf. Technol.*, vol. 51, no. 1, pp. 209–214, 2002, doi: 10.1016/S0007-8506(07)61501-7.

[2] S. Ai, "NOVEL TESTING METHODS OF MATERIAL DEFORMATION AND FRACTURE MECHANISM," no. August, 2019.

[3] W. F. Hosford and J. L. Duncan, "Sheet Metal Forming: A Review," *Jom*, vol. 51, no. 11, pp. 39–44, 1999, doi: 10.1007/s11837-999-0221-5.

[4] O. Music, J. M. Allwood, and K. Kawai, "A review of the mechanics of metal spinning," *J. Mater. Process. Technol.*, vol. 210, no. 1, pp. 3–23, 2010, doi: 10.1016/j.jmatprotec.2009.08.021.

[5] Centurymetalspinning.com, "Aerospace | centurymetalspinning," 2018. http://www.centurymetalspinning.com/aerospace/ (accessed Aug. 29, 2018).

[6] "Stainless Steel Housing - LETIPTOP Metal Spinning Machine Cases." https://www.metalspinningmachine.com/portfolio-items/stainless-steel-housing/ (accessed Jun. 16, 2021).

[7] Metal-spinners, "Metal Spinning," 2018. https://www.metal-spinners.net/ (accessed Aug. 29, 2018).

[8] Staff.aist.go, "Metal Spinning of Non-axisymmetric Products," 2018. https://staff.aist.go.jp/h.arai/nonsym_e.html (accessed Aug. 29, 2018).

[9] Custompartnet.com, "Sheet Metal Forming," 2018. http://www.custompartnet.com/wu/sheet-metal-forming (accessed Aug. 29, 2018).

[10] K. 'Lange, *Handbook of Metal Forming*. SME publications, 1985.

[11] M. 'Runge, *Spinning and Flow Forming*. Leifeld GmbH, 1994.

[12] M. Watson and H. Long, "Wrinkling failure mechanics in metal spinning," *Procedia Eng.*, vol. 81, no. October, pp. 2391–2396, 2014, doi: 10.1016/j.proeng.2014.10.339.

[13] C. C. Wong, T. A. Dean, and J. Lin, "A review of spinning, shear forming and flow forming processes," *Int. J. Mach. Tools Manuf.*, vol. 43, no. 14, pp. 1419–1435, 2003, doi: 10.1016/S0890-6955(03)00172-X.

[14] T. Childerhouse, "An Investigation into the Effects of Various Process Parameters when Shear Spinning Conical Parts," 2018.

[15] T. Childerhouse and H. Long, "Processing maps for wrinkle free and quality enhanced parts by shear spinning," *Procedia Manuf.*, vol. 29, pp. 137–144, 2019, doi: 10.1016/j.promfg.2019.02.118.

[16] Z. Shao *et al.*, "Experimental investigation of forming limit curves and deformation features in warm forming of an aluminium alloy," *J. Mater. Process. Technol.*, vol. 2, no. 1, pp. 1–15, Apr. 2018, doi: 10.1177/0954405416645776.

[17] B. Avitzur and C. T. Yang, "Analysis of Power Spinning of Cones," *J. Eng. Ind.*, vol. 82, no. 3, pp. 231–244, Aug. 1960, doi: 10.1115/1.3663052.

[18] S. Kalpakcioglu, "On the mechanics of shear spinning," *J. Manuf. Sci. Eng. Trans. ASME*, vol. 83, no. 2, pp. 125–130, 1961, doi: 10.1115/1.3664441.

[19] H. R. Beni, Y. T. Beni, and F. R. Biglari, "An experimental-numerical investigation of a metal spinning process," *Proc. Inst. Mech. Eng. Part C J. Mech. Eng. Sci.*, vol. 225, no. 3, pp. 509–519, 2011, doi: 10.1243/09544062JMES2133.

[20] I. Shimizu, "Asymmetric forming of aluminum sheets by synchronous spinning," *J. Mater. Process. Technol.*, vol. 210, no. 4, pp. 585–592, 2010, doi: 10.1016/j.jmatprotec.2009.11.002.

[21] H. Razavi, F. R. Biglari, and A. Torabkhani, "Study of Strains Distribution in Spinning Process Using FE Simulation and Experimental Work," *Tehran Int. Congr. Manuf. Eng.*, pp. 1–9, 2005.

[22] H. K. M. Hayama, T. Murota, "Deformation modes and wrinkling of flange on shear spinning," *Bull. JSME*, vol. 9, no. 34, pp. 423–433, 1966, doi: 10.1248/cpb.37.3229.

[23] I. Jones *et al.*, "A Good Practices Guide for Digital Image Correlation," *Int. Digit. Image Correl. Soc.*, p. 94, 2018, [Online]. Available: http://idics.org/guide/

[24] Abaqus, "Abaqus Analysis User's Manual Vol2," *HKS, Inc. Provid. RI, USA*, vol. II, 2011.

[25] F. J. Harewood and P. E. McHugh, "Comparison of the implicit and explicit finite element

methods using crystal plasticity," *Comput. Mater. Sci.*, vol. 39, no. 2, pp. 481–494, 2007, doi: 10.1016/j.commatsci.2006.08.002.
[26] A. Hilber, "IMPROVED NUMERICAL DISSIPATION FOR TIME INTEGRATION ALGORITHMS IN STRUCTURAL DYNAMICS," 1976.
[27] A. Hrennikoff, "Solution of Problems of Elasticity by the Framework Method," *J. Appl. Mech.*, vol. 8, no. 4, pp. A169–A175, 1941, doi: 10.1115/1.4009129.
[28] R. COURANT, "Variational Methods For The Solution of Problems of Equilibrium And Vibrations," *Phys. Rev. E - Stat. Physics, Plasmas, Fluids, Relat. Interdiscip. Top.*, vol. 67, no. 1, p. 11, 1943, doi: 10.1103/PhysRevE.67.016108.
[29] E. Quigley and J. Monaghan, "Enhanced finite element models of metal spinning," *J. Mater. Process. Technol.*, vol. 121, no. 1, pp. 43–49, 2002, doi: 10.1016/S0924-0136(01)01138-4.
[30] L. Wang and H. Long, "A study of effects of roller path profiles on tool forces and part wall thickness variation in conventional metal spinning," *J. Mater. Process. Technol.*, vol. 211, no. 12, pp. 2140–2151, 2011, doi: 10.1016/j.jmatprotec.2011.07.013.
[31] M. Watson, H. Long, and B. Lu, "Investigation of wrinkling failure mechanics in metal spinning by Box-Behnken design of experiments using finite element method," *Int. J. Adv. Manuf. Technol.*, vol. 78, no. 5–8, pp. 981–995, 2015, doi: 10.1007/s00170-014-6694-6.
[32] L. Wang, "Analysis of Material Deformation and Wrinkling Failure in Conventional Metal Spinning Process," *Phd thesis*, 2012.
[33] J. L. D. S. J. H. Z. Marciniak, "Mechanics of Sheet Metal Forming," 1979, doi: 10.1007/978-1-4613-2880-3.
[34] S. P. Keeler, "Determination of forming limits in automotive stampings," *SAE Tech. Pap.*, 1965, doi: 10.4271/650535.
[35] G. M. Goodwin, "Application of strain analysis to sheet metal forming problems in the press shop," *SAE Tech. Pap.*, pp. 380–387, 1968, doi: 10.4271/680093.
[36] M. Gensamer, "Strength and Ductility," *Metallogr. Microstruct. Anal.*, vol. 6, no. 2, pp. 171–185, 1946, doi: 10.1007/s13632-017-0341-1.
[37] H. W. Swift, "Plastic instability under plane stress," *J. Mech. Phys. Solids*, vol. 1, no. 1, pp. 1–18, 1952, doi: 10.1016/0022-5096(52)90002-1.
[38] R. Hill, "General Stability Theory in of," *J. Mech. Phys. Solids*, vol. 6, no. 3, pp. 236–249, 1958.
[39] S. Stören and J. R. Rice, "Localized necking in thin sheets," *J. Mech. Phys. Solids*, vol. 23, no. 6, pp. 421–441, 1975, doi: 10.1016/0022-5096(75)90004-6.
[40] J. D. Bressan and J. A. Williams, "The use of a shear instability criterion to predict local necking in sheet metal deformation," *Int. J. Mech. Sci.*, vol. 25, no. 3, pp. 155–168, 1983, doi: 10.1016/0020-7403(83)90089-9.
[41] Z. Marciniak, K. Kuczyński, and T. Pokora, "Influence of the plastic properties of a material on the forming limit diagram for sheet metal in tension," *Int. J. Mech. Sci.*, vol. 15, no. 10, pp. 789–800, 1973, doi: 10.1016/0020-7403(73)90068-4.
[42] Z. Marciniak and K. Kuczyński, "Limit strains in the processes of stretch-forming sheet metal," *Int. J. Mech. Sci.*, vol. 9, no. 9, pp. 609–620, 1967, doi: 10.1016/0020-7403(67)90066-5.
[43] V. R. Shinge and U. A. Dabade, "Experimental Investigation on Forming Limit Diagram of Mild Carbon Steel Sheet," *Procedia Manuf.*, vol. 20, pp. 141–146, 2018, doi: 10.1016/j.promfg.2018.02.020.
[44] S. K. Paul, "Controlling factors of forming limit curve: A review," *Adv. Ind. Manuf. Eng.*, vol. 2, no. January, p. 100033, 2021, doi: 10.1016/j.aime.2021.100033.
[45] W. C. Emmens, D. H. van der Weijde, and A. H. van den Boogaard, "The FLC, Enhanced Formability, and Incremental Sheet Forming," *IDDRG 09 Conf. Proc.*, no. June, pp. 773–784, 2009, [Online]. Available: http://doc.utwente.nl/69291/
[46] R. Arrieux, "Determination and use of the forming limit stress diagrams in sheet metal forming," *J. Mater. Process. Tech.*, vol. 53, no. 1–2, pp. 47–56, 1995, doi: 10.1016/0924-0136(95)01960-M.
[47] T. B. Stoughton, "General forming limit criterion for sheet metal forming," *Int. J. Mech. Sci.*, vol. 42, no. 1, pp. 1–27, 2000, doi: 10.1016/S0020-7403(98)00113-1.
[48] T. B. Stoughton and J. W. Yoon, "Path independent forming limits in strain and stress spaces," *Int. J. Solids Struct.*, vol. 49, no. 25, pp. 3616–3625, 2012, doi: 10.1016/j.ijsolstr.2012.08.004.
[49] M. Z. Haque and J. W. Yoon, "Stress based prediction of formability and failure in incremental

sheet forming," *Int. J. Mater. Form.*, vol. 9, no. 3, pp. 413–421, 2016, doi: 10.1007/s12289-015-1237-8.
[50] C. M. 'Muscat-Fenech, S. 'Arndt, and A. G. 'Atkins, "The determination of fracture forming limit diagrams from fracture toughness," *Sheet Met.*, vol. 1, pp. 249–260, 1996.
[51] N. Park, H. Huh, S. J. Lim, Y. Lou, Y. S. Kang, and M. H. Seo, "Fracture-based forming limit criteria for anisotropic materials in sheet metal forming," *Int. J. Plast.*, vol. 96, pp. 1–35, 2017, doi: 10.1016/j.ijplas.2016.04.014.
[52] P. Scallan, *Process Planning : The design / manufacture interface*, no. December. 2002.
[53] R. Lumley, *Fundamentals of aluminium metallurgy*. 2011. doi: 10.1533/9780857090256.
[54] ASTM E8, "ASTM E8/E8M standard test methods for tension testing of metallic materials 1," *Annu. B. ASTM Stand. 4*, no. C, pp. 1–27, 2010, doi: 10.1520/E0008.
[55] "Tensile Properties." https://web.archive.org/web/20140216090902/http://www.ndt-ed.org/EducationResources/CommunityCollege/Materials/Mechanical/Tensile.htm (accessed Aug. 10, 2021).
[56] N. Khlystov and J. Zheng, "Uniaxial Tension and Compression Testing of Materials," pp. 1–19, 2013.
[57] Z. Marciniak, J. L. Duncan, and S. J. Hu, *Mechanics of Sheet Metal Forming*, Second. London: Edward Arnold, 2002. doi: 10.1007/BF02330250.
[58] ISO, "Metallic materials sheet and strip determination of biaxial stress strain curve by means of bulge test with optical measuring systems," *61010-1 © Iec2001*, p. 13, 2014.
[59] L. Lăzărescu, D. S. Comşa, I. Nicodim, I. Ciobanu, and D. Banabic, "Characterization of plastic behaviour of sheet metals by hydraulic bulge test," *Trans. Nonferrous Met. Soc. China (English Ed.*, vol. 22, no. SUPPL.2, pp. 275–279, 2012, doi: 10.1016/S1003-6326(12)61719-1.
[60] K. Jawale, J. F. Duarte, A. Reis, and M. B. Silva, "Characterizing fracture forming limit and shear fracture forming limit for sheet metals," *J. Mater. Process. Technol.*, vol. 255, no. 2010, pp. 886–897, 2018, doi: 10.1016/j.jmatprotec.2018.01.035.
[61] INTERNATIONAL and STANDARD, "Metallic materials Determination of forming limit curves for sheet and in the laboratory," vol. 2021, 2021.
[62] L. Zhang, J. Min, J. E. Carsley, T. B. Stoughton, and J. Lin, "Experimental and theoretical investigation on the role of friction in Nakazima testing," *Int. J. Mech. Sci.*, vol. 133, no. August, pp. 217–226, 2017, doi: 10.1016/j.ijmecsci.2017.08.020.
[63] Z. Shao *et al.*, "Experimental investigation of forming limit curves and deformation features in warm forming of an aluminium alloy," *Proc. Inst. Mech. Eng. Part B J. Eng. Manuf.*, vol. 232, no. 3, pp. 465–474, 2018, doi: 10.1177/0954405416645776.
[64] A. Groseclose, H. S. Son, J. Dykeman, and T. Altan, "Determination of biaxial flow stress using frictionless dome test," *Procedia Eng.*, vol. 81, no. October, pp. 1079–1083, 2014, doi: 10.1016/j.proeng.2014.10.144.
[65] H. J. Kim, S. C. Choi, K. T. Lee, and H. Y. Kim, "Experimental Determination of Forming Limit Diagram and Springback Characteristics of AZ31B Mg Alloy Sheets at Elevated Temperatures," *Mater. Trans.*, vol. 49, no. 5, pp. 1112–1119, 2008, doi: 10.2320/matertrans.MC200778.
[66] S. Bruschi *et al.*, "Testing and modelling of material behaviour and formability in sheet metal forming," *CIRP Ann. - Manuf. Technol.*, vol. 63, no. 2, pp. 727–749, 2014, doi: 10.1016/j.cirp.2014.05.005.
[67] M. Bruchhausen *et al.*, "European standard on small punch testing of metallic materials," *Ubiquity Proc.*, vol. 1, no. S1, p. 11, 2018, doi: 10.5334/uproc.11.
[68] M. Bruchhausen *et al.*, "Recent developments in small punch testing: Tensile properties and DBTT," *Theor. Appl. Fract. Mech.*, vol. 86, pp. 2–10, 2016, doi: 10.1016/j.tafmec.2016.09.012.
[69] Y. W. Ma and K. B. Yoon, "Assessment of tensile strength using small punch test for transversely isotropic aluminum 2024 alloy produced by equal channel angular pressing," *Mater. Sci. Eng. A*, vol. 527, no. 16–17, pp. 3630–3638, 2010, doi: 10.1016/j.msea.2010.02.057.
[70] D. K. Cheong, "On the influence of the through-thickness strain gradients for characterization of formability and fracture of sheet metal alloys," 2019.
[71] Z. Deng and J. P. McGuire, "Development of novel forming limit curve testing method," *IOP Conf. Ser. Mater. Sci. Eng.*, vol. 418, no. 1, 2018, doi: 10.1088/1757-899X/418/1/012049.
[72] E345-93(08), "Standard Test Methods of Tension Testing of Metallic Foil 1," *ASTM B. Stand.*,

vol. 93, no. Reapproved 2008, pp. 1–5, 2013, doi: 10.1520/E0345-16.2.
[73] ASTM D638-14, “Standard Test Method for Tensile Properties of Plastics,” *ASTM Int.*, vol. 82, no. C, pp. 1–15, 2016, doi: 10.1520/D0638-14.1.
[74] I. Standard, “Metallic materials - Sheet and strip - Biaxial tensile testing methods using a cruciform test piece,” vol. 2003, 2003.
[75] T. Kuwabara, S. Ikeda, and K. Kuroda, “Measurement and analysis of differential work hardening in cold-rolled steel sheet under biaxial tension,” *J. Mater. Process. Technol.*, vol. 80–81, pp. 517–523, 1998, doi: 10.1016/S0924-0136(98)00155-1.
[76] Y. Hanabusa, H. Takizawa, and T. Kuwabara, “Numerical verification of a biaxial tensile test method using a cruciform specimen,” *J. Mater. Process. Technol.*, vol. 213, no. 6, pp. 961–970, 2013, doi: 10.1016/j.jmatprotec.2012.12.007.
[77] D. A. Kelly, “Problems in creep testing under biaxial stress systems,” *J. Strain Anal.*, vol. 11, no. 1, pp. 1–6, 1976.
[78] A. Hannon and P. Tiernan, “A review of planar biaxial tensile test systems for sheet metal,” *J. Mater. Process. Technol.*, vol. 198, no. 1–3, pp. 1–13, 2008, doi: 10.1016/j.jmatprotec.2007.10.015.
[79] Y. Yu, M. Wan, X. D. Wu, and X. Bin Zhou, “Design of a cruciform biaxial tensile specimen for limit strain analysis by FEM,” *J. Mater. Process. Technol.*, vol. 123, no. 1, pp. 67–70, 2002, doi: 10.1016/S0924-0136(02)00062-6.
[80] X. Song, “Identification of forming limits of sheet metals with an in-plane biaxial tensile test,” 2018.
[81] W. C. Emmens and A. H. van den Boogaard, “Incremental forming by continuous bending under tension -- An experimental investigation,” *J. Mater. Process. Technol.*, vol. 209, no. 14, pp. 5456–5463, 2009, doi: 10.1016/j.jmatprotec.2009.04.023.
[82] J. C. Benedyk, B. L. Kinsey, Y. P. Korkolis, and T. J. Roemer, *Fundamental Studies of Continuous Bending under Tension (CBT) and Potential Automotive Forming Applications*, vol. 2, no. 10. Elsevier Ltd., 2015. doi: 10.1016/j.matpr.2015.10.089.
[83] A. Hadoush, A. H. Van den Boogaard, and W. C. Emmens, “A numerical investigation of the continuous bending under tension test,” *J. Mater. Process. Technol.*, vol. 211, no. 12, pp. 1948–1956, 2011, doi: 10.1016/j.jmatprotec.2011.06.013.
[84] T. Barrett, B. L. Kinsey, M. Knezevic, and Y. P. Korkolis, “Numerical and experimental investigation of formability enhancement during continuous-bending-under-tension (CBT) of AA6022-T4,” *Procedia Eng.*, vol. 207, pp. 1940–1945, 2017, doi: 10.1016/j.proeng.2017.10.965.
[85] M. Zecevic, T. J. Roemer, M. Knezevic, Y. P. Korkolis, and B. L. Kinsey, “Residual ductility and microstructural evolution in Continuous-Bending-under-Tension of AA-6022-T4,” *Materials (Basel).*, vol. 9, no. 3, 2016, doi: 10.3390/ma9030130.
[86] S. Ai, R. Dai, and H. Long, “Investigating formability enhancement in double side incremental forming by developing a new test method of tension under cyclic bending and compression,” *J. Mater. Process. Technol.*, vol. 275, no. January 2019, p. 116349, 2020, doi: 10.1016/j.jmatprotec.2019.116349.
[87] R. Dai, “Experimental study of incremental sheet forming by tension under bending and compression test,” 2018.
[88] S. Ai and H. Long, “Finite element modelling of material deformation and damage by tension under cyclic bending and compression test,” *AIP Conf. Proc.*, vol. 2113, 2019, doi: 10.1063/1.5112750.
[89] S. Ai, “Novel Testing Methods of Material Deformation and Fracture Mechanism,” 2019.
[90] R. L. Kegg, “A New Test Method for Determination of Spinnability of Metals,” *Trans. ASME, Ser. B, J. Eng. Ind.*, vol. 83, no. B, pp. 119–124, 1961.
[91] S. C. Chang *et al.*, “Tube spinnability of AA 2024 and 7075 aluminum alloys,” *J. Mater. Process. Technol.*, vol. 80–81, pp. 676–682, 1998, doi: 10.1016/S0924-0136(98)00174-5.
[92] T. H. CHEN Fanglei, ZHANG Zhimin, “The Application of Spinning Technique in Belt Sheave,” *China Acad. J. Electron. Publ. House*, vol. 1, p. 4, 2007.
[93] M. ’HAYAMA and A. ’TAGO, “The fracture of walls on shear spinning - study on the spinnability of aluminium plates,” *Bull. Fac. Eng.*, vol. 17, pp. 93–103, 1968.
[94] M. and H. K. HAYAMA, “Experimental Study of Tube Spinning,” *Chem. Pharm. Bull.*, vol. 22, no. 167, pp. 769–775, 1979, [Online]. Available: https://www.jstage.jst.go.jp/article/bpb1993/17/11/17_11_1460/_pdf/-char/ja

[95] K. 'Kawai, "A Fact Data Base on Spinning Technology," *Int. Acad. Publ.*, pp. 59–62, 1989.
[96] K. 'Kawai, "A trial approach to spinning data base," *Form Tech Rev.*, pp. 44–55, 1992.
[97] H. D. Azodi, B. M. Dariani, H. Sedaghat, and H. Mohammadi, "Formability study and forming path optimization in single-point incremental forming process," *J. Adv. Manuf. Technol.*, vol. 11, no. 1, 2017.
[98] M. Kleiner, R. Göbel, H. Kantz, C. Klimmek, and W. Homberg, "Combined methods for the prediction of dynamic instabilities in sheet metal spinning," *CIRP Ann. - Manuf. Technol.*, vol. 51, no. 1, pp. 209–214, 2002, doi: 10.1016/S0007-8506(07)61501-7.
[99] M. 'HAYAMA, M. 'NAKAMURA, T. 'WATANABE, and H. 'HAMANO, "Roller pass programming in conventional spinning by N.C. spinning machine," *J. Japan Soc. Technol. Plast.*, vol. 27, no. 308, pp. 1053–1059, Sep. 1986.
[100] L. Wang, H. Long, D. Ashley, M. Roberts, and P. White, "Effects of the roller feed ratio on wrinkling failure in conventional spinning of a cylindrical cup," *Proc. Inst. Mech. Eng. Part B J. Eng. Manuf.*, vol. 225, no. 11, pp. 1991–2006, 2011, doi: 10.1177/0954405410396024.
[101] S. Kobayashi, "Instability in conventional spinning of cones," *J. Manuf. Sci. Eng. Trans. ASME*, vol. 85, no. 1, pp. 44–48, 1963, doi: 10.1115/1.3667585.
[102] M. and H. K. HAYAMA and T. Shinokura, "Study of the pass schedule in conventional simple spinning," *Bull. JSME*, vol. 13, no. 65, pp. 1358–1365, 1970, [Online]. Available: https://www.jstage.jst.go.jp/article/bpb1993/17/11/17_11_1460/_pdf/-char/ja
[103] Z. H. Li and H. Long, "An analytical model integrated with toolpath design for wrinkling prediction in conventional spinning," *J. Mater. Process. Technol.*, vol. 300, no. July, p. 117399, 2022, doi: 10.1016/j.jmatprotec.2021.117399.
[104] S. 'Takuya and Y. 'Shuji, "On the spinnability of steel sheets," *Int. Conf. Rotary Met. Process.*, vol. Proc. of 2nd, 1982.
[105] K. 'Yoshida, "Purpose and feature of Yoshida buckling test (YBT)," *J. Japan Soc. Technol. Plast.*, 1983.
[106] D. Y. Yang, J. B. Kim, and J. W. Yoon, "Wrinkling initiation and growth in modified Yoshida buckling test: Finite element analysis and experimental comparison," *Int. J. Mech. Sci.*, vol. 42, pp. 1683–1714, 2000.
[107] Z. H. Li *et al.*, "Characterization of sheet buckling subjected to controlled boundary constraints," *J. Mater. Process. Technol.*, vol. 4, no. 3, pp. 493–501, Apr. 2000, doi: 10.1115/1.1475990.
[108] W. 'Chenghe, L. 'Kezhang, and Z. 'Lu, *Metal spinning technology*, 2nd ed. Fujian: Fujian Technology Press, 2017.
[109] Dassault Systèmes Simulia, "Analysis User's Manual Volume 4," *Abaqus 6.12*, vol. IV, pp. 29.3.8–10, 2012.
[110] H. Long, L. Wang, and P. Jagger, "Tool force analysis in multi-pass conventional spinning by finite element simulation and experimental measurement," *Proc. 10th Int. Conf. Technol. Plast. ICTP 2011*, pp. 547–553, 2011.
[111] M. Kleiner, B. Heller, R. Gobel, C. Klimmek, and H. Kantz, "Finite Element Analysis of Sheet Metal Forming by Spinning," *J. Korean Soc. Precis. Eng.*, vol. 17, no. 4, pp. 38–47, Apr. 2000, [Online]. Available: http://www.dbpia.co.kr/journal/articleDetail?nodeId=NODE00845463
[112] Q. Xia, G. Xiao, H. Long, X. Cheng, and X. Sheng, "A review of process advancement of novel metal spinning," *Int. J. Mach. Tools Manuf.*, vol. 85, no. 381, pp. 100–121, 2014, doi: 10.1016/j.ijmachtools.2014.05.005.
[113] C. A. E. User, "Abaqus 6.1 2".
[114] L. Wang, "Analysis of Material Deformation and Wrinkling Failure in Conventional Metal Spinning Process," *Phd thesis*, 2012.
[115] L. Wang and H. Long, "A study of effects of roller path profiles on tool forces and part wall thickness variation in conventional metal spinning," *J. Mater. Process. Technol.*, vol. 211, no. 12, pp. 2140–2151, 2011, doi: 10.1016/j.jmatprotec.2011.07.013.
[116] S. Z. Li, "AN ANALYTICAL WRINKLING PREDICTION METHOD FOR FIRST-PASS CONVENTIONAL SPINNING," no. September, 2020.
[117] M. Shakeri, A. Sadough, and B. M. Dariani, "Effect of pre-straining and grain size on the limit strains in sheet metal forming," *Proc. Inst. Mech. Eng. Part B J. Eng. Manuf.*, vol. 214, no. 9, pp. 821–827, 2000, doi: 10.1243/0954405001517892.

[118] G. Sebastiani, A. Brosius, R. Ewers, M. Kleiner, and C. Klimmek, “Numerical investigation on dynamic effects during sheet metal spinning by explicit finite-element-analysis,” *J. Mater. Process. Technol.*, vol. 177, no. 1–3, pp. 401–403, 2006, doi: 10.1016/j.jmatprotec.2006.04.080.

[119] Rutlands Limited, “Precision Centre Finder - 200mm.” https://www.rutlands.com/sp+measuring-squares-centre-finders-precision-centre-finder-200mm-rutlandsŽ+r9007?utm_campaign=Googlebase&utm_medium=organic&utm_source=Googlebase&geoip=GB&gclid=CjwKCAjwt7SWBhAnEiwAx8ZLat0MdUV-PB54O1YISNCGJ_EAs72VMpweRC1GDC64EsCu (accessed Jul. 13, 2022).